



The
University
Of
Sheffield.

DOCTORAL THESIS

Clinical Applications of Angiographic Optical Coherence Tomography

Author:

Robert A. BYERS

Supervisor:

Prof. Stephen J. MATCHER

*A thesis submitted in fulfillment of the requirements
for the degree of Doctor of Philosophy
Electronic and Electrical Engineering*

September 17, 2018

Declaration of Authorship

I, Robert A. BYERS, declare that this thesis titled, "Clinical Applications of Angiographic Optical Coherence Tomography" and the work presented in it is my own. I confirm that:

- This work was done wholly or mainly while in candidature for a research degree at this University.
- Where I have consulted the published work of others, this is always clearly attributed.
- Where I have quoted from the work of others, the source is always given. With the exception of such quotations, this thesis is entirely my own work.
- I have acknowledged all main sources of help.
- Where the thesis is based on work done by myself jointly with others, I have made clear exactly what was done by others and what I have contributed myself.

Signed:

Date:

THE UNIVERSITY OF SHEFFIELD

Abstract

Electronic and Electrical Engineering

Clinical Applications of Angiographic Optical Coherence Tomography

by Robert A. BYERS

Angiographic optical coherence tomography (OCTA) has rapidly found utility within many facets of medical research. Here OCTA algorithms are enabled on a commercial OCT system and verified through correlation with intra-vital light microscopy (IVM). While the vast majority of vessels were accurately measured, smaller vessels ($< 30\mu m$) have a tendency to appear dilated in comparison to IVM. The technique was also expanded upon to facilitate the imaging of subcutaneous murine fibrosarcoma tumours, negating the requirement for an intra-vital window. It was found that vessel measurement sensitivity was sufficiently high such that the morphologies of vessels within tumours expressing unique vascular endothelial growth factor (VEGF) isoforms could be differentiated, potentially providing a new angle of approach in the study of anti-angiogenic treatments. OCTA was then applied to human studies of atopic dermatitis, where it was found that metrics corresponding to vessel depth and morphology could be correlated with the sub-clinical severity of the condition. Knowledge of this could be utilised to observe the therapeutic response to treatment, past the point of clinical remission. A range of image-processing techniques were also developed, including automatic segmentation of the epidermal layer within skin being utilised to quantify the degree of epidermal thinning in response to applied skin strain, calculation of the skin capillary loop density and the response of skin vessels to temperature and pressure.

Acknowledgements

I'd like to express sincere gratitude to:

Prof. Stephen Matcher, Prof. Gillian Tozer & Prof. Nicola Brown for being excellent supervisors, guiding me all throughout my research and providing valuable insight, critique and expertise at every step of the journey.

Prof. Michael Cork, Dr Simon Danby, Mrs Kirsty Brown, Mrs Elaine Pang & Mrs Bethany Mitchell for their support and guidance within the Dermatology department at the Royal Hallamshire Hospital, Sheffield.

Mr Matthew Fisher for both training and assisting me in surgical techniques and procedures, and for being there to support all of my work within the Oncology department at Sheffield.

Prof. Roger Lewis, Dr Raman Maiti & Dr Matt Carré for all of their valuable assistance and insight regarding the mechanical engineering aspects of my project.

Dr Zenghai Lu, Dr Xuesong Hu, Dr Joseph Boadi, Mrs Chrisandrea Charalambous & Mr Wei Li for a wonderful time working together, with lots of fruitful discussion regarding OCT.

Prof. Adrian Podoleanu & Dr Ali Gooya for their insightful comments and feedback.

EPSRC for their funding support.

And indeed, all of my friends and family, and those who I have met along the way; for their patience, encouragement and emotional support all throughout my PhD.

Journal and conference papers

Publications

1. **R. A. Byers**, M. Fisher, N. J. Brown, G. M. Tozer, and S. J. Matcher, "Vascular patterning of subcutaneous mouse fibrosarcomas expressing individual VEGF isoforms can be differentiated using angiographic optical coherence tomography," *Biomedical optics express.*, vol. 8, no. 10, pp. 459–467, 2017.
2. **R. A. Byers**, R. Maiti, S. G. Danby, E. J. Pang, B. Mitchell, M. J. Carré, R. Lewis, M. J. Cork and S. J. Matcher, "Sub-clinical assessment of atopic dermatitis severity using angiographic optical coherence tomography," *Biomedical optics express.*, 2018.
3. N. H. Green, R. M. Delaine-Smith, H. J. Askew, **R. Byers**, G. C. Reilly, and S. J. Matcher, "A new mode of contrast in biological second harmonic generation microscopy," *Nature Scientific Reports.*, vol. 7, no. 1, p. 13331, Dec. 2017.
4. R. Maiti, L. C. Gerhardt, Z. S. Lee, **R. A. Byers**, D. Woods, J. A. Sanz-Herrera, S. E. Franklin, R. Lewis, S. J. Matcher, and M. J. Carré, "In vivo measurement of skin surface strain and sub-surface layer deformation induced by natural tissue stretching," *J. Mech. Behav. Biomed. Mater.*, vol. 62, pp. 556–569, 2016.
5. **R. A. Byers**, G. Tozer, N. J. Brown, and S. J. Matcher, "High-resolution label-free vascular imaging using a commercial, clinically approved dermatological OCT scanner," 2016, p. 96890M. (SPIE Conference proceedings)
6. **R. A. Byers**, R. Maiti, S. G. Danby, E. J. Pang, B. Mitchell, M. J. Carré, R. Lewis, M. J. Cork, and S. J. Matcher, "Characterizing the microcirculation of atopic dermatitis using angiographic optical coherence tomography," 2017, p. 100370V. (SPIE Conference proceedings)

Conference presentations

1. 2015 British Microcirculation Society meeting - Manchester, UK.
Optimising Correlation-Mapping and Speckle-Variance Optical Coherence Tomography for In-Vivo Microcirculation Imaging (**Oral presentation**).
2. 2016 SPIE Photonics West - San Francisco, US.
High-resolution label-free vascular imaging using a commercial, clinically approved dermatological OCT scanner (**Oral presentation - Given by Prof. Matcher**).
3. 2016 British Microcirculation Society meeting - Newcastle, UK.
Angiographic OCT as a Means of Enhancing Traditional Intravital Microscopy for the Study of Tumour Vascularisation (**Poster presentation**).
4. 2016 International Symposium on Atopic Dermatitis - São Paulo, Brazil.
Advances in understanding atopic dermatitis – a morphological and functional comparison with healthy skin (**Oral presentation - Given by Dr. Danby**).
5. 2017 SPIE Photonics West - San Francisco, US.
Characterizing the Microcirculation of Atopic Dermatitis Using Angiographic Optical Coherence Tomography (**Oral presentation**).
6. 2017 Sheffield Cancer Research day - Sheffield, UK.
Microcirculatory imaging of subcutaneously implanted tumours using optical coherence tomography (OCT) (**Oral presentation**).
7. 2017 BMS & UKCAS Joint Conference - Birmingham, UK.
Non-invasive visualisation of the microvasculature within subcutaneously implanted tumours using optical coherence tomography (OCT) (**Oral presentation**).
8. 2017 BMS & UKCAS Joint Conference - Birmingham, UK.
Robust measurements of subclinical inflammation in skin affected by atopic dermatitis using angiographic optical coherence tomography. (**Poster presentation**).

Awards

1. **2017 Moor Instruments Best Technology Abstract Prize - Birmingham, UK.**
Awarded for a poster demonstrating how a non-invasive imaging modality (Angiographic optical coherence tomography) can be used to aid clinical assessment of atopic dermatitis (Eczema).
2. **2017 SPIE - Student Travel Grant - San Francisco, USA.**
Awarded \$700 to aid in travel to and from San Francisco to present a paper at Photonics West 2017.
3. **2017 BMS Student Assistant Scheme grant - Birmingham, UK.**
Awarded £250 for travel to Birmingham for the 67th Annual meeting of the British Microcirculation Society.

Contents

Declaration of Authorship	iii
Abstract	v
Acknowledgements	vii
Journal and conference papers	ix
Contents	xiii
List of Figures	xix
List of Tables	xxiii
List of Abbreviations	xxv
1 Background and Literature Review	1
1.1 Optical Coherence Tomography	1
1.1.1 Background and basic principles	1
Axis terminology	3
1.2 Swept-source OCT (SSOCT)	3
1.3 Angiographic OCT (OCTA)	6
1.3.1 Visualising the microcirculation	7
1.3.2 Intensity-based methods	8
Speckle-variance OCT	8
Correlation-mapping OCT	10
Split-spectrum amplitude-decorrelation OCT	10
1.3.3 Phase-based methods	10

1.3.4	Complex-signal methods	11
1.3.5	Summary	12
1.4	Study aims	15
References		17
2	Materials and Methods	25
2.1	Angiographic processing pipeline	25
2.1.1	The OCT system	25
2.1.2	Step 1 - Data acquisition	28
2.1.3	Step 2 - Bulk tissue motion (BTM) correction	29
	In-plane motion	33
	Out-of-plane motion	37
2.1.4	Step 3 - Converting the data from structural to angiographic format	38
	Speckle-variance OCT processing	38
	Correlation-mapping OCT processing	39
	Signal masking	39
2.1.5	Step 4 - Flattening the tissue surface	40
2.1.6	Step 5 - Motion artefact post-processing	42
	Mean intensity interpolation	43
	Wavelet/Fourier filtering	44
2.1.7	Step 6 - Optional post-processing and data visualization	49
	Visualization through <i>en-face</i> projection	49
	Visualization in 3D	52
2.1.8	In summary	53
References		57
3	Paper 1 - Angiographic OCT for the study of subcutaneous tumours.	61
3.1	Introduction	67
3.2	Materials and methods	69

3.2.1	Subcutaneous tumour implantation	69
3.2.2	Data acquisition and imaging protocol	69
3.2.3	Post-processing of data	71
3.2.4	Quantification of vessel parameters	74
3.2.5	Statistics	76
3.3	Results and discussion	78
3.3.1	Visual inspection of VEGF120 and 188 expressing tumours . . .	78
3.3.2	Evaluation of longitudinal tumour monitoring	79
3.3.3	Evaluation of OCT depth penetration	82
3.3.4	Quantitative vessel metrics	87
3.4	Conclusions	91
	References	93
4	Paper 2 - Angiographic OCT for the study of atopic dermatitis.	99
4.1	Introduction	105
4.2	Materials and Methods	108
4.2.1	Participants	108
4.2.2	Imaging protocol	108
4.2.3	Automatic quantification of vascular morphology	111
4.2.4	Automatic quantification of vascular depth	113
4.2.5	Statistics	114
4.3	Results and Discussion	116
4.3.1	Scan Cohorts	116
4.3.2	Automatic structural measurements of epidermal thickness . .	116
4.3.3	The effect of local severity on vascular depth	120
4.3.4	The effect of severity on vascular morphology in the superfi- cial vascular plexus	124
4.4	Conclusions	129
	References	131

5	Vascular morphology: correlation of OCT with IVM	139
5.1	Introduction	145
5.1.1	Background	145
5.1.2	Intravital Light Microscopy	146
5.1.3	Study aim	147
5.2	Methods	148
5.2.1	DSWC surgery	148
5.2.2	Imaging protocol	149
	IVM imaging	149
	OCT imaging	150
5.2.3	Correlation of IVM and OCT datasets	152
5.2.4	Skeletonisation of IVM and OCT datasets	155
5.3	Results and discussion	158
5.3.1	Qualitative comparison between OCT and IVM	158
5.3.2	Quantitative comparison between OCT and IVM	165
5.4	Conclusions	171
	References	173
6	Structural OCT measures of <i>in-vivo</i> skin deformation	181
6.1	Introduction	185
6.2	Materials and methods	186
6.2.1	Participant	186
6.2.2	Digital image correlation (DIC)	186
6.2.3	Optical coherence tomography	188
6.2.4	Experimental protocol	189
6.2.5	Data analysis and processing	189
	Strain analysis with DIC	189
	Epidermal thickness and skin roughness analysis with OCT	190
6.2.6	Statistics	195
6.3	Results and discussion	196

6.3.1	Results of DIC analysis	196
6.3.2	Results of OCT analysis	199
6.4	Limitations	200
6.5	Conclusions	201
References		203
7 Further image processing		209
7.1	Scan setting optimisation	209
7.2	Quantitative capillary loop analysis	215
7.3	Vascular response towards applied surface pressure	219
7.4	Vascular response towards surface temperature	222
7.5	Visualisation of wound healing processes	225
7.6	Enhanced field-of-view through vascular mosaicing	227
References		231
8 General discussion and conclusions		235
8.1	General discussion	235
8.2	Conclusion	243
A Appendix		245
A.1	Multi-beam Optical Coherence Tomography	245
A.2	Sub-pixel accurate image registration	248
A.3	Wavelet-FFT algorithm - Supporting information	252
A.4	Fractal dimension analysis - Supporting information	257
A.5	ANOVA and Tukey's HSD test - Supporting information	258
A.6	Vivosight depth calibration	260
A.7	Vivosight phase stability analysis	262
Appendix References		265

List of Figures

1.1	Example of a structural OCT scan	2
1.2	Michelson interferometer schematic	5
1.3	Summary of angiographic OCT techniques	9
1.4	Advantages and disadvantages of OCTA techniques	13
2.1	The Vivosight OCT system	26
2.2	The Vivosight probe clamp	27
2.3	svOCT data acquisition protocol	30
2.4	cmOCT data acquisition protocol	31
2.5	Feature-based image registration	33
2.6	Intensity-based image registration	35
2.7	Layers of vasculature within skin	40
2.8	B-scan flattening process	41
2.9	Artefacts persisting after image registration	42
2.10	Interpolation method of removing vertical artefacts	43
2.11	Removal of vertical line artefacts in the Fourier domain	46
2.12	Single-level wavelet decomposition	47
2.13	Multi-level wavelet decomposition	48
2.14	The effect of wavelet/fft filtering	50
2.15	Depth projected image generation	51
2.16	3D image generation	53
2.17	Flowchart of the angiographic processing pipeline	54
2.18	Angiographic GUI	55
3.1	Experimental setup for subcutaneous tumour imaging	70

3.2	Effect of wavelet-FFT filtering on a fs188 tumour	72
3.3	Skeletonisation procedure for subcutaneous tumour imaging	75
3.4	Angiographic OCT images of vessels inside both baseline murine skin and subcutaneous tumours	77
3.5	Longitudinal visualisation of vessel growth within subcutaneous tu- mours	80
3.6	Quantitative vessel length within subcutaneous tumours	81
3.7	Comparison between histology and OCT (Subcutaneous tumours) . . .	83
3.8	Hypodermis thickness in subcutaneous tumours compared to healthy skin	84
3.9	CD31 immunohistochemistry demonstrating the presence of endothe- lial cells lining the vessels within the rear-dorsum skin of CD1 nude mice	86
3.10	Quantitative metrics extracted from the subcutaneous tumour micro- circulation	90
4.1	The structure of skin affected by epidermal thickening	107
4.2	Experimental setup for AD imaging	109
4.3	Skeletonisation procedure for AD imaging	111
4.4	Automatic quantification of vascular depth	115
4.5	Structural measurement of epidermal thickness within AD skin	118
4.6	Vessel morphologies at a range of AD severities	121
4.7	Charts showing differences in the CLD, SPD and epidermal-dermal junction depth at both the cubital fossa and popliteal fossa skin sites for a range of AD severities	122
4.8	Vessel morphologies at a range of AD severities	126
4.9	Quantitative measurements of vessel morphology in AD patients . . .	127
5.1	DSWC model	147
5.2	IVM imaging setup	150
5.3	OCT imaging setup	151

5.4	Flattening of DSWC datasets	152
5.5	Initial registration of IVM and OCT images	154
5.6	Normal vasculature within DSWCs	159
5.7	Verification of the fatty layer	160
5.8	Tumour vasculature within DSWCs	162
5.9	Longitudinal OCT/IVM of an fs188 tumour growing in a DSWC . . .	164
5.10	Comparison of automatically measured and registered vessel diameters with OCT/IVM	166
5.11	Graphs showing variation in measured vessel metrics within DSWCs .	167
5.12	Histogram of vessel diameters across all DSWCs	168
6.1	DIC setup for skin strain imaging	187
6.2	OCT setup for skin strain imaging	189
6.3	Pre-processed OCT B-scan	191
6.4	Detected SC and DEJ	192
6.5	Normalization of detected SC and DEJ	193
6.6	Refined epidermal thickness measurements	195
6.7	Skin surface strain measured with DIC	196
6.8	OCT images of forearm skin in different quasi-static positions	198
7.1	Layers used for svOCT and cmOCT comparison	211
7.2	svOCT and cmOCT comparison (Scans A-D)	212
7.3	svOCT and cmOCT comparison (Scans E-H)	213
7.4	Zoomed svOCT and cmOCT comparison)	214
7.5	Capillary loop analysis	218
7.6	Vascular response towards applied surface pressure	222
7.7	Vascular response towards surface temperature	224
7.8	Wound healing image 1	226
7.9	Wound healing image 2	227
7.10	svOCT scan mosaicking	229
8.1	Gate-width implementation	236

8.2	Comparison between OCTA techniques	238
8.3	Capillary loop GUI	241
A.1	Multi-beam OCT generation	245
A.2	Multi-beam OCT arrangement	246
A.3	Channel blending	247
A.4	Image registration algorithm 4	252
A.5	Wavelet-FFT comparison 2	253
A.6	Wavelet-FFT comparison 2	254
A.7	Wavelet FFT algorithm	257
A.8	Hausdorff fractal dimension calculation	258
A.9	Vivosight thickness calibration	261
A.10	Vivosight phase stability 1	262
A.11	Vivosight phase stability 2	263
A.12	Vivosight phase stability 3	264

List of Tables

2.1	Key parameters and their effect on angiographic imaging	32
2.2	Overview of GUI features	56
6.1	Strains measured using DIC	197

List of Abbreviations

Optical coherence tomography terms

cmOCT	Correlation-mapping OCT
OCT	Optical Coherence Tomography
OCTA	OCT Angiography
OFDI	Optical Frequency Domain Imaging
OMAG	Optical Microangiography
SBOCT	Spectrometer-based OCT
SDOCT	Spectral-domain OCT
SSOCT	Swept Source OCT
svOCT	Speckle-variance OCT
TDOCT	Time-domain OCT

Mathematical/statistical operations

ANOVA	Analysis of Variance
CLAHE	Contrast Limited Adaptive Histogram Equalization
FFT	Fast-Fourier Transform
HSD	Honest Significant Difference
IDFT	Inverse Discrete Fourier Transform
MIP	Mean Intensity Projection
SD	Standard Deviation

Anatomical/biological terms

CLA	Capillary Loop Area
CLD	Capillary Loop Depth/Density
DEJ	Dermal-Epidermal Junction
SC	Stratum Corneum
SPD	Superficial Plexus Depth
VEGF	Vascular Endothelial Growth Factor

Imaging modalities (Excluding OCT)

DIC	Digital Image Correlation
IVM	Intra-Vital Microscopy
MPM	Multi-Photon Microscopy
VC	Video Capillaroscopy

General terms

AD	Atopic Dermatitis
BTM	Bulk Tissue Motion
CD31	Cluster of Differentiation 31
DSWC	Dorsal Skin-fold Window Chamber
EASI	Eczema Area and Severity Index
FDML	Fourier Domain Mode Locked
FOV	Field of View
GPU	Graphical Processing Unit
GUI	Graphical User Interface
H&E	Hamatoxylin and Eosin
IP	Intraperitoneal
NA	Numerical Aperture
POV	Point of View
SCID	Severe Combined Immunodeficiency
SCORAD	Severity Scoring of Atopic Dermatitis
SURF	Speeded up Robust Features
TEWL	Trans-Epidermal Water Loss

Chapter 1

Background and Literature Review

1.1 Optical Coherence Tomography

Optical coherence tomography (OCT) is an imaging modality which utilises interference between the backscattered signal from a sample under investigation and a local reference signal to perform non-invasive imaging. In its regular configuration, one-dimensional axial scans (Termed A-scans) are generated which quantify the sample reflectivity profile as a function of depth. A transverse scanner can then be employed to move the beam laterally across the sample, collating adjacent A-scans to produce two-dimensional cross-sectional images in an axial/lateral coordinate system (Termed B-scans). Commonly, a second transverse scanner is employed in a direction perpendicular to the first, enabling three-dimensional volumetric data collection. This scanning approach to volume acquisition is illustrated in fig. 1.1 below.

1.1.1 Background and basic principles

Since the early developments in biomedical interferometry[1] and its initial introduction by Huang *et al* in 1991[2], the rapid development and application of OCT has cemented its position as a highly sensitive optical modality with many potential biomedical applications[3]. One key advantage of the technique is that the axial resolution within tissue is decoupled from the numerical aperture of the microscope objective, making it an ideal technology for studying tissues such as the eye[4].

The primary mechanism by which OCT generates images of tissue morphology is known as low coherence interferometry, a process in which two light waves are

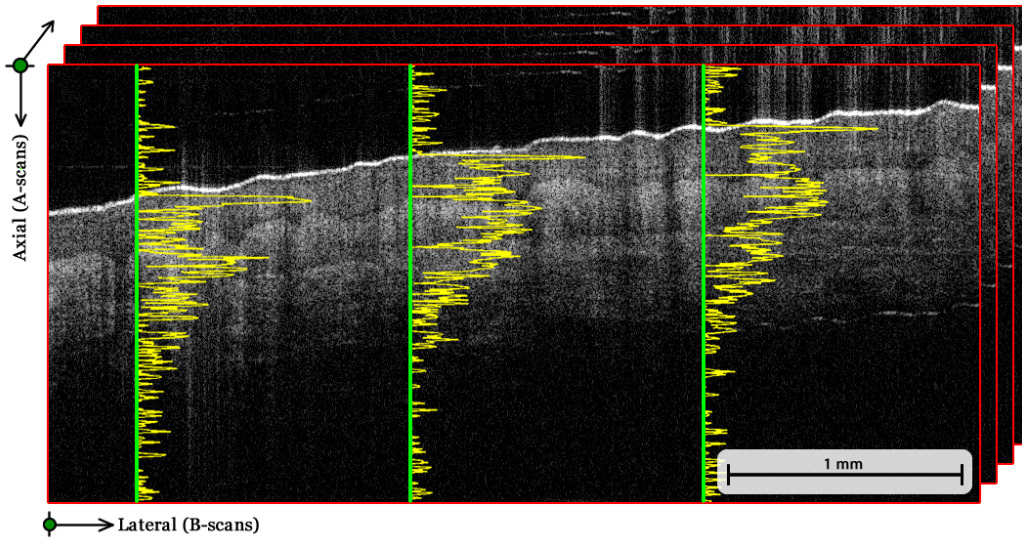


FIGURE 1.1: A stack of structural B-scan OCT images of the fingertip showing the demodulated OCT signal at three different A-scan positions ($x = 90,370,670$). Green lines show the lateral location of the one-dimensional A-scans, yellow lines show the corresponding demodulated signal amplitude. Each 952×447 B-scan was produced by scanning the sample beam laterally across the sample surface, taking a total of 952 A-scans per image.

superimposed upon one another in order to extract useful information. To achieve this, the output of a low-coherence (Coherence length l_c) optical source is directed to a beam-splitter, with one beam traveling down a reference arm (path length l_r) while the second beam travels down a sample arm (path length l_s). The optical path difference (OPD) is defined as the absolute difference between the two beam paths $|l_s - l_r|$. The beam that travels down the reference arm is reflected from a reference mirror while the beam that travels down the sample arm enters the sample and is partially reflected upon encountering any impedance mismatch between interfaces. Following reflection, both beams are directed back through the beam-splitter, interfering together before being detected at a photodetector. Due to the low-coherence source, stable interference will only occur when the optical path difference is less than the coherence length of the source beam ($OPD < l_c$), a concept known as coherence-gating.

Currently, two main configurations of OCT exist: time-domain OCT (TDOCT)

and spectral-domain OCT (SDOCT). TDOCT modulates the OPD by mechanically moving the reference mirror and changing the path length of the reference arm. Comparatively, SDOCT spectrally interrogates the interferometer output in order to deliver the entire reflectivity profile simultaneously, this is achieved either through the use of a spectrometer based photodetector coupled to a broadband source (Spectrometer based OCT - SBOCT), or a system utilising a frequency swept, narrow-band light source (Swept-source OCT - SSOCT). The latter of which (SSOCT) is used primarily within the work of this thesis, and will be described in greater detail in Sec.1.2 below.

Axis terminology

Throughout this thesis, the following terminology is used when referring to the imaging dimensions of OCT:

- **X-axis** - Defined as the transverse "fast-scanning" direction.
- **Y-axis** - Defined as the transverse "slow-scanning" direction.
- **Z-axis** - Defined as the the axial direction (Along the direction of the beam).

1.2 Swept-source OCT (SSOCT)

The underlying principles of SSOCT were first demonstrated experimentally in 1997[5], [6], however the relative performance advantages in comparison to TDOCT were not fully understood at that time. While TDOCT systems are limited in speed due to the mechanical movement of the reference mirror[7], SSOCT systems are primarily limited by the tuning speed of the optical source. Recent developments in swept-frequency optical sources have enabled SSOCT axial scan speeds in excess of 5MHz[8], far exceeding the speeds reachable by TDOCT ($\approx 30kHz$ using air-turbine driven rotational mirrors[9]). In addition to axial scanning speed, studies have also highlighted the increased sensitivity of SDOCT, beginning with Mitsui *et al* demonstrating that the dynamic range of an SBOCT system exceeds that of a comparable

TDOCT system by a factor proportional to the number of independent pixels of the spectrometer[10] (Also known as Fellgett's advantage), similar observations have since been made for SSOCT[11].

Figure 1.2 shows a typical SSOCT setup. As described in Sec. 1.1.1, signal from the reference and sample arms have a time offset determined by the OPD. Since the frequency of the source is being swept as a function of time, backscattered light in the sample arm will have a frequency offset from the light in reference arm. When the two waves interfere together, the result is a modulation or "beat" at a frequency corresponding to the offset between the two waves. As a result, backscattered signals originating from unique depths within the sample are encoded as unique modulation frequencies in the output measured by the photodetector. An A-scan is thus generated by digitising the output of the photodetector while the frequency is swept, and Fourier-transforming the result in order to extract the magnitude of signal corresponding to each echo-delay. Any non-linearities in the frequency sweep of the laser must be corrected prior to Fourier-transforming such that the signal is sampled in intervals of frequency rather than time, a process which can be performed by either numerically resampling the acquired interference signal (if a calibration of frequency vs time of the laser sweep has been performed) or by clocking the digitiser in the photodetector at equal frequency intervals (requires a hardware "k-clock")[12].

Numerous parameters hold critical importance to the performance of an SSOCT system. Axial resolution determines the systems ability to discern structures along the axis of the beam, in the axial-direction, intuitively it is determined by the coherence length of the source:

$$Axial\ resolution(\delta z) = l_c = \frac{\lambda_0^2}{\Delta\lambda} \quad (1.1)$$

Here λ_0 is the central wavelength of the optical-source, and $\Delta\lambda$ is the tuning range of the frequency sweep.

Lateral resolution determines the ability of the system to discriminate between structures in the *en-face* transverse plane, as discussed in Sec. 1.1.1 one of the key advantages of OCT imaging is that the axial and lateral resolutions are de-coupled,

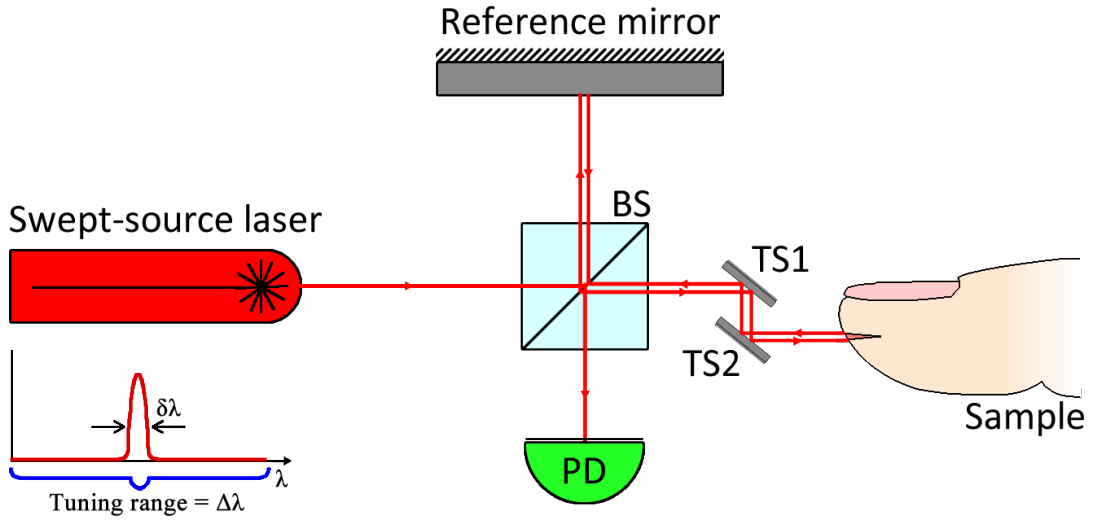


FIGURE 1.2: Schematic of a SSOCT system showing a traditional Michelson interferometer setup. The output from a narrow-band, sweeping frequency laser source is fed into a beam-splitter with signal being directed to a reference and sample arm. The recombined signal is then detected by a photodetector. BS: Beam-splitter, TS1/2: Transverse scanners, PD: Photodetector.

with only lateral resolution depending upon the microscope optics:

$$Lateral\ resolution(\delta x) = \frac{4\lambda_0 f}{\pi d} \quad (1.2)$$

Here f is the focal length of the objective lens and d is the size of the incident beam. In short, higher lateral resolution relies on a large numerical aperture, focusing the beam to a small spot size incident to the sample.

One of the key disadvantages of SSOCT in comparison to TDOCT is a loss of sensitivity with imaging depth. For SSOCT, maximum sensitivity is centered upon zero OPD and reduces as the delay increases. This is due to the limited linewidth ($\delta\lambda$) of the sweeping laser placing restrictions on the discernible resolution of the interference spectrum. An equivalent coherence length (L_c) can be defined for SSOCT, which is inversely proportional to the linewidth of the source and can be thought of as an upper bound for the axial range:

$$Maximum\ axialrange = L_c = \frac{\lambda_0^2}{\delta\lambda} \quad (1.3)$$

This is not to be confused with penetration depth, which is limited by scattering and absorption of the incident beam within the sample. Overall, the maximum penetration depth is defined as the depth at which the returning sample waveform retains enough strength to achieve an interferogram signal exceeding the noise of the system.

Another notable downside of both SDOCT methods in comparison to TDOCT is the presence of mirror artefacts originating from sample structures positioned above the zero-OPD point of the system[13]. While it is possible to remove such artefacts and gain access to the full axial imaging range through application of phase shifted complex inteferograms[14] or Talbot bands[15], most applications simply position the zero-OPD point of the system above the sample to imaged. This infers a relative loss of sample sensitivity compared to a case where the zero-OPD point can be positioned in the center of the sample under consideration.

Overall, despite the limitations of SSOCT, the superior imaging speed and sensitivity make it an excellent candidate for applications which benefit from high-speed image acquisition. Notably *in-vivo* imaging of mobile samples or functional OCT imaging of fluid flow (See Sec. 1.3) both benefit greatly from increased imaging speed.

1.3 Angiographic OCT (OCTA)

The principles and developments discussed in sec. 1.1 illustrate how simple structural OCT imaging is performed. In testament to the flexibility of the OCT modality, numerous functional extensions have also been developed over the years. Such functional extensions include: angiographic OCT (OCTA)[16], polarisation-sensitive OCT (PS-OCT)[17] and optical coherence elastography (OCE)[18]. The former of which (OCTA), was the primary technique utilised for this work. The following subsection will introduce OCTA and illustrate the mechanisms by which previously unavailable contrast can be extracted from the structural OCT images.

1.3.1 Visualising the microcirculation

Within the superficial layers of the skin, a dense horizontal plexus of microvessels branch into perforating capillary loops which rise upwards towards the epidermis. These vessels play a vital role in the homoeostasis of the local environment, being partially responsible for the regulation of body temperature, regulation of vascular resistance, blood pressure and localised blood flow[19]. Furthermore, this microcirculation facilitates the diffusion of nutrients and metabolic waste between the epidermis and the dermal papillae[20]. As such, this superficial vascular plexus represents a key model in the understanding and evaluation of both vascular function and dysfunction[21]. Structural and functional abnormalities in both the capillary loops and underlying horizontal plexus have shown to be indicative of various pathological conditions, including: type-1/2 diabetes[22], dermatomyositis[23], [24], Reynaud's phenomenon[25] and non-melanoma skin cancer[26], [27]. Furthermore, the ability to visualise alterations within the microcirculation has demonstrated direct clinical application in both the early diagnosis[28] and monitoring[29], [30] of disease progression.

One of the most widespread applications of OCTA is within ophthalmology for the imaging of the human retina and anterior segment of the eye, providing morphological images which are comparable to the gold standard of fluorescein angiography while also being non-invasive[31]. Here OCT provides a high axial-resolution, allowing for segmentation of the layers (e.g ganglion cell layer, inner/outer plexiform layer) within the eye. Applications of OCTA within ophthalmology include the assessment of macular holes[32], diagnosis of macular edema[33] and in the assessment of age-related macular degeneration[34], among a host of other applications.

Given the immediate clinical desire to visualize and study such microvessels, it is perhaps unsurprising that numerous extensions have been developed for OCT to achieve this purpose. In short, angiographic OCT is a broad term describing a set of processing techniques which aim to extract information pertaining to the microcirculation within tissue. These techniques can be broadly categorized into three main subsets: those that utilise the intensity of the OCT signal, those that utilise the phase

of the OCT signal and those that combine both aspects and make use of the complex signal amplitude. A selection of these methods is summarized in fig. 1.3.

1.3.2 Intensity-based methods

Intensity-based OCT angiography is generally implemented through decorrelative measurement techniques which utilise the structural (Intensity) information from processed OCT B-scans. Moving fluids or tissue interfaces cause the intensity within a voxel to decorrelate over time, which can be detected as either a high localised speckle-variance, or a low inter-frame correlation coefficient. Comparatively, the signal intensity within stationary, solid regions of tissue remains comparatively stable over time, only fluctuating due to noise.

Speckle-variance OCT

One technique that uses this decorrelative nature of flow is termed speckle-variance OCT (svOCT), which was introduced by Barton *et al* in 2005[35]. This work was expanded upon by Mariampillai *et al* in 2008 who used a high-speed Fourier domain mode locked (FDML) swept source laser to rectify the low resolution and frame-rate hindrances that were present in the previous work[36]. This method remains popular since it does not require the sensitive OCT phase information that is central to the phase and complex-signal processing methods described below, it does however require dense sampling of OCT B-scans in order to extract the temporal speckle-decorrelation.

Briefly, speckle-variance OCT measures the decorrelation within individual voxels over a period of time. To estimate the magnitude of decorrelation, a number of frames are acquired from the same cross-section of tissue and the variance in signal intensity for each pixel is quantified. This method is used extensively within this thesis and is detailed further in Sec. 2.1.2.

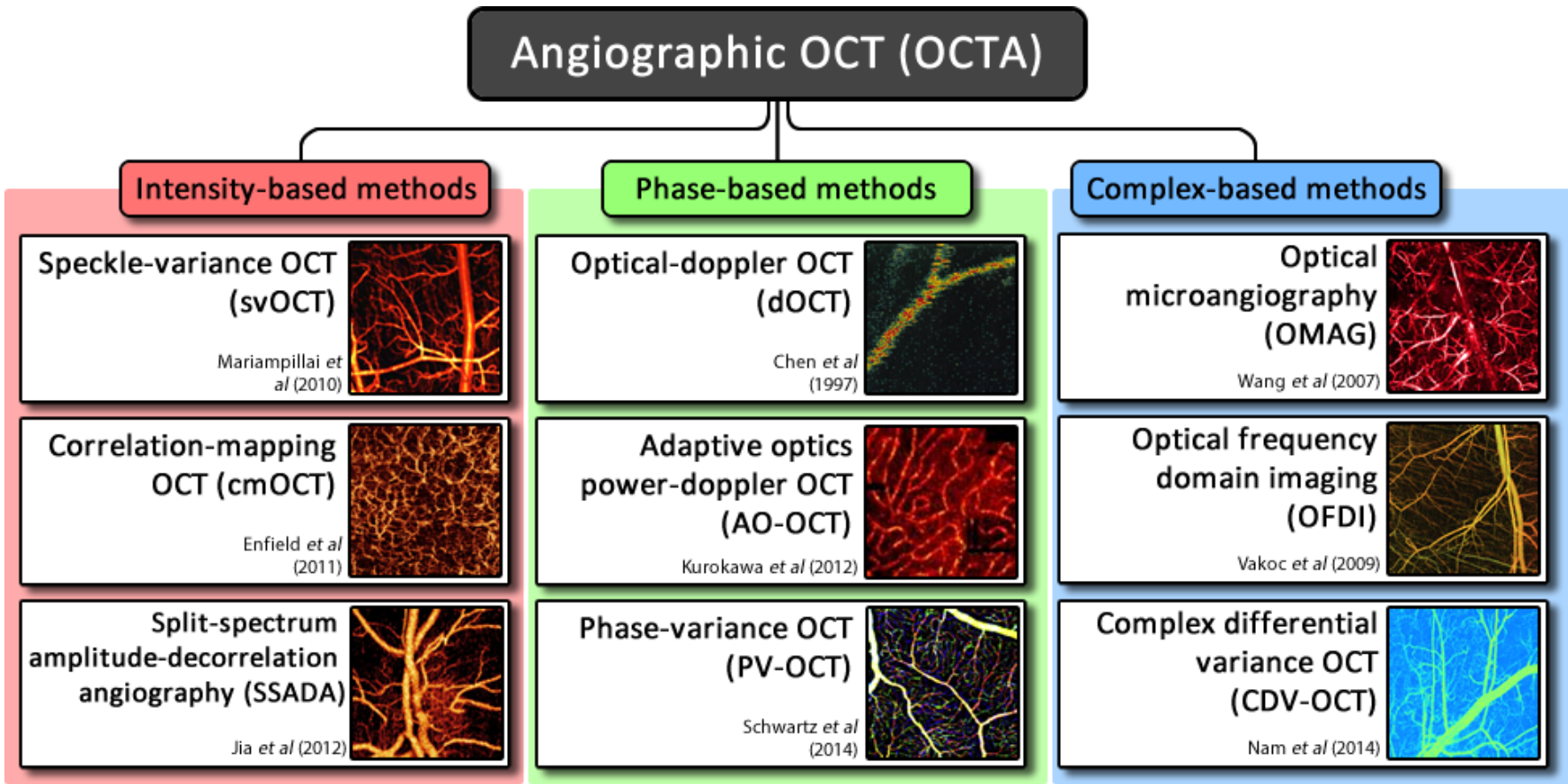


FIGURE 1.3: A selection of angiographic OCT techniques that have been previously demonstrated. These can be subdivided into three main categories, those that utilise the intensity decorrelation information, those that utilise phase-differences and those that utilise the entire complex OCT signal.

Correlation-mapping OCT

In 2011, Leahy *et al* demonstrated an alternative method of quantifying the intensity-variance within a volume, using a method known as correlation-mapping OCT (cmOCT)[37], [38]. This method uses the cross-correlation between two frames captured at the same spatial location to infer variance over kernels in the imaging (X-Z) plane. This is advantageous in that a dense sampling of images is no longer required at each y-location, decreasing imaging times, however spatial resolution in the imaging (X-Z) plane is sacrificed due to the kernel cross-correlation operation. For example, if a kernel size of 3x3 pixels is used, the cross-correlation process is effectively averaging the decorrelation over an area of 9-pixels. This method is detailed further in Sec. 2.1.2 and is compared with svOCT in Sec. 7.1.

Split-spectrum amplitude-decorrelation OCT

A third technique, known as split-spectrum amplitude-decorrelation angiography was developed in 2012 by Jia *et al*[39]. This technique splits the OCT imaging spectrum into several narrow spectral bands and performs the decorrelation measurement between each band, averaging the result. Resulting in an improved signal-to-noise ratio (SNR) when compared to svOCT and cmOCT[39].

For this work, svOCT and cmOCT were identified as ideal candidates for performing OCTA imaging using the Vivosight OCT system (Sec. 2.1.1), owing to limited phase stability which is required for the methods detailed below (Appendix A.7). A comparison between these two processing methodologies was performed (Sec. 7.1), with svOCT being selected as the primary processing method for the remainder of the study.

1.3.3 Phase-based methods

Phase-based OCT angiography gained interest due to its ability to quantify the axial flow velocity of blood cells within a vessel using the Doppler effect[40], [41]. This is achieved through analysis of the phase-difference ($\Delta\phi$) between either laterally

or temporally adjacent A-scans. The axial-velocity (v_{axial}) of the fluid can then be calculated as:

$$v_{axial} = \frac{\lambda \Delta \phi}{4\pi n \Delta t} \quad (1.4)$$

Here n is the refractive index of the tissue, λ is the centre wavelength of the source and Δt is the time interval between the A-scan acquisitions. Morphological phase-based OCT angiography has also been achieved through calculation of the absolute phase-difference in a similar manner to svOCT[42], or the squared phase difference (power Doppler)[43]. The applicability and effectiveness of these techniques is reliant on a phase-stable light source and stable sample[44].

1.3.4 Complex-signal methods

Complex-signal processing methods emerged to exploit both the intensity and phase information of OCT signals in order to achieve a higher level of vascular contrast and stability than that demonstrated by purely intensity or phase-based methods. Similar to phase-based methods, the signal of either laterally or temporally adjacent A-scans is analysed and processed in order to extract meaningful angiographic information. Previously this has been demonstrated using a complex differential variance approach, which utilised the additional degree of phase-information to intrinsically reject the effect of axial movements through suppression of phase-modulations[45]. In addition, both optical microangiography (OMAG)[46] and optical frequency-domain imaging (OFDI)[47], [48] have demonstrated highly sensitive morphological vascular imaging. Since the time-interval (Δt) between A-scans is inversely proportional to the flow-speed of the blood (eq. 1.4), a large time-interval is required in order to capture the slower flowing blood within smaller capillaries. Thus to enable capillary imaging without compromising the overall volume scan speed of the OCT system, processing developments such as ultra-high sensitive OMAG have been demonstrated, which utilise inter B-scan comparison in order to evaluate the angiographic signal[49].

1.3.5 Summary

Fig. 1.4 summarises some of the advantages and disadvantages of the discussed techniques.

Intensity-based methods	
Speckle-variance OCT (svOCT)	<ul style="list-style-type: none"> + Simple in terms of implementation and data processing. + Does not require the sensitive phase-information. + Flexible choice in imaging parameters – The gate-width can be extended to facilitate the capture of slower flowing fluids. - Provides no quantitative information regarding the flow speed of the blood (Unless the rate of decorrelation can be measured). - The quality of the resulting images is dependent on a large enough gate-width (N), leading to lengthy scan times.
Correlation-mapping OCT (cmOCT)	<ul style="list-style-type: none"> + Simple in terms of implementation and data processing. + Does not require the sensitive phase-information. + Can be applied to clinical scanning strategies, providing the spacing of scans in the lateral direction is small enough that complete inter-frame decorrelation is avoided. + Fast to acquire as only two-frames are required for each measure of decorrelation. - Loss of resolution in the imaging plane (X-Z) due to the cross-correlation operation. Can be minimised by using smaller kernel sizes at the expense of scan quality. - Provides no quantitative information regarding the flow speed of the blood. - Non-trivial to scale this method based on the application, generally processing is fixed between two-frames only.
Split-spectrum amplitude-decorrelation OCT (SSADA)	<ul style="list-style-type: none"> + Greater vessel sensitivity than other intensity-based methods. + Does not require the sensitive phase-information. + Flexible choice in imaging parameters – The gate-width can be extended to facilitate the capture of slower flowing fluids. - More complex data processing requirements, increasing the amount of offline processing required. - Provides no quantitative information regarding the flow speed of the blood.

Fig. 1.4 continues on the following page...

Phase-based methods	
Optical-doppler OCT (dOCT)	<ul style="list-style-type: none"> + Provides quantitative flux information regarding the speed of fluid flow relative to the beam angle. - Requires sensitive phase-information, and is thus very sensitive to bulk-tissue motion. - Flow information cannot be directly quantified without prior knowledge of the vessel morphology. (Lack of signal from flow which is perpendicular to the beam direction). - Phase wrapping must be accounted for, increasing complexity.
Adaptive optics power-doppler OCT (AO-OCT)	<ul style="list-style-type: none"> + Improved vessel sensitivity compared to intensity-based methods in certain regions. Doppler methods work well in areas where flow is expected to be high in a direction parallel to the beam. + Increased lateral resolution when compared to dOCT due to the tight focusing of the probe beam by the adaptive optics. - Requires additional hardware (Deformable mirror). - Very sensitive to bulk-tissue motion. - Phase wrapping must be accounted for, increasing complexity.
Phase-variance OCT (PV-OCT)	<ul style="list-style-type: none"> + Simple implementation (Similar to svOCT but using the phase information). + Theoretically more sensitive to slower flowing blood than comparable intensity-based methods. The method has less angular dependence than dOCT by measuring the variance of the phase-shift - Reliance on the phase information increases the sensitivity to bulk tissue motion and requires a phase-stable optical source. - Lack of quantitative information regarding fluid flow speed, but the potential to measure this due to the increased phase sensitivity.
Complex-based methods	
Optical-microangiography (OMAG)	<ul style="list-style-type: none"> + Use of both phase and amplitude information improves the sensitivity of flow detection (i.e flow can be detected even when only the sensitive phase information is affected) while retaining the robustness towards bulk tissue motion as seen in the intensity based methods. + Is capable of providing flow directionality information. - Requires a phase-stable optical source.
Optical frequency domain imaging (OFDI)	<ul style="list-style-type: none"> + Use of both phase and amplitude information improves the sensitivity of flow detection (i.e flow can be detected even when only the sensitive phase information is affected) while retaining the robustness towards bulk tissue motion as seen in the intensity based methods. - Requires a phase-stable optical source.
Complex differential variance OCT (CDV-OCT)	<ul style="list-style-type: none"> + Achieves higher vascular contrast and sensitivity in comparison to purely intensity based methods. + CDV algorithm intrinsically rejects axial bulk tissue motion artefacts, further improving image quality. - Requires a phase-stable optical source.

FIGURE 1.4: The advantages and disadvantages of each OCTA technique.

As mentioned above, the speckle-variance and correlation-mapping methods were used within this thesis. For the applications herein, often the primary concern was measuring the morphological angiographic signal from vessels which were positioned almost perpendicular to the incident OCT beam. For example, the superficial vascular plexus (measured in chapter 4) within skin is situated in a mostly flat plane below the dermal epidermal junction. Similarly, vessels within a dorsal-skin fold chamber (measured in chapter 5) are situated mostly flat against the glass. Such vessels have a very low axial-velocity which yields a low signal-to-noise (SNR) ratio from the phase based methods. In addition, the use of a swept-source OCT system meant that phase-noise (Introduced by timing "jitters" and variations in the cycle-to-cycle tuning) made phase variance methods challenging (Investigated further in the appendix, App. A.7). Thus intensity based methods were selected as the primary processing methodology.

1.4 Study aims

The primary aim of this research was to integrate OCTA on a commercial OCT system (Described in Sec. 2.1.1) and develop software which allowed for robust measures of tissue vasculature to be performed. Following software development (Chapter 2), the aim was to apply the technique to a range of clinically relevant scenarios:

- **Oncology** - The study of vasculature within murine fibrosarcoma tumours grown both intravitally (Chapter 5) and subcutaneously (Chapter 3). In particular, we aimed to evaluate the potential of OCTA as a tool for studying resistance mechanisms towards anti-angiogenic therapy targeted at tumours.
- **Dermatology** - The study of vasculature within inflammatory skin conditions such as Atopic Dermatitis (Chapter 4) and Psoriasis. In particular, if there are any subclinical traces of the condition that persist in the microcirculation which could aid in treatment optimization.
- **Tribology** - We aimed to investigate the relationship between applied surface strains and the deformation of underlying skin layers (Chapter 6). Providing information regarding the response of skin to mechanical loading and stretching.
- **Validation** - To verify the accuracy of any detected vessels. Correlation of OCTA with an established imaging technique would provide confidence that vessels are being accurately represented at all scales (Chapter 5).

References

- [1] E. Kleberger, H. .-J. Plöhn, and G. Simonsohn, "Zur Brechungsindexverteilung in der Augenlinse", *Albrecht von Graefe's Archive for Clinical and Experimental Ophthalmology*, vol. 176, no. 2, pp. 155–159, Oct. 1968, ISSN: 0065-6100. DOI: 10.1007/BF02385044 (cit. on p. 1).
- [2] D. Huang, E. A. Swanson, C. P. Lin, J. S. Schuman, W. G. Stinson, W. Chang, M. R. Hee, T. Flotte, K. Gregory, C. A. Puliafito, J. G. Fujimoto, and E. A. Swanson, "Optical Coherence Tomography", *Science, New Series*, vol. 254, no. 5035, pp. 1178–1181, 1991 (cit. on p. 1).
- [3] A. F. Fercher, W. Drexler, C. K. Hitzenberger, and T. Lasser, "Optical coherence tomography – development, principles, applications", *Zeitschrift für Medizinische Physik*, vol. 20, no. 4, pp. 251–276, 2010, ISSN: 0939-3889. DOI: <http://dx.doi.org/10.1016/j.zemedi.2009.11.002> (cit. on p. 1).
- [4] W. DREXLER and J. FUJIMOTO, "State-of-the-art retinal optical coherence tomography", *Progress in Retinal and Eye Research*, vol. 27, no. 1, pp. 45–88, Jan. 2008, ISSN: 13509462. DOI: 10.1016/j.preteyeres.2007.07.005 (cit. on p. 1).
- [5] S. R. Chinn, E. A. Swanson, and J. G. Fujimoto, "Optical coherence tomography using a frequency-tunable optical source", *Optics Letters*, vol. 22, no. 5, p. 340, Mar. 1997, ISSN: 0146-9592. DOI: 10.1364/OL.22.000340 (cit. on p. 3).
- [6] B. Golubovic, B. E. Bouma, G. J. Tearney, and J. G. Fujimoto, "Optical frequency-domain reflectometry using rapid wavelength tuning of a Cr⁴⁺:forsterite laser", *Optics Letters*, vol. 22, no. 22, p. 1704, Nov. 1997, ISSN: 0146-9592. DOI: 10.1364/OL.22.001704 (cit. on p. 3).

-
- [7] Y. K. Kim and Y. P. Kim, "High-speed time-domain optical coherence tomography with an imaging speed of ten frames per second with 2000 A-scan", *Optical Engineering*, vol. 49, no. 5, p. 055 601, May 2010, ISSN: 0091-3286. DOI: 10.1117/1.3425659 (cit. on p. 3).
- [8] W. Wieser, B. R. Biedermann, T. Klein, C. M. Eigenwillig, and R. Huber, "Multi-megahertz OCT: High quality 3D imaging at 20 million A-scans and 4.5 GVoxels per second.", *Optics express*, vol. 18, no. 14, pp. 14 685–704, Jul. 2010, ISSN: 1094-4087 (cit. on p. 3).
- [9] J. Szydlo, N. Delachenal, R. Gianotti, R. Wälti, H. Bleuler, and R. Salathé, "Airturbine driven optical low-coherence reflectometry at 28.6-kHz scan repetition rate", *Optics Communications*, vol. 154, no. 1-3, pp. 1–4, Aug. 1998, ISSN: 0030-4018. DOI: 10.1016/S0030-4018(98)00303-4 (cit. on p. 3).
- [10] T. Mitsui, "Dynamic Range of Optical Reflectometry with Spectral Interferometry", *Japanese Journal of Applied Physics*, vol. 38, no. Part 1, No. 10, pp. 6133–6137, Oct. 1999, ISSN: 0021-4922. DOI: 10.1143/JJAP.38.6133 (cit. on p. 4).
- [11] M. Choma, M. Sarunic, C. Yang, and J. Izatt, "Sensitivity advantage of swept source and Fourier domain optical coherence tomography.", *Optics express*, vol. 11, no. 18, pp. 2183–9, Sep. 2003, ISSN: 1094-4087 (cit. on p. 4).
- [12] A. F. Fercher, W. Drexler, C. K. Hitzenberger, and T. Lasser, "Optical coherence tomography — principles and applications", *REPORTS ON PROGRESS IN PHYSICS*, vol. 66, pp. 239–303, 2003 (cit. on p. 4).
- [13] A. G. PODOLEANU, "Optical coherence tomography", *Journal of Microscopy*, vol. 247, no. 3, pp. 209–219, Sep. 2012, ISSN: 00222720. DOI: 10.1111/j.1365-2818.2012.03619.x (cit. on p. 6).
- [14] A. Bachmann, R. Leitgeb, and T. Lasser, "Heterodyne Fourier domain optical coherence tomography for full range probing with high axial resolution", *Optics Express*, vol. 14, no. 4, p. 1487, Feb. 2006, ISSN: 1094-4087. DOI: 10.1364/OE.14.001487 (cit. on p. 6).

-
- [15] A. Bradu and A. G. Podoleanu, "Attenuation of mirror image and enhancement of the signal-to-noise ratio in a Talbot bands optical coherence tomography system", *Journal of Biomedical Optics*, vol. 16, no. 7, p. 076 010, Jul. 2011, ISSN: 10833668. DOI: 10.1117/1.3598446 (cit. on p. 6).
- [16] T. E. de Carlo, A. Romano, N. K. Waheed, and J. S. Duker, "A review of optical coherence tomography angiography (OCTA)", *International Journal of Retina and Vitreous*, vol. 1, no. 1, p. 5, 2015, ISSN: 2056-9920. DOI: 10.1186/s40942-015-0005-8 (cit. on p. 6).
- [17] J. F. de Boer and T. E. Milner, "Review of polarization sensitive optical coherence tomography and Stokes vector determination", *Journal of Biomedical Optics*, vol. 7, no. 3, p. 359, 2002, ISSN: 10833668. DOI: 10.1117/1.1483879 (cit. on p. 6).
- [18] S. Wang and K. V. Larin, "Optical coherence elastography for tissue characterization: a review", *Journal of Biophotonics*, vol. 8, no. 4, pp. 279–302, Apr. 2015, ISSN: 1864063X. DOI: 10.1002/jbio.201400108 (cit. on p. 6).
- [19] C. Lal and M. J. Leahy, "An Updated Review of Methods and Advancements in Microvascular Blood Flow Imaging", *Microcirculation*, vol. 23, no. 5, pp. 345–363, 2016, ISSN: 15498719. DOI: 10.1111/micc.12284 (cit. on p. 7).
- [20] I. M. Braverman, *The Cutaneous Microcirculation*, 2000 (cit. on p. 7).
- [21] L. A. Holowatz, C. S. Thompson-Torgerson, and W. L. Kenney, "The human cutaneous circulation as a model of generalized microvascular function.", *Journal of applied physiology (Bethesda, Md. : 1985)*, vol. 105, no. 1, pp. 370–2, Jul. 2008, ISSN: 8750-7587. DOI: 10.1152/japplphysiol.00858.2007 (cit. on p. 7).
- [22] I. Barchetta, V. Riccieri, M. Vasile, K. Stefanantoni, P. Comberati, L. Taverniti, and M. G. Cavallo, "High prevalence of capillary abnormalities in patients with diabetes and association with retinopathy.", *Diabetic medicine : a journal of the British Diabetic Association*, vol. 28, no. 9, pp. 1039–44, Sep. 2011, ISSN: 1464-5491. DOI: 10.1111/j.1464-5491.2011.03325.x (cit. on p. 7).

- [23] H. Schmeling, S. Stephens, C. Goia, C. Manlhiot, R. Schneider, S. Luthra, E. Stringer, and B. M. Feldman, "Nailfold capillary density is importantly associated over time with muscle and skin disease activity in juvenile dermatomyositis.", *Rheumatology (Oxford, England)*, vol. 50, no. 5, pp. 885–93, May 2011, ISSN: 1462-0332. DOI: 10.1093/rheumatology/keq407 (cit. on p. 7).
- [24] A. Scheja, R. Elborgh, and M. Wildt, "Decreased capillary density in juvenile dermatomyositis and in mixed connective tissue disease.", *The Journal of rheumatology*, vol. 26, no. 6, pp. 1377–81, Jun. 1999, ISSN: 0315-162X (cit. on p. 7).
- [25] M. Cutolo, W. Grassi, and M. Matucci Cerinic, "Raynaud's phenomenon and the role of capillaroscopy.", *Arthritis and rheumatism*, vol. 48, no. 11, pp. 3023–30, Nov. 2003, ISSN: 0004-3591. DOI: 10.1002/art.11310 (cit. on p. 7).
- [26] T. Micantonio, a. Gulia, E. Altobelli, a. Di Cesare, R. Fidanza, a. Riitano, M. C. Fargnoli, and K. Peris, "Vascular patterns in basal cell carcinoma.", *Journal of the European Academy of Dermatology and Venereology : JEADV*, vol. 25, no. 3, pp. 358–61, Mar. 2011, ISSN: 1468-3083. DOI: 10.1111/j.1468-3083.2010.03734.x (cit. on p. 7).
- [27] K. Deinert, R. Kiesslich, M. Vieth, M. F. Neurath, and H. Neuhaus, "In-vivo microvascular imaging of early squamous-cell cancer of the esophagus by confocal laser endomicroscopy.", *Endoscopy*, vol. 39, no. 4, pp. 366–8, Apr. 2007, ISSN: 1438-8812. DOI: 10.1055/s-2007-966217 (cit. on p. 7).
- [28] I. Alba-Alejandre, S. Hiedl, and O. Genzel-Boroviczeny, "Microcirculatory changes in term newborns with suspected infection: an observational prospective study.", *International journal of pediatrics*, vol. 2013, p. 768 784, Jan. 2013, ISSN: 1687-9740. DOI: 10.1155/2013/768784 (cit. on p. 7).
- [29] M. Chierago, C. Verdant, and D. De Backer, "Microcirculatory alterations in critically ill patients.", *Minerva anesthesiologica*, vol. 72, no. 4, pp. 199–205, Apr. 2006, ISSN: 0375-9393 (cit. on p. 7).

- [30] C. Verdant and D. De Backer, "How monitoring of the microcirculation may help us at the bedside.", *Current opinion in critical care*, vol. 11, no. 3, pp. 240–4, Jun. 2005, ISSN: 1070-5295 (cit. on p. 7).
- [31] K. A. Kwiterovich, M. G. Maguire, R. P. Murphy, A. P. Schachat, N. M. Bressler, S. B. Bressler, and S. L. Fine, "Frequency of adverse systemic reactions after fluorescein angiography. Results of a prospective study.", *Ophthalmology*, vol. 98, no. 7, pp. 1139–42, Jul. 1991, ISSN: 0161-6420 (cit. on p. 7).
- [32] A. Shahlaee, E. Rahimy, J. Hsu, O. P. Gupta, and A. C. Ho, "Preoperative and postoperative features of macular holes on en face imaging and optical coherence tomography angiography", *American Journal of Ophthalmology Case Reports*, vol. 5, pp. 20–25, Apr. 2017, ISSN: 24519936. DOI: 10.1016/j.ajoc.2016.10.008 (cit. on p. 7).
- [33] G. Vangipuram and K. A. Rezaei, "Optical Coherence Tomography Angiography as an Imaging Modality for Evaluation of Diabetic Macular Edema.", *Journal of ophthalmic & vision research*, vol. 12, no. 4, pp. 359–360, 2017, ISSN: 2008-2010. DOI: 10.4103/jovr.jovr_175_17 (cit. on p. 7).
- [34] P. Malamos, G. Tsolkas, M. Kanakis, G. Mylonas, D. Karatzenis, N. Oikonomopoulos, J. Lakoumentas, and I. Georgalas, "OCT-Angiography for monitoring and managing neovascular age-related macular degeneration", *Current Eye Research*, vol. 42, no. 12, pp. 1689–1697, Dec. 2017, ISSN: 0271-3683. DOI: 10.1080/02713683.2017.1356336 (cit. on p. 7).
- [35] J. Barton and S. Stromski, "Flow measurement without phase information in optical coherence tomography images.", *Optics express*, vol. 13, no. 14, pp. 5234–9, Jul. 2005, ISSN: 1094-4087 (cit. on p. 8).
- [36] A. Mariampillai, M. K. K. Leung, M. Jarvi, B. a. Standish, K. Lee, B. C. Wilson, A. Vitkin, and V. X. D. Yang, "Optimized speckle variance OCT imaging of microvasculature.", *Optics letters*, vol. 35, no. 8, pp. 1257–9, Apr. 2010, ISSN: 1539-4794 (cit. on p. 8).

- [37] E. Jonathan, J. Enfield, and M. J. Leahy, "Correlation mapping method for generating microcirculation morphology from optical coherence tomography (OCT) intensity images", *Journal of Biophotonics*, vol. 4, no. 9, pp. 583–587, 2011, ISSN: 1864063X. DOI: 10.1002/jbio.201000103 (cit. on p. 10).
- [38] J. Enfield, E. Jonathan, and M. Leahy, "In vivo imaging of the microcirculation of the volar forearm using correlation mapping optical coherence tomography (cmOCT)", vol. 2, no. 5, pp. 1184–1193, 2011. DOI: 10.1002/jbio.201000103/abstract (cit. on p. 10).
- [39] Y. Jia, O. Tan, J. Tokayer, B. Potsaid, Y. Wang, J. J. Liu, M. F. Kraus, H. Subhash, J. G. Fujimoto, J. Hornegger, and D. Huang, "Split-spectrum amplitude-decorrelation angiography with optical coherence tomography", *Optics Express*, vol. 20, no. 4, p. 4710, 2012, ISSN: 1094-4087. DOI: 10.1364/OE.20.004710 (cit. on p. 10).
- [40] Z. Chen, T. E. Milner, S. Srinivas, X. Wang, A. Malekafzali, M. J. C. van Gemert, and J. S. Nelson, "Noninvasive imaging of in vivo blood flow velocity using optical Doppler tomography", *Optics Letters*, vol. 22, no. 14, p. 1119, Jul. 1997, ISSN: 0146-9592. DOI: 10.1364/OL.22.001119 (cit. on p. 10).
- [41] R. a. Leitgeb, R. M. Werkmeister, C. Blatter, and L. Schmetterer, "Doppler optical coherence tomography.", *Progress in retinal and eye research*, vol. 41, pp. 26–43, 2014, ISSN: 1873-1635. DOI: 10.1016/j.preteyeres.2014.03.004 (cit. on p. 10).
- [42] D. M. Schwartz, J. Fingler, D. Y. Kim, R. J. Zawadzki, L. S. Morse, S. S. Park, S. E. Fraser, and J. S. Werner, "Phase-variance optical coherence tomography: A technique for noninvasive angiography", *Ophthalmology*, vol. 121, no. 1, pp. 180–187, 2014, ISSN: 01616420. DOI: 10.1016/j.opthta.2013.09.002 (cit. on p. 11).
- [43] K. Kurokawa, K. Sasaki, S. Makita, Y.-J. Hong, and Y. Yasuno, "Three-dimensional retinal and choroidal capillary imaging by power Doppler optical coherence

- angiography with adaptive optics”, *Optics Express*, vol. 20, no. 20, p. 22796, 2012, ISSN: 1094-4087. DOI: 10.1364/OE.20.022796 (cit. on p. 11).
- [44] S. H. Yun, G. Tearney, J. de Boer, and B. Bouma, “Motion artifacts in optical coherence tomography with frequency-domain ranging.”, *Optics express*, vol. 12, no. 13, pp. 2977–98, Jun. 2004, ISSN: 1094-4087 (cit. on p. 11).
- [45] A. S. Nam, I. Chico-Calero, and B. J. Vakoc, “Complex differential variance algorithm for optical coherence tomography angiography”, *Biomedical Optics Express*, vol. 5, no. 11, p. 3822, 2014, ISSN: 2156-7085. DOI: 10.1364/B0E.5.003822 (cit. on p. 11).
- [46] R. K. Wang, S. L. Jacques, Z. Ma, S. Hurst, S. R. Hanson, and A. Gruber, “Three dimensional optical angiography”, *Optics Express*, vol. 15, no. 7, p. 4083, 2007, ISSN: 1094-4087. DOI: 10.1364/OE.15.004083 (cit. on p. 11).
- [47] B. J. Vakoc, R. M. Lanning, J. A. Tyrrell, T. P. Padera, L. A. Bartlett, T. Stylianopoulos, L. L. Munn, G. J. Tearney, D. Fukumura, R. K. Jain, and B. E. Bouma, “Three-dimensional microscopy of the tumor microenvironment in vivo using optical frequency domain imaging”, *Nature Medicine*, vol. 15, no. 10, pp. 1219–1223, 2009, ISSN: 1078-8956. DOI: 10.1038/nm.1971. arXiv: NIHMS150003 (cit. on p. 11).
- [48] S. Kim, T. Park, S.-J. Jang, A. S. Nam, B. J. Vakoc, and W.-Y. Oh, “Multi-functional angiographic OFDI using frequency-multiplexed dual-beam illumination”, *Optics Express*, vol. 23, no. 7, p. 8939, 2015, ISSN: 1094-4087. DOI: 10.1364/OE.23.008939 (cit. on p. 11).
- [49] L. An, J. Qin, and R. K. Wang, “Ultrahigh sensitive optical microangiography for in vivo imaging of microcirculations within human skin tissue beds.”, *Optics express*, vol. 18, no. 8, pp. 8220–8, Apr. 2010, ISSN: 1094-4087 (cit. on p. 11).

Chapter 2

Materials and Methods

This chapter will detail the methodology behind general techniques which were used throughout the entire thesis. Techniques which were specific to a particular experiment have been detailed in the subsequent chapters.

2.1 Angiographic processing pipeline

The background principles and development of angiographic OCT were described in Sec. 1.3. This section will overview the implementation of these methodologies in the context of this work, further detailing the numerous supporting algorithms which were developed and illustrating the overall processing pipeline which converts raw OCT data into a visible angiographic format.

2.1.1 The OCT system

All angiographic imaging for this study was performed using a multi-beam OCT system (Vivosight®, Michelson Diagnostics Ltd, Orpington, Kent, UK - Fig. 2.1). This system utilises a swept-source 1305nm Axsun laser with a tuning range of 147nm (-10dB), achieving a resolution of approximately $5\mu\text{m}$ axially and $7.5\mu\text{m}$ laterally (In tissue). A-scans are captured at a line rate of 20 kHz and contain structural information to a depth of between 1-2mm, depending on the tissue type. The Vivosight system is a uses a multi-beam design, capturing 4 channels, each with a slightly different beam focal depth. For this study a single channel was used for

image analysis, more information and justification for this decision can be found in Appendix A.1.



FIGURE 2.1: Vivosight OCT system with handheld optical probe

The use of a commercial system such as the Vivosight imposed two small caveats that made angiographic imaging challenging. Firstly, while the mobile imaging probe was flexible, it introduced an additional source of movement into captured volumetric OCT datasets; the operator. Since angiographic measurements are effectively measures of spatial decorrelation, bulk tissue motion (BTM) resulting from the operator's movement can result in full-frame decorrelation and the loss of any meaningful vascular derived signal. To rectify this, a mobile clamp (Fig. 2.2) was designed to hold the probe and facilitate movement with 6 degrees-of-freedom. To further reduce patient movement, a plastic standoff (Fig. 2.2D) bridged the gap between the imaging probe and the skin, this gently contacted the skin surface such that any lateral movement was reduced. Fixation of the imaging probe in this manner is important as it removes an additional source of movement from the resulting data.

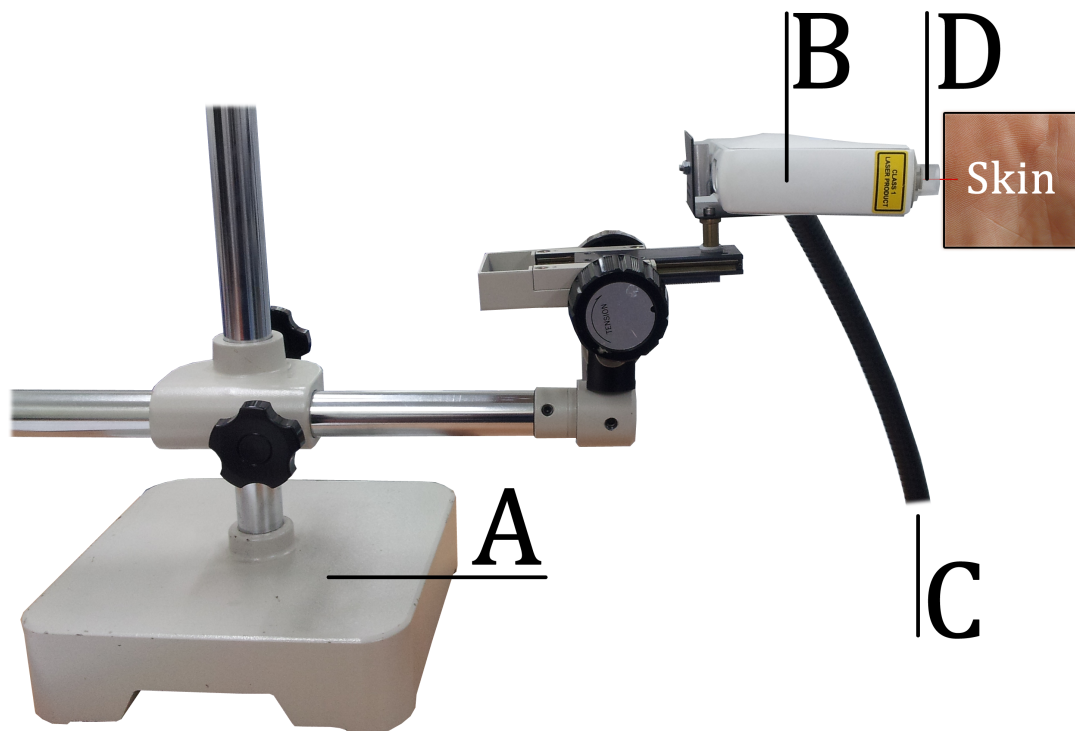


FIGURE 2.2: A) Weighted clamp with 6 degrees of freedom which was used to reduce motion artefacts in the acquired OCT datasets. B) The Vivosight imaging probe. C) Optical cable leading to the laser and optical processing unit. D) Plastic standoff which contacts the skin surface to reduce any lateral slipping.

The second challenge was related to the image acquisition itself. The Vivosight itself is generally shipped with integral software designed for clinical use. This software is optimized for clinical visualization of structural OCT data and as such is capable of capturing 2D slices and sparsely sampled 3D volumes. While it has previously been demonstrated that angiographic OCT measurements are achievable using clinical OCT scanning strategies (i.e stepping the second transverse scanner in the y-direction between each subsequent scan), the sampling area of adjacent B-scans must be sufficiently high such that interframe correlation is not lost [1]. This is problematic, as the sparsely sampled clinical volume scans of the Vivosight do not lend themselves well to this application. Furthermore, simply increasing the sampling area of scans vastly increases the amount of data which needs to be stored to disk, increasing the required processing time. To rectify this issue, the manufacturer provided research grade acquisition software (image4) based within LabVIEW (National Instruments). We were able to adapt and modify (See Sec. 8.1 for further details) this software to run the Vivosight with non-standard beam scanning patterns, in particular to add the ability to capture multiple frames at the same spatial location. As the frames were captured at the same spatial location, noise derived from spatial changes in the structure of the tissue is minimized.

Due to the usage of a swept light source, the phase differences between successive A-scans were deemed too unstable to perform phase-based angiography (Appendix A.7), instead intensity-based (Sec. 1.3.2) angiographic acquisition methods were utilised, which are detailed in the following section.

2.1.2 Step 1 - Data acquisition

The utilisation of the Labview control framework allowed for scans to be acquired from precise locations within the sample. Two distinct scanning strategies were designed to facilitate angiographic imaging, as described in Sec. 1.3.2, speckle-variance OCT (svOCT) and correlation-mapping (cmOCT). These were both programmed into LabVIEW for use on the Vivosight system. For svOCT, a gate-width of N repeat frames were captured at the same y-location by sweeping the x-galvanometer

repeatedly, the y-galvanometer was then stepped through a displacement Δy with the process being repeated until the required FOV was acquired. This scanning strategy is illustrated on Fig. 2.3.

The scanning strategy used for cmOCT differs from svOCT in that only 2 frames are collected from each unique spatial location, this means that while maintaining the same number of acquired frames, the interframe spacing (Δy) can be reduced by a factor $\frac{N}{2}$ in comparison to svOCT, corresponding to an up-sampling in the lateral y-direction. To compensate for the reduction in data across the gate-width, correlation mapping is performed across a kernel of size X-by-Z. This acquisition protocol is illustrated on Fig. 2.4.

These acquisition techniques both highlight localised decorrelations within the tissue, however there are subtle differences in the resulting vascular detection within the angiographic images. A comparison between the two methods is described in Sec. 7.1.

For both of these methods there are several key acquisition parameters which remain flexible. The inter A-scan spacings (Δx and Δy) together with the lateral resolution of the system ($7.5\mu m$) determine the smallest resolvable structures within the tissue. The scan dimensions (X and Y) determine the field-of-view of the scans and in the case of svOCT the gate-width (N) influences the quality of the resulting angiographic measurements. In general, to obtain a higher-quality angiographic scan or increase the field-of-view it is necessary to increase the overall scan time, therefore for each application there is generally a trade-off between practicality and quality to be assessed. In cases where field-of-view is important, it is generally optimal to increase the volume length (Y) as opposed to increasing the image width (X). This is because changing Y does not affect the frame rate and thus does not increase susceptibility to motion artefacts. Table 2.1 summarizes these parameters in detail.

2.1.3 Step 2 - Bulk tissue motion (BTM) correction

Directly following the data acquisition, data processing was performed externally within MATLAB (R2016a – MathWorks). To minimize processing time, each stack of

Processing strategy — Speckle-variance OCT (Gate width = 6)

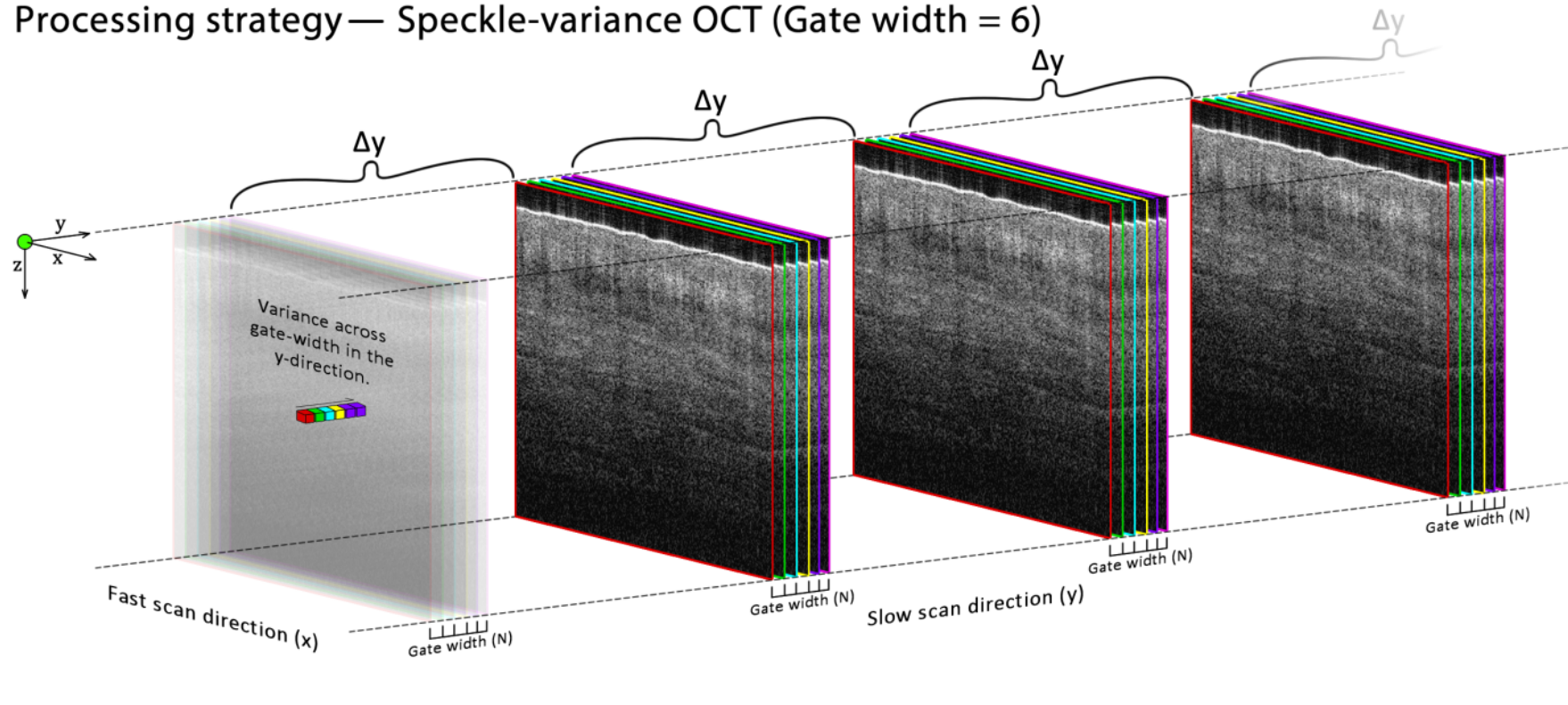


FIGURE 2.3: Illustration of an svOCT scanning strategy using a gate-width (N) of 6 frames. Note: The small spaces between the gate-width frames are for illustrative purposes only, during acquisition these 6 frames would be collected at the same location (Overlapping). Speckle-variance is calculated pixel-wise in the y -direction across the gate-width of frames, a high variance implies that the region is fluid as its scattering properties are decorrelating rapidly with respect to time. The gate-width (N) is a flexible parameter, higher values of which will result in increased scan quality through a more accurate assessment of the regional decorrelation but increase the overall scanning time. A full comparison between this method and cmOCT (Fig. 2.4) can be found in Sec. 7.1.

Processing strategy — Correlation-mapping OCT (5x5 kernel)

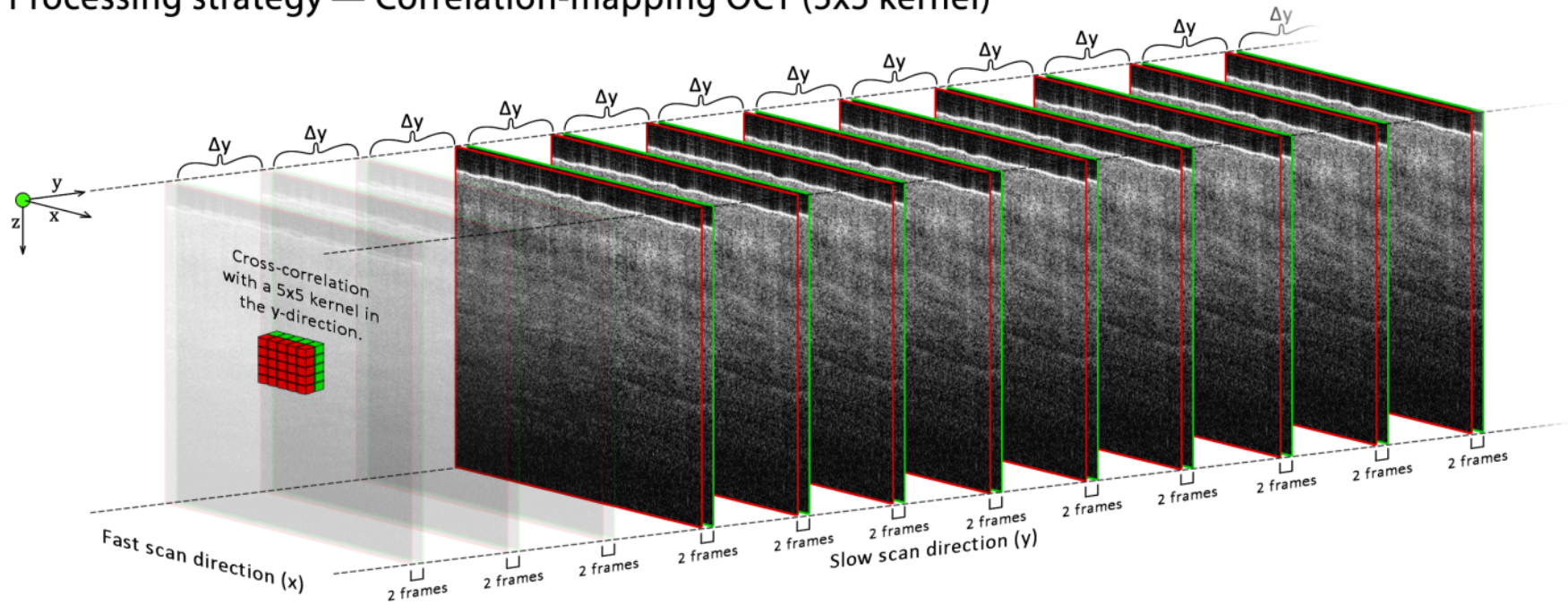


FIGURE 2.4: Illustration of cmOCT scanning strategy. Note: The small space between the red and green frames is for illustrative purposes only, during acquisition these 2 frames would be collected at the same location (Overlapping). Correlation is calculated in the y-direction using a kernel of size M -by- N , an absolute correlation close to 1 implies that the region is solid, correlations close to 0 suggest the region is highly decorrelative and hence implies fluid. The kernel size (M, N) is flexible, with higher values more accurately capturing the decorrelation properties of the region, but reducing the resolution of the resulting angiographic image. A full comparison between this method and svOCT (Fig. 2.3) can be found in Sec. 7.1.

TABLE 2.1: Key parameters and their effect on angiographic imaging

Parameter	Description	Effect on the resulting data
A-scan spacing (Δx)	The spacing between adjacent A-scans defined by the sweep rate of the x-galvanometer.	Higher values of Δx increase the frame-rate but reduce resolution. $5 - 10\mu m$ is ideal as it closely matches the lateral resolution of the OCT system.
B-scan stack spacing (Δy)	The spacing between adjacent B-scan stacks defined by the step size of the y-galvanometer.	Higher values of Δy reduce overall imaging time but also reduce resolution. $5 - 10\mu m$ is ideal as it closely matches the lateral resolution of the OCT system.
Image width (X)	Total width of the B-scans.	Higher values of X result in a lower frame rate and longer overall imaging time but wider field-of-view. Low values of X should be used in areas of high patient movement.
Volume length (Y)	Width of the C-scan in the y-direction. (Δy).	Higher values of Y increase overall imaging time but also increase the field-of-view.
Stack size (N)	The number of B-scans that comprise the gate-width. Captured at the same spatial y-coordinate.	Higher values of N reduce noise in svOCT images and enable the visualization of slower flowing blood. It also increases the overall imaging time. N is generally fixed at 2 for cmOCT.
Kernel size (M, N)	The size of the kernel over which cross-correlation is performed for cmOCT.	A larger kernel will capture more information regarding the regional decorrelation but degrade the resolution of the resulting angiographic image.

B-scans was processed in parallel using a graphical processing unit (GPU) (NVIDIA GeForce GTX 780), which was achieved through utilisation of the parallel computing toolbox within MATLAB. As the data at this point was stored in the form of raw OCT interferograms, it was first necessary to pre-process the data into a visible image format. This is done following the methodology detailed in Sec. ??, with the Fourier-transform and resampling steps being performed on the GPU.

The following section will describe two measures which were programmed in an attempt to reduce the influence of BTM on the resulting angiographic datasets. Since both svOCT and cmOCT rely on decorrelation between subsequent frames,

both unwanted in-plane (x - z plane) and out-of-plane (x - y plane) movements can result in full frame decorrelation and a loss of any meaningful angiographic signal.

In-plane motion

One method of correcting in-plane motion is termed image-registration, which refers to the alignment of subsequent frames such that any in-plane movement between them is minimised. Traditionally these methods can be classified into two main categories: intensity-based and feature-based registration. Feature-based registration utilises unique "features" of an image which can be tracked between subsequent frames, if multiple features can be identified then it is possible to extract an affine transformation matrix which quantifies any displacement, rotation and scaling that has occurred between the slices. An implementation of this method utilising the speeded up robust features (SURF) algorithm[2] is illustrated in Fig. 2.5 below.

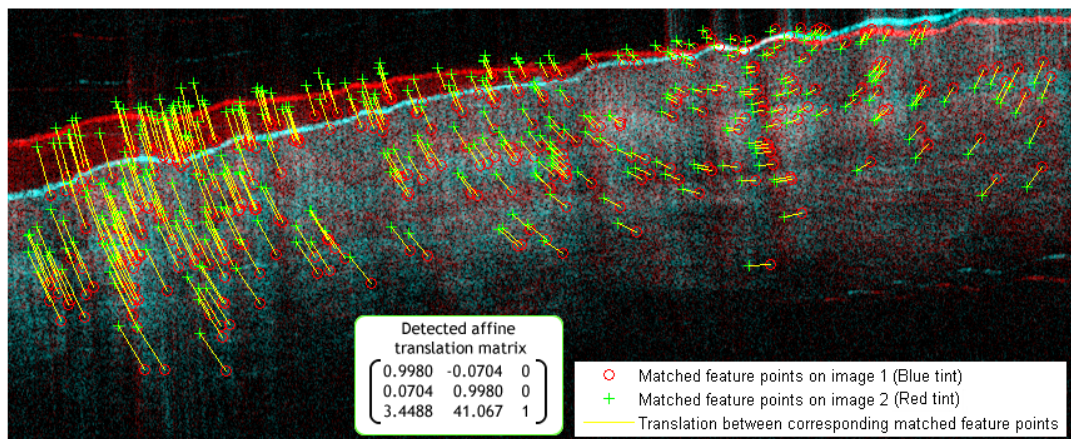


FIGURE 2.5: Detection of matching feature points between two OCT B-scans of the fingertip, which can then be used to calculate an affine translation matrix describing any offset between the two images[3]

In practice, this method is unreliable for large image volumes with a high degree of BTM as matching features often cannot be found, particularly in regions of tissue with poor contrast. Furthermore, random speckle-noise inherent to the OCT modality often results in anomalous feature-points being detected and the affine-transform remaining unsolvable[3].

A more robust method of image-registration for OCT purposes involves directly cross-correlating the intensity of subsequent frames, such that a localised correlation maximum can be identified which minimises any intensity differences between a target and a reference image. Cross-correlation based methods have previously been applied successfully to reduce BTM induced artefacts within angiographic OCT datasets[4], [5]. Such methods can be performed in the Fourier-domain in order to rapidly accelerate the registration process, this process is detailed below.

If two OCT B-scans, $a(x, y)$ and $b(x, y)$ have been shifted by in-plane BTM through a displacement $(\Delta x, \Delta y)$ such that:

$$a(x, y) = b(x - \Delta x, y - \Delta y)$$

then the discrete Fourier transforms of $a(x, y)$ and $b(x, y)$ are related such that:

$$B(u, v) = A(u, v)e^{-2\pi i(\frac{u\Delta x}{X} + \frac{v\Delta y}{Y})} \quad (2.1)$$

Following the Fourier shift theorem, where X and Y are the image dimensions. This introduces the assumption that a and b are circularly shifted images, which does not hold true for continuous OCT datasets, however providing the relative movements are reasonably restrained, the approximation is good enough for registration purposes. Since $|e^{-2\pi i(\frac{u\Delta x}{X} + \frac{v\Delta y}{Y})}| = 1$ it follows that the normalised cross-power spectrum (R) is:

$$R(u, v) = \frac{A * B^*}{|A * B^*|}$$

We can then sub in B using the result from equation 2.1, giving:

$$R(u, v) = \frac{A * A^* e^{-2\pi i(\frac{u\Delta x}{X} + \frac{v\Delta y}{Y})}}{|A * A^*|}$$

$$R(u, v) = e^{-2\pi i(\frac{u\Delta x}{X} + \frac{v\Delta y}{Y})}$$

Transforming this result back into the time-domain through an inverse discrete Fourier transform (iDFT) results in a delta function positioned at a location in the image corresponding to the displacement due to BTM:

$$iDFT(R) = r(x, y) = \delta(x + \Delta x, y + \Delta y)$$

For real OCT images which contain speckle-noise and minor out-of-plane motion, it is unlikely that the delta function will reach a value of 1. However there is likely to be a local maximum in the resulting $iDFT(R)$ matrix which corresponds to the offset between images. Fig. 2.6 illustrates the detection of this peak.

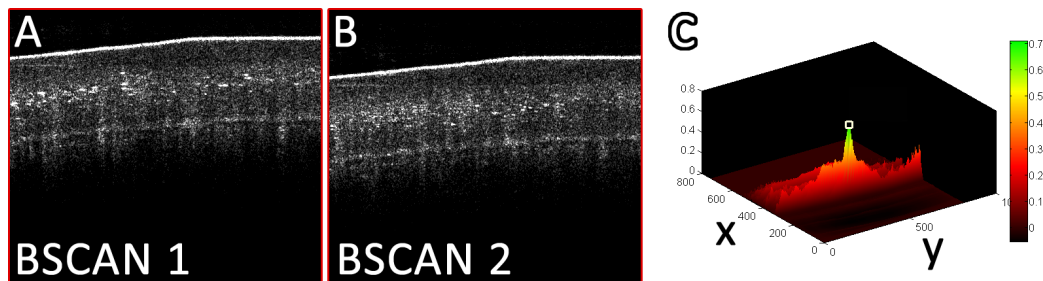


FIGURE 2.6: Cross-correlation based image registration A) First B-scan of the fingernail. B) Second B-scan of the fingernail. C) Surface plot of $iDFT(R)$ showing the resultant peak at the point of maximum cross-correlation.

The above process demonstrates how the cross-power spectrum of two Fourier-transformed B-scans can be inverse Fourier transformed to find the translational offset between the images. Fourier transform based cross-correlation such as this has the advantage of being both effective and extremely efficient computationally[6], lending itself well for rapid, real-time imaging applications. For greater registration

accuracy, it is desirable to expand this technique such that sub-pixel accurate registration can be performed. A simple method of accomplishing this would involve upsampling the original images $a(x, y)$ and $b(x, y)$ using interpolation techniques before performing the above Fourier transform based cross-correlation technique. The detected peak can then be converted back into the normal coordinate system with greater decimal accuracy. This method quickly becomes unfeasible when working with large images. For example, the registration of two 1000x1000 B-scans to an accuracy of $\frac{1}{10}$ of a pixel would require the computation of a 10000x10000 Fourier transform, a process which would require large memory and computational power.

In order to avoid the usage of large-scale Fourier transforms, an implementation of an image-registration algorithm by Guizar *et al*[7] was modified to make use of the GPU architecture. This method utilises the pixel-accurate method described above in order to calculate an initial estimate for the location of the correlation peak. Upsampled discrete Fourier transforms are then computed in the area directly surrounding the correlation-peak using matrix-multiplication methods, a process that is far more efficient in both memory usage and computational time when compared to calculating upsampled fast Fourier transforms directly. The cross-correlation analysis is then performed on each of the local-area DFT's with the resulting pixel offset being recorded. The exact location of the correlation peak can then be refined to a sub-pixel accurate location through conversion of the pixel offset back into the normal coordinate space through division of the upsampling factor. For this work, registration between neighbouring B-scans was performed to an accuracy of $\frac{1}{100}$ of a pixel, thus a recorded displacement of 1 pixel in the upsampled space would correspond to an actual shift of 0.01 pixel.

The above algorithm is described in greater detail (Including source code) in the Appendix (App. A.2). This algorithm is limited to rigid translational movement, which compared to non-rigid methods cannot locally warp the processed image to more closely match the reference image. As a result, internal deformations resulting from tissue palpation may fail to be captured. The primary reason a rigid-translation

algorithm was used (instead of an elastic/non-rigid model such as the demons approach[8]) was image processing speed, as demonstrated in App. A.2, a single registration between two frames can be performed in 0.045s using the GPU implementation of the Guizar *et al* algorithm. Comparatively, the same registration using a MATLAB implementation of the demons algorithm (imregdemons.m) with 100 iterations across 3 pyramid levels took 1.57 seconds, a factor of 35 slower due to the added complexity and lack of GPU optimisation.

Out-of-plane motion

Out-of-plane motion refers to any motion in the x-y plane (Perpendicular to the fast-scan direction). Generally this is far more challenging to rectify than in-plane motion owing to a lack of spatial reference points without performing computationally intensive 3D image-registration. Various methods have been demonstrated with the aim of correcting out of plane movement, including orthogonal scanning strategies[9], fiducial marker tracking[10], parallel-strip registration[11] and a combination of rigid and nonrigid registration across simultaneously acquired volumetric scans[12]. Many of the aforementioned techniques which are capable of effectively removing out-of-plane motion artefacts rely on oversampling the dataset through additional data acquisition, a process which extends the overall volume acquisition time considerably. Methods exist which attenuate out-of-plane BTM artefacts through consideration of the individual B-scans themselves, including mean decorrelation subtraction[13] and more recently, dynamic thresholding of the decorrelation[14].

For this work, frames which exhibited poor correlation with neighbouring frames within the gate-width (N) were excluded from further processing. Firstly, each frame was assigned a score equal to its average correlation with all other frames within the gate-width, the frame with the highest average correlation was assigned as the base-frame. Allocation of the base-frame in this manner ensured that the frame in question was unlikely to be affected by large magnitudes of out-of-plane motion, given

its strong correlation to other frames collected at the same spatial location. Following this, the k frames which exhibited the highest correlation with the base-frame were maintained for further processing, with the remaining frames being discarded. The parameter k is dynamic and can be changed depending on the magnitude of BTM expected, for example in regions where out-of-plane motion is unlikely to occur, assigning a high value of k ($\frac{N}{2} \leq k \leq N$) ensures that the majority of frames are maintained. Meanwhile for areas exhibiting a high magnitude of BTM, low values of k ($2 \leq k \leq \frac{N}{2}$) can be assigned in an attempt to suppress any undesirable movement. This technique is simple to implement and avoids the tricky allocation of a dynamic threshold value, however the reduction in the overall dataset size through the deletion of frames, particularly for low values of k has the potential to reduce the overall contrast of the angiographic images. Furthermore, due to the correlation matrix being computed within each gate-width of acquired frames, this method is incompatible with the cmOCT acquisition methodology described in Sec. 2.1.2.

2.1.4 Step 3 - Converting the data from structural to angiographic format

In steps 1-2, structural OCT data was acquired and registered such that any inter-frame BTM was reduced. The next step involved extracting the temporal decorrelations which are indicative of fluid flow directly from these 4-dimensional datasets (x-y-z-time).

Speckle-variance OCT processing

As described in Sec. 2.1.2, svOCT involves the acquisition of numerous gate-widths (N) of data at each spatial location. The speckle-variance signal is calculated from the 4-dimensional OCT data using a variance equation adapted from previous work by Mariampillai *et al*[15]:

$$SV_{x,y,z} = \text{median} \left(\sum_{n=1}^k (I_{x,y,z,n} - \frac{1}{k} \sum_{n=1}^k I_{x,y,z,n})^2 \right)$$

Here x, y and z correspond to voxel indices within each frame, k is the total number of retained frames within each gate-width (Sec. 2.1.3), n represents the frame index within each gate-width and I is the corresponding pixel intensity at a particular spatial location. The 1D median function is performed across each stack ($n = 1 : k$ where $k \leq N$) and further serves to attenuate outlier values of variance, such as those caused by sudden interface movements. Note that the result is a reduction from the 4-dimensional structural dataset to a 3-dimensional angiographic dataset.

Correlation-mapping OCT processing

As described in Sec. 2.1.2, cmOCT involves the acquisition of two frames (I_A and I_B) at each spatial-location, a cross-correlation is then performed between each image pair with a kernel size (M, N) . This process follows the algorithm originally described by Enfield *et al*[1], which is described in the equation below:

$$CM(x, y, z) = \sum_{m=0}^M \sum_{n=0}^N \dots \frac{(I_A(x+m, y, z+n) - \overline{I_A(x, y, z)})(I_B(x+m, y, z+n) - \overline{I_B(x, y, z)})}{\sqrt{(I_A(x+m, y, z+n) - \overline{I_A(x, y, z)})^2 + (I_B(x+m, y, z+n) - \overline{I_B(x, y, z)})^2}}$$

Here x, y and z correspond to voxel indices within each frame, I_A and I_B refer to the pixel intensities of both images respectively. The resulting volume (CM) contains values between -1 and 1, with strong values of correlation (close to -1 or 1) indicating solid regions of tissue and weak values of correlation (close to 0) indicating fluid regions of tissue.

Signal masking

To remove noise-dominated areas of the angiograms containing little to no structural information, a masking filter was applied to each dataset. For this, each gate-width of structural B-scans was averaged and 2D Gaussian filtered with kernel size 5x5 pixels and a standard deviation of 2. A mask was then generated through binary segmentation of the resulting images, with the threshold being defined as the 95th

percentile of pixel intensities situated within the 10 deepest image rows. The lower rows were selected as they typically exhibit close to zero structural signal, instead consisting entirely of noise. This mask was then applied to the corresponding svOCT or cmOCT image, deleting areas that contained negligible OCT signal.

2.1.5 Step 4 - Flattening the tissue surface

Following the calculation of the angiographic signal, it was necessary to flatten any curvature in the surface of the tissue such that flat horizontal sections of the vasculature could be considered as a function of tissue depth. This is important as the vasculature within skin generally aligns into horizontally oriented superficial or deep vascular plexuses, joined with vertical linkages. Notably, the superficial subpapillary plexus is situated beneath the dermal-epidermal junction (DEJ) and provides nutrients to the epidermis through rising capillary loops[16]. The layering of vasculature within the skin is shown on Fig. 2.7.

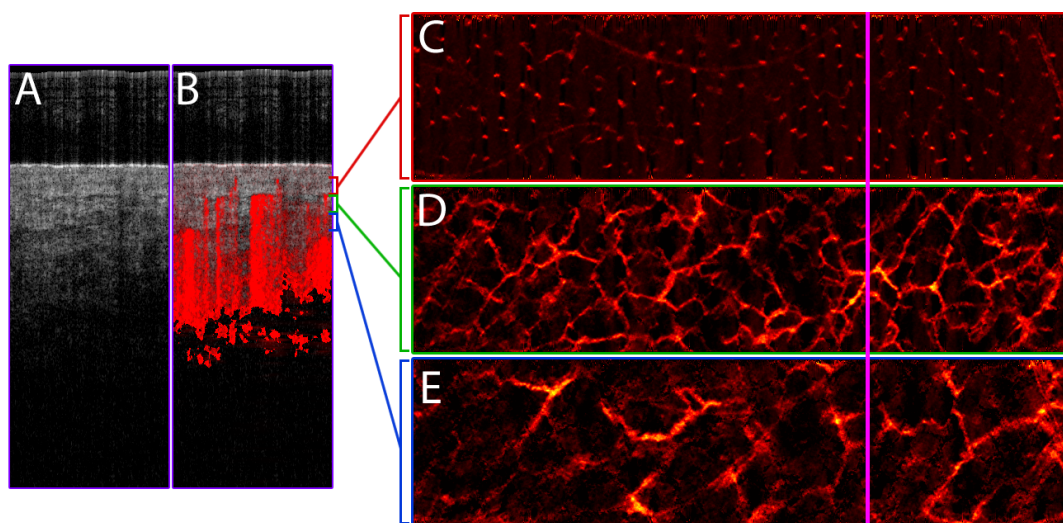


FIGURE 2.7: Visualization of depth encoded flattened svOCT datasets. A) A single 1x2mm B-scan of the dataset captured from the dorsal hand. B) Previous B-scan with overlaid speckle-variance data, note the shadowing artefact beneath vessels. C) 1x4mm mean intensity projection (MIP) between depths 59-137 μ m showing the tips of the capillary loops. D) 1x4mm MIP between depths 137-215 μ m showing the superficial subpapillary plexus. E) 1x4mm MIP between depths 215-293 μ m showing deeper vasculature within the tissue. The vertical pink line represents B-scan location from A and B.

Structural features such as hairs and ridges, in addition to bright artefacts originating at the interface between the stratum corneum and air, make it challenging to accurately segment the surface of the skin. Hence surface detection was achieved using the averaged B-scans that were previously used for thresholding purposes, an optimized horizontal Sobel edge detection filter was applied to each of the averaged B-scans in order to generate a mask with little occurrence of strong vertical reflections (in-depth). Furthermore, a second mask was generated by considering the differential between pixels in the depth (z) direction of the B-scan images; highlighting only regions with a large increase (dark to bright) in intensity. These masks were first combined with a logical AND operation, morphological area opening was then applied in order to remove any detected regions which filled below a certain predefined area. A spur operation was applied to the resulting surface detection in order to remove any small offshoots resulting from noise. The most superficial detections for each column (z) were then recorded and any gaps in the resulting surface line were interpolated across. This surface detection process for a single B-scan is illustrated in Fig. 2.8 below.

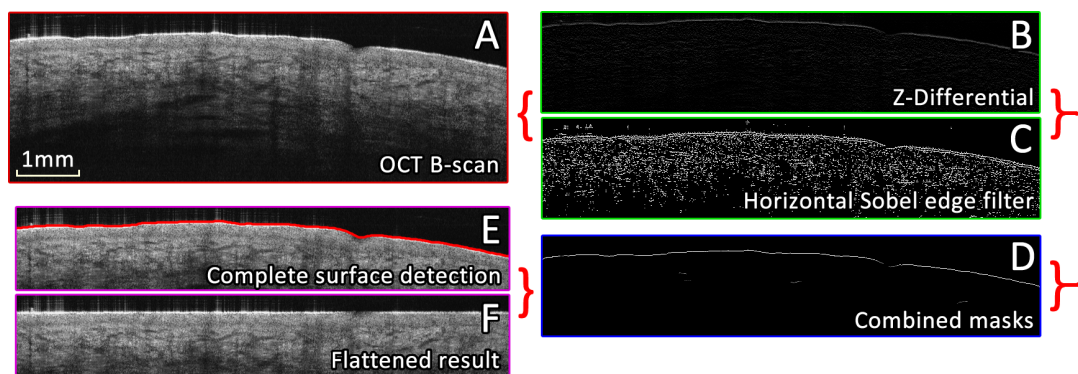


FIGURE 2.8: The process of flattening the skin surface within OCT datasets. A) OCT B-scan of the dorsal palm. B) Differential of the intensity data in the z-direction. C) Horizontal Sobel edge filter. D) The combination of B and C with applied morphological opening and spur operations. E) Superficial surface detection with interpolation applied. F) Each column of the B-scan flattened using the curve seen in E.

For volumetric scans, as was the case for the majority of angiographic datasets, the surface detection process was repeated for each of the B-scan stacks, with the 2D

surface detections being combined to produce a 3D surface plot. To improve detection further, the 3D surface was 2D median filtered with a 20x20 kernel to eliminate outlier detection and used to normalize each column of the angiographic data to a certain predefined depth.

2.1.6 Step 5 - Motion artefact post-processing

Despite the registration and correction methods set in place to reduce the influence of BTM artefacts on the angiographic data (Sec. 2.1.3), numerous artefacts remained visible in the *en face* visualisations of the vasculature. Fig. 2.9 demonstrates how image registration reduces the intensity of the artefacts, but does not eliminate them entirely.

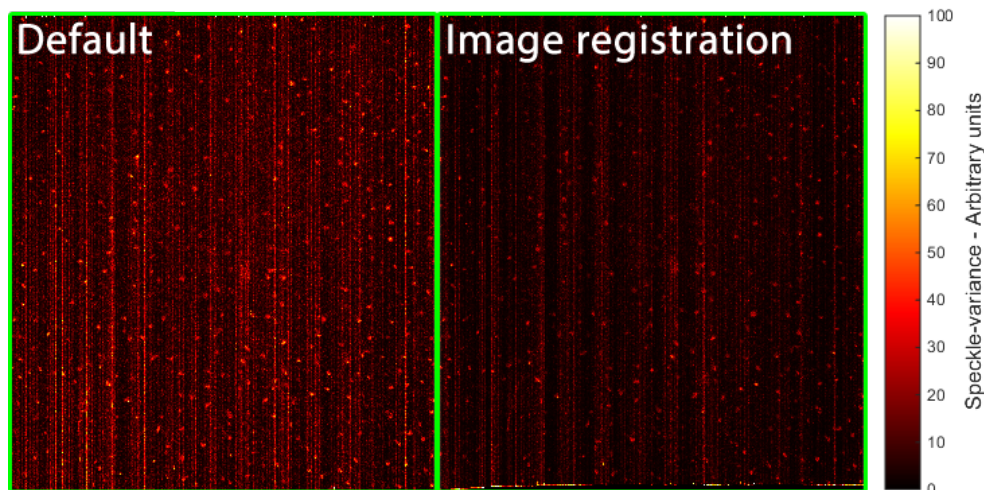


FIGURE 2.9: Left) *En-face* angiographic projection image of the capillary loops within skin without any image registration being applied. Right) *En-face* angiographic projection image of the capillary loops within skin with image registration applied. Vertical line artefacts originating from BTM are reduced in intensity but not eliminated entirely.

The persistence of motion artefacts despite the registration and correction steps could have numerous reasons. Firstly, elastic deformations in the tissue between frame acquisitions could result in anomalous decorrelation being detected. Elastic deformations occur if the tissue is deformed in a non-rigid manner. While elastic image registration is feasible within a GPU environment[17] using fully automated

grey-scale based algorithms such as the demons approach[8], it is time consuming and often inaccurate due to the random speckle effect within OCT images. Secondly, it is possible that the correlation optimisation step discussed in Sec. 2.1.3 would allow some out-of-plane motion to persist, particularly if the sample was moving throughout the entire gate-width acquisition period.

Mean intensity interpolation

To remove the remaining vertical line artefacts, code was written which aimed to detect and suppress such lines. Initially, a simplistic approach was taken whereby the mean column-wise intensity of each image (Fig. 2.10A) was calculated, a threshold was then defined empirically as the upper 95th percentile of datapoints, columns exceeding this threshold were removed (Fig. 2.10B), any gaps were then interpolated across using 2D bilinear interpolation (Fig. 2.10C).

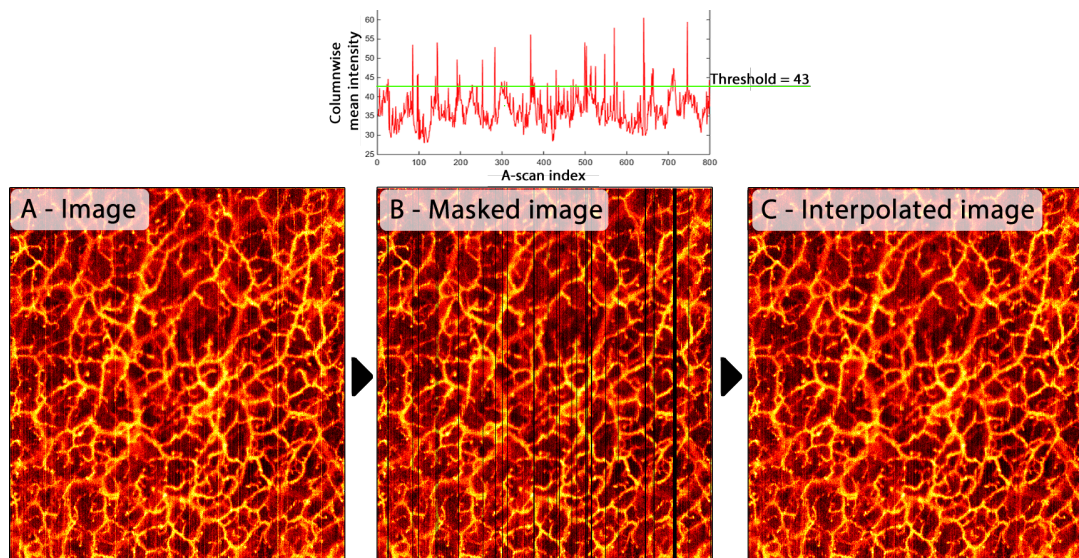


FIGURE 2.10: Simple interpolation approach to the removal of vertical-line artefacts caused by tissue movement. A) The column-wise mean intensity of the image is calculated and plotted, a threshold is defined empirically. B) Columns which exceed the threshold mean intensity are removed. C) The removed columns are interpolated across using 2D bilinear interpolation.

While this simplistic approach worked well for regions containing only small irregular movements, which resulted in thin sparse vertical lines, the 2D interpolation

did not scale well for datasets with large areas of motion corrupted data. Furthermore, this approach requires the assignment of a dynamic threshold value, the ideal value of which is likely to change as a function of how much BTM was present within the dataset. Indeed without careful optimisation of the threshold, low-intensity lines which are below the threshold will remain unaffected. Lastly, the lines themselves are likely to contain some degree of angiographic information which is lost when simply discarding them. To address these concerns, a more robust approach was developed which made use of the Fourier-domain.

Wavelet/Fourier filtering

For a filter to be effective in the removal of vertical line artefacts, it needs to be capable of de-stripping the image while maintaining the underlying structural detail. A method of stripe and ring artefact removal outlined by Münch *et al* was adapted and reprogrammed for this purpose[18]. This method works by considering that a vertical line artefact has a high-frequency component in the horizontal (x) direction, and a low frequency component in the vertical (y) direction. The 2D Fourier transform of an image $f(x, y)$ yields $F(x, y)$, with perfect vertical lines being represented as Dirac delta functions along the x-axis ($\delta(y)$). In short, the Fourier coefficients describing perfect vertical lines are compressed to the axis ($y = 0$) and can be removed by simply masking the coefficients of $F(x, y)$ along the x-axis. It is worth noting that in the case of the fast-Fourier transform (FFT) filter, the coefficients stored at $F(0, y)$ contain information regarding the intensity-offsets across the entire image and thus are not removed. Fig. 2.11 shows this filtering process being applied to an image of the skin vasculature.

While sufficient for the removal of "perfect" line artefacts, or lines which have a constant intensity along their length and are a single pixel in width; "imperfect" lines contain a vertical frequency component which results in them not being aligned to the x-axis in the Fourier domain. To remove such "imperfect" artefacts, the mask applied to $F(x, y)$ can be increased in height such that coefficients deviating from the x-axis are also removed. For this a Gaussian damping function is used[18]:

$$\text{Mask}(x, y) = 1 - e^{-\frac{y^2}{2\sigma^2}}$$

Here σ defines the radius of removed coefficients, hence higher values of σ result in the removal of increasingly imperfect artefacts. This process is not entirely lossless however, and large values of σ will begin to visibly degrade the underlying structural information contained in the image.

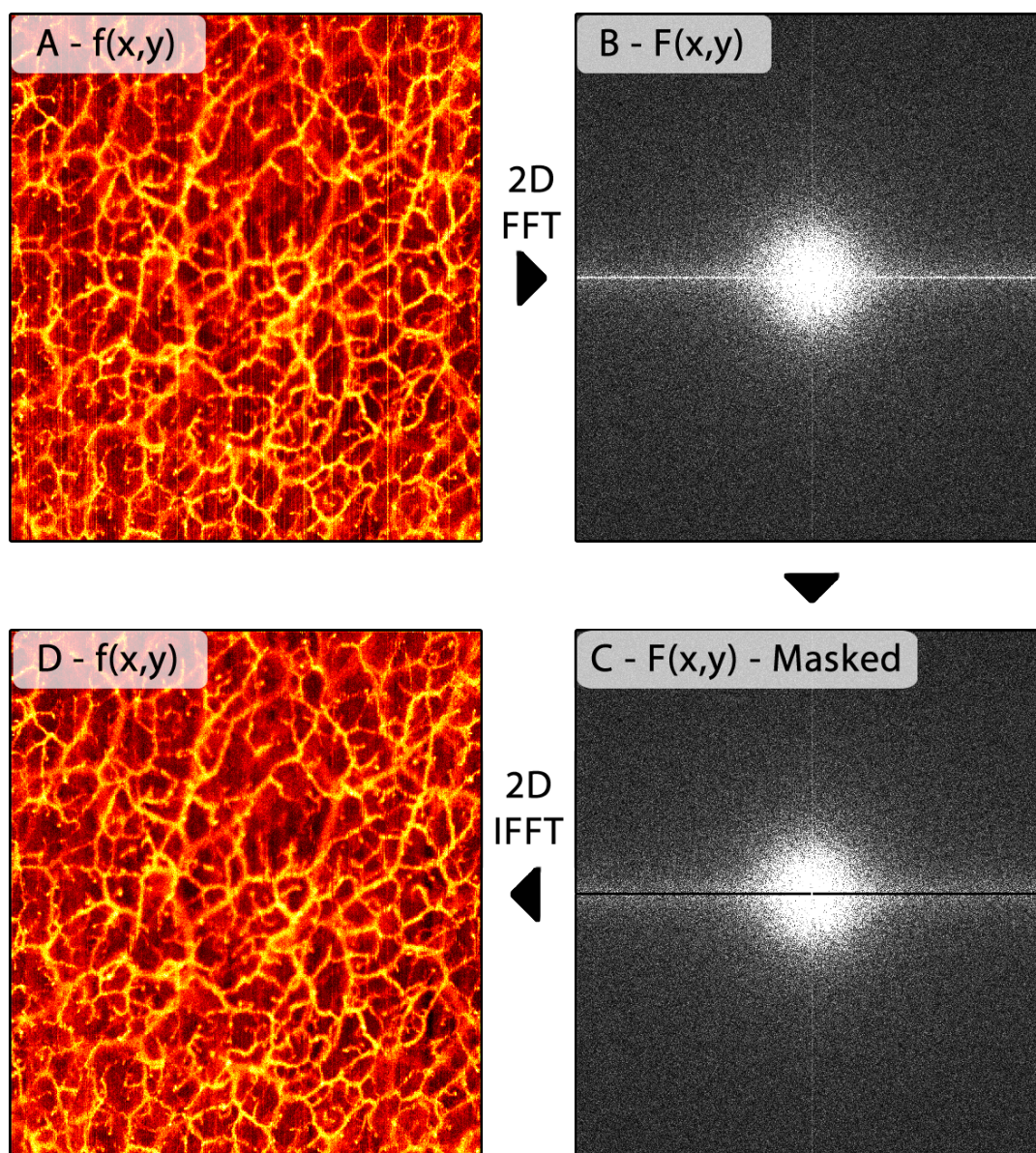


FIGURE 2.11: Removal of vertical line artefacts in the Fourier domain
 A) An *en face* angiographic OCT image of skin vasculature affected by vertical motion artefacts. B) 2D fast Fourier-transformed version of A, vertical line artefacts are compressed to the x-axis. C) A mask is used to delete coefficients along the x-axis, avoiding coefficients at $F(0, y)$. D) An inverse fast Fourier-transformed C, where the artefacts have been effectively suppressed. Imperfect line artefacts in more heavily motion corrupted data would remain following this process however, the removal of which would require the removal of more Fourier coefficients surrounding the x-axis. This process would begin to visibly degrade the structural information in the angiographic image, thus an alternate method utilising wavelet filters is preferred.

The loss of structural information resulting from high values of σ negatively affects quantitative measurements of vessel morphology. To avoid this, multi-level wavelet decompositions were used to separate the vertical stripe information from the structural information, allowing the algorithm to effectively attenuate less than perfect-lines while maintaining the underlying structural information. A single-level wavelet decomposition is illustrated in Fig. 2.12 below:

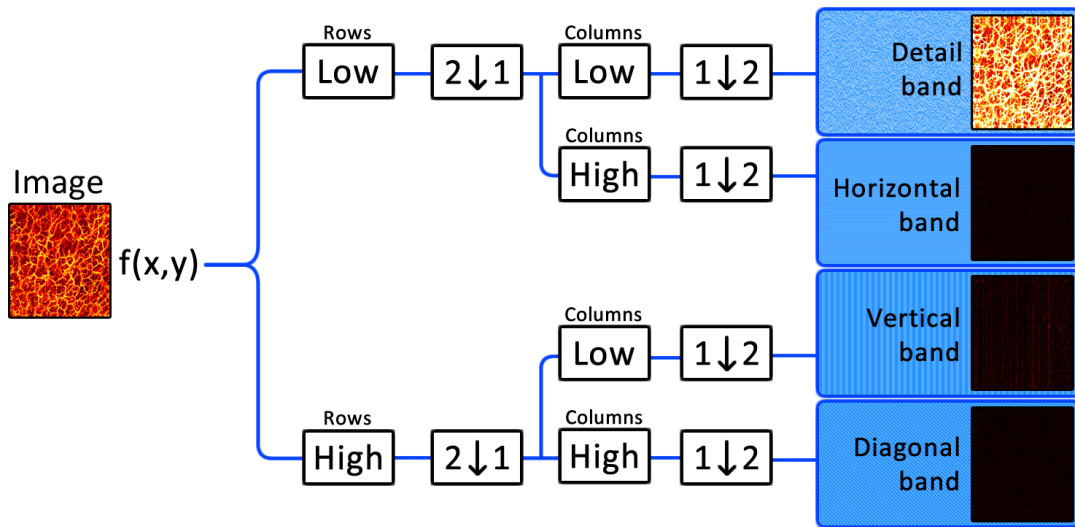


FIGURE 2.12: A single-level wavelet decomposition. `Low` and `High` refer to a Daubechies decomposition low-pass filter and high-pass filter respectively, the image data is convolved with these filters along either the columns or rows. `1 ↓ 2` refers to a down-sampling of the rows (Keeping the even indexed rows). `2 ↓ 1` refers to a down-sampling of the columns (Keeping the even indexed columns).

The result of a single-level wavelet decomposition is the image being broken up into 4 sub-images, each a quarter of the size of the original. The application of a low-pass wavelet filter to both the rows and columns captures the detail within the image. Low-pass filtering the rows and high-pass filtering the columns captures horizontal lines within the image. Conversely, high-pass filtering the rows and low-pass filtering the columns captures vertical lines within the image. High-pass filtering both the rows and columns captures diagonal lines within the image. This process can be repeated, with a multi-level wavelet decomposition simply repeating the process on the detail band on the image (Fig. 2.13). Importantly the entire

process is reversible, meaning the separated bands can be compiled back together in order to regain the original image.

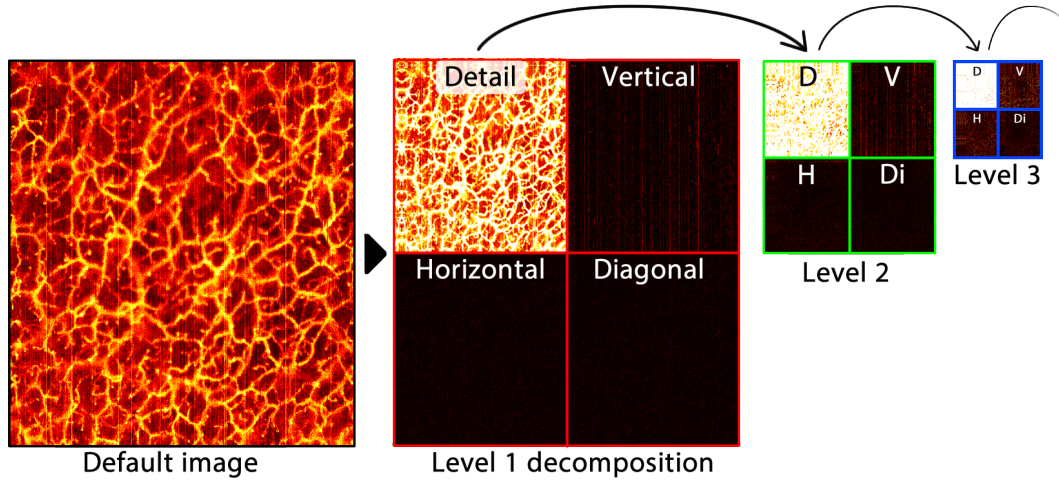


FIGURE 2.13: A multi-level wavelet decomposition. Successive application of the filtering steps illustrated on Fig. 2.12 allow for condensation of the vertical, horizontal and diagonal features within an image into strictly isolated subimages.

The important aspect of the multi-level wavelet filtering is that the vertical information within the images is increasingly condensed into the vertical band sub-images. Since these sub-images contain very little structural information, the FFT filtering technique discussed above can be applied to each using a large value of σ . The resulting filtered vertical band images can then be repackaged using an inverse wavelet filter in order to regain the original image, free of vertical line artefacts. For the purposes of this work, a 5-level Daubechies filter was used with σ being set to 10, both of these values were determined empirically. While higher levels of σ do not effect the combined Wavelet-FFT method greatly (App. A.3), a value of 10 was chosen as it was sufficient to remove the majority of artefacts observed herein.

To summarise the entire process: An image $f(x, y)$ is broken into detail, horizontal, vertical and diagonal sub-images using a Daubechies wavelet decomposition which is repeated 5-times. Each of the vertical sub-images are then Fourier transformed to give $F(x, y)$ and coefficients surrounding the x-axis are suppressed through application of a Gaussian damping function. Each vertical image is then

inverse Fourier-transformed and repackaged with the detail, horizontal and diagonal bands through means of an inverse-wavelet filter. The result is an image free of vertical line artefacts (Fig. 2.14).

More information on the combined Wavelet-FFT filter can be found in the Appendix (App. A.3), including a comparison between the simple FFT method and the combined Wavelet-FFT method described above.

2.1.7 Step 6 - Optional post-processing and data visualization

Following the removal of vertical motion artefacts with combined wavelet/FFT filtering, the angiographic dataset was ready for visualization. This was done in one of two ways: *en-face* projection or by direct 3D rendering of the dataset.

Visualization through *en-face* projection

One characteristic of angiographic OCT datasets is an observed forward scattering of the beam photons following their interaction with blood[19]. This results in an artefact which is commonly termed the waterfall effect or vessel shadowing, visible as a column of angiographic signal directly beneath each vessel (Fig. 2.7B). While this artefact is disadvantageous in that it optically occludes the visualization of vessels which are located directly beneath more superficial vessels, it can be utilised to improve two-dimensional visualization of the microcirculation. This is performed through the calculation of a mean intensity projection in the depth (z) direction over a depth range ($a \rightarrow b$):

$$Projection(x, y) = \frac{1}{b - a} \left(\sum_{z=a}^b (SV(x, y, z)) \right)$$

As this process effectively flattens a 3D volume into a 2D plane, subtle information regarding the depth of the resulting microcirculation is lost.

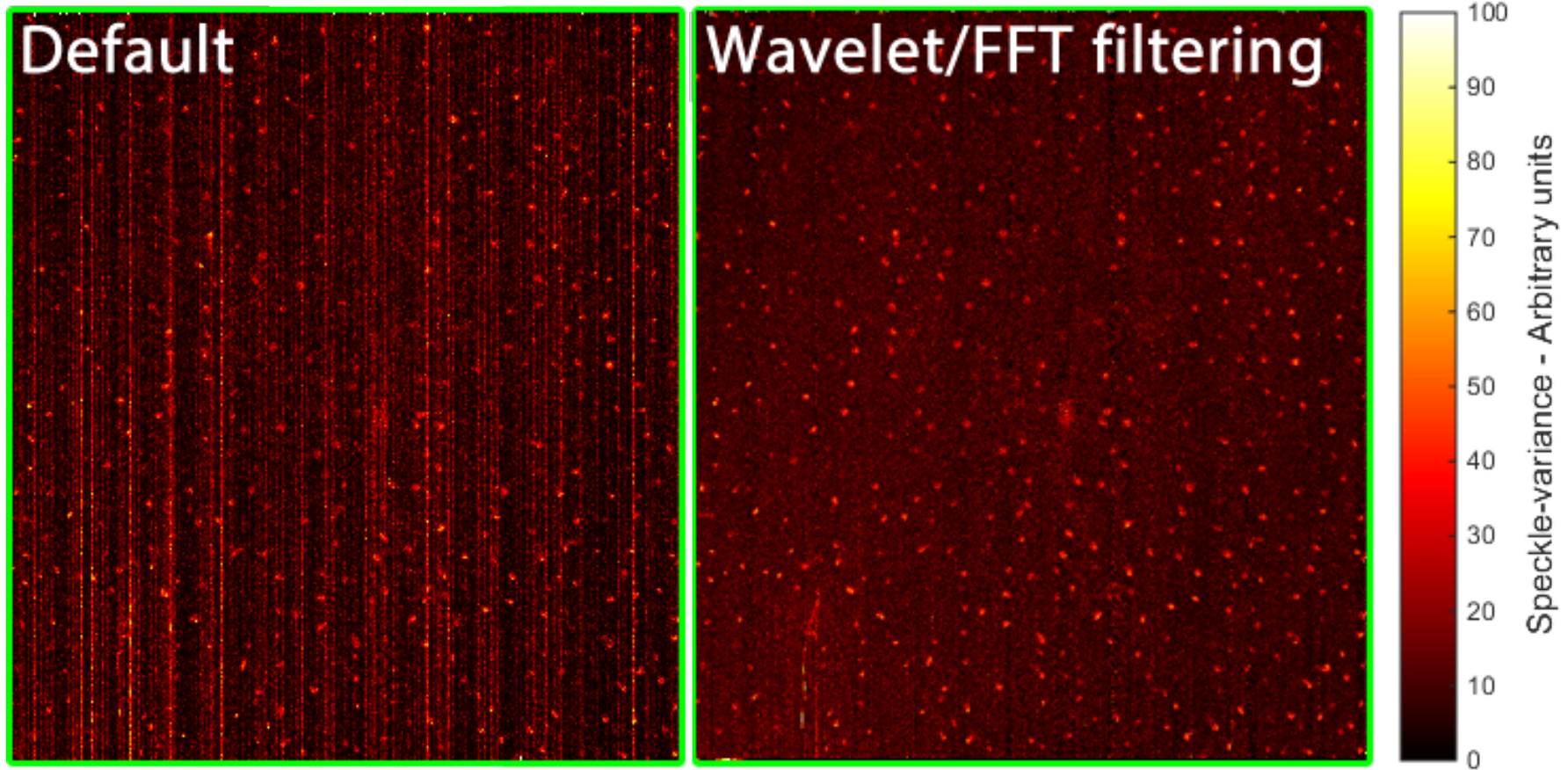


FIGURE 2.14: The result of wavelet/FFT filtering on an *en face* image of capillary loops within the skin. Vertical line artefacts resulting from patient BTM are effectively suppressed with minimal degradation to the underlying vascular morphology. Despite improving qualitative visualisation of the vasculature, this process is also advantageous for quantification purposes, as the capillary loops in the image on the left would be nearly impossible to segment from the background noise, however the capillary loops on the right can be effectively segmented and quantified through application of a simple binarisation threshold.

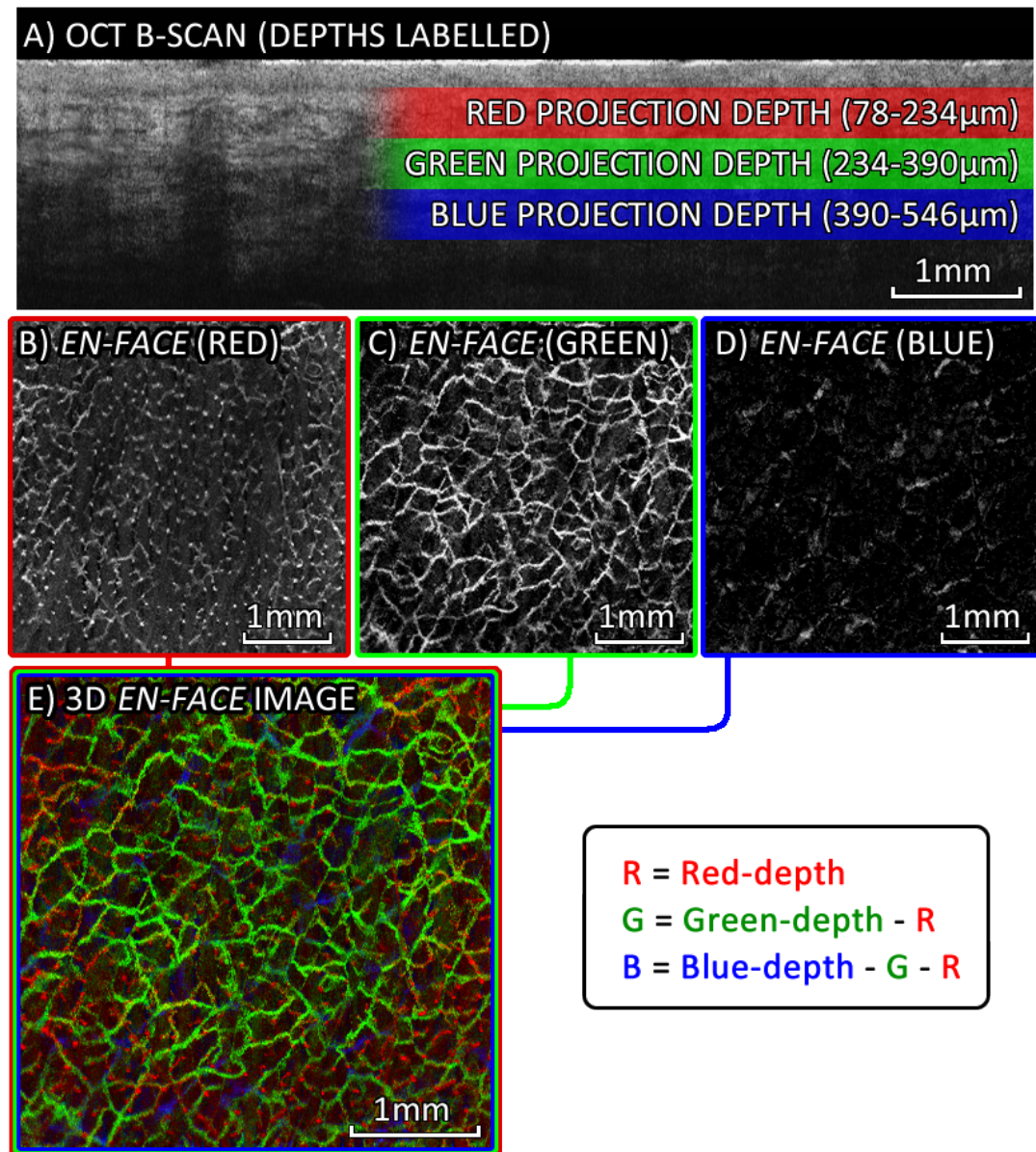


FIGURE 2.15: Mean intensity projections being used to assemble a depth projected vascular image. A) OCT B-scan with projections depths overlaid in colour. B-D) Each successive mean intensity projection over the depth range illustrated in A. E) Each projection is assigned a single channel in an RGB image, where colour now corresponds to depth within the tissue.

To regain some perception of vessel depth, multiple *en-face* mean intensity projections can be performed over a range of depths and recombined using the RGB channels of a colour image. Fig. 2.15 illustrates this process, showing how a projection over the depth range $78 \rightarrow 234\mu\text{m}$ can be mapped to red, the range $234 \rightarrow 390\mu\text{m}$

to green and the range $390 \rightarrow 546\mu m$ mapped to blue. Effectively creating a two-dimensional image with depth information represented with RGB colours.

In general the projection technique is ideal for cases where further processing of the datasets are required, such as skeletonisation (Sec. 3.2.4). This is because the averaging of the angiographic data in the depth direction improves the vessel contrast by reducing the intensity of speckle-noise without degrading the vessels themselves (Due to the presence of the vessel shadowing or waterfall effect), and thus is preferable to simply using *en-face* plane images of the dataset.

Visualization in 3D

While the observed vessel shadowing has the benefit of improving projection images of the vasculature, it obscures the 3D visualization of vessels. Thus in order to render vessels in 3D it was first necessary to apply a step-down exponential filter to the angiographic volume:

$$SV(x, y, z) = SV(x, y, z) * e^{-\frac{1}{\gamma} * \sum_{n=1}^z SV(x, y, n)}$$

Here γ represents an attenuation factor that is selected empirically, with greater values of γ corresponding to a faster roll-off of angiographic signal with depth, typical values of γ used in this study are ≈ 100 .

Following the removal of the shadowing artefact using the step-down exponential filter, the angiographic volume was rendered in 3D using Amira (FEI Visualization Sciences Group) and displayed for analysis. Fig. 2.16 illustrates the result.

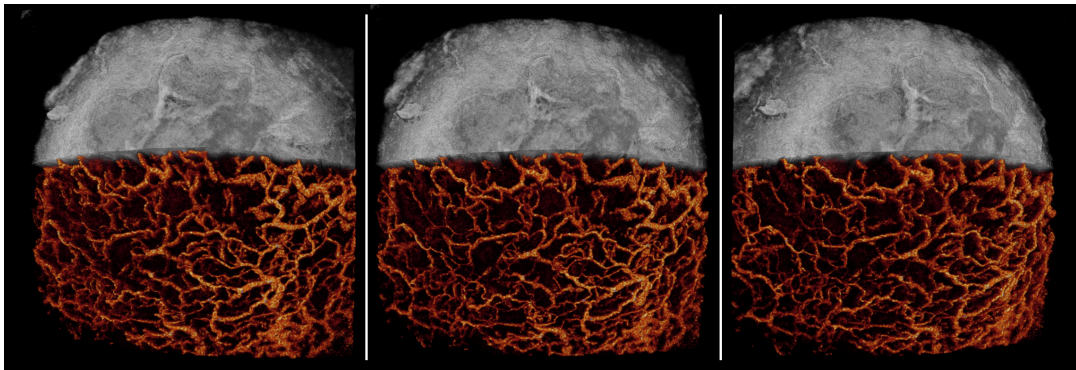


FIGURE 2.16: Rendered 3D visualisation of the vasculature within a subcutaneously implanted fibrosarcoma tumour. The top half (Grey) displays the structural OCT information, while the bottom half (Red) shows a 3D representation of the vessels within the tumour. The volume was pre-processed with the step-down exponential filter ($\gamma = 100$) prior to rendering within Amira.

2.1.8 In summary

In summary, the angiographic processing pipeline consists of numerous parallel algorithms which were all designed to improve the visibility and contrast of the resulting microcirculation. Fig. 2.17 summarises the entire process in flowchart form. Furthermore, to enable rapid processing of angiographic OCT datasets, a MATLAB graphical user interface (GUI) containing the entire angiographic processing pipeline was programmed and compiled. The GUI facilitates both *en-face* and B-scan visualisation of both the structural and vascular information, and can export frames for further analysis in a 3D rendering program. Additionally, the program automatically detects the presence of a graphical processing unit (GPU) on the host computer, and can utilise this device to greatly accelerate the processing algorithms through utilisation of parallel processing. Fig. 2.18 shows the main screen of the GUI with labelled features being elaborated upon in table 2.2.

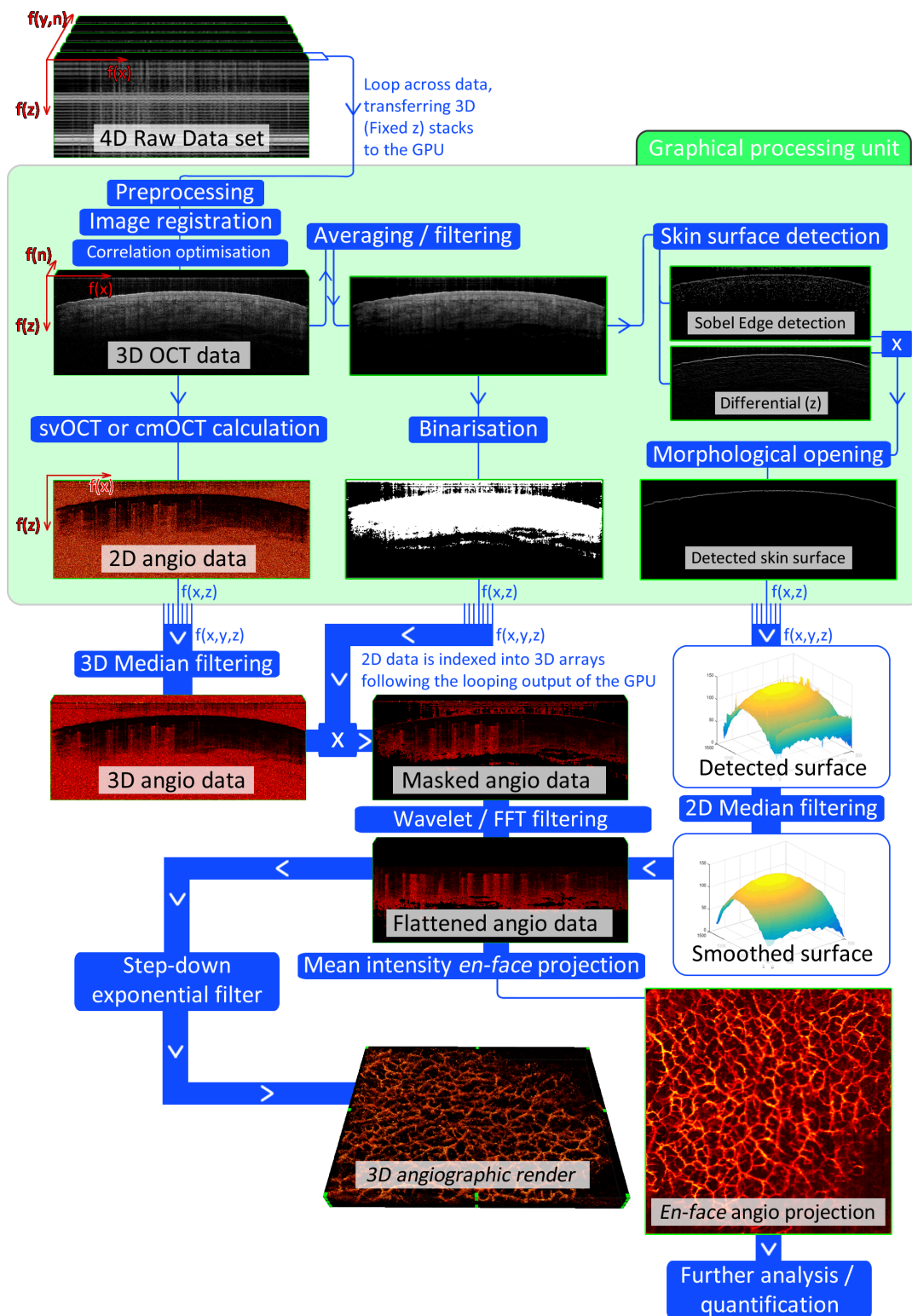


FIGURE 2.17: Flowchart showing the entire angiographic processing pipeline which was utilised for this work.

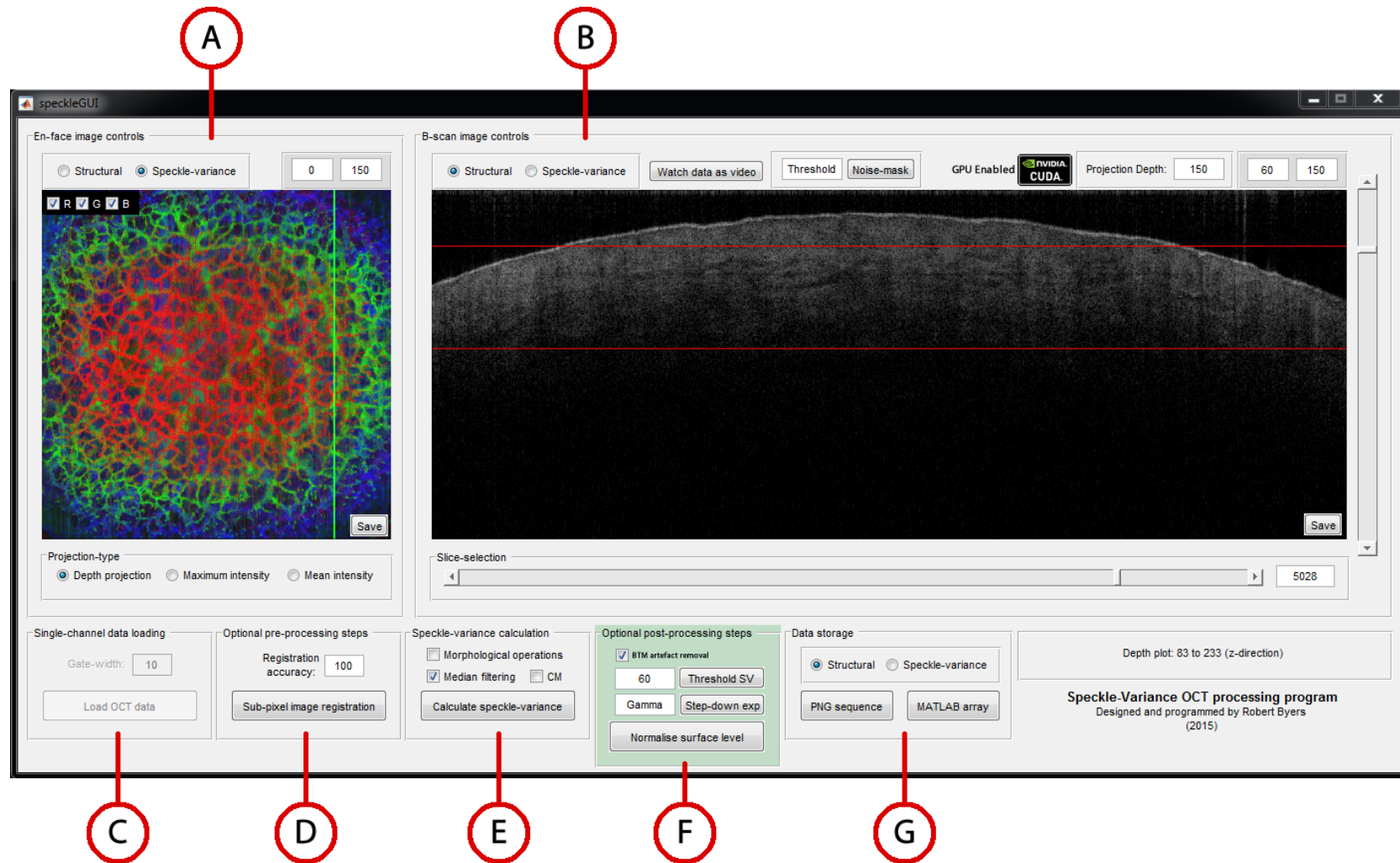


FIGURE 2.18: Compiled GUI which was developed for the processing of raw OCT data. Labels A-G are described in detail in table 2.2 below. Briefly: A) *En-face* view of the current structural or vascular projection. B) B-scan view of either the structural or vessel data. C) Data loading panel and gate-width selection. D) Pre-processing functions such as image-registration. E) Angiographic calculation including the svOCT and cmOCT algorithms. F) Post-processing steps such as the step-down exponential filter and surface normalisation. G) Data output to save the results to disk.

TABLE 2.2: Overview of GUI features

Feature	Description
A) <i>En-face</i> panel	User can display an <i>en-face</i> views of either the structural or vasculature data. Projection depth is chosen manually (See Sec. 2.1.7)
B) B-scan panel	User can view individual B-scan slices or the corresponding svOCT or cmOCT data. Projection depth is chosen numerically in units of pixels, with the starting depth being controlled by the slider on the right.
C) Data loading	The gate-width needs to be provided by the user (N is always 2 for cmOCT). Raw data is loaded directly from the output of the Labview VI which collects images (.oct files), it's then resampled to k-space, scaled and Fourier transformed to form viewable B-scan images.
D) Pre-processing	Contains the controls for the image-registration step (Sec. 2.1.3)
E) Angiographic processing	This section allows the user to perform either svOCT (Default) or cmOCT as per the previously defined algorithms.
F) Post-processing	Contains post-processing tools such as the wavelet-FFT filter (Sec. 2.1.6), step-down exponential filter (Sec. 2.1.7) and surface normalization (Sec. 2.1.5).
G) Data output	The user can save the processed data as either a MATLAB array or as sequences of PNG files. This is useful when further analysis is required, for example 3D visualization.

References

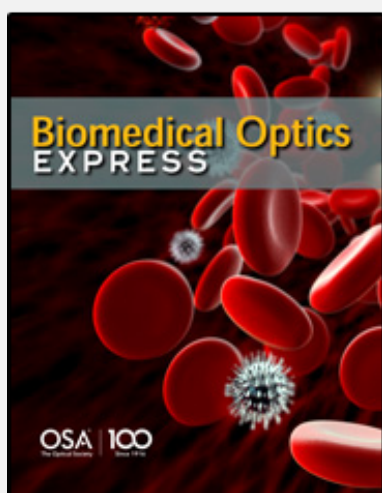
- [1] J. Enfield, E. Jonathan, and M. Leahy, "In vivo imaging of the microcirculation of the volar forearm using correlation mapping optical coherence tomography (cmOCT)", vol. 2, no. 5, pp. 1184–1193, 2011. DOI: 10.1002/jbio.201000103/abstract (cit. on pp. 28, 39).
- [2] H. Bay, A. Ess, T. Tuytelaars, and L. Van Gool, "Speeded-Up Robust Features (SURF)", 2008 (cit. on p. 33).
- [3] R. Byers, "In-Vivo Measurements of Skin Microvasculature using GPU-Accelerated Speckle-Variance Optical Coherence Tomography", Dissertation, The University of Sheffield, 2014, pp. 1–95 (cit. on p. 33).
- [4] J. Lee, V. Srinivasan, H. Radhakrishnan, and D. A. Boas, "Motion correction for phase-resolved dynamic optical coherence tomography imaging of rodent cerebral cortex.", *Optics express*, vol. 19, no. 22, pp. 21 258–70, Oct. 2011, ISSN: 1094-4087 (cit. on p. 34).
- [5] L. An, H. M. Subhush, D. J. Wilson, and R. K. Wang, "High-resolution wide-field imaging of retinal and choroidal blood perfusion with optical microangiography", *Journal of Biomedical Optics*, vol. 15, no. 2, p. 026 011, Mar. 2010, ISSN: 1083-3668. DOI: 10.1117/1.3369811 (cit. on p. 34).
- [6] Y. Keller, A. Averbuch, and O. Miller, "Robust Phase Correlation", *Pattern Recognition*, vol. 2, pp. 740–743, 2004 (cit. on p. 35).
- [7] M. Guizar-Sicairos, S. T. Thurman, and J. R. Fienup, "Efficient subpixel image registration algorithms", *Optics Letters*, vol. 33, no. 2, p. 156, 2008, ISSN: 0146-9592. DOI: 10.1364/OL.33.000156 (cit. on p. 36).

- [8] J.-p. Thirion, "Image matching as a diffusion process : an analogy with Maxwell 's demons", 2011 (cit. on pp. 37, 43).
- [9] M. F. Kraus, B. Potsaid, M. a. Mayer, R. Bock, B. Baumann, J. J. Liu, J. Hornegger, and J. G. Fujimoto, "Motion correction in optical coherence tomography volumes on a per A-scan basis using orthogonal scan patterns.", *Biomedical optics express*, vol. 3, no. 6, pp. 1182–99, Jun. 2012, ISSN: 2156-7085. DOI: 10.1364/B0E.3.001182 (cit. on p. 37).
- [10] Y. M. Liew, R. A. McLaughlin, F. M. Wood, and D. D. Sampson, "Motion correction of in vivo three-dimensional optical coherence tomography of human skin using a fiducial marker.", *Biomedical optics express*, vol. 3, no. 8, pp. 1774–86, Aug. 2012, ISSN: 2156-7085. DOI: 10.1364/B0E.3.001774 (cit. on p. 37).
- [11] P. Zang, G. Liu, M. Zhang, C. Dongye, J. Wang, A. Pechauer, T. Hwang, D. Wilson, D. Huang, D. Li, and Y. Jia, "Automated motion correction using parallel-strip registration for wide-field en face OCT angiogram", *Biomedical Optics Express*, vol. 7, no. 7, pp. 3822–3832, 2016, ISSN: 21567085. DOI: 10.1364/B0E.7.002823 (cit. on p. 37).
- [12] D. W. Wei, A. J. Deegan, and R. K. Wang, "Automatic motion correction for *in vivo* human skin optical coherence tomography angiography through combined rigid and nonrigid registration", *Journal of Biomedical Optics*, vol. 22, no. 6, p. 066013, 2017, ISSN: 1083-3668. DOI: 10.1117/1.JBO.22.6.066013 (cit. on p. 37).
- [13] Y. Jia, S. T. Bailey, D. J. Wilson, O. Tan, M. L. Klein, C. J. Flaxel, B. Potsaid, J. J. Liu, C. D. Lu, M. F. Kraus, J. G. Fujimoto, and D. Huang, "Quantitative Optical Coherence Tomography Angiography of Choroidal Neovascularization in Age-Related Macular Degeneration", *Ophthalmology*, vol. 121, no. 7, pp. 1435–1444, Jul. 2014, ISSN: 01616420. DOI: 10.1016/j.ophtaha.2014.01.034 (cit. on p. 37).
- [14] A. Camino, Y. Jia, G. Liu, J. Wang, and D. Huang, "Regression-based algorithm for bulk motion subtraction in optical coherence tomography angiography.",

- Biomedical optics express*, vol. 8, no. 6, pp. 3053–3066, Jun. 2017, ISSN: 2156-7085. DOI: 10.1364/B0E.8.003053 (cit. on p. 37).
- [15] A. Mariampillai, M. K. K. Leung, M. Jarvi, B. a. Standish, K. Lee, B. C. Wilson, A. Vitkin, and V. X. D. Yang, “Optimized speckle variance OCT imaging of microvasculature.”, *Optics letters*, vol. 35, no. 8, pp. 1257–9, Apr. 2010, ISSN: 1539-4794 (cit. on p. 38).
- [16] S. Paxton, M. Peckham, K. Adele, S. Paxton, K. Adele, and M. Peckham, *The Leeds Histology Guide*, 2003 (cit. on p. 40).
- [17] X. Gu, H. Pan, Y. Liang, R. Castillo, D. Yang, D. Choi, E. Castillo, A. Majumdar, T. Guerrero, and S. B. Jiang, “Implementation and evaluation of various demons deformable image registration algorithms on a GPU”, *Physics in Medicine and Biology*, vol. 55, no. 1, pp. 207–219, 2010, ISSN: 0031-9155. DOI: 10.1088/0031-9155/55/1/012. arXiv: 0909.0928 (cit. on p. 42).
- [18] B. Münch, P. Trtik, F. Marone, and M. Stampanoni, “Stripe and ring artifact removal with combined wavelet-Fourier filtering”, *EMPA Activities*, vol. 17, no. 2009-2010 EMPA ACTIVITIES, pp. 34–35, 2009, ISSN: 16601394. DOI: 10.1364/0E.17.008567 (cit. on p. 44).
- [19] A. Maeda, M. K. K. Leung, L. Conroy, Y. Chen, J. Bu, P. E. Lindsay, S. Mintzberg, C. Virtanen, J. Tsao, N. A. Winegarden, Y. Wang, L. Morikawa, I. A. Vitkin, D. A. Jaffray, R. P. Hill, and R. S. DaCosta, “In vivo optical imaging of tumor and microvascular response to ionizing radiation.”, *PloS one*, vol. 7, no. 8, e42133, Jan. 2012, ISSN: 1932-6203. DOI: 10.1371/journal.pone.0042133 (cit. on p. 49).

Chapter 3

Paper 1 - Angiographic OCT for the study of subcutaneous tumours.



This chapter contains excerpts, with permission, from the following published work:

Vascular patterning of subcutaneous mouse fibrosarcomas expressing individual VEGF isoforms can be differentiated using angiographic optical coherence tomography.

Robert A. Byers, Matthew Fisher, Nicola J. Brown, Gillian M. Tozer, and Stephen J. Matcher

Biomedical Optics Express

Vol. 8, [Issue 10](#), pp. 4551-4567 (2017)

<https://doi.org/10.1364/B0E.8.004551>

This chapter contains the "Author Accepted" version of the manuscript.

Statement of contribution

Concerning the publication:

Vascular patterning of subcutaneous mouse fibrosarcomas expressing individual VEGF isoforms can be differentiated using angiographic optical coherence tomography.

Contributor	Statement of contribution
Robert A. Byers Signed: _____	I am the primary contributor to this work. Having performed all of the data acquisition, processing and analysis. <ul style="list-style-type: none">• Prepared the manuscript.• Performed OCT imaging/ data collection.• Performed all data analysis and interpretation.• Assisted with animal welfare duties (Together with M. Fisher)
Matthew Fisher Signed: _____	<ul style="list-style-type: none">• Implanted subcutaneous tumours/culture and growth of tumour cells.• Assisted with OCT data collection. Assisted with animal welfare duties (Together with R. Byers)

Principle supervisor confirmation

I have sighted email or other correspondence from all co-authors confirming their certifying authorship.

Name: _____

Signature: _____

Date: _____

Vascular patterning of subcutaneous mouse fibrosarcomas expressing individual VEGF isoforms can be differentiated using angiographic optical coherence tomography.

ROBERT A. BYERS,¹ MATTHEW FISHER,² NICOLA J. BROWN,² GILLIAN M. TOZER,² AND STEPHEN J. MATCHER¹

¹ *Biophotonics Group, Krotov Research Institute, University of Sheffield, Sheffield, UK*

² *Department of Oncology & Metabolism, The Medical School, University of Sheffield, Sheffield, UK*

NB: GT and SM are Joint Senior Authors

Abstract: Subcutaneously implanted experimental tumours in mice are commonly used in cancer research. Despite their superficial location, they remain a challenge to image non-invasively at sufficient spatial resolution for microvascular studies. Here we evaluate the capabilities of optical coherence tomography (OCT) angiography for imaging such tumours directly through the murine skin *in-vivo*. Datasets were collected from mouse tumours derived from fibrosarcoma cells genetically engineered to express only single splice variant isoforms of vascular endothelial growth factor A (VEGF); either VEGF120 or VEGF188 (fs120 and fs188 tumours respectively). Measured vessel diameter was found to be significantly ($p < 0.001$) higher for fs120 tumours ($60.7 \pm 4.9 \mu\text{m}$) compared to fs188 tumours ($45.0 \pm 4.0 \mu\text{m}$). The fs120 tumours also displayed significantly higher vessel tortuosity, fractal dimension and density. The ability to differentiate between tumour types with OCT suggests that the visible abnormal vasculature is representative of the tumour microcirculation, providing a robust, non-invasive method for observing the longitudinal dynamics of the subcutaneous tumour microcirculation.

©2017 Optical Society of America

OCIS codes: (170.3880) Medical and biological imaging; (110.4500) Optical coherence tomography; (170.2655) Functional monitoring and imaging; (100.2000) Digital image processing.

3.1 Introduction

Within the body, the structural features of major arteries and veins are genetically controlled during embryonic development and generally remain consistent between individuals. The microvasculature however can be dynamically remodeled as a result of molecular and mechanical stimuli within the local microenvironment[1]. Tumour growth relies on a continual process of micro-vascularisation, notably via angiogenesis, which also facilitates metastasis[2]. The resulting tumour vasculature is both morphologically and functionally abnormal[3], the study of which potentially offers valuable insight into tumour development and pathophysiology.

Angiographic imaging of murine models of cancer has proved particularly important to oncological research, greatly aiding our understanding of tumour growth, progression and treatment within living animals[4]. Traditional necropsy methods such as immunohistochemistry have retained their importance for quantifying the microcirculation within implanted tumours[5]. However modern non-invasive imaging techniques have quickly gained traction due to the potential of longitudinal vascular visualisation, vastly reducing the number of animals required to produce statistically robust data. Currently, intravital microscopy is widely utilised to study tumour growth, typically involving the surgical replacement of the highly scattering skin layer with a transparent glass coverslip[6]. Using this model, angiographic optical coherence tomography (OCT) imaging has been used to enable high-resolution longitudinal imaging of tumour dynamics and response to treatment[7]. Furthermore, *in-vivo* full field angiography of subcutaneously grown tumours, with overlying skin intact, has previously been achieved with perfusion computed tomography[8] and dynamic magnetic resonance imaging[9], [10]. More recently, multi-spectral optoacoustic tomography has been utilised to visualise vascular morphology and oxygenation at $70\mu\text{m}$ resolution over entire 1cm^3 tumour volumes[11].

Despite these advances, it remains challenging to non-invasively image the microscale circulation within subcutaneously implanted tumours because optical modalities are required to resolve these vessels (The average capillary being $\approx 3.7\mu\text{m}$ in diameter[12]), and these modalities are often unable to penetrate through the highly

scattering layer of skin. OCT is an established imaging technique which has been widely utilised to capture both structural and angiographic images within human skin[13]. Most notably, OCT offers depth penetration of up to $\approx 1\text{mm}$ within tissue and is capable of extracting depth encoded data such that individual layers of tissue can be visualized at a high resolution. Compared to human skin (Where OCT typically is used to assess only the epidermal/papillary dermis layers of skin), which can be many millimeters thick; female CD-1 nude mice generally exhibit superficial tissue layers approximately $\approx 550\mu\text{m}$ in thickness ($\approx 30\mu\text{m}$ epidermis, $\approx 220\mu\text{m}$ dermis, $\approx 300\mu\text{m}$ hypodermis)[14]; thus the superficial vasculature of subcutaneously implanted tumours may be visible and within the field of view of OCT. Speckle-variance OCT (svOCT) can be used to extract volumetric flow information from four-dimensional OCT data sets (X-Y-Z-Time), with multiple data points being collected at each spatial location[15]. This is based on the fact that a fluid pixel will display rapidly evolving temporal variations in the OCT signal (speckle patterns) when compared to solid tissue pixels. Hence by calculating the variance of pixels at the same spatial location as a function of time, contrast is generated between stationary solids and moving liquids.

This study aimed to develop and evaluate the performance of angiographic svOCT in the context of murine subcutaneous tumour imaging. In particular, we attempt to differentiate the vascular morphologies within mouse tumours derived from fibrosarcoma cells genetically engineered to express only single splice variant isoforms of vascular endothelial growth factor A (VEGF); either VEGF120 or VEGF188 (fs120 and fs188 tumours respectively). Previously, using tumours grown in transparent chambers implanted into the rear dorsum of mice and conventional intravital optical microscopy, Tozer *et al* observed that fs120 tumour blood vessels were larger, more disorganised and formed more tortuous vascular networks than those of fs188 tumours[16]. This study aimed to identify whether these differential vascular patterns were also present within the microcirculation of subcutaneously grown tumours, independent of the dorsal skin-fold window chamber.

3.2 Materials and methods

All animal experiments were conducted according to the United Kingdom Animals (Scientific Procedures) Act 1986 (UK Home Office Project License PPL40/3649) and with local University of Sheffield ethical approval.

3.2.1 Subcutaneous tumour implantation

In order to evaluate the capabilities of OCT for the imaging of subcutaneously implanted tumours, mouse fibrosarcoma tumour cells (1×10^6 in 0.05 ml serum-free Dulbecco's Minimal Essential Medium) expressing VEGF as only its highly soluble VEGF120 isoform (fs120 tumour cells) or its highly matrix-bound isoform VEGF188 (fs188 tumour cells) were subcutaneously injected into the rear dorsum of female CD1 nude mice aged 8-12 weeks. Development of these cell lines has been described previously[16]. Female nude mice were chosen due to their absence of hair, and having slightly thinner dermis/hypodermis skin layers than male nude mice[17]. OCT imaging of each tumour was performed daily, with the mice under isoflurane anaesthesia. Daily calliper measurements were made of the three orthogonal tumour diameters and animals were sacrificed once the largest tumour diameter reached no more than 12mm. Excised tumours with overlying skin intact were halved and fixed in 10% neutral buffered formalin overnight and then paraffin-embedded prior to processing for histological analysis with hematoxylin and eosin (H&E) staining and immunohistochemistry for rat anti-mouse cluster of differentiation 31 (CD31) monoclonal antibodies (Cat No. DIA-310, Dianova GmbH, Hamburg, Germany), as a marker of vascular endothelial cells.

3.2.2 Data acquisition and imaging protocol

All imaging for this study was performed using a commercial CE-marked multi-beam OCT system (Vivosight®, Michelson Diagnostics Ltd, Orpington, Kent, UK). This system utilises a swept-source 1305nm Axsun laser with a bandwidth of 147nm, achieving a resolution of approximately $5\mu\text{m}$ axially and $7.5\mu\text{m}$ laterally (In tissue). One-dimensional A-scans are captured at a line rate of 20 kHz and contain structural

information to a depth of approximately 1mm in murine skin. The imaging beam is scanned laterally across the surface of the tumour in order to collect a 3-dimensional image. In an effort to reduce the degree of motion within the collected OCT scans, the mobile imaging probe of the Vivosight was clamped into position and manually lowered to the correct height. A plastic standoff bridged the gap between the imaging probe and the skin. The standoff gently contacted the skin surface such that any lateral movement was reduced. Fixation of the imaging probe in this manner is important as it removes a source of movement from the resulting data. In order to minimise homeostatic effects on the circulation as a result of temperature variation, the rectal temperature of the mouse was maintained at 37°C. during imaging using a heating mat which was thermostatically controlled via a rectal thermocouple probe. Furthermore, all imaging was conducted inside a plastic chamber which was heated to an internal temperature of 32°C. This experimental set-up is illustrated in 3.1.

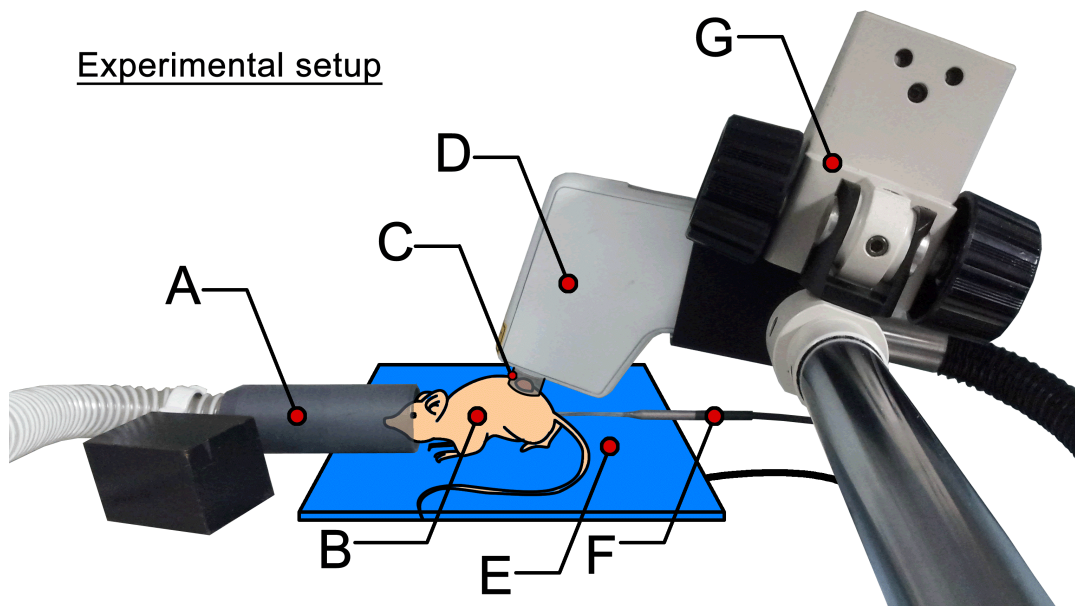


FIGURE 3.1: Experimental setup within a plastic chamber which was heated to 32°C internal temperature. A) Rodent facemask for administration of isoflurane gaseous anesthesia. B) CD-1 Nude mouse. C) Plastic standoff which gently contacts the skin around the subcutaneous tumour. D) The OCT imaging probe (Vivosight). E) Feedback controlled heated mat. F) Rectal temperature probe (Feeds back to the heated mat). G) Mobile clamp for repositioning of the OCT imaging probe.

For this study, the scan size was set at 6mm in both the x and y directions, giving a wide field of view across the tumour. The spacing between A-scans was fixed at $10\mu\text{m}$ in order to closely match the lateral resolution of the OCT system while maintaining a high scan speed. Five repeat frames ($N = 5$) were collected at each stepped y-location and later used to evaluate the speckle-variance within each voxel. With these settings, each dataset took approximately 90 seconds to acquire, the raw data was stored to disk and processed offline.

3.2.3 Post-processing of data

The processing of svOCT datasets described here was previously described in detail in Sec. 2.1, and has thus been omitted for conciseness. Displayed images are shown with vessel depth being encoded with colour (Red = superficial, green = deeper, blue = deepest) as described in Sec. 2.1.7)

Despite the processing steps, strong vertical motion artefacts remained visible on the *en-face* images of the tumour vasculature. These arise because of global decorrelation caused by the animals breathing, heartbeat or muscular spasms during the imaging process. To improve visualisation of the data and enable accurate quantification of vascular morphology to be performed, it was necessary to remove these artefacts. Previous publications have utilised consecutively acquired 3D volumes and vessel layer segmentation in order to mosaic and eliminate such vertical bands with no notable image degradation[18], providing they are at a different location on each consecutive scan. However, to avoid doubling the required scan time for each volume, these bands were instead removed entirely through software. This was achieved using a combined wavelet-FFT filter similar to that previously described[19], the filter is also described in greater detail in Sec. 2.1.6 and App. A.3. Briefly, the filter attenuates high frequency components along the y-direction of the OCT volume, notably the sharp decorrelations caused by movement, which result in similarly sharp spikes in svOCT image intensity. Such vertical components are separated from the underlying detailed image using a multi-level Daubechies wavelet transform. Each “vertical” image from the wavelet decomposition was then 2D

Fourier transformed and the central frequencies surrounding the x -axis were attenuated through application of a 11-pixel high mask, designed to remove non-uniform (in y) vertical line artefacts. The vertical image is then inverse Fourier transformed and recombined with its corresponding “horizontal” and “detail” images using successive inverse wavelet transforms. While removal of perfect vertical artefacts is achievable simply using the Fourier transform, the additional wavelet transformations allowed for imperfect artefacts to be removed with minimal effect on the underlying detail. Fig. 3.2 shows the result of wavelet filtering on the vasculature of an fs188 tumour. Since the vertical lines are effectively being blurred in the y -direction (due to the attenuation of high frequency y -components in the image), this process can result in visible banding within the background intensity of the image, particularly around areas which contained wide or numerous line artefacts. Despite these banding artefacts, the underlying image clarity was greatly improved and binarisation was able to be performed without the anomalous detection of the strong vertical lines (3.2.4).

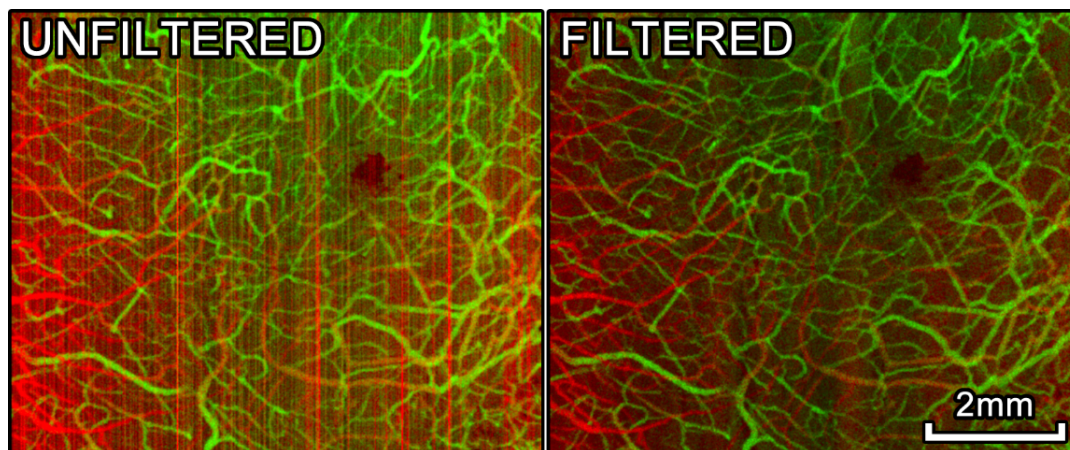
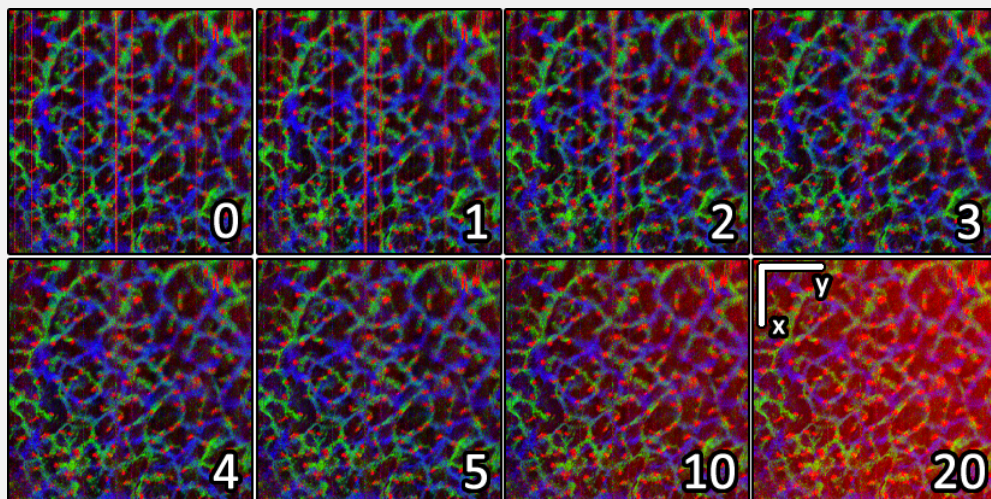


FIGURE 3.2: *En-face* svOCT images of an fs188 tumour before (Left) and after (Right) wavelet/FFT filtering was performed using a Daubechies wavelet to a decomposition level of 5. The colours correspond to the depth of the detected vessels, red vessels are $0 - 300\mu m$ and green vessels are $300 - 600\mu m$ beneath the skin surface.

Following post-processing, as described above, the resulting SV matrix contains 3-dimensional information pertaining to the location of the microvasculature.

Despite the CD1-nude mice being anaesthetised, bulk-tissue motion was a primary concern throughout this study. The primary contributor to this motion being the strong vertical movement of the torso due to the rapid breathing motions. While much of this movement was suppressed by the plastic standoff (Fig. 3.1C), strong vertical lines remained during post-processing. Such lines are caused by either the entire frame shifting with respect to previously acquired frames (Causing full frame decorrelation) or by non-uniform sampling due to tissue deformation, resulting in smaller localised areas of bright decorrelation signal. Thus the wavelet-FFT filter was of paramount importance for improving image clarity for quantification. One caveat of this filter however is that as the number of levels increases (See Fig. 2.13) the vertical lines are increasingly blurred in the y-direction.



The images above were wavelet-FFT filtered, with the white number corresponding to the decomposition level. Here visible image degradation begins to occur between 5-10 levels of decomposition, thus 5 was chosen as the decomposition level for this study. Often, a slight banding remains visible in the background intensity of filtered images; this is an artefact caused by the blurring out of motion artefacts.

3.2.4 Quantification of vessel parameters

Quantification of vessel parameters required binarisation of each angiographic image such that a vascular skeleton could be generated. For this, volume projections of the OCT datasets were generated by performing a mean-intensity projection (MIP) over the depth range $0 - 800\mu m$. The resulting angiographic OCT images were often noisy, with both vessels and background being highly non-uniform in pixel intensity (Fig. 3.3B). As a result of this, simple intensity thresholds are challenging to assign, generally yielding an overly complex skeleton with noise being anomalously detected as vasculature. To address this issue, the images were median filtered with a 3×3 kernel before being processed with a multiscale Hessian filtering algorithm[20] (MATLAB implementation by Marc Schrijver available on the MATLAB file exchange). This algorithm attempts to measure the “vesselness” of a pixel through consideration of the eigenvalues of the local Hessian matrix, assigning a value close to 1 for regions which are tubular in nature and 0 for regions which remain flat. Four parameters were required for the filtering process, the scale range and step size were set to $[1:10]$ (Corresponding to $10 - 100\mu m$) and 1 respectively based on the size of visible vessels within the tumours. These two parameters aimed to minimise any artificial vessel dilation or constriction in the resulting image by repeating the process over a range of vessel scales, with the maximum filter value for each pixel across all scales being recorded in the final image (Fig. 3.3C). The remaining parameters were two correction constants (F_1 and F_2), which were fixed at 0.5 and 15 after empirical experimentation with the resulting vessel detection. The filtered image was then pixel-wise multiplied by the original image to suppress the background noise and improve contrast (Fig. 3.3D). This combined image was then binarised using an automatically defined Otsu threshold[21] before being skeletonised (Fig. 3.3E/F).

A user defined field-of-view was used for quantification to ensure that only representative areas were selected. Areas of expected low angiographic signal such as the corners or gaps/holes in the image were discarded. Using the skeleton and binary data, vessel diameter was defined at each point on the skeleton as width of the

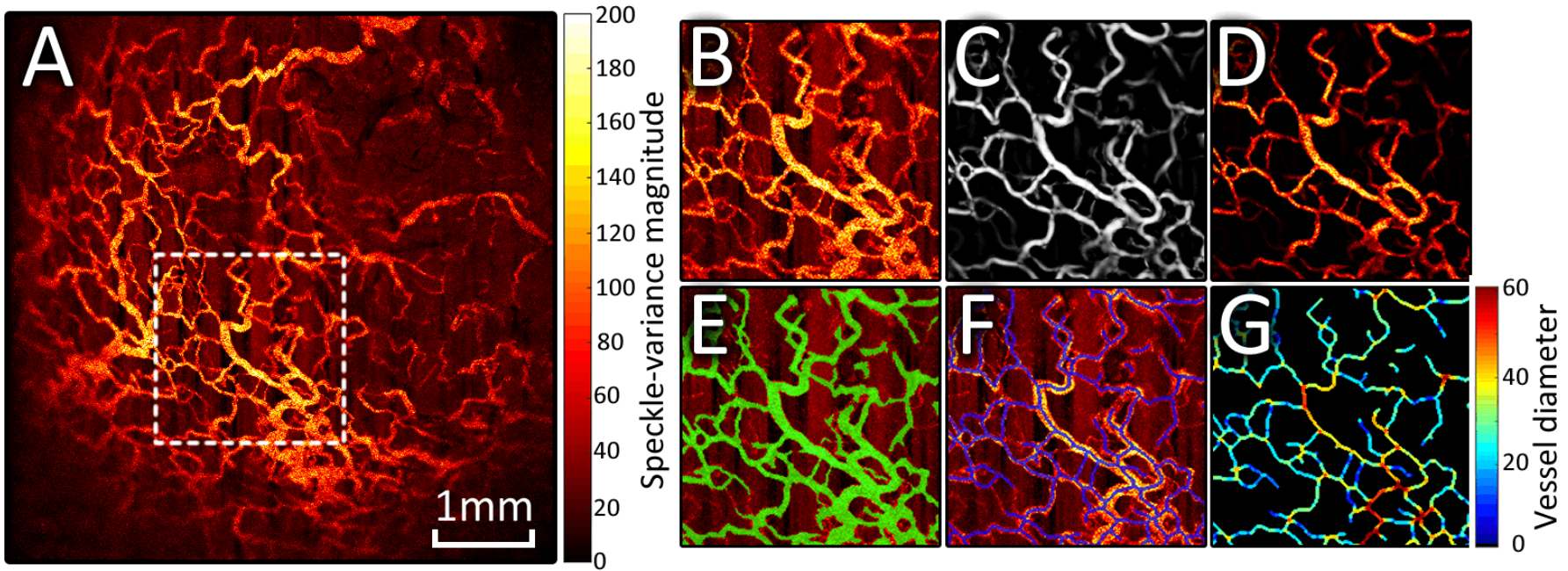


FIGURE 3.3: Skeletonisation procedure for subcutaneous tumour imaging. A) An *En-face* svOCT image captured from a subcutaneous fs120 tumour 17 days post-implantation. Dashed box shows zoomed section from B-G. B) Zoomed section of the *en-face* svOCT image. C) The result of the hessian-based filtering algorithm, which identifies tubular regions of an image. D) The result of $B \cdot C$, which improves vascular contrast against the background noise. E) Binary thresholding of D shown in green overlaid on the original image. F) Skeleton derived from the binary image in blue overlaid on the original image. G) Map of vessel diameter calculated using the binary threshold and the skeleton data from E and F.

binarised data perpendicular to the skeleton, a mean vessel diameter was then calculated by averaging across all skeleton points within the field-of-view. Total vessel length per mm^2 was calculated by averaging the total length of skeleton contained within 1mm^2 sub-blocks of the image. Vessel density (%) was simply the percentage of pixels within the field-of-view that were identified as vascular. Tortuosity was calculated as the average ratio between shortest path length and Euclidean distance between distant end-points at opposite sides of the skeleton. To calculate vessel segment length, the skeleton was broken into vessel segments by removing bifurcation points from the network, segment length was then defined as the path length between segment end points. Lastly, the fractal dimension of the skeleton was calculated using the box-counting method, resulting in a value between 0 and 3, with lower values indicating a more regular network[22].

For the longitudinal comparison of svOCT images captured from the same tumour over a period of time (3.3.2), elastic image registration was performed in order to ensure accurate vessel correlation between frames. This was achieved using a vector-spline method which has been detailed previously[23].

3.2.5 Statistics

Statistical analysis was carried out using MATLAB (R2014b – Mathworks). The unpaired Students t-test was used to test for significant differences between the two tumour types (fs188 and fs120). For cases where comparisons were made between three groups (Healthy, fs188 and fs120) a one-way ANOVA followed by the Tukey-Kramer honest significance difference (HSD) test was used. In all cases, comparisons were described as significant if the probability of the null hypothesis was <0.05 . All stated measurements are of the form $\text{mean} \pm \text{SD}$.

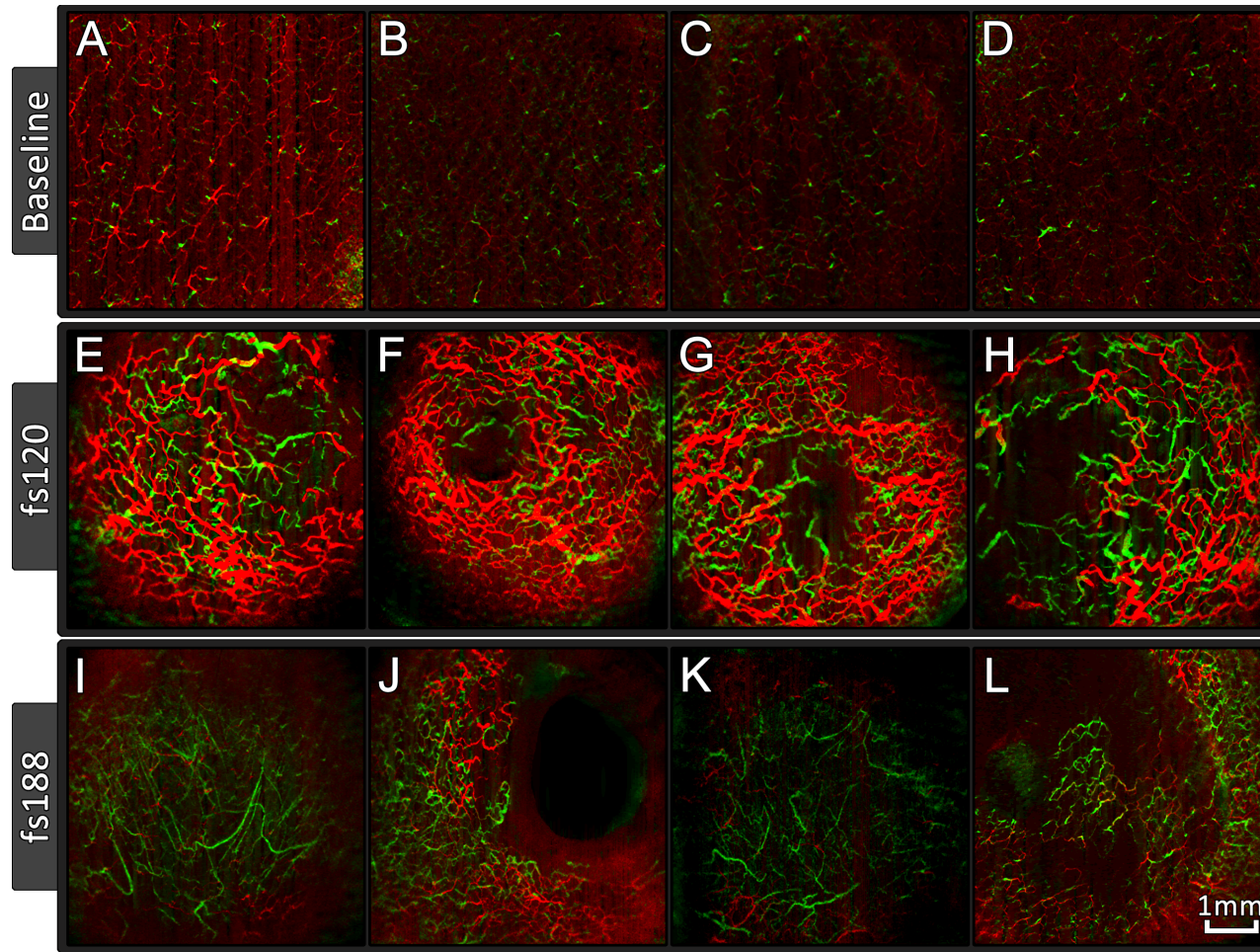


FIGURE 3.4: A selection of 6x6mm *en-face* svOCT images. A-D) Images of baseline murine skin vasculature without the presence of a tumour. E-L) Images of established subcutaneous tumour vasculature, each image is of a separate tumour captured once the largest tumour diameter exceeded 10mm. Middle row (E-H) shows tumours expressing only the VEGF120 isoform (fs120) and bottom row (I-L) shows tumours expressing only the VEGF188 isoform (fs188). All images were captured from different animals. The colours correspond to the depth of the detected vessels, red vessels are 0 – 400 μ m and green vessels are 400 – 800 μ m beneath the skin surface. E-L) Number of days post-implantation > 14 days.

3.3 Results and discussion

3.3.1 Visual inspection of VEGF120 and 188 expressing tumours

Fig. 3.4 shows a selection of *en-face* depth encoded svOCT images captured from both baseline skin and the subcutaneously implanted tumours of CD1 nude mice. The large abnormal vessel networks such as those seen in Fig. 3.4E-L only became visible to svOCT approximately 8-15 days post implantation. Prior to this, more regular organised vessel networks as represented in Fig. 3.4A-D were visible. This suggests that the early stages of tumour vessel development remain too deep within the tissue to be effectively imaged by OCT. However, after sufficient tumour expansion, typically 10-days post-implantation, large abnormal vessels were clearly visible within the field-of-view of the OCT system. This longitudinal vascular growth is further discussed in Sec. 3.3.2. Interestingly, the baseline vasculature appeared to be absent from the late-stage scans as evidenced by a comparatively lower angiographic signal at the “red depth” ($0 - 400\mu\text{m}$) aside from that attributed to larger abnormal vessels, suggesting that as the skin stretches over the surface of the tumour the flow in regular vessels ceases.

Furthermore, it appears that the fs120 tumours are more infiltrative than the fs188 variants, with a large portion of abnormal vessels appearing at superficial depths within skin. This is clearly visible in Fig. 3.4, where a large portion of the fs120 vessels appear red ($0 - 400\mu\text{m}$ depth), whereas the majority of the fs188 vessels appear green ($400 - 800\mu\text{m}$). This effect may be related to the distinct phenotype of the fibrosarcoma cells, with fs120 cells demonstrating a more proliferative phenotype than the fs188 variants both *in-vitro* and *in-vivo*. Furthermore, fs120 tumours have an additional ability to adopt both mesenchymal and amoeboid morphologies, which is considered an advantage for invasion[24]. One limitation of the svOCT technique is an observed shadowing effect beneath detected vessels caused by the forward scattering of photons by blood, which can occlude underlying vasculature[7]. For the case of the fs120 tumours, many of the vessels which are likely to be at the $400 - 800\mu\text{m}$ depth range (Green) are occluded by more superficial vessels

at the 0 – 400 μm depth range (Red), making vessels density calculations challenging to perform at an equivalent depth. This limitation is discussed further in Sec. 3.3.3.

3.3.2 Evaluation of longitudinal tumour monitoring

One key advantage of non-invasive subcutaneous tumour imaging is the potential for longitudinal observation of tumour growth and vascular development. Fig. 3.5 shows an example of longitudinal data acquisition, with images being acquired from the same fs120 and fs188 tumours over a period of 5 days, as well as a longer timescale visualisation of vascular development within an fs188 tumour from days 0 to 15.

The scans have been elastically co-registered such that vessels are aligned, following a similar methodology to that detailed previously[18]. For the case of the fs120 tumour, the mean vessel length per mm^2 is highest at day 14 post-implantation (4.1mm^{-1}), it then decreases to 1.4mm^{-1} at day 15, recovers to 3.5mm^{-1} on day 17 before decreasing again to 2.1mm^{-1} on day 18. Comparatively the fs188 tumour rises from 1.1mm^{-1} on day 14 (excluding the lower region which was outside of the scan field-of-view), to 2.2mm^{-1} on day 15, reduces to 2.0mm^{-1} on day 17, before returning to 2.2mm^{-1} at day 18.

To investigate this effect over a larger sample size, the standard deviation of mean vessel length per mm^2 was calculated for each tumour within both the fs120 and fs188 cohorts over days 14 to 18 post-implantation. A two-sample independent t-test was then used to evaluate significance. A majority of the tumours had unsuitable datasets and thus were omitted from this analysis. Omission was a result of either the data having a non-complimentary field of view (non-overlapping scan site on subsequent days), or certain days displaying motion corrupted vascular signal, both being unsuitable for comparison. In total, the number of viable datasets used was $n=4$ for both the fs120 and fs188 groups. Whilst the fs120 group had a higher variation in measured vessel lengths over time ($\text{SD} = 1.4\text{mm}^{-1}$) when compared to the fs188 group ($\text{SD} = 0.4\text{mm}^{-1}$), this result did not reach statistical significance ($p=0.063$) due to the small sample number. Thus it is unclear if fs120 tumours

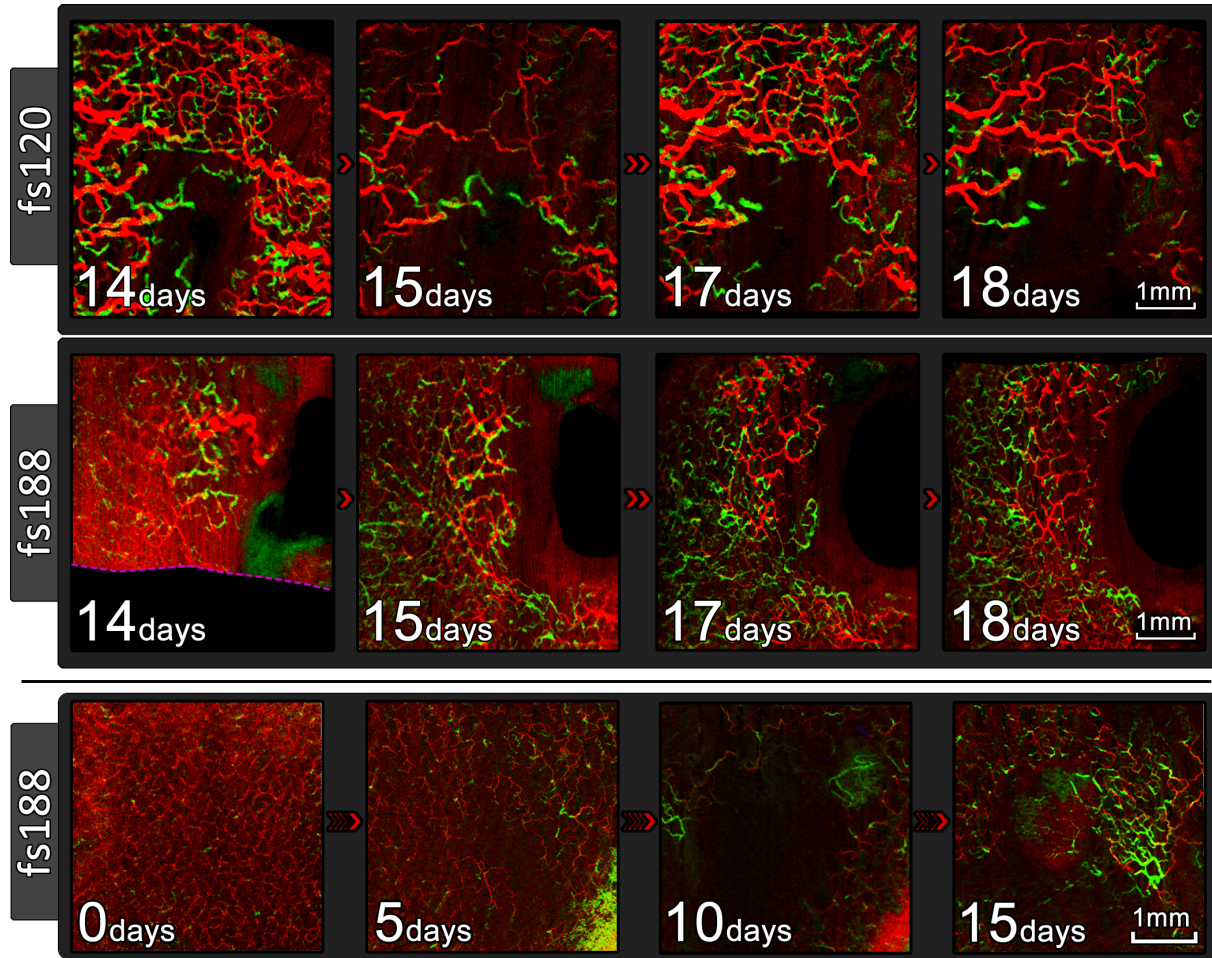


FIGURE 3.5: Top and middle rows) Depth encoded short-term longitudinal svOCT images of both an fs120 and an fs188 tumour over a period of 5 days. Images have been elastically registered together using UnwarpJ[23] such that the same vessels align on subsequent frames. Bottom row) 4x4mm (Zoomed) *en-face* svOCT images showing long-term longitudinal vascular progression from pre- tumour implantation to 15-days post- tumour implantation. Each separate row represents longitudinal data that was captured from one unique animal. The colours correspond to the depth of the detected vessels, red vessels are 0 – 400 μm and green vessels are 400 – 800 μm beneath the skin surface. The white number in the lower left corner of each image corresponds to the number of days post-tumour implantation that the image was captured.

demonstrate increased day-day variation in mean vessel length. Fig. 3.6 shows the changes in mean vessel length per mm^2 for each animal over time.

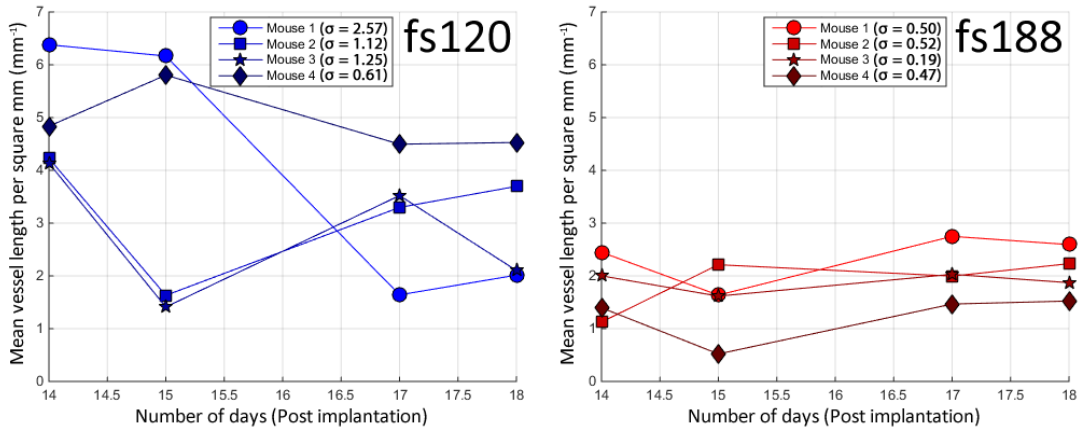


FIGURE 3.6: Line plots showing the variation in measured vessel length per square mm as a function of time within subcutaneous tumours expressing either the VEGF120 isoform (blue) or the VEGF188 isoform (red). The standard deviation in the measured mean vessel length for each animal is calculated as a function of time, and represents how much variance is visible within the measurement. The average of these standard deviations across all four fs120 mice (1.4mm^{-1}) is higher than those in the fs188 cohort (0.4mm^{-1}), however this result does not reach statistical significance ($p = 0.063$).

Such variability in the number of visible vessels from one day to the next is unlikely to be a result of vascular remodeling. It could potentially be a direct result of increased pressure being applied to the surface by the plastic standoff cap (Seen in Fig. 3.1C). In this case, one might expect the more superficial (red) vessels to occlude first, which does not appear to be the case. A previous study into the effects of applied surface pressure on the underlying vasculature demonstrated that both the superficial and deeper vasculature plexus are both affected by surface pressure (Sec. 7.3), thus this could still be the case. Alternatively, it is possible that reduced localised flow within the disappearing vessel linkages is responsible for the loss of visualisation, as if the decorrelation time of the slow-flowing blood reduces below the frame acquisition interval (30ms) of the OCT system, then the flow signal is lost. Another explanation for the loss of vessel density is that vasoconstriction or upstream vascular shunting may be occurring as the region homeostatically responds

to small changes in external stimuli such as temperature. It is also highly likely that the use of isoflurane anaesthetic is both influencing the degree of thermoregulatory inhibition and acting as a cardiovascular depressant, reducing the blood pressure [25], [26]. For this study, given the relatively low volume acquisition rate of the Vivosight OCT system (0.01 Hz), it was not feasible to perform angiographic imaging of solid tumours without the use of anaesthetic. Recent developments in MHz range swept source lasers have enabled angiographic OCT volume scans to be acquired at video rate (1-25 Hz)[27], [28]. This may enable high-speed imaging of the subcutaneous tumour microcirculation without the requirement of anaesthetic.

3.3.3 Evaluation of OCT depth penetration

Fig. 3.7 shows a direct comparison between the OCT B-scans and histological samples taken from the rear-dorsum of CD1 nude mice. In healthy skin (Fig. 3.7A/B) a thick hypodermis layer ($\approx 400\mu m$) is filled with dense hair follicles which scatter the incident 1300nm OCT beam, preventing the light from penetrating deeper into the tissue. A thin section of the striated muscle layer is visible to the right side of the OCT image, but structures are not discernible beneath this layer.

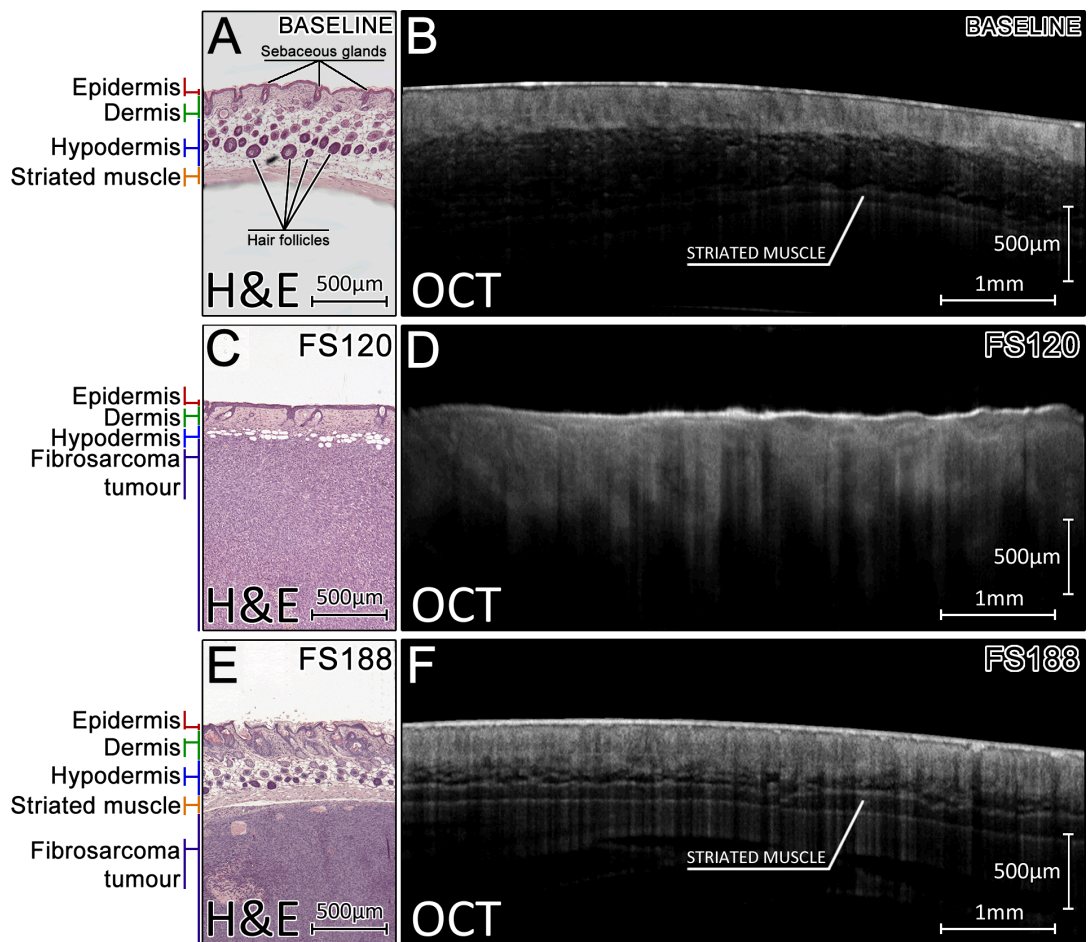


FIGURE 3.7: Comparing the depth penetration of OCT against histological sections of murine rear-dorsum skin. A) H&E stained section of healthy skin. B) OCT B-scan of healthy skin (Different animal to A). C) H&E stained section of the skin above an fs120 tumour, showing the lack of the muscular layer. D) OCT B-scan of the skin above an fs120 tumour (Same animal as C). E) H&E stained section of skin with an fs188 tumour visible beneath the muscular (panniculus carnosus) layer of the skin. F) OCT B-scan of the skin above an fs188 tumour (Same animal as E).

While the thickness of the hypodermis within murine skin is known to be modulated by the hair cycle[29], the presence of a tumour has clearly altered the outer skin morphology (Fig. 3.7C/E). To investigate this, multiple measurements of the hypodermal thickness were acquired from sections of skin. Given the variable contrast of the hypodermis on the cross-sectional OCT images, particularly for the fs120 tumours (Fig. 3.7D), these measurements were made using histological sections of the skin. For each unique skin section, the upper and lower layer of the hypodermis

were manually traced within MATLAB (R2015b – MathWorks), an average value of hypodermis thickness was then calculated by considering the vertical distance between these upper and lower boundaries. These measurements of hypodermis thickness were acquired from healthy skin (n=7) and compared to similar measurements acquired from skin surrounding the fs188 and fs120 tumours at the end of the study (n=7 per group). A balanced one-way ANOVA was performed between the three groups, followed by the Tukey-Kramer HSD test to evaluate significance, these results are summarized in Fig. 3.8.

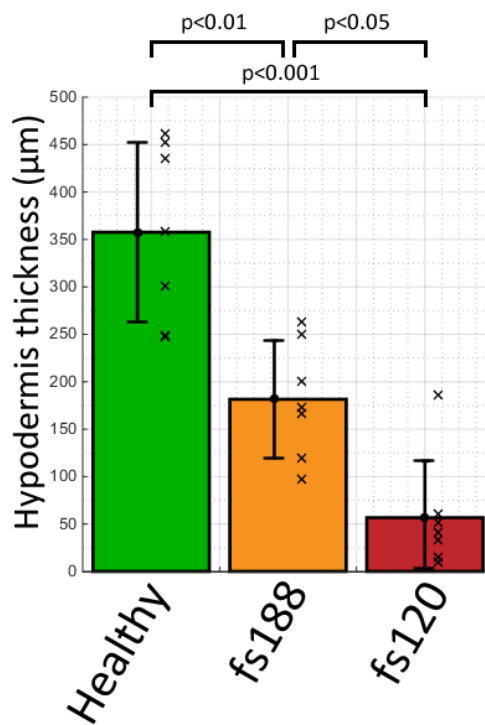


FIGURE 3.8: Variation in the thickness of the hypodermis (fat) layer within healthy skin compared to that of the skin encapsulating ≈ 12 mm diameter fs188 and fs120 tumours. The fatty layer is significantly thicker in healthy skin than both fs188 and fs120 skin, furthermore this layer is also significantly thicker in fs188 skin than fs120 skin. A thicker fat layer appears to correlate with an increase in the number of hair follicles present, reducing the depth penetration of the OCT imaging beam. (columns, mean; bars, standard deviation; crosses, datapoints). All groups contain n=7 samples, significance calculated using a one-way ANOVA followed by a Tukey-Kramer HSD test.

The thickness of the hypodermis was found to be significantly greater in healthy skin ($357 \pm 94 \mu\text{m}$) compared to that of skin covering an fs188 tumour ($182 \pm 62 \mu\text{m}$,

$p < 0.01$) or fs120 tumour ($57 \pm 60 \mu\text{m}$, $p < 0.001$). There was also a significant reduction in skin thickness between the fs188 and fs120 groups ($p = 0.015$), which could be caused by abnormal strains placed on the skin as it stretches over the growing tumour. An example of the thinned hypodermis is seen for the fs188 tumour (Fig. 3.7E/F); in these cases OCT is able to capture the upper layers of skin (epidermis, dermis), the adipose layer of fat cells (hypodermis), the muscular layer and approximately $500 \mu\text{m}$ deep into the fs188 tumour, representing a total depth penetration of $\approx 1\text{mm}$. Fig. 3.7C/D show similar comparisons for an fs120 tumour. Interestingly, most fs120 tumours exhibited a unique skin morphology in that the layer of striated muscle was absent and in some extreme cases the hypodermis was also heavily disrupted, with adipocytes scattered within the tumour, there was also a notable absence of hair follicles within the hypodermis (Fig. 3.7C). This could again be indicative of the more invasive phenotype of this tumour type[24]. In such cases, the remaining layers of superficial skin were $\approx 200 \mu\text{m}$ thick, consisting of only the epidermis, dermis and extremely thinned hypodermis. This resulted in a much deeper view into the tumour tissue with OCT as seen in Fig. 3.7D, potentially explaining why large abnormal tumour vasculature was visible at superficial depths of less than $300 \mu\text{m}$ in Fig. 3.4.

Fig. 3.9 shows a comparison between H&E and CD31 stained sections of healthy, fs120 and fs188 skin. In the case of healthy skin (Fig. 3.9A/D/G), CD31 immunostaining has highlighted the presence of vascular endothelial cells throughout the dermis, hypodermis and striated muscle layers of the murine skin. The largest visible vessel lumen, highlighted by the red arrow is $\approx 15 \mu\text{m}$ in diameter. For the skin containing an fs120 tumour (Fig. 3.9B/E/H), the majority of vessels are visible at the periphery of the tumour, the largest of which is $\approx 65 \mu\text{m}$ in diameter (red arrow). For the skin overlying an fs188 tumour (Fig. 3.9C/F/I), there is evidence of vascularisation within the dermis/hypodermis, however the majority of visible vessels are inside the tumour, directly below the striated muscle layer at a depth of $\approx 600 \mu\text{m}$, the largest of which is $\approx 50 \mu\text{m}$ (red arrow). These are likely to be the vessels which appeared green on Fig. 3.4. Fs120 tumour cells have clearly invaded

deep into the hypodermis, whereas the fs188 tumour remains contained beneath the striated muscle layer. Due to the increased infiltration of the fs120 tumours, these vessels are situated at a depth of $300\mu\text{m}$ and appear red on the depth resolved OCT scans shown in Fig. 3.4.

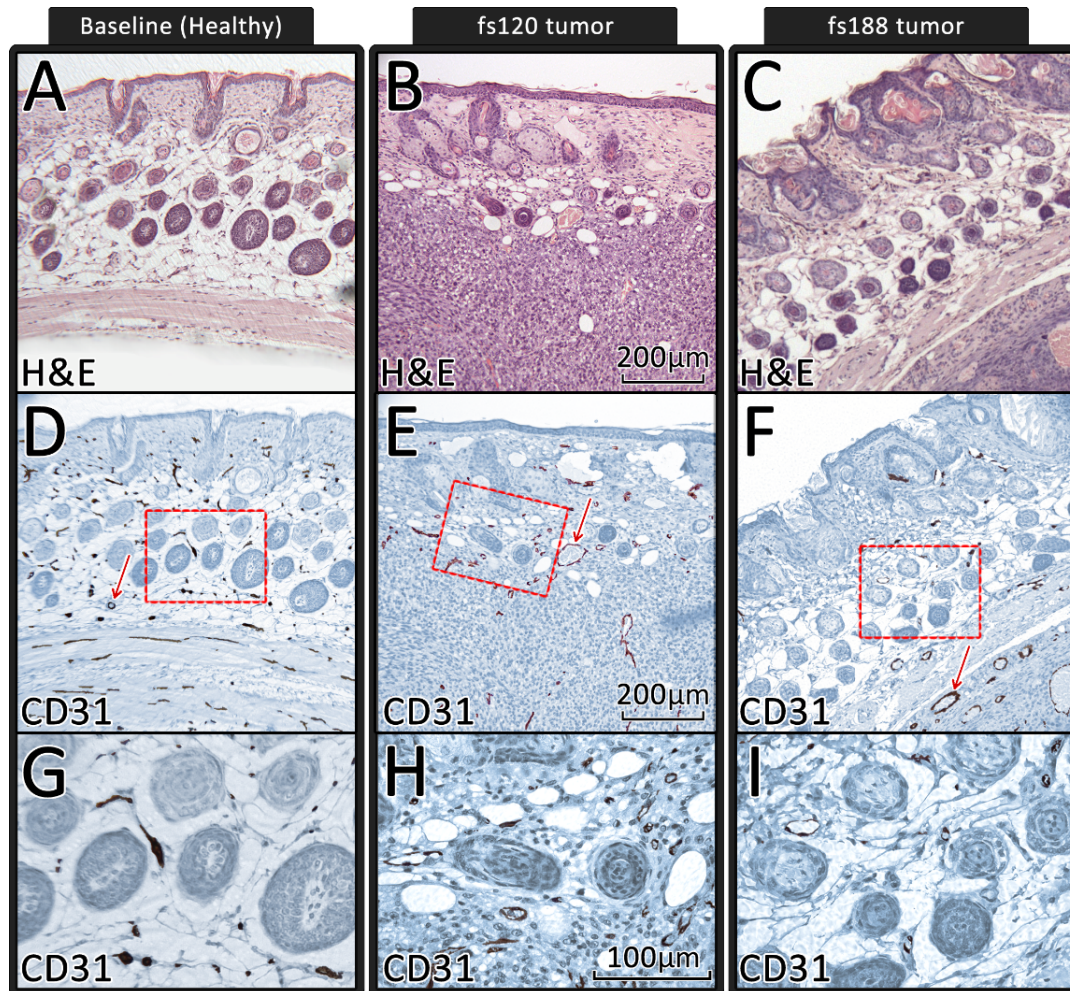


FIGURE 3.9: CD31 immunohistochemistry demonstrating the presence of endothelial cells lining the vessels within the rear-dorsum skin of CD1 nude mice. A-C) H&E stained serial sections of healthy, fs120 and fs188 skin respectively. D-F) CD31 immunostained serial sections of healthy, fs120 and fs188 skin respectively. Endothelial cells are stained in brown. Red arrows represent the largest visible vessel lumen. Red boxes represent the zoomed sections from G-I. G-I) Zoomed view of vessels within the hypodermis of the CD31 stained sections. The fs120 tumour shown here was excised 14 days post-implantation and is a different tumour to the one shown in Fig. 3.8. The fs188 tumour shown here was excised 20 days post-implantation, and is the same tumour shown in Fig. 3.8.

In general, depth penetration appears sufficient to capture the superficial layers of vasculature within both fs120 and fs188 tumours. However, achieving high axial depth penetration at a particular location remains dependent on the absence of highly scattering structures in the upper skin layers. Shadows from superficial scattering structures such as hair follicles can be seen as a banding pattern on Fig. 3.7B/D/F, and may occlude the angiographic signal from vessels directly below the structure.

3.3.4 Quantitative vessel metrics

Fig. 3.10 shows the variation of each of the quantitative parameters detailed in Sec 3.2.4 as a function of tumour type at study endpoint. Independent two-sample t-tests were used to calculate significance between the tumour types, with the significance levels between tumour types being listed above each graph. Mean vessel diameter was significantly higher for the fs120 tumours ($60.7 \pm 4.9\mu m$) than the fs188 tumours ($45.0 \pm 4.0\mu m$), an observation which agrees with previous intravital observations of the same tumour types grown in window-chambers[16]. It is likely that measured vessel diameters below $20\mu m$ are overestimated when viewed through OCT, due in-part to spatial aliasing. Given that the OCT datasets for this study were acquired with lateral spacing ($\Delta x, \Delta y$) of $10\mu m$, Nyquist sampling suggests that vessels $< 20\mu m$ will be affected by aliasing. Indeed, in the context of window-chamber imaging, Vakoc *et al* demonstrated good correlation between multiphoton microscopy and OCT angiograms (Using a mean lateral spacing of $\approx 6.3\mu m$) for large vessels, however capillaries which were below $12\mu m$ in diameter exhibited poor correlation due to them appearing wider with OCT[7]. Given the qualitatively thinner vessel morphologies visible within the fs188 tumours (Fig. 3.4) it is likely that this spatial dilation has a larger effect on the mean fs188 vessel diameters than the corresponding fs120 measurements. However, the differences between tumour types remain significant. This dilatory effect of OCT angiography for smaller vessels is explored further in Sec. 5. It is also worth noting that this observed dilation of smaller vessels could be an artefact introduced by the usage of the Hessian filtering

detailed in Sec. 3.2.4.

The total vessel length per mm^2 (mm/mm^2) was significantly higher for the fs120 tumours ($4.3 \pm 1.5\text{mm}^{-1}$) than the fs188s ($2.2 \pm 0.7\text{mm}^{-1}$). Similarly, a higher overall vessel density was measured in the fs120 tumours ($31.7 \pm 11.1\%$) compared to the fs188 tumours ($14.8 \pm 5.0\%$). These observations agree with density calculations performed by CD31 stained vessel counting[30]. Interestingly, window-chamber observations yielded a lower total vessel length per mm^2 for fs120 tumours, the opposite to what is observed here[16]. It is highly likely that such discrepancies result from the different depths / quantification methods of the tumour circulation under consideration. Indeed, the reduced infiltration of the fs188 tumour vasculature to the more superficial layers of skin, as observed in Sec 3.3.1 and Sec. 3.3.3, would directly result in lower lengths of overall detected fs188 vasculature, particularly since skeletonisation was performed on projections over a large $0 - 800\mu\text{m}$ depth range. It would be useful to compare the observed length per mm^2 at equivalent depths within the tissue. However, a direct comparison between vessel lengths at the green depth of Fig. 3.4 ($400 - 800\mu\text{m}$) would yield inaccurate results for the fs120 tumours because much of the green vasculature is directly occluded due to the shadowing artefact cast downwards from the more superficial red vasculature[7]. An alternative is to perform the measurement over a smaller depth "window", e.g. by considering only the first $100\mu\text{m}$ of visible vasculature, decoupled from its axial position within the tissue. To investigate this, mean-intensity-projection images were captured over a $100\mu\text{m}$ depth with the superficial layer of the projection window placed where the first tumour vasculature was visible. When processed in this manner, the fs120 tumours displayed significantly ($p=0.04$) lower vessel length per mm^2 ($1.5 \pm 0.7\text{mm}^{-1}$) compared to fs188 tumours ($2.2 \pm 0.3\text{mm}^{-1}$). However, it remains unclear if depth dependent metrics such as total vascular length / density are reliable when compared at different depths within the tissue. Another source of potential discrepancy which was not considered here is the initial injection depth of the tumour cells, since in theory a more superficial SC injection would lead to a more superficial tumour growth. It is unlikely that this had a large effect on the observations made however,

due to the consistent difference in observed vessel depth between the two tumour types.

No significant difference in the mean vessel segment length between the tumour types was observed, in agreement with the previous window-chamber observations[16]. Both the mean tortuosity and the fractal dimension of the vessel networks were found to be significantly higher for the fs120s (1.56 ± 0.29 and 1.33 ± 0.17 respectively) compared to the fs188s (1.33 ± 0.13 and 0.98 ± 0.18 respectively). Given that there was no difference in the mean vessel segment length between the tumour types, a higher tortuosity for the fs120 tumours must mean that the branch points of the fs120 network are closer together than those of the fs188 tumours but the vessels themselves are more tortuous between the branchpoints. This is reflected in the fractal dimension measurements, with the lower value of fractal dimension for fs188s being indicative of a more regular, organized vessel network. This is again consistent with the previous observations of these tumour types with intravital microscopy, with fs120 vessels being described as generally wider and very chaotic in their arrangement, while fs188 vessels are described as regularly organized and uniformly narrow[16].

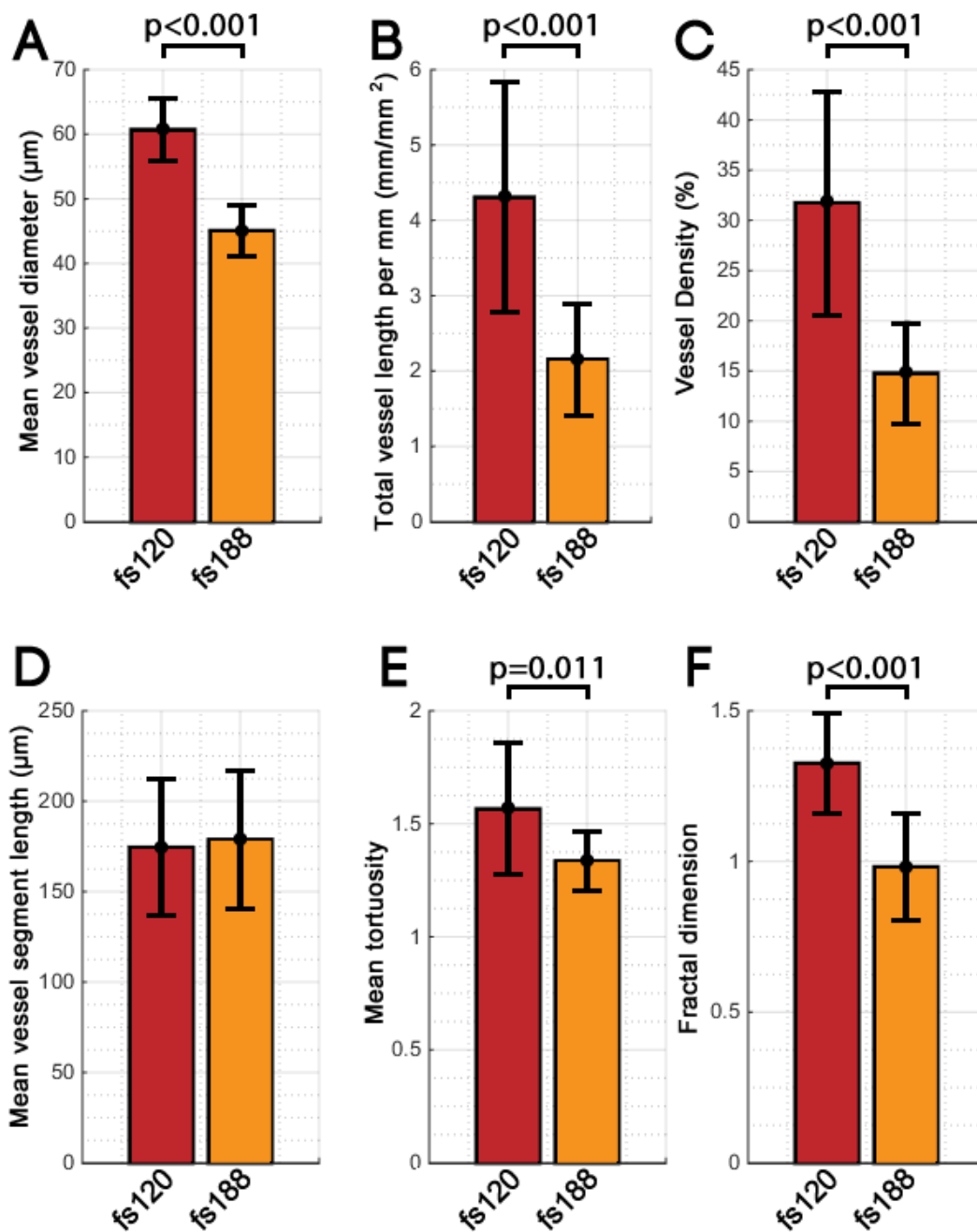


FIGURE 3.10: The variation in quantitative vessel parameters between fs120 tumours (n=9) and fs188 tumours (n=8) at the study endpoint. Columns: The average value of each respective quantitative parameter across the entire fs120 or fs188 group. (bars, standard deviation). Statistical significance calculated using an independent two-sample t-test between the fs120 and fs188 datasets.

3.4 Conclusions

OCT is able to non-invasively quantify morphological differences in the superficial vasculature of subcutaneously implanted murine tumours expressing different VEGF isoforms, providing results that are consistent with those acquired by more conventional methods in previous studies[16]. OCT does not require the use of a transparent optical window and allows tumours to grow and be observed in a three-dimensional environment. Bulk-tissue-motion artefacts resulting from breathing or other muscular movements are effectively suppressed through a combination of in-plane registration, correlation optimization and combined wavelet-FFT filtering. Longitudinal tumour monitoring is achievable, with a high degree of vessel co-registration between scans. However rapid variations in day-to-day vascular density are present, which may arise from the use of general anaesthesia. This limitation could potentially be addressed in future through utilisation of a high-speed OCT system, which may negate the requirements for anaesthesia and physical pressure to reduce movement. This would make it feasible to longitudinally quantify the effects of angiogenic inhibitors or other treatments that directly affect the vasculature within solid tumours.

Tumours that solely express the VEGF120 isoform were more invasive, penetrating to more superficial levels of the skin than the VEGF188 variants. Thinning of the hypodermis in the skin encapsulating both types of solid tumour leads to an improved depth penetration compared to healthy skin. Furthermore, disruption of the striated muscle (panniculus carnosus) layer was particularly common for the VEGF120 expressing tumours. Morphologically, the fs120 vessels appeared wider and formed dense, more disorganized networks when compared to the fs188 vessels, which tended to form thinner more organized networks. This is evidenced by a significantly higher mean vessel diameter, length, tortuosity and fractal dimension for fs120 tumours. The successful differentiation between these tumour types with OCT suggests that the known morphological differences in tumour vascularity persist outside of the window chamber model and are measurable without surgical

intervention. Furthermore, the wound healing response to surgical intervention involves release of angiogenic factors such as angiopoietin-2 (Ang-2) from endothelial cells[31], which can compromise the use of the window chamber model in studies of putative anti-angiogenic therapeutics[32]. OCT has the necessary spatial resolution to provide an alternative and non-invasive method to quantify the vascular response of superficial tumours to such therapy.

References

- [1] P. Carmeliet and R. K. Jain, "Molecular mechanisms and clinical applications of angiogenesis.", *Nature*, vol. 473, pp. 298–307, 2011, ISSN: 0028-0836. DOI: 10.1038/nature10144 (cit. on p. 67).
- [2] D. Hanahan and R. A. Weinberg, "Hallmarks of cancer: the next generation.", *Cell*, vol. 144, no. 5, pp. 646–74, Mar. 2011, ISSN: 1097-4172. DOI: 10.1016/j.cell.2011.02.013 (cit. on p. 67).
- [3] S. Goel, D. G. Duda, L. Xu, L. L. Munn, Y. Boucher, D. Fukumura, and R. K. Jain, "Normalization of the Vasculature for Treatment of Cancer and Other Diseases", *Physiological Reviews*, vol. 91, no. 3, 2011 (cit. on p. 67).
- [4] A.-I. Puaux, L. C. Ong, Y. Jin, I. Teh, M. Hong, P. K. H. Chow, X. Golay, and J.-p. Abastado, "A Comparison of Imaging Techniques to Monitor Tumor Growth and Cancer Progression in Living Animals", vol. 2011, 2011. DOI: 10.1155/2011/321538 (cit. on p. 67).
- [5] B. Nico, V. Benagiano, D. Mangieri, N. Maruotti, A. Vacca, and D. Ribatti, "Evaluation of microvascular density in tumors: pro and contra.", *Histology and histopathology*, vol. 23, no. 5, pp. 601–7, May 2008, ISSN: 1699-5848 (cit. on p. 67).
- [6] H. A. Lehr, M. Leunig, M. D. Menger, D. Nolte, and K. Messmer, "Dorsal skin-fold chamber technique for intravital microscopy in nude mice.", *The American journal of pathology*, vol. 143, no. 4, pp. 1055–62, Oct. 1993, ISSN: 0002-9440 (cit. on p. 67).
- [7] B. J. Vakoc, R. M. Lanning, J. A. Tyrrell, T. P. Padera, L. A. Bartlett, T. Stylianopoulos, L. L. Munn, G. J. Tearney, D. Fukumura, R. K. Jain, and B. E. Bouma,

- “Three-dimensional microscopy of the tumor microenvironment in vivo using optical frequency domain imaging.”, *Nature medicine*, vol. 15, no. 10, pp. 1219–23, Oct. 2009, ISSN: 1546-170X. DOI: 10.1038/nm.1971 (cit. on pp. 67, 78, 87–88).
- [8] F. Kiessling, S. Greschus, M. P. Lichy, M. Bock, C. Fink, S. Vosseler, J. Moll, M. M. Mueller, N. E. Fusenig, H. Traupe, and W. Semmler, “Volumetric computed tomography (VCT): a new technology for noninvasive, high-resolution monitoring of tumor angiogenesis.”, *Nature medicine*, vol. 10, no. 10, pp. 1133–8, Oct. 2004, ISSN: 1078-8956. DOI: 10.1038/nm1101 (cit. on p. 67).
- [9] T. Jeswani and A. R. Padhani, “Imaging tumour angiogenesis.”, *Cancer imaging : the official publication of the International Cancer Imaging Society*, vol. 5, no. 1, pp. 131–8, 2005, ISSN: 1470-7330. DOI: 10.1102/1470-7330.2005.0106 (cit. on p. 67).
- [10] C. Fink, F. Kiessling, M. Bock, M. P. Lichy, B. Misselwitz, P. Peschke, N. E. Fusenig, R. Grobholz, and S. Delorme, “High-resolution three-dimensional MR angiography of rodent tumors: Morphologic characterization of intratumoral vasculature”, *Journal of Magnetic Resonance Imaging*, vol. 18, no. 1, pp. 59–65, 2003, ISSN: 10531807. DOI: 10.1002/jmri.10318 (cit. on p. 67).
- [11] A. Chekkoury, A. Nunes, J. Gateau, P. Symvoulidis, S. V. Ovsepian, and A. Walch, “High-Resolution Multispectral Optoacoustic Tomography of the Vascularization and Constitutive Hypoxemia of Cancerous Tumors 1”, *Neo*, vol. 18, no. 8, pp. 459–467, 2016, ISSN: 1476-5586. DOI: 10.1016/j.neo.2016.06.004 (cit. on p. 67).
- [12] M. P. Wiedeman, “Dimensions of blood vessels from distributing artery to collecting vein.”, *Circulation research*, vol. 12, pp. 375–378, 1963, ISSN: 0009-7330. DOI: 10.1161/01.RES.12.4.375 (cit. on p. 67).
- [13] J. Enfield, E. Jonathan, and M. Leahy, “In vivo imaging of the microcirculation of the volar forearm using correlation mapping optical coherence tomography

- (cmOCT)", vol. 2, no. 5, pp. 1184–1193, 2011. DOI: 10.1002/jbio.201000103/abstract (cit. on p. 68).
- [14] K. Calabro, A. Curtis, J.-R. Galarneau, T. Krucker, and I. J. Bigio, "Gender variations in the optical properties of skin in murine animal models.", *Journal of biomedical optics*, vol. 16, no. January, p. 011 008, 2011, ISSN: 10833668. DOI: 10.1117/1.3525565 (cit. on p. 68).
- [15] A. Mariampillai, M. K. K. Leung, M. Jarvi, B. a. Standish, K. Lee, B. C. Wilson, A. Vitkin, and V. X. D. Yang, "Optimized speckle variance OCT imaging of microvasculature.", *Optics letters*, vol. 35, no. 8, pp. 1257–9, Apr. 2010, ISSN: 1539-4794 (cit. on p. 68).
- [16] G. M. Tozer, S. Akerman, N. A. Cross, P. R. Barber, M. A. Björndahl, O. Greco, S. Harris, S. A. Hill, D. J. Honess, C. R. Ireson, K. L. Pettyjohn, V. E. Prise, C. C. Reyes-Aldasoro, C. Ruhrberg, D. T. Shima, and C. Kanthou, "Blood vessel maturation and response to vascular-disrupting therapy in single vascular endothelial growth factor-A isoform-producing tumors.", en, *Cancer research*, vol. 68, no. 7, pp. 2301–11, Apr. 2008, ISSN: 1538-7445. DOI: 10.1158/0008-5472.CAN-07-2011 (cit. on pp. 68–69, 87–89, 91).
- [17] K. Calabro, A. Curtis, J.-R. Galarneau, T. Krucker, and I. J. Bigio, "Gender variations in the optical properties of skin in murine animal models", *Journal of Biomedical Optics*, vol. 16, no. 1, p. 011 008, 2011, ISSN: 10833668. DOI: 10.1117/1.3525565 (cit. on p. 69).
- [18] D. W. Wei, A. J. Deegan, and R. K. Wang, "Automatic motion correction for *in vivo* human skin optical coherence tomography angiography through combined rigid and nonrigid registration", *Journal of Biomedical Optics*, vol. 22, no. 6, p. 066 013, 2017, ISSN: 1083-3668. DOI: 10.1117/1.JBO.22.6.066013 (cit. on pp. 71, 79).
- [19] R. A. Byers, G. Tozer, N. J. Brown, and S. J. Matcher, "High-resolution label-free vascular imaging using a commercial, clinically approved dermatological OCT scanner", B. Choi, N. Kollias, H. Zeng, H. W. Kang, B. J. F. Wong, J. F.

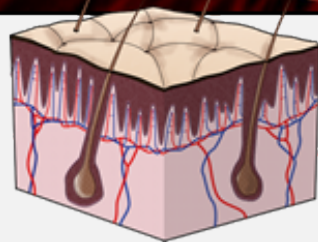
- Ilgner, G. J. Tearney, K. W. Gregory, L. Marcu, M. C. Skala, P. J. Campagnola, A. Mandelis, and M. D. Morris, Eds., Feb. 2016, p. 96890M. DOI: 10.1117/12.2212222 (cit. on p. 71).
- [20] A. F. Frangi, W. J. Niessen, K. L. Vincken, and M. a. Viergever, "Multiscale vessel enhancement filtering", *Medial Image Computing and Computer-Assisted Invervention - MICCAI'98. Lecture Notes in Computer Science, vol 1496*, vol. 1496, pp. 130–137, 1998, ISSN: 13618415. DOI: 10.1016/j.media.2004.08.001 (cit. on p. 74).
- [21] N. Otsu, "A Threshold Selection Method from Gray-Level Histograms", *IEEE Transactions on Systems, Man, and Cybernetics*, vol. 9, no. 1, pp. 62–66, 1979, ISSN: 0018-9472. DOI: 10.1109/TSMC.1979.4310076 (cit. on p. 74).
- [22] K. Jurczyszyn, B. J. Osiecka, P. Ziółkowski, and P. Kowski, "The Use of Fractal Dimension Analysis in Estimation of Blood Vessels Shape in Transplantable Mammary Adenocarcinoma in Wistar Rats after Photodynamic Therapy Combined with Cysteine Protease Inhibitors", *Computational and Mathematical Methods in Medicine*, vol. 2012, pp. 1–6, 2012, ISSN: 1748-670X. DOI: 10.1155/2012/793291 (cit. on p. 76).
- [23] C. Sorzano, P. Thevenaz, and M. Unser, "Elastic Registration of Biological Images Using Vector-Spline Regularization", *IEEE Transactions on Biomedical Engineering*, vol. 52, no. 4, pp. 652–663, Apr. 2005, ISSN: 0018-9294. DOI: 10.1109/TBME.2005.844030 (cit. on pp. 76, 80).
- [24] C. Kanthou, G. U. Dachs, D. V. Lefley, A. J. Steele, C. Coralli-Foxon, S. Harris, O. Greco, S. A. Dos Santos, C. C. Reyes-Aldasoro, W. R. English, and G. M. Tozer, "Tumour Cells Expressing Single VEGF Isoforms Display Distinct Growth, Survival and Migration Characteristics", *PLoS ONE*, vol. 9, no. 8, C. L. Addison, Ed., e104015, Aug. 2014, ISSN: 1932-6203. DOI: 10.1371/journal.pone.0104015 (cit. on pp. 78, 85).

- [25] J. Xiong, A. Kurz, D. I. Sessler, O. Plattner, R. Christensen, M. Dechert, and T. Ikeda, "Isoflurane produces marked and nonlinear decreases in the vasoconstriction and shivering thresholds.", *Anesthesiology*, vol. 85, no. 2, pp. 240–5, Aug. 1996, ISSN: 0003-3022 (cit. on p. 82).
- [26] D. I. Sessler, J. McGuire, J. Hynson, A. Moayeri, and T. Heier, "Thermoregulatory vasoconstriction during isoflurane anesthesia minimally decreases cutaneous heat loss.", *Anesthesiology*, vol. 76, no. 5, pp. 670–5, May 1992, ISSN: 0003-3022 (cit. on p. 82).
- [27] U. Baran, W. Wei, J. Xu, X. Qi, W. O. Davis, and R. K. Wang, "Video-rate volumetric optical coherence tomography-based microangiography", *Optical Engineering*, vol. 55, no. 4, p. 040 503, 2016, ISSN: 0091-3286. DOI: 10.1117/1.OE.55.4.040503 (cit. on p. 82).
- [28] Z. Zhi, W. Qin, J. Wang, W. Wei, and R. K. Wang, "4D optical coherence tomography-based micro-angiography achieved by 16-MHz FDML swept source", *Optics Letters*, vol. 40, no. 8, p. 1779, Apr. 2015, ISSN: 0146-9592. DOI: 10.1364/OL.40.001779 (cit. on p. 82).
- [29] L. S. Hansen, J. E. Coggle, J. Wells, and M. W. Charles, "The influence of the hair cycle on the thickness of mouse skin", *The Anatomical Record*, vol. 210, no. 4, pp. 569–573, Dec. 1984, ISSN: 0003-276X. DOI: 10.1002/ar.1092100404 (cit. on p. 83).
- [30] W. R. English, S. J. Lunt, M. Fisher, D. V. Lefley, M. Dhingra, Y. C. Lee, K. Bingham, J. E. Hurrell, S. K. Lyons, C. Kanthou, and G. M. Tozer, "Differential expression of VEGFA isoforms regulates metastasis and response to anti-VEGFA therapy in sarcoma", *Cancer Research*, vol. 77, no. 10, pp. 2633–2646, 2017, ISSN: 15387445. DOI: 10.1158/0008-5472.CAN-16-0255. arXiv: arXiv:1011.1669v3 (cit. on p. 88).
- [31] H. Kämpfer, J. Pfeilschifter, and S. Frank, "Expressional regulation of angiotensin-1 and -2 and the tie-1 and -2 receptor tyrosine kinases during cutaneous wound

- healing: a comparative study of normal and impaired repair.", *Laboratory investigation; a journal of technical methods and pathology*, vol. 81, no. 3, pp. 361–73, Mar. 2001, ISSN: 0023-6837 (cit. on p. 92).
- [32] N. M. Biel, J. a. Lee, B. S. Sorg, and D. W. Siemann, "Limitations of the dorsal skinfold window chamber model in evaluating anti-angiogenic therapy during early phase of angiogenesis.", *Vascular cell*, vol. 6, no. 1, p. 17, 2014, ISSN: 2045-824X. DOI: 10.1186/2045-824X-6-17 (cit. on p. 92).

Chapter 4

Paper 2 - Angiographic OCT for the study of atopic dermatitis.



This chapter contains excerpts, with permission, from the following work which is currently in submission for Biomedical Optics Express:

Sub-clinical assessment of atopic dermatitis severity using angiographic optical coherence tomography.

Robert A. Byers, Raman Maiti, Simon G. Danby, Elaine J. Pang, Bethany Mitchell, Matt J. Carré, Roger Lewis, Michael J. Cork and Stephen J. Matcher

Biomedical Optics Express
(2018)

Accepted for publication.

This chapter contains the "Author Accepted" version of the manuscript.

Statement of contribution

Concerning the publication:

Sub-clinical assessment of atopic dermatitis severity using angiographic optical coherence tomography.

Contributor	Statement of contribution
Robert A. Byers Signed: _____	I am the primary contributor to this work. Having performed all of the angiographic data acquisition, processing and analysis. <ul style="list-style-type: none"> • Prepared the manuscript. • Performed OCT and imaging/data collection. (Together with R. Maiti) • Performed all data analysis and interpretation.
Raman Maiti Signed: _____	<ul style="list-style-type: none"> • Collected structural OCT data (Together with R. Byers).

Principle supervisor confirmation

I have sighted email or other correspondence from all co-authors confirming their certifying authorship.

Name: _____

Signature: _____

Date: _____

Sub-clinical assessment of atopic dermatitis severity using angiographic optical coherence tomography

**ROBERT A. BYERS,¹ RAMAN MAITI,² SIMON G. DANBY,³
ELAINE J. PANG,³ BETHANY MITCHELL,³ MATT J. CARRÉ,²
ROGER LEWIS,² MICHAEL J. CORK,³ AND STEPHEN J. MATCHER¹**

¹ *Department of Electronic and Electrical Engineering, University of Sheffield, Sheffield, UK.*

² *Department of Mechanical Engineering, University of Sheffield, Sheffield, UK.*

³ *Sheffield Dermatology Research, Department of Infection, Immunity & Cardiovascular Disease, The Royal Hallamshire Hospital, University of Sheffield, Sheffield, UK.*

Abstract: The severity of atopic dermatitis (AD) is characterised by a range of sub-clinical factors. Structural measures of epidermal thickness by optical coherence tomography (OCT) are often made challenging due to the lack of a clearly delineated dermal-epidermal junction in AD patients. Alternatively, angiographic OCT measurements of vascular depth and morphology may represent a robust biomarker for quantifying the severity of localised inflammation. To investigate this, angiographic datasets were acquired from 32 patients with a range of AD severities. Deeper vascular layers within skin were found to correlate with increasing clinical severity. Furthermore, for AD patients exhibiting no clinical symptoms, the superficial plexus depth was found to be significantly deeper than healthy patients at both the elbow ($p=0.04$) and knee ($p<0.001$), suggesting that sub-clinical changes in severity can be detected. Furthermore, the morphology of vessels appeared altered in patients with severe AD, with significantly different vessel diameter, length, density and fractal dimension. These metrics provide valuable insight into the sub-clinical severity of the condition, allowing treatments to potentially be monitored past the point of clinical remission.

©2018 Optical Society of America

OCIS codes: (170.3880) Medical and biological imaging; (110.4500) Optical coherence tomography; (170.2655) Functional monitoring and imaging; (170.1870) Dermatology.

4.1 Introduction

Atopic dermatitis (AD - Eczema) is a chronic, inflammatory disorder of the skin. The prevalence of the condition within the US is estimated to be approximately 10.7% for child AD[1] (Global – 7.3%[2]) and 10.2% for adult AD[3], and is generally increasing within both the developed and developing world[2], [4]. Common symptoms include dry, itchy plaques of the skin which exhibit abnormalities such as a notably increased trans-epidermal water loss (TEWL)[5]. These symptoms arise due to complex interactions between many different genes and environmental factors, which lead to a defective epidermal barrier[6]. Clinical assessment of the extent and severity of AD is typically performed using external grading systems such as the severity scoring of AD[7] (SCORAD) or the eczema area and severity index[8] (EASI) which look for specific signs and coverage of the condition. These externally visible signs often include erythema, edema, papulation, excoriation, lichenification and oozing[8]. There is however substantial evidence that unaffected, lesion-free skin sites of AD patients can remain abnormal, even following remission of the condition[9]. Such "subclinical" abnormalities include significant differences in TEWL, pH and capacitance between healthy and unaffected skin[10], [11] as well as structural abnormalities such as epidermal thickening[9]. Indeed it appears clear that externally healthy looking skin of previously diagnosed AD patients is likely to contain hidden abnormalities beneath the skin surface[12]. Identification of these subclinical factors could facilitate improved treatments which aim to monitor and suppress progression of the disorder past the point of clinical remission[9].

Optical Coherence Tomography (OCT) is an established non-invasive medical-imaging technique which utilises near-infrared light to capture a reflectance profile of the sub-surface layers within skin. Previous studies have utilised the high axial resolution (5 – 10 μ m) of OCT to delineate the dermal-epidermal junction (DEJ) within skin, allowing for automated measurements of epidermal thickness[13], [14].

In the context of AD, measurements of epidermal atrophy (thinning) following corticosteroid treatment have been well documented using both OCT[15] and other non-invasive modalities[16]. In contrast, epidermal thickening, associated with skin inflammation[12], is more challenging to accurately quantify using simple structural OCT, owing to a reduction in contrast between the epidermal and dermal layers of the skin as the epidermis thickens and the dermal papillae extend upwards (Sec. 4.3.2). To avoid subjective and time-consuming manual measurements of epidermal thickness, an alternative method of quantifying the degree of thickening could be to measure the depth of vascular layers of the skin. Firstly, the superficial plexus which lies horizontally in the upper papillary dermis could be considered a lower bound for the true DEJ location. Secondly, the tips of the capillary loops which extend vertically into each of the dermal papillae represent the thinnest points of the epidermis and could be considered an upper bound for the DEJ location (Fig. 4.1). The depths of these vessel layers are likely to be influenced by inflammation, as a thickening epidermis will push the superficial plexus deeper into the tissue.

Recently developed processing methods have enabled the extraction of three-dimensional angiographic data from oversampled structural OCT datasets[17], [18]. One such method, termed speckle-variance OCT (svOCT) identifies the presence of fluid flow by considering the temporal evolution of intensity (speckle) within each pixel of a volume. Pixels in a solid region of tissue exhibit intensities which can be characterized by a Gaussian distribution, due to static coherent speckle and random acquisition noise. Comparatively, pixels in a fluid region of tissue will exhibit intensities in a Rayleigh distribution, as a combination of both acquisition noise and moving speckle[19]. This gives rise to contrast between solid and fluid regions of the skin.

The aims of this study are two-fold: firstly, we aim to develop and validate angiographic OCT for automated measurements of epidermal thickness within skin affected with a range of AD severities. Secondly, we aim to investigate whether sub-clinical morphological differences within the microcirculation of AD patients correlate with the severity of the condition.

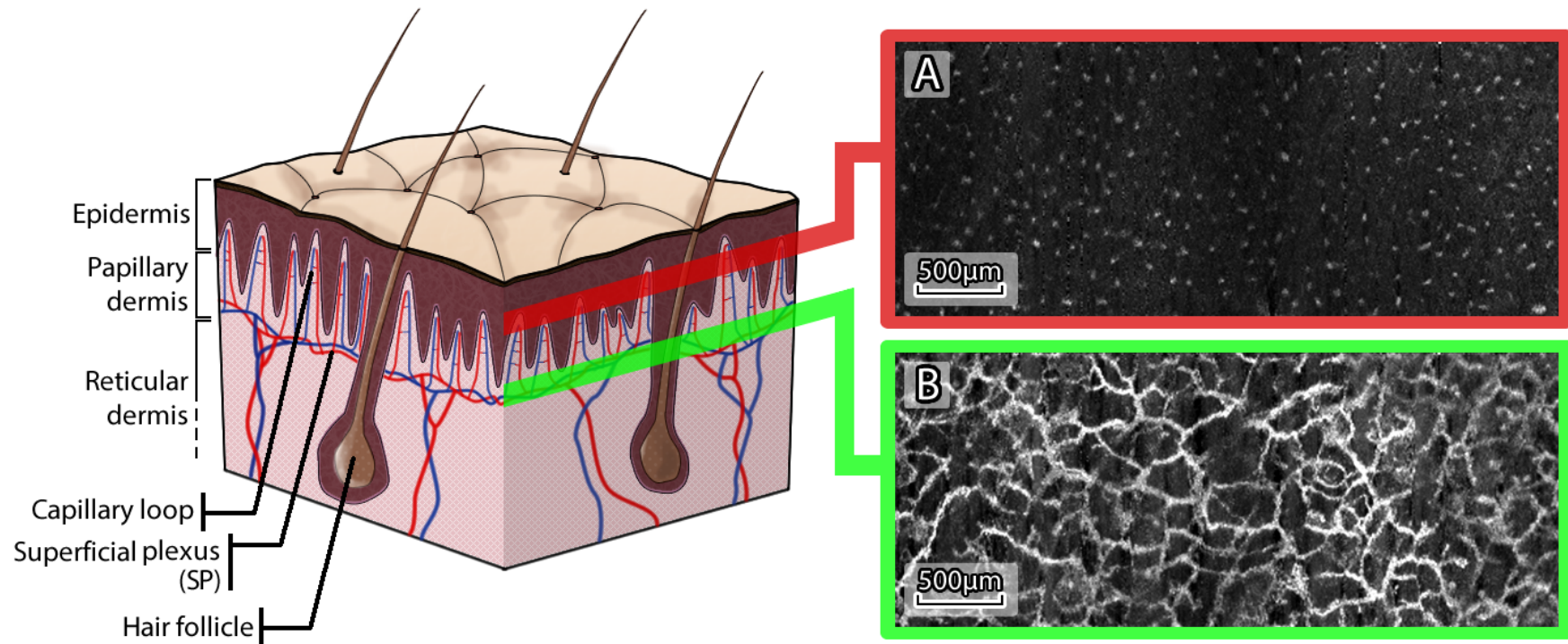


FIGURE 4.1: The structure of skin affected by epidermal thickening (Sebaceous glands and sweat ducts omitted for clarity). Vertical arteries and capillaries rise from the deep plexus and form a horizontal network termed the superficial plexus (SP). From this, capillary loops consisting of both rising arterioles and falling venules form hairpin like structures in the dermal papillae. A) An *en-face* angiographic svOCT image captured at a depth corresponding to the tips of the capillary loops, visible as small dots in the *en-face* perspective. B) An *en-face* angiographic svOCT image captured at a depth corresponding to the SP. Large interconnected vessels are visible. The depth of these layers may provide a direct measure of the tissue inflammation.

4.2 Materials and Methods

4.2.1 Participants

A total of 32 volunteers were recruited for this study. Both male and female volunteers aged 18-60 with Fitzpatrick skin type I-III (Mexameter®melanin reading of <350) were considered on a first-come first served basis. Exclusion criteria included pregnancy, folliculitis, acne, suntan, hyperpigmentation, multiple nevi, tattoos, blemishes or dense body hair in the test areas. Cosmetic products were also restricted prior to the study initiation. Of the 32 participants; 5 were healthy, having no prior history of any chronic skin condition (Including AD). The remaining 27 participants had currently active AD (As defined by the UK working party diagnostic criteria) at a range of severities, as well as having no history of any other chronic skin conditions. Informed consent was obtained from each participant prior to imaging. The National Research Ethics Service (NRES) Committee East Midlands–Derby, formally known as Trent Multicentre Research Ethics Committee (MREC), approved the study, under the project reference 04/MREC/70.

4.2.2 Imaging protocol

All imaging for this study was performed using a multi-beam OCT system (Vivosight®, Michelson Diagnostics Ltd, Orpington, Kent, UK) running at 20 kHz line acquisition rate. This system utilises a swept-source 1305nm Axsun laser with a bandwidth of 147nm, allowing visualisation of structures to a depth of ≈ 1 mm in skin. Four imaging sites which commonly exhibit AD symptoms were chosen for the study, these being the left and right cubital fossa (crook of the elbow) as well as the left and right popliteal fossa (crook of the knee).

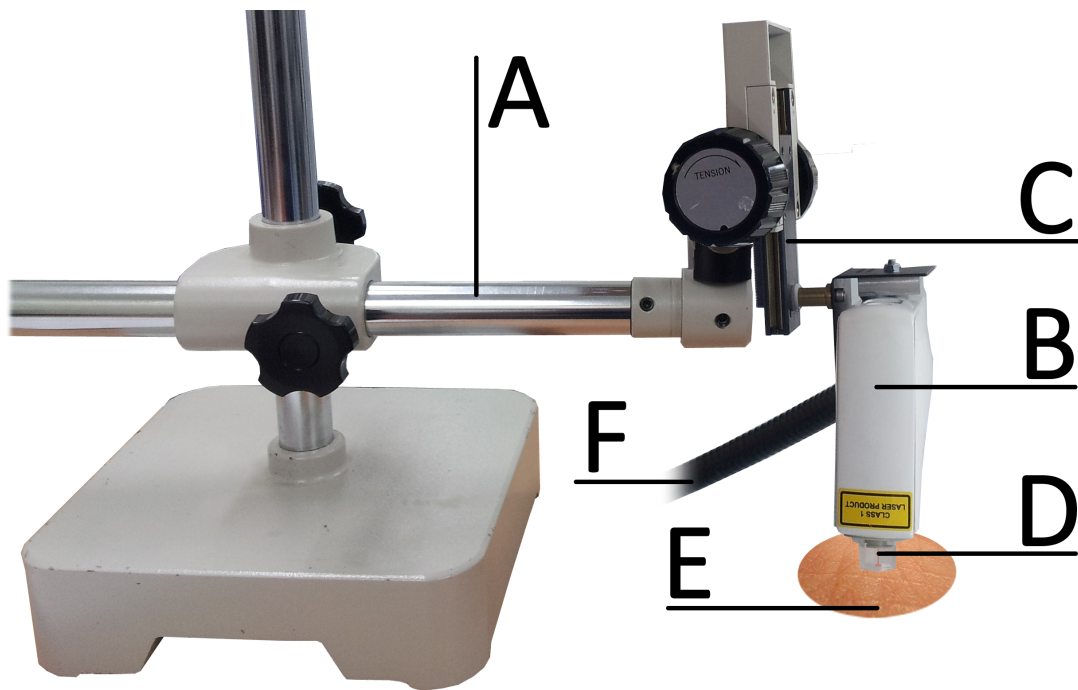


FIGURE 4.2: The OCT imaging set-up used for this study. A mechanical clamp (A) was used to fix the Vivosight imaging probe (B) into place above the region of interest. The vertical stage of the clamp (C) was then lowered such that the plastic cap (D) gently touched the surface of the skin (E). This plastic cap reduced any lateral (sliding) motion between the probe and the skin. Data was then transferred to the optical processing unit of the OCT system through a cable (F).

Prior to imaging, each participant was asked to wait 20 minutes in the study room with the skin of the test sites exposed, this process aimed to acclimatise each of the test sites such that any homeostatic variance was minimised. Following this, each skin site of the participant was assessed independently by two different graders to establish severity scores based on dryness, erythema, edema/papulation, excoriation and lichenification, assigning a number between 0-3 for each. A 0 in this context meant no sign of the clinical symptom, a 1 indicated mild evidence of the clinical sign, 2 for moderate evidence of the sign and 3 for severe evidence of the sign, with half-points being applicable. A local EASI score for each specific skin site was defined as the sum of each of these severity scores, averaged between the two assessors. A global (full-body) EASI score was calculated for each participant through a similar scoring and area coverage assessment at the head/neck, upper limbs, trunk

and lower limb regions following previously described weighting and methodology[8] following the Harmonising Outcome Measures for Eczema (HOME) guidelines. The handheld probe of the OCT system was then positioned for imaging using a mechanical clamp, such that any movement artifacts originating from the operator were eliminated. A plastic cap bridged the gap between the OCT probe and the skin, which was deemed necessary to reduce any lateral sliding of the skin surface during imaging. The OCT imaging set-up is illustrated in Fig. 4.2. Given that the imaging protocol involves physical contact with the skin surface, one might expect some degree of vasoconstriction through the white dermographism response which is common within AD affected skin[20]. White dermographism within AD is known to have a relatively long onset ($23\pm 1.4s$) with comparatively short duration ($6\pm 1s$)[21]. Thus, in order to reduce the influence of this effect on the resulting vascular data, a delay of approximately 30 seconds was added following the fixation of the imaging probe.

Imaging was then performed, with four-dimensional (x-y-z-time) structural OCT volumes being collected from each skin site in turn. All scans captured a volume of $4\times 4\times 2mm$ with 10 repeat B-scans being collected at each y-location such that a measure of variance could be calculated as per the svOCT methodology. The first 12 AD patient datasets were acquired with a $10\mu m$ A-scan spacing in the x-direction (fast scan) and a $20\mu m$ A-scan spacing in the y-direction (slow scan), with these scans taking approximately 50 seconds to acquire and save (40-frames/s). While the angiographic quality of these scans was sufficiently high for vessel depth measurement, the decision was made to decrease the A-scan spacing in the y-direction to $10\mu m$ such that uniform spacing between scans was achieved, further increasing scan quality while doubling the required acquisition time. 20 datasets were acquired with this $10\mu m$ A-scan spacing (In both x and y) with each set taking approximately 100 seconds to acquire and save. The increased resolution of these scans had no notable effect on the measurement of vascular layers (Sec. 4.2.4) but greatly enhanced the vascular morphology measurements (Sec. 4.2.3), thus quantification of vascular

morphology was restricted only to datasets which were acquired with the higher resolution. The raw data was processed offline in MATLAB (R2014b – MathWorks) into an angiographic format following the methodology described in Sec. 2.1. Notably, a combined wavelet-FFT filter is utilised to effectively suppress motion artefacts with minimal degradation to the underlying vascular information[22].

4.2.3 Automatic quantification of vascular morphology

For both automatic quantification of microvessel morphology and plexus depth (Sec. 4.2.4) it was necessary to binarise the angiographic data such that vascular skeletons could be generated. Fig. 4.3 shows the steps that were taken to skeletonise the data.

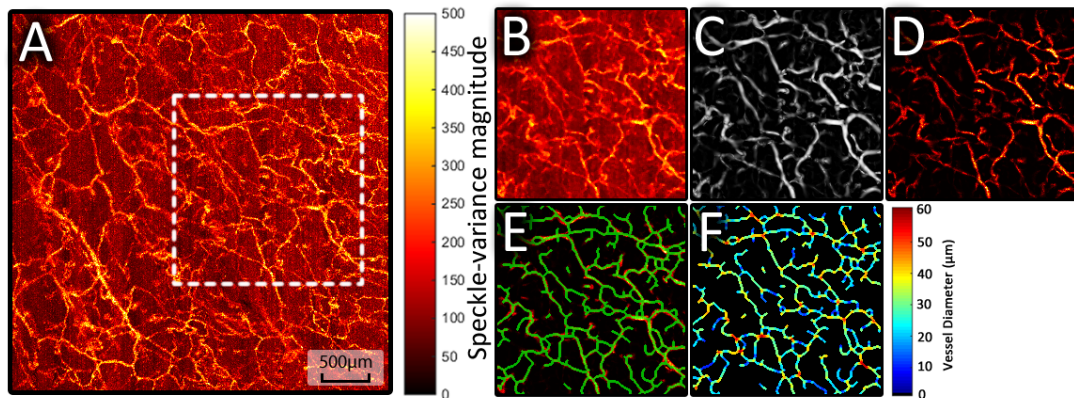


FIGURE 4.3: Steps taken to skeletonise and quantify vascular parameters from angiographic datasets. A) *En-face* mean intensity projection captured from the popliteal fossa site of a healthy participant. White box shows the FOV used for B-G. B) Median filtering step. C) Multi-scale Hessian filtering. D) Result of masking B with the “vesselness” data in C. E) Resulting skeleton (Green) overlaid on the masked data. F) Measured vessel diameter at each point along the vessel.

Firstly, an angiographic image was generated by performing mean-intensity-projections (MIP) over the depth range of interest (Fig. 4.3A), this image was median filtered to remove noise (Fig. 4.3B). The image was then processed with a multiscale Hessian filtering algorithm[23], which quantifies the “vesselness” of a pixel through consideration of the eigenvalues of the local Hessian matrix. To minimize artificial vessel dilation following Hessian filtering, a multi-scale approach was used. Compared to a single-scale approach, which uses gaussian kernels with a single value of

σ in order to build the Hessian matrix, the multi-scale approach uses a range of σ values in order to consider a range of vessel scales. Here values of 1:10 were used for σ , corresponding to vessel scales of 10 – 100 μm , with the strongest detection (maximum value) of each pixel across all vessel scales being recorded (Fig. 4.3C). The values of σ were selected empirically and offered reliable performance over the vessel scales observed here, with minimal vessel dilation being qualitatively visible. The filtered image was then used to compose a mask for the original data, preserving only areas of signal which were likely to be vascular derived (Fig. 4.3D). These filtering steps were deemed necessary due to the large magnitude of svOCT background noise, some of which is derived from movement of the participant during imaging. Following these steps, the image was binarised using an automatically determined threshold (Otsu's method[24]), with this binary image then being used to generate a vessel skeleton (Fig. 4.3E). It is worth mentioning that while 3D vesselness filtering exists, the 2D method was chosen for this work as the observed shadowing artefact beneath vessels (Discussed in Sec. 2.1.7) made 3D classification challenging and less reliable than the 2D variant. This is perhaps a result of the vessels not having a very "tubular" morphology when viewed in a 3D perspective, even following application a step-down exponential filter to attenuate the shadow artefacts, the vessels has a "squashed" morphology in the axial direction.

Four quantitative parameters were extracted using both the binarised data together with the vascular skeleton. Average vessel diameter (μm) was defined as double the average distance from the skeleton to the closest zero in the binarised image. Average vessel length (μm) was defined as the average length of skeleton segments between branching points in the skeleton, measured using a geodesic distance transform[25], which considers the distance between two neighboring skeleton points (x_1, x_2) and (y_1, y_2) as $\max(|x_1 - x_2|, |y_1 - y_2|)$, summing the overall length of each segment in this manner. Vessel density (Vessels/ mm^2) was calculated by dividing the total number of vessel segments in the image by the size of the area (16mm^2). Lastly, the fractal dimension of the skeleton network was calculated using the box-counting method[26], which outputs a value between 0 and 3, with higher values

indicating a more irregular and tortuous network.

4.2.4 Automatic quantification of vascular depth

As discussed in Sec. 4.1, the capillary loop depth (CLD) and superficial plexus depth (SPD) within skin could potentially be used as a robust measure of acanthosis. In our previous work, measurements of CLD and SPD were acquired qualitatively through visual observation of an *en-face* flythrough of the corresponding angiographic data[27]. Here, the skeletonisation procedure outlined in Sec. 4.2.3 is used to automate this step. Firstly, a pseudo-3D skeleton was generated over the entire visible depth range (0-1mm) by applying the skeletonisation methodology to each z-depth in turn. With OCT angiography, forward scattering of photons by the red blood cells result in a shadowing artefact beneath detected vasculature[28]. This effect was utilised to improve the skeletonisation further, as signal derived from the vasculature was present over a range of depths within the tissue, while noise-derived signal was inconsistent with respect to depth. A simple median filter of 3-pixel window size in the z-direction was used to remove skeleton points which were inconsistent with depth. The total number of independent skeleton segments was then calculated for each z-depth in the volume. In this context, an independent skeleton section was defined as a section of skeleton that was disconnected from other sections of the skeleton. As there is no vasculature present in the upper sections of the epidermis, there were no independent skeleton segments detected for superficial depths. Once the tips of capillary loops start entering the field-of-view (typically around 40 – 100 μm in depth) the number of independent skeleton segments increased rapidly until reaching a local maximum. This maximum value represents the point at which the maximum number of unconnected capillary loops are visible, and is thus defined as the CLD. Typically at the CLD, between 200-500 independent skeleton sections were observed (corresponding to 13-31 capillaries per mm^2), this is in agreement with known measurements of the capillary density within skin, which typically range from 10-70 capillaries per mm^2 of skin[29]. Following the CLD, one might expect the number of independent skeleton segments to plateau as

subsequent depths are simply following each loop along its axis. Instead, the value gradually reduces, suggesting that the vessel network almost immediately begins to interconnect. This is potentially a direct result of the ascending and descending limbs of each capillary loop spreading slightly apart with depth, as OCT lacks the resolution to clearly discriminate between each limb. The result is a dilation of the visible loops, with neighboring loops potentially merging together though not physically connected. At sufficient depth, the gradient of the curve of skeleton segment number vs depth reaches 0, suggesting that the network is fully connected; this point is defined as the SPD. The SPD depth was more challenging to automatically quantify, owing to an increase in noise and a lack of OCT signal at deeper depths in the tissue. To improve reliability of this detection, the curve was smoothed with a moving averaging filter which spanned $20\mu m$ and each detection was manually checked for reliability. In future, SPD detection can potentially be improved through use of an alternate metric which would peak at the SPD depth, such as the total vessel signal or length, however this was not explored in the context of this study. Typically, past the SPD depth, the number of independent skeleton sections fluctuate slightly due to inconsistencies in the shadowing artefact of the vasculature, until reaching the noise floor, at which point a final reduction in value is observed. The noise floor in this context is the point at which the entire *en-face* angiogram shows detected speckle-variance due to random noise in the corresponding structural images, resulting in an extremely interconnected skeleton and a low number of independent skeleton segments. Fig. 4.4 illustrates this process for both healthy and AD skin, with healthy skin typically exhibiting a thin peak at superficial depths and AD skin typically exhibiting a much wider peak at comparatively deeper depths in the tissue.

4.2.5 Statistics

Statistical analysis was carried out using MATLAB (R2014b – Mathworks). A one-way ANOVA followed by the Tukey-Kramer honest significance difference (HSD) test was used to test for significant differences between four different datasets (Sec. 4.3.1). In all cases, comparisons were described as significant if the probability of the

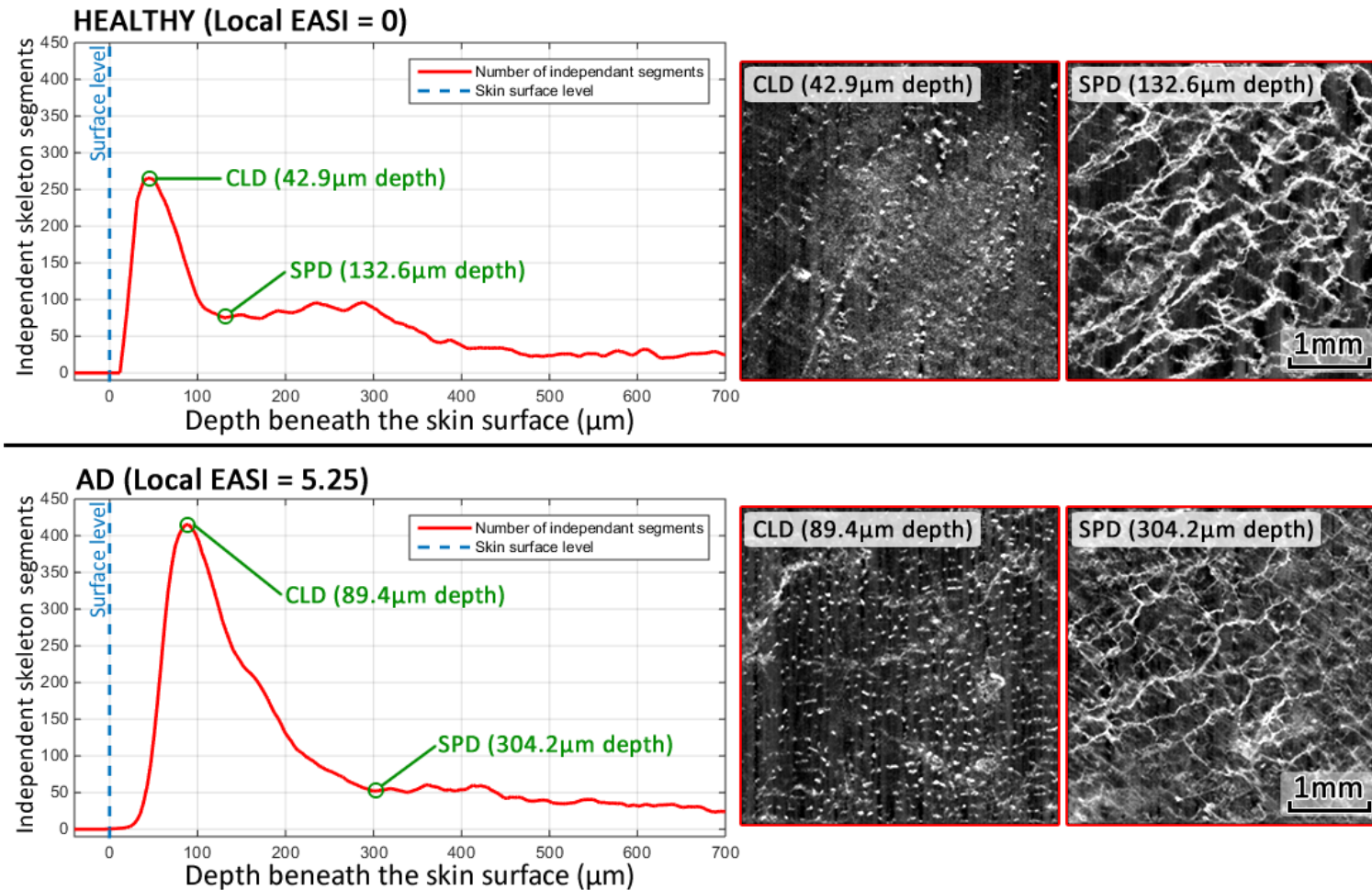


FIGURE 4.4: Automatic measurement of CLD and SPD through consideration of the number of independent (non-connected) skeleton segments as a function of tissue depth. Zero-depth corresponds to the skin surface level. The top row shows the results for a healthy participant at the left cubital fossa: the local maximum (CLD) is located at $42.9\mu\text{m}$ beneath the skin surface, while the following local minima (SPD) is located at $132.6\mu\text{m}$ beneath the surface. The bottom row shows the results for a participant with AD (Local EASI = 5.25) at the left cubital fossa: the local maximum (CLD) is located at $89.4\mu\text{m}$ beneath the skin surface, while the following local minima (SPD) is located at $304.2\mu\text{m}$ beneath the surface.

null hypothesis was <0.05 . All stated and graphed measurements are of the form mean \pm standard deviation.

4.3 Results and Discussion

4.3.1 Scan Cohorts

A total of 128 OCT datasets were acquired from the 32 participants, corresponding to 64 scans at the cubital and popliteal fossa sites respectively. To aid in analysis, these scans were separated into four different datasets based on the presence of localised AD and their local EASI score. The healthy dataset ($n=20$) consisted of skin sites of participants with no prior history of AD. The unaffected dataset ($n=35$) consisted of the skin sites of AD participants with a local EASI score of 0, thus showing no visible external symptoms of AD. The mild AD dataset ($n=40$) consisted of the skin sites with a local EASI greater than 0 and less than 5. Lastly the severe AD dataset ($n=33$) consisted of the skin sites with a local EASI greater than 5. The average global EASI score (full body) was 1.84 ± 0.92 for the unaffected dataset, 4.29 ± 4.69 for the mild dataset and 7.57 ± 6.62 for the severe dataset. It is important to note that in this context, a skin site being allocated to the severe/mild AD datasets simply meant that the localised AD appeared severe/mild and did not necessarily imply that the global severity would be graded as severe/mild. There was however a strong correlation to this effect, as evidenced by the comparatively higher average global EASI scores for the mild and severe AD datasets.

4.3.2 Automatic structural measurements of epidermal thickness

To enable comparison with the vessel derived metrics, average epidermal thickness was automatically quantified for each of the datasets using an algorithm which has been previously validated in healthy skin[13]. Briefly, this automatic algorithm first detects the air-skin (stratum corneum) boundary through application of a Sobel edge detection filter which was optimised for detecting any sharp changes in image intensity (dark to bright) in the depth-direction. Superficial detected edges which

were below a size threshold of 15-pixels ($150\mu m$) were detected and removed using the function "bwareaopen.m" within the MATLAB Image Processing Toolbox. The thresholding of smaller detected edges reduced the sensitivity of this technique to noise and other artefacts, such as superficial hairs. The value of 15-pixels was determined empirically as the majority of noise and artefact related detections were below this threshold, with most detected sections of the skin surface being much larger in size. The remaining larger superficial segments were identified and interpolated across such that the entire stratum-corneum was detected. The second step of the automatic algorithm aimed to detect the DEJ itself, which is characterised by a deeper hyporeflective (dark to bright) boundary where the grainy keratinocytes of the spinosum meet the basement membrane of the papillary dermis. At this location, a decreasing optical-intensity with depth within the epidermis gives way to an increasing optical-intensity with depth within the upper papillary dermis, which is detected as a local-minima within each A-scan[30]. Minima which are sufficiently connected are interpolated between to form the complete DEJ detection. The average distance between the detected stratum-corneum and DEJ was used as a measure of the average epidermal thickness.

The above method of quantifying epidermal thickness by detection of the DEJ is comprised of a single algorithm, it is indeed likely that other algorithms may offer superior performance in the detection of the DEJ boundary. Recently, ultra high-resolution OCT was shown to enhance the detection of the DEJ layer in comparison to images captured using a Vivosight system[31]. Similarly deep learning algorithms have had success delineating this boundary in reflectance confocal microscopy[32] and have recently been applied to OCT in segmentation of layers within the eye[33].

To demonstrate this process, the structural OCT images seen in Fig. 4.5 have been averaged over 50 consecutive frames to reduce speckle-noise and improve clarity of the DEJ. The stratum corneum and DEJ in each image were segmented both manually by hand and automatically using the algorithm discussed above. Despite the

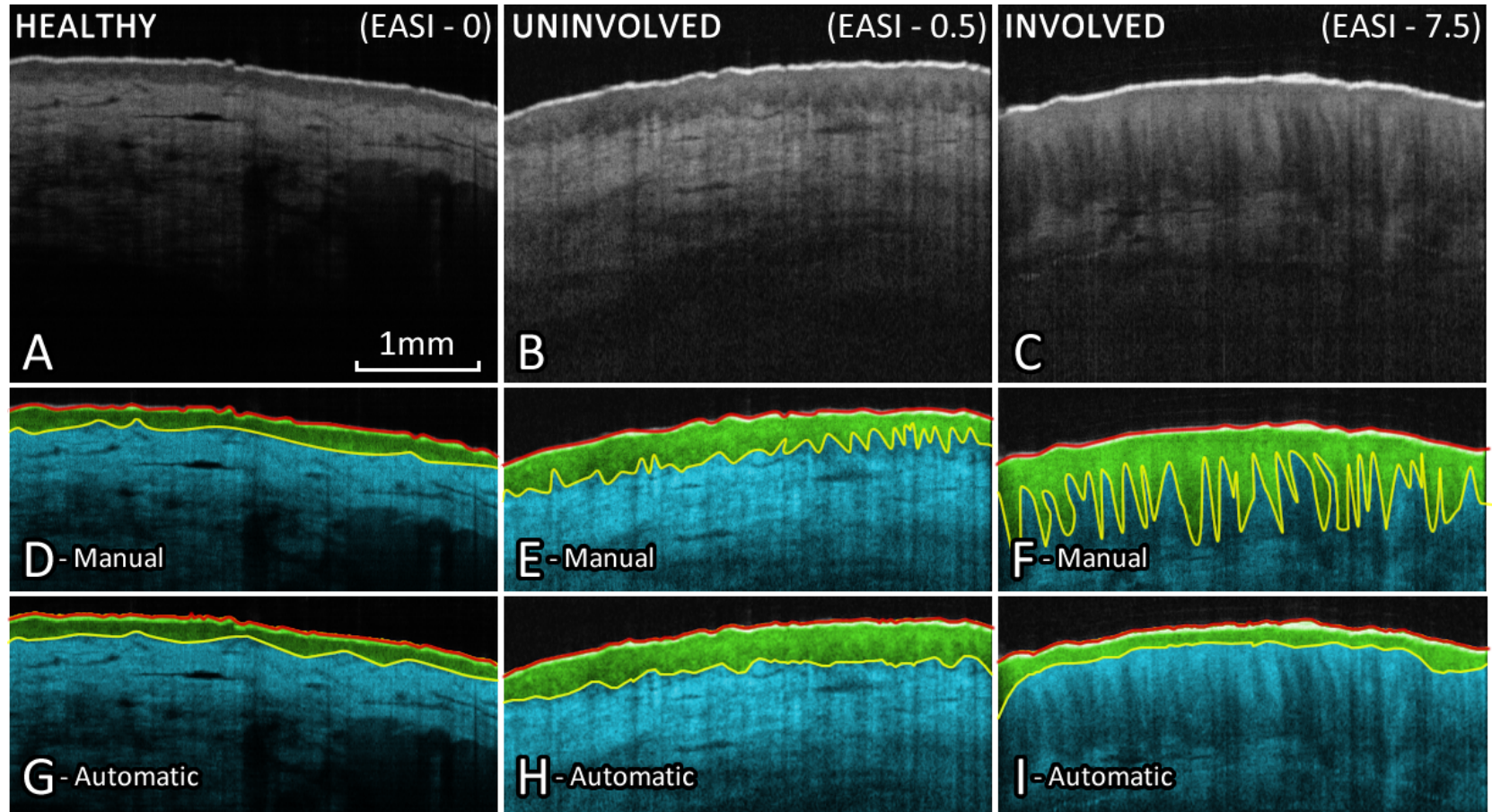


FIGURE 4.5: Averaged ($n=50$ – acquired at the same location) OCT B-scans of the popliteal-fossa highlighting the reduction of DEJ contrast as epidermal thickness increases. A) OCT image captured from a healthy subject (Local EASI = 0), showing clear delineation of the epidermis and dermis. B) OCT image captured from an uninvolved site on an eczema patient, showing slightly extended rete-pegs and an undulating DEJ. C) OCT image captured from an involved site on a different eczema patient, showing what appears to be inflammatory acanthosis (Long thin epidermal papillae/rete-pegs). D-F) Manually segmented skin layers. G-I) Automatically segmented skin layers using the algorithm described above. For D-I, red lines are the skin surface / stratum corneum layer. Green colouration represents the epidermis, Yellow-lines are the DEJ and blue colouration represents the dermis.

averaging, the automated algorithm failed to accurately capture the complex geometry of the DEJ at the involved site, severely underestimating the true epidermal thickness. Failure in this case was determined through visual observation of each volume to check that the automatic segmentation was reasonable, and was defined as a failure if the automatic detection was significantly displaced ($\pm \approx 20$ -pixels) across the majority of the image when compared to manual assessment. This is problematic, as manual assessment of epidermal thickness is a time consuming and subjective task, particularly across volume regions of tissue. Across all datasets, detection of the DEJ using the automatic algorithm failed in 41 cases, with a high tendency towards failure at higher local EASI scores (Healthy = 1 failure, Mild AD = 11 failures, Severe AD = 29 failures). The primary reason for failure was a distinct lack of contrast at the DEJ for many of the AD skin sites. Comparatively, automatic assessment of the CLD and SPD failed in 13 cases (Healthy = 1 failure, Unaffected AD = 2 failures, Mild AD = 5 failures, Severe AD = 5 failures) with motion corrupted data being the primary reason for failure. Angiographic post-processing at the bedside would enable repeat measurements to be made in cases where motion artefacts have corrupted the data, potentially reducing the failure rates of the angiographic method. For the structural method, we believe the loss of contrast at the DEJ is related to the presence of localised acanthosis; which involves the elongation of the rete-pegs/dermal papillae into the thickening epidermis, a condition previously documented in AD affected skin[34]. The result is a highly oscillatory DEJ which rises and falls around each individual rete-peg, these sharp undulations result in the lack of a clearly defined border between the epidermis and dermis. Furthermore, it remains challenging to consistently define epidermal thickness under these conditions as measurements fluctuate between thin sections of epidermis at the tips of the dermal papillae and at comparatively thick sections of epidermis along the deepest points along each rete-peg.

4.3.3 The effect of local severity on vascular depth

Fig. 4.6 shows a selection of 3D angiographic datasets from each dataset at each unique skin site. Each image shows the depth resolved vasculature over a depth range of $40 - 275\mu\text{m}$ beneath the skin surface. It is worth clarifying that exact measurement of depth with OCT is challenging, owing to changes in the propagation speed of light v as a function of the refractive index of the medium ($n = \frac{c}{v}$). For this work a depth of $3.9\mu\text{m}$ per pixel was assumed based on previous calibration experiments, details of these experiments can be found in the appendix (App. A.6).

For the healthy datasets seen in Fig. 4.6, a highly connected plexus was visible over this depth range, suggesting that the epidermis remains relatively thin. In contrast, in cases of severe localised AD, numerous dots (capillary loops) could be seen with very few connecting vessels joining them together. As expected, this suggests that a thickened epidermis is present, as the superficial plexus has been pushed deeper into the tissue ($> 275\mu\text{m}$). Cases of unaffected or mild localised AD appear to bridge this gap with the connecting vascular plexus becoming less visible as the epidermis thickens.

Fig. 4.7 summarises the results of automatic quantification of the CLD, SPD and epidermal-dermal junction depth across the entire dataset. Measurements of the epidermal thickness (Blue columns) were included for comparative purposes. As expected due to localised inflammation, the thickness of the epidermis increases as the severity of localised AD increases. However, particularly for mild or severe cases of localised AD, the reported value of mean epidermal thickness is likely to be underestimated. This is a result of the automatic epidermal-dermal junction segmentation algorithm having an increased tendency to fail at thicker skin sites compared to areas with a thinner epidermis as discussed in Sec. 4.3.2 as evidenced by the comparatively smaller cohort sizes used for the mild/severe AD epidermal thickness measurements. This may explain the lack of any significant differences between the epidermal thickness of unaffected, mild and severe localised AD at the popliteal fossa skin site, as any thicknesses above approximately $100\mu\text{m}$ are unlikely to be measured accurately.

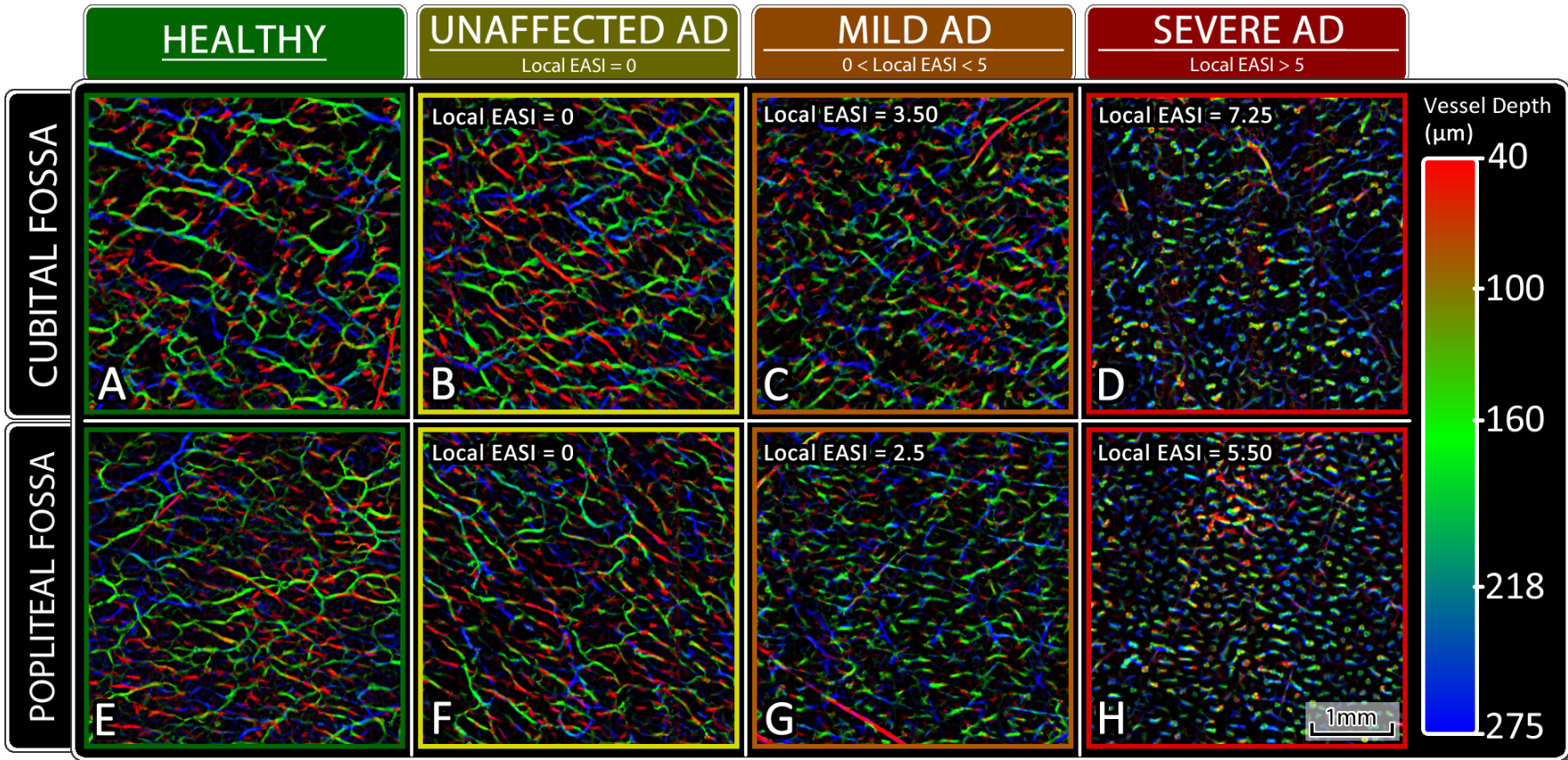


FIGURE 4.6: A selection of 3D angiographic OCT images projected over a depth range of $40 - 275\mu\text{m}$ beneath the skin surface, showing the changes in microcirculation depth and morphology as a function of AD severity. A-D) Scans from each dataset captured from the cubital fossa (Elbow) skin site. E-H) Scans from each dataset captured from the popliteal fossa (Knee) skin site. The healthy datasets (A & E) show a dense interconnected vascular network with capillary loops visible as small, superficial red dots. This transitions through unaffected AD (B & F) and mild AD (C & G) to severe AD (D & H) where very few interconnecting vessels are visible as they have been pushed deeper within the tissue. All images are $4\times 4\text{mm}$.

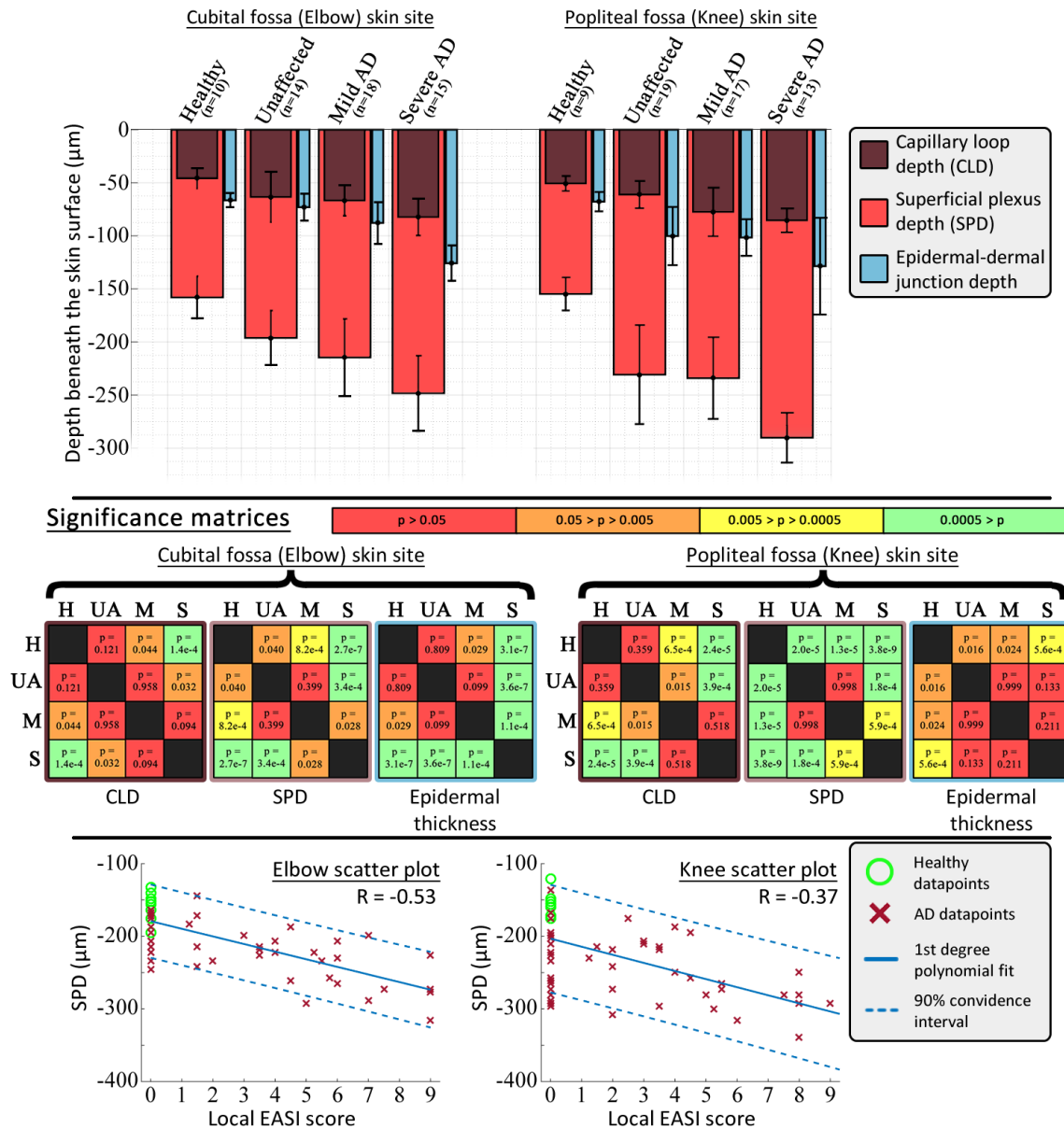


FIGURE 4.7: Charts showing differences in the CLD, SPD and epidermal-dermal junction depth at both the cubital fossa and popliteal fossa skin sites for a range of AD severities. Columns: Mean depth. Bars: Standard deviation. Significance was calculated at each skin site independently using a one-way ANOVA followed by the Tukey-Kramer honest significance difference (HSD) test. Significance matrix colours correspond to the measured p-value ($p > 0.05$ - Red, $0.05 > p > 0.005$ - Orange, $0.005 > p > 0.0005$ - Yellow, $0.0005 > p$ - Green). Quoted dataset sizes reflect angiography measurements only, as automatic epidermal-dermal junction assessment failed in a greater number of cases (With a bias towards failing in severe AD cases). Cohort sizes for the epidermal-dermal junction values were as follows: (From left to right): $n = 9, 12, 14, 7, 9, 18, 13, 5$. Bottom) Scatter plots showing the ungrouped SPD as a function of local EASI score, with a negative correlation visible at both sites. 1st degree polynomial fit was generated using all data points (Including healthy data). 90% confidence bounds were calculated as: $C = b \pm 1.645\sqrt{S}$ where b are the fit coefficients, and S is a diagonal vector of elements from the estimated covariance matrix.

Both the CLD (brown columns) and SPD (red columns) follow a similar trend to that of epidermal thickness, with an increase in depth as the severity of the localised AD increases (Fig. 4.7). For the case of the CLD, the differences are relatively small, with no significant differences found between the healthy and unaffected datasets at either skin site. Significant differences in CLD were however found between the healthy dataset and the mild/severe datasets at both skin sites, suggesting that a significantly deepened CLD may be an indicator that the condition is clinically active with moderate localised severity. The SPD displayed comparatively greater differences between each dataset. Of particular interest, significant differences in SPD were found between the healthy and unaffected datasets at both the elbow ($p=0.04$) and the knee ($p<0.001$), suggesting that this metric could be used to as a means of differentiating between the two. This could prove useful when aiming to monitor the efficacy of a treatment for AD, past the point of clinical remission. Furthermore, for both skin sites, significant differences in SPD were recordable between the healthy and mild/severe datasets as well as between the severe and unaffected/mild datasets. This suggests that the metric may remain robust and be able to differentiate between more severe cases of the condition.

Of potentially greater interest, SPD did discriminate between healthy (do not suffer from AD) skin and skin at the site of a healed flare (i.e. "unaffected"), whereas EASI did not (both skin types are assessed as $EASI=zero$). Similarly, no OCT-derived parameter, structural or angiographic, provided a strong discrimination between skin scored as unaffected and skin scored as mildly inflamed, even though the EASI scores are different. This could indicate that what is clinically scored as "healed" skin retains some physically detectable traits which are characteristic of mildly inflamed skin. In general, all three metrics followed a negative correlation as the local AD severity increased, suggesting that vascular measurements of CLD and SPD may have potential as robust measures of skin inflammation alongside epidermal thickness. Such measurement of the vascular layers may prove useful for monitoring the delicate balance between epidermal atrophy and acanthosis in response to topical corticosteroid application[15], [16], [35], particularly in areas of extreme thickening.

Furthermore, since the inflammatory skin of AD can be characterized by altered angiogenesis[36], [37], the depth and shape of the vasculature may hold additional information regarding the state of inflammation that is not provided by simple measures of epidermal thickness. Future research may focus on monitoring baseline variations of these parameters within the same patient over a period of time, a case where biological variability is far less likely to influence the data. Interestingly, overall it appeared that the vascular-derived metrics held a higher degree of significance between cohorts at the knee site when compared to the elbow.

The scatter plots shown at the bottom of Fig. 4.7 show how the ungrouped SPD measurements vary as a function of the local EASI score. While there is a negative correlation visible between the SPD and local EASI score at both the elbow ($R=-0.53$) and knee ($R=-0.37$), the variation in the recorded measurements is high. This makes it unlikely that accurate estimates of the local EASI score could be inversely attained from measurements of the SPD. In a sense this is not concerning, as 100% correlation would imply that the SPD biomarker, which is technically difficult and expensive to measure, offers no additional information over EASI score, which is cheap and easy to assess by eye. Given that much of this variability can also likely be attributed to biological variations in the skin between different volunteers, one potential avenue of future work will be assessing how much variation remains when considering intra-patient measurements over a period of time. Furthermore, local EASI is a composite metric, combining multiple skin features (redness, excoriation, oedema and lichenification) in order to quantify the severity of the condition. The current study population was deemed insufficient for stratification on the individual signs, but it may be that SPD correlates more robustly with a particular sign. This idea is to be assessed in the future.

4.3.4 The effect of severity on vascular morphology in the superficial vascular plexus

One key output of the angiographic OCT processing technique is the availability of depth-resolved *en-face* visualisations of the vascular network. The skin of patients

with AD can be characterised by an abnormal erythematous vascular pattern visible from the surface of the skin[38]. Furthermore it is known that such patients exhibit abnormal vasoconstrictive responses to stimuli, including mechanical pressure (white dermographism[21]) and temperature[20]. Previously, differences in the microcirculatory flow of AD patients following treatment with a pimecrolimus cream have been quantified using laser doppler flowmetry[39]. Furthermore svOCT has been utilised to demonstrate the relevance of morphological vascular changes within inflammatory skin conditions including psoriasis and scleroderma[40]. Thus, it is highly likely that the morphology of the vessels themselves will present some information regarding the severity of the AD.

Previously we have shown that measurable morphological differences between healthy and AD scans are attainable using svOCT depth projections over a wide depth range ($30 - 300\mu\text{m}$)[27], however it is unclear if the differences were related to true morphological differences or simply a result of the AD vessels being much deeper in the skin. To investigate this, the SPD data from Sec. 4.3.3 was utilised to acquire depth projections only over the depth range of the SPD ($\pm 30\mu\text{m}$). For example, if the SPD was recorded at a depth of $200\mu\text{m}$, a projection image for quantification would be generated over the range $170 - 230\mu\text{m}$, normalising the depth considered to that of the SPD. This projection image was then skeletonised and quantified following the methodology outlined in Sec 4.2.3.

Fig. 4.8 shows a selection of the depth projected angiographic images which were used for quantification, while Fig. 4.9 shows the results of the quantification. Due to the sensitivity of these measurements to noise, and as discussed in Sec. 4.2.2, only scans which were acquired using the higher quality scan settings ($10\mu\text{m}$ y-resolution) and which were deemed sufficiently noise free were used for these measurements, resulting in a reduction in overall group size. Qualitative observation of the angiographic SPD images shown in Fig. 4.8 shows the morphology of scans in the healthy, unaffected AD and mild AD cohorts are difficult to differentiate, as they all display long, thin vascular morphology. Comparatively scans of sites with severe localized AD showed a dense network of small, comparatively wide vessels.

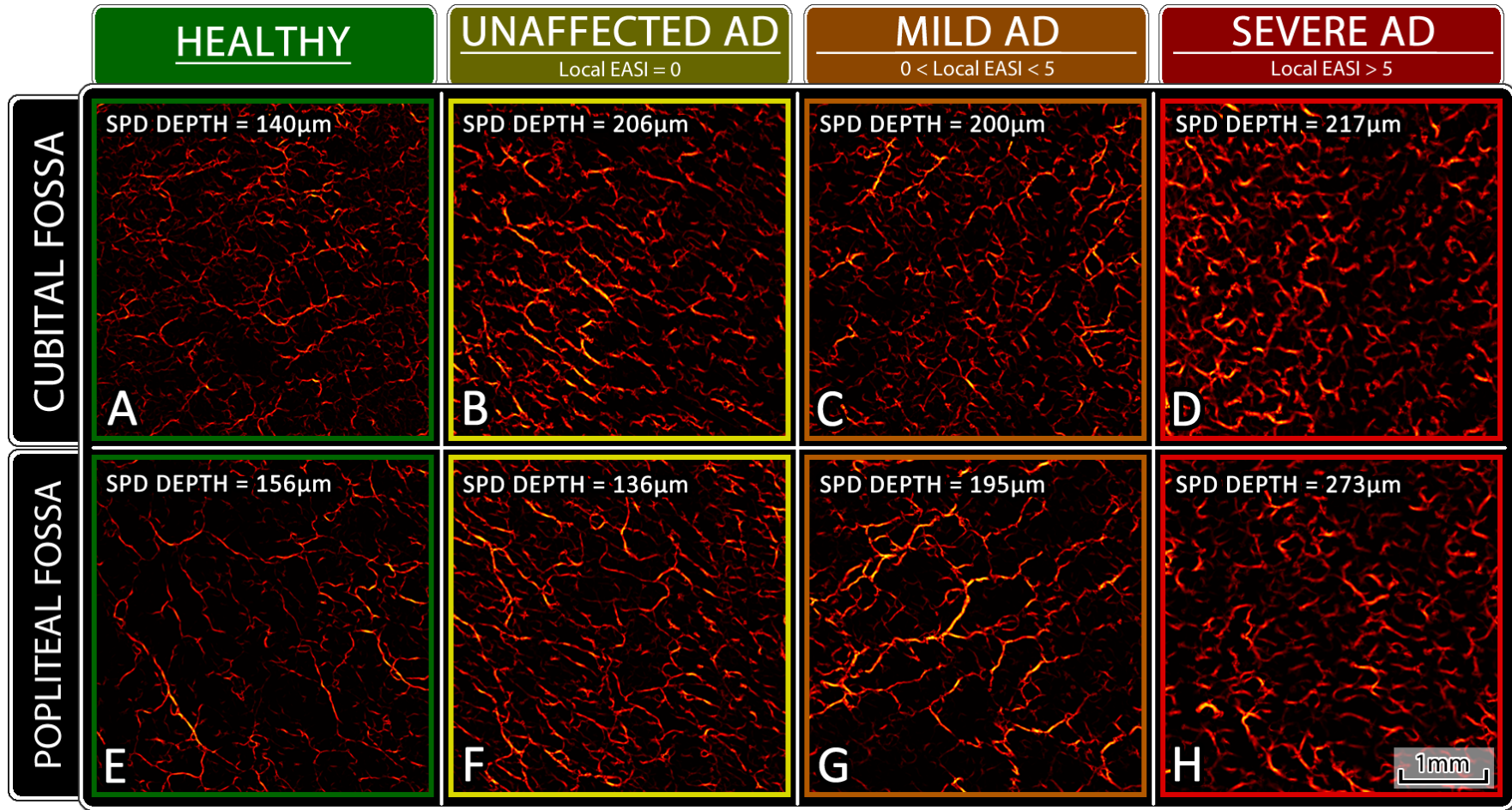


FIGURE 4.8: A selection of 2D angiographic OCT images projected over a depth range of $\pm 30\mu\text{m}$ around the detected SPD, showing morphological differences in the SPD. A-D) Scans from each dataset captured from the cubital fossa (Elbow) skin site. E-H) Scans from each dataset captured from the popliteal fossa (Knee) skin site. All images are 4x4mm.

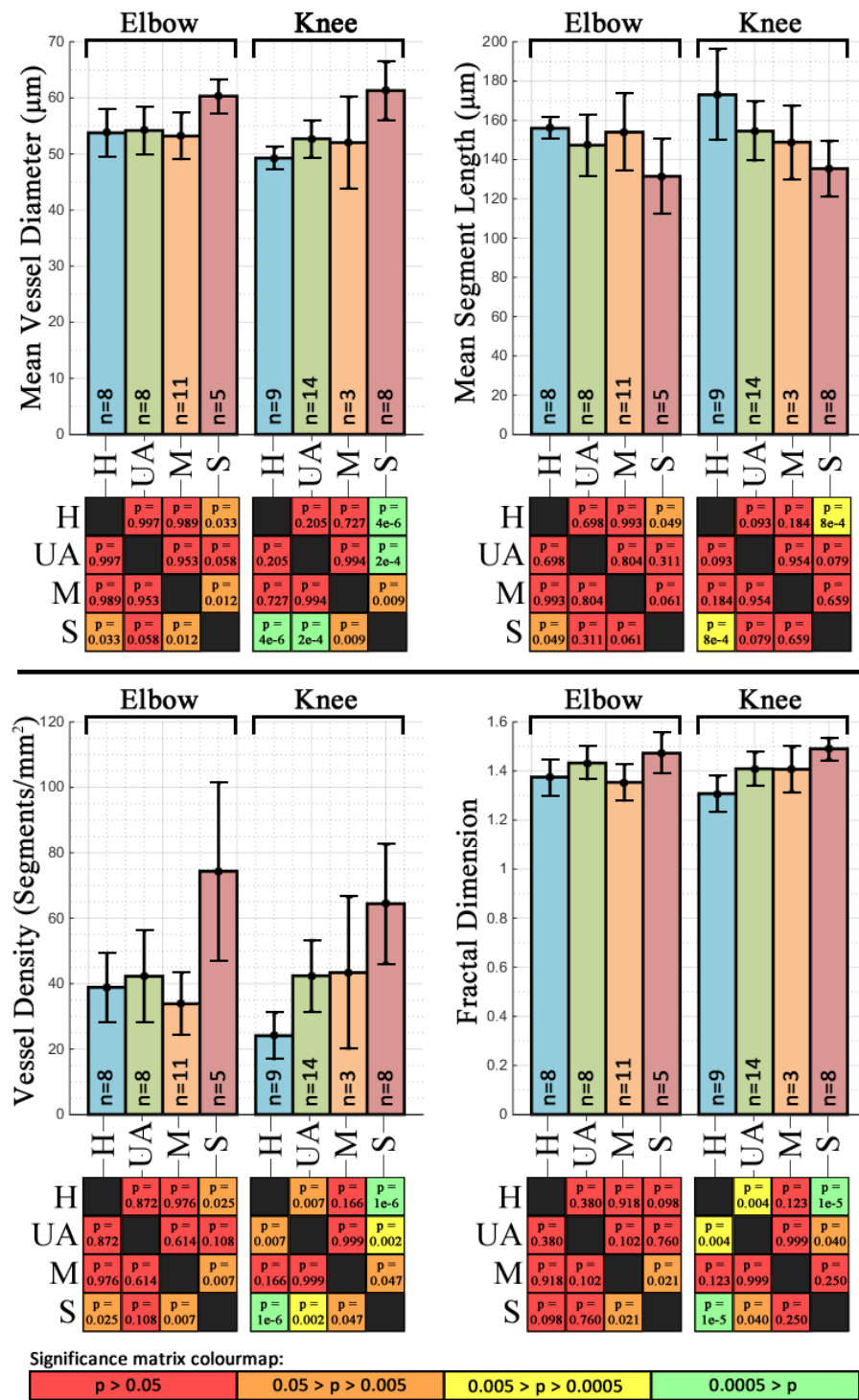


FIGURE 4.9: Bar charts showing the variance of quantitative parameters which were automatically extracted from the superficial vascular plexus layer of datasets following the binarisation and skeletonisation steps outlined in Sec. 4.2.3. Columns: Mean depth. Bars: Standard deviation. Significance was calculated at each skin site independently using a one-way ANOVA followed by the Tukey-Kramer honest significance difference (HSD) test. H=Healthy, U=Unaffected, M=Mild localised AD, S=Severe localised AD. Numbers at the base of each column correspond to group size (n).

The measured mean vessel diameter was found to be significantly higher for patients with severe localised AD, when compared to all other datasets at both skin sites. The sole exception being the unaffected elbow, which did not quite reach significance ($p=0.058$). Vascular enlargement is one of the primary alterations to the cutaneous circulation within inflammatory skin conditions such as AD, psoriasis and rosacea[41], thus it is unsurprising that the vessel diameter is measurable larger for severe cases of localised AD.

Mean vessel segment length was significantly higher in the healthy dataset than in the severe AD dataset at both skin sites. This suggests that for severe localised AD patients, the individual vessel segments are shortened, with more branch points. There was however no significant discrimination in vessel segment length between healthy skin and skin graded as unaffected or mildly inflamed. Vessel density was found to be significantly higher for the severe AD dataset when compared to all other datasets, with the unaffected elbow being the exception ($p=0.108$). In general, these two metrics correspond to an observed increase in vessel growth and branching within the severe AD dataset. This is expected, as lesioned skin affected by AD has previously been shown to exhibit higher levels of the angiogenic growth factor VEGF compared to healthy skin[42], [43], which is associated with increased levels of vascular remodeling[44].

Lastly, the differences in fractal dimension between the healthy and severe datasets did not reach significance at the elbow site ($p=0.098$), however a significant increase in fractal dimension was found for higher severities at the knee site suggesting those vessel networks became more tortuous and irregular as severity increased. Previously, the study of the fractal dimension of vascular networks has proven to be a fast, reliable and robust parameter for observing and evaluating angiographic processes[45], thus it may prove a useful metric when considering the increased angiogenic proliferation within AD.

4.4 Conclusions

Unequivocal assessment of the severity of AD is a challenging and subjective task to perform, particularly within flare-free AD patients. This is a result of many of the external, clinical features of the condition being characteristic, but not specific indicators of severity. Sub-clinical measurements of epidermal thickening remain robust for areas exhibiting mild symptoms, but become increasingly difficult as the epidermis increasingly thickens due to the extension of the dermal papillae during acanthosis. Here we demonstrate how the visualisation and quantification of the microcirculatory depth using OCT can be utilised as an alternative means of achieving this measurement, as the superficial plexus remains relatively flat regardless of its depth within the tissue. It is shown that the superficial plexus depth (SPD) differs significantly between healthy patients and those who are unaffected or suffering from mild or severe localised AD, and thus can potentially be utilized as a metric for monitoring the severity of the condition. Recent treatment strategies for AD emphasize the importance of treating a flare (e.g. with topical corticosteroids) beyond the point at which visible lesions have disappeared. Of particular relevance to this idea, we have shown that the SPD metric differs significantly ($p = 0.04$ at the elbow, $p = 2.0 * 10^{-5}$ at the knee) between healthy (do not suffer from AD) subjects and AD subjects whose flares have indeed disappeared visually. Hence SPD has potential as a non-invasive biomarker of sub-clinical inflammation. Furthermore, the morphology of the vessels themselves appear to be altered with the presence of AD, with significant changes in vessel diameter, length, density and fractal dimension between healthy and severe localised AD patients. These metrics provide a means of quantifying and differentiating between subtle changes in the condition, particularly past the point of clinical-remission.

Limitations of the current study include the need to make physical contact with the skin surface, which may induce some degree of vasoconstriction within the observed vessels. Contactless scans were deemed impractical at the imaging speeds used herein, but faster OCT systems could potentially be used to acquire contactless

angiographic scans without inducing excessive motion artefacts in the data. Furthermore, we only considered one algorithm for measuring the structural epidermal thickness. It is possible that more advanced detection algorithms will have a greater success rate for DEJ detection and should be considered moving forward.

Future developments will focus on the further refinement of both angiographic and structural detection methods. In particular, the application of the techniques described herein to long-term clinical observations of drug and treatment efficacy may help to assess clinical benefit. Angiographic OCT may also provide a valuable guide to determining how long treatments for AD should be continued after visible lesions have resolved, in order to induce clearance of all sub clinical manifestations of AD. This OCT biomarker can therefore be used to stratify patients into those requiring different durations of therapy to achieve optimal long-term control of their AD. Angiographic OCT could also be used to determine the long-term safety of therapies such as topical corticosteroids, by providing a robust, non-invasive measure of epidermal atrophy.

References

- [1] T. E. Shaw, G. P. Currie, C. W. Koudelka, and E. L. Simpson, "Eczema Prevalence in the United States: Data from the 2003 National Survey of Children's Health", *Journal of Investigative Dermatology*, vol. 131, no. 1, pp. 67–73, Jan. 2011, ISSN: 0022202X. DOI: 10.1038/jid.2010.251 (cit. on p. 105).
- [2] J. A. Odhiambo, H. C. Williams, T. O. Clayton, C. F. Robertson, and M. I. Asher, "Global variations in prevalence of eczema symptoms in children from ISAAC Phase Three", *Journal of Allergy and Clinical Immunology*, vol. 124, no. 6, 1251–1258.e23, 2009, ISSN: 00916749. DOI: 10.1016/j.jaci.2009.10.009 (cit. on p. 105).
- [3] J. I. Silverberg and J. M. Hanifin, "Adult eczema prevalence and associations with asthma and other health and demographic factors: A US population-based study", *Journal of Allergy and Clinical Immunology*, vol. 132, no. 5, pp. 1132–1138, 2013, ISSN: 00916749. DOI: 10.1016/j.jaci.2013.08.031 (cit. on p. 105).
- [4] S. T. Holgate, "The epidemic of allergy and asthma", *Nature*, vol. 402, no. 6760supp, pp. 2–4, Nov. 1999, ISSN: 00280836. DOI: 10.1038/35037000 (cit. on p. 105).
- [5] T. Bieber, "Atopic Dermatitis", *New England Journal of Medicine*, vol. 358, no. 14, pp. 1483–1494, Apr. 2008, ISSN: 0028-4793. DOI: 10.1056/NEJMra074081 (cit. on p. 105).
- [6] M. J. Cork, S. G. Danby, Y. Vasilopoulos, J. Hadgraft, M. E. Lane, M. Moustafa, R. H. Guy, A. L. MacGowan, R. Tazi-Ahnini, and S. J. Ward, "Epidermal Barrier Dysfunction in Atopic Dermatitis", *Journal of Investigative Dermatology*, vol. 129, no. 8, pp. 1892–1908, Aug. 2009, ISSN: 0022202X. DOI: 10.1038/jid.2009.133 (cit. on p. 105).

- [7] European Task Force on Atopic Dermatitis, "Severity scoring of atopic dermatitis: the SCORAD index.", *Dermatology (Basel, Switzerland)*, vol. 186, no. 1, pp. 23–31, 1993, ISSN: 1018-8665 (cit. on p. 105).
- [8] J. M. Hanifin, M. Thurston, M. Omoto, R. Cherill, S. J. Tofte, and M. Graeber, "The eczema area and severity index (EASI): assessment of reliability in atopic dermatitis. EASI Evaluator Group.", *Experimental Dermatology*, vol. 10, no. 1, p. 18, 2001, ISSN: 0906-6705. DOI: 10.1034/j.1600-0625.2001.100102.x (cit. on pp. 105, 110).
- [9] T. S. Tang, T. Bieber, and H. C. Williams, "Are the concepts of induction of remission and treatment of subclinical inflammation in atopic dermatitis clinically useful?", *Journal of Allergy and Clinical Immunology*, vol. 133, no. 6, 1615–1625.e1, 2014, ISSN: 10976825. DOI: 10.1016/j.jaci.2013.12.1079 (cit. on p. 105).
- [10] S. Seidenari and G. Giusti, "Objective assessment of the skin of children affected by atopic dermatitis: a study of pH, capacitance and TEWL in eczematous and clinically uninvolved skin.", *Acta dermato-venereologica*, vol. 75, no. 6, pp. 429–33, Nov. 1995, ISSN: 0001-5555 (cit. on p. 105).
- [11] J. Gupta, E. Grube, M. B. Ericksen, M. D. Stevenson, A. W. Lucky, A. P. Sheth, A. H. Assa'ad, and G. K. Khurana Hershey, "Intrinsically defective skin barrier function in children with atopic dermatitis correlates with disease severity", *Journal of Allergy and Clinical Immunology*, vol. 121, no. 3, 725–730.e2, Mar. 2008, ISSN: 00916749. DOI: 10.1016/j.jaci.2007.12.1161 (cit. on p. 105).
- [12] M. Suárez-Fariñas, S. J. Tintle, A. Shemer, A. Chiricozzi, K. Nograles, I. Cardinale, S. Duan, A. M. Bowcock, J. G. Krueger, and E. Guttman-Yassky, "Nonlesional atopic dermatitis skin is characterized by broad terminal differentiation defects and variable immune abnormalities", *Journal of Allergy and Clinical Immunology*, vol. 127, no. 4, 2011, ISSN: 00916749. DOI: 10.1016/j.jaci.2010.12.1124. arXiv: NIHMS150003 (cit. on pp. 105–106).

- [13] R. Maiti, L. C. Gerhardt, Z. S. Lee, R. A. Byers, D. Woods, J. A. Sanz-Herrera, S. E. Franklin, R. Lewis, S. J. Matcher, and M. J. Carré, "In vivo measurement of skin surface strain and sub-surface layer deformation induced by natural tissue stretching", *Journal of the Mechanical Behavior of Biomedical Materials*, vol. 62, pp. 556–569, 2016, ISSN: 18780180. DOI: 10.1016/j.jmbbm.2016.05.035 (cit. on pp. 105, 116).
- [14] J. Delacruz, J. Weissman, and K. Gossage, "Automated measurement of epidermal thickness from optical coherence tomography images using line region growing", N. Kollias, B. Choi, H. Zeng, R. S. Malek, B. J. Wong, J. F. R. Ilgner, K. W. Gregory, G. J. Tearney, L. Marcu, H. Hirschberg, S. J. Madsen, A. Mandelis, A. Mahadevan-Jansen, and E. D. Jansen, Eds., Feb. 2010, 75480E. DOI: 10.1117/12.842353 (cit. on p. 105).
- [15] J. Boadi, Z. Lu, S. Danby, M. Cork, and S. J. Matcher, "Optical coherence tomography demonstrates differential epidermal thinning of human forearm volar skin after 2 weeks application of a topical corticosteroid vs a non-steroidal anti-inflammatory alternative", vol. 8565, p. 85650C, 2013, ISSN: 16057422. DOI: 10.1117/12.2006104 (cit. on pp. 106, 123).
- [16] L. Kolbe, a. M. Kligman, V. Schreiner, and T. Stoudemayer, "Corticosteroid-induced atrophy and barrier impairment measured by non-invasive methods in human skin.", *Skin research and technology : official journal of International Society for Bioengineering and the Skin (ISBS) [and] International Society for Digital Imaging of Skin (ISDIS) [and] International Society for Skin Imaging (ISSI)*, vol. 7, no. 2, pp. 73–77, 2001, ISSN: 0909-752X. DOI: 10.1034/j.1600-0846.2001.70203.x (cit. on pp. 106, 123).
- [17] A. Mariampillai, B. a. Standish, E. H. Moriyama, M. Khurana, N. R. Munce, M. K. Leung, J. Jiang, A. Cable, B. C. Wilson, I. A. Vitkin, and V. X. D. Yang, "Speckle variance detection of microvasculature using swept-source optical coherence tomography.", *Optics letters*, vol. 33, no. 13, pp. 1530–2, Jul. 2008, ISSN: 0146-9592 (cit. on p. 106).

- [18] R. A. Byers, G. Tozer, N. J. Brown, and S. J. Matcher, "High-resolution label-free vascular imaging using a commercial, clinically approved dermatological OCT scanner", in *SPIE BiOS*, B. Choi, N. Kollias, H. Zeng, H. W. Kang, B. J. F. Wong, J. F. Ilgner, G. J. Tearney, K. W. Gregory, L. Marcu, M. C. Skala, P. J. Campagnola, A. Mandelis, and M. D. Morris, Eds., International Society for Optics and Photonics, Feb. 2016, p. 96890M. DOI: 10.1117/12.2212222 (cit. on p. 106).
- [19] E. Y. Lam and J. W. Goodman, "A mathematical analysis of the DCT coefficient distributions for images.", *IEEE transactions on image processing : a publication of the IEEE Signal Processing Society*, vol. 9, no. 10, pp. 1661–6, Jan. 2000, ISSN: 1057-7149. DOI: 10.1109/83.869177 (cit. on p. 106).
- [20] M. Steinhoff, A. Steinhoff, B. Homey, T. a. Luger, and S. W. Schneider, "Role of vasculature in atopic dermatitis.", *The Journal of allergy and clinical immunology*, vol. 118, no. 1, pp. 190–7, 2006, ISSN: 0091-6749. DOI: 10.1016/j.jaci.2006.04.025 (cit. on pp. 110, 125).
- [21] S. S. Wong, C. Edwards, and R. Marks, "A study of white dermographism in atopic dermatitis", *Journal of Dermatological Science*, vol. 11, no. 2, pp. 148–153, 1996, ISSN: 09231811. DOI: 10.1016/0923-1811(95)00436-X (cit. on pp. 110, 125).
- [22] R. A. Byers, M. Fisher, N. J. Brown, G. M. Tozer, and S. J. Matcher, "Vascular patterning of subcutaneous mouse fibrosarcomas expressing individual VEGF isoforms can be differentiated using angiographic optical coherence tomography", *Biomedical Optics Express*, vol. 8, no. 10, p. 4551, Oct. 2017, ISSN: 2156-7085. DOI: 10.1364/BOE.8.004551 (cit. on p. 111).
- [23] A. F. Frangi, W. J. Niessen, K. L. Vincken, and M. a. Viergever, "Multiscale vessel enhancement filtering", *Medial Image Computing and Computer-Assisted Invervention - MICCAI'98. Lecture Notes in Computer Science, vol 1496*, vol. 1496, pp. 130–137, 1998, ISSN: 13618415. DOI: 10.1016/j.media.2004.08.001 (cit. on p. 111).

- [24] N. Otsu, "A Threshold Selection Method from Gray-Level Histograms", *IEEE Transactions on Systems, Man, and Cybernetics*, vol. 9, no. 1, pp. 62–66, 1979, ISSN: 0018-9472. DOI: 10.1109/TSMC.1979.4310076 (cit. on p. 112).
- [25] P. Soille, "Geodesic Transformations", in *Morphological Image Analysis*, Berlin, Heidelberg: Springer Berlin Heidelberg, 2004, pp. 183–218. DOI: 10.1007/978-3-662-05088-0_6 (cit. on p. 112).
- [26] K. Jurczyszyn, B. J. Osiecka, P. Ziółkowski, and P. Kowski, "The Use of Fractal Dimension Analysis in Estimation of Blood Vessels Shape in Transplantable Mammary Adenocarcinoma in Wistar Rats after Photodynamic Therapy Combined with Cysteine Protease Inhibitors", *Computational and Mathematical Methods in Medicine*, vol. 2012, pp. 1–6, 2012, ISSN: 1748-670X. DOI: 10.1155/2012/793291 (cit. on p. 112).
- [27] R. A. Byers, R. Maiti, S. G. Danby, E. J. Pang, B. Mitchell, M. J. Carr?, R. Lewis, M. J. Cork, and S. J. Matcher, "Characterizing the microcirculation of atopic dermatitis using angiographic optical coherence tomography", B. Choi, H. Zeng, and N. Kollias, Eds., International Society for Optics and Photonics, Feb. 2017, p. 100370V. DOI: 10.1117/12.2252407 (cit. on pp. 113, 125).
- [28] B. J. Vakoc, R. M. Lanning, J. A. Tyrrell, T. P. Padera, L. A. Bartlett, T. Stylianopoulos, L. L. Munn, G. J. Tearney, D. Fukumura, R. K. Jain, and B. E. Bouma, "Three-dimensional microscopy of the tumor microenvironment in vivo using optical frequency domain imaging.", *Nature medicine*, vol. 15, no. 10, pp. 1219–23, Oct. 2009, ISSN: 1546-170X. DOI: 10.1038/nm.1971 (cit. on p. 113).
- [29] G. M. Drzewiecki and J. K.-J. Li, *Analysis and Assessment of Cardiovascular Function*. Springer New York, 1998, p. 387, ISBN: 146121744X (cit. on p. 113).
- [30] G. Abignano, S. Z. Aydin, C. Castillo-Gallego, V. Liakouli, D. Woods, A. Meekings, R. J. Wakefield, D. G. McGonagle, P. Emery, and F. Del Galdo, "Virtual skin biopsy by optical coherence tomography: the first quantitative imaging biomarker for scleroderma", *Annals of the Rheumatic Diseases*, vol. 72, no. 11,

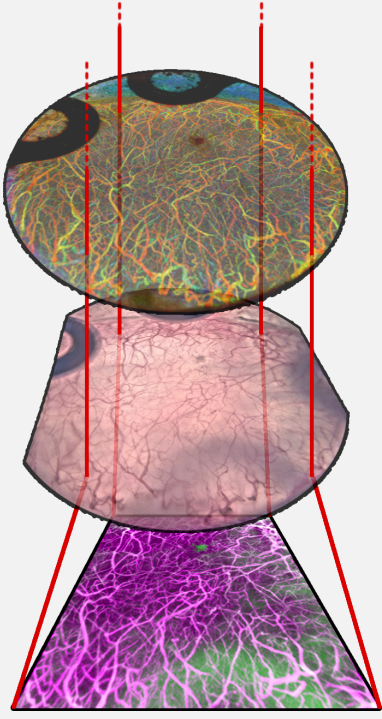
- pp. 1845–1851, Nov. 2013, ISSN: 0003-4967. DOI: 10.1136/annrheumdis-2012-202682 (cit. on p. 117).
- [31] N. M. Israelsen, M. Maria, M. Mogensen, S. Bojesen, M. Jensen, M. Haedersdal, A. Podoleanu, and O. Bang, “The value of ultrahigh resolution OCT in dermatology - delineating the dermo-epidermal junction, capillaries in the dermal papillae and vellus hairs”, *Biomedical Optics Express*, vol. 9, no. 5, p. 2240, May 2018, ISSN: 2156-7085. DOI: 10.1364/B0E.9.002240 (cit. on p. 117).
- [32] S. Kurugol, K. Kose, B. Park, J. G. Dy, D. H. Brooks, and M. Rajadhyaksha, “Automated delineation of dermal-epidermal junction in reflectance confocal microscopy image stacks of human skin.”, *The Journal of investigative dermatology*, vol. 135, no. 3, pp. 710–717, Mar. 2015, ISSN: 1523-1747. DOI: 10.1038/jid.2014.379 (cit. on p. 117).
- [33] C. S. Lee, A. J. Tyring, N. P. Deruyter, Y. Wu, A. Rokem, and A. Y. Lee, “Deep-learning based, automated segmentation of macular edema in optical coherence tomography.”, *Biomedical optics express*, vol. 8, no. 7, pp. 3440–3448, Jul. 2017, ISSN: 2156-7085. DOI: 10.1364/B0E.8.003440 (cit. on p. 117).
- [34] M. C. Mihm, N. A. Soter, H. F. Dvorak, and K. F. Austen, “The Structure Of Normal Skin And The Morphology Of Atopic Eczema”, *Journal of Investigative Dermatology*, vol. 67, no. 3, pp. 305–312, 1976, ISSN: 0022202X. DOI: 10.1111/1523-1747.ep12514346 (cit. on p. 119).
- [35] L. Barnes, G. Kaya, and V. Rollason, “Topical Corticosteroid-Induced Skin Atrophy: A Comprehensive Review”, *Drug Safety*, vol. 38, no. 5, pp. 493–509, May 2015, ISSN: 0114-5916. DOI: 10.1007/s40264-015-0287-7 (cit. on p. 123).
- [36] G. Varricchi, F. Granata, S. Loffredo, A. Genovese, and G. Marone, “Angiogenesis and lymphangiogenesis in inflammatory skin disorders”, *Journal of the American Academy of Dermatology*, vol. 73, no. 1, pp. 144–153, Jul. 2015, ISSN: 01909622. DOI: 10.1016/j.jaad.2015.03.041 (cit. on p. 124).

- [37] D. A. Groneberg, C. Bester, A. Grützkau, F. Serowka, A. Fischer, B. M. Henz, and P. Welker, "Mast cells and vasculature in atopic dermatitis - potential stimulus of neoangiogenesis", *Allergy*, vol. 60, no. 1, pp. 90–97, Jan. 2005, ISSN: 01054538. DOI: 10.1111/j.1398-9995.2004.00628.x (cit. on p. 124).
- [38] C. Schuster, J. Smolle, W. Aberer, and B. Kränke, "Vascular pattern of the palms - A clinical feature of atopic skin diathesis", *Allergy: European Journal of Allergy and Clinical Immunology*, vol. 61, no. 12, pp. 1392–1396, 2006, ISSN: 01054538. DOI: 10.1111/j.1398-9995.2006.01168.x (cit. on p. 125).
- [39] R. Aschoff, U. Schwanebeck, M. Bräutigam, and M. Meurer, "Skin physiological parameters confirm the therapeutic efficacy of pimecrolimus cream 1% in patients with mild-to-moderate atopic dermatitis", *Experimental Dermatology*, vol. 18, no. 1, pp. 24–29, 2009, ISSN: 09066705. DOI: 10.1111/j.1600-0625.2008.00756.x (cit. on p. 125).
- [40] M. Ulrich, L. Themstrup, N. De Carvalho, M. Manfredi, C. Grana, S. Ciardo, R. Kästle, J. Holmes, R. Whitehead, G. B. Jemec, G. Pellacani, and J. Welzel, "Dynamic Optical Coherence Tomography in Dermatology", *Dermatology*, vol. 232, no. 3, pp. 298–311, 2016, ISSN: 14219832. DOI: 10.1159/000444706 (cit. on p. 125).
- [41] R. Huggenberger and M. Detmar, "The cutaneous vascular system in chronic skin inflammation", *J Invest Dermatol*, vol. 15, no. 1, pp. 24–32, 2012. DOI: 10.1038/jidsymp.2011.5.The (cit. on p. 128).
- [42] Z. Samochocki, J. Bogaczewicz, A. Sysa-Jedrzejowska, D. P. McCauliffe, E. Kontny, and A. Wozniacka, "Expression of vascular endothelial growth factor and other cytokines in atopic dermatitis, and correlation with clinical features.", *International journal of dermatology*, vol. 55, no. 3, e141–6, Mar. 2016, ISSN: 1365-4632 (Electronic). DOI: 10.1111/ijd.13132 (cit. on p. 128).

-
- [43] Y. Zhang, H. Matsuo, and E. Morita, "Increased production of vascular endothelial growth factor in the lesions of atopic dermatitis", *Archives of Dermatological Research*, vol. 297, no. 9, pp. 425–429, Mar. 2006, ISSN: 0340-3696. DOI: 10.1007/s00403-006-0641-9 (cit. on p. 128).
- [44] M. Detmar, "The role of VEGF and thrombospondins in skin angiogenesis.", *Journal of dermatological science*, vol. 24, pp. 78–84, Dec. 2000, ISSN: 0923-1811 (cit. on p. 128).
- [45] D. Mancardi, G. Varetto, E. Bucci, F. Maniero, and C. Guiot, "Fractal parameters and vascular networks: facts & artifacts", *Theoretical Biology and Medical Modelling*, vol. 5, no. 1, p. 12, 2008, ISSN: 1742-4682. DOI: 10.1186/1742-4682-5-12 (cit. on p. 128).

Chapter 5

Vascular morphology: correlation of OCT with IVM



This chapter contains the following unpublished work which is formatted ready for publication:

**Vascular morphology:
correlation of OCT with IVM.**

*Robert A. Byers, Matthew Fisher, Nicola J. Brown,
Gillian M. Tozer, and Stephen J. Matcher*

Boxes such as this one will contain supplementary detail.

Statement of contribution

Concerning the publication:

Vascular morphology: correlation of OCT with IVM

Contributor	Statement of contribution
Robert A. Byers Signed: _____	I am the primary contributor to this work. Having performed all of the data acquisition, processing and analysis. <ul style="list-style-type: none"> • Prepared the manuscript. • Performed OCT and IVM imaging/data collection. • Performed all data analysis and interpretation. • Performed DSWC surgery in full (Together with M. Fisher). Assisted with animal welfare duties (Together with M. Fisher)
Matthew Fisher Signed: _____	<ul style="list-style-type: none"> • Performed DSWC surgery (Together with R. Byers). Performed culture and growth of tumour cell spheroids. <ul style="list-style-type: none"> • Assisted with IVM data collection. Assisted with animal welfare duties (Together with R. Byers)

Principle supervisor confirmation

I have sighted email or other correspondence from all co-authors confirming their certifying authorship.

Name: _____

Signature: _____

Date: _____

Vascular morphology: correlation of OCT with IVM.

ROBERT A. BYERS,¹ MATTHEW FISHER,² GILLIAN M. TOZER,²
NICOLA J. BROWN,² AND STEPHEN J. MATCHER¹

¹ Biophotonics Group, Kroto Research Institute, University of Sheffield, Sheffield, UK

² Department of Oncology & Metabolism, The Medical School, University of Sheffield, Sheffield, UK

NB: NJB and SJM are Joint Senior Authors

Abstract: Angiographic optical coherence tomography has emerged as an effective tool for the *in-vivo* imaging of microcirculatory networks. Here, the vessel detection capabilities and accuracy of OCT are validated through direct comparison with transmitted-light intravital microscopy (IVM). Window chambers containing fibrosarcoma tumours expressing either the VEGF120 isoform (designated fs120) or the VEGF188 isoform (designated fs188) were implanted into the dorsal skin of SCID mice (n=25), with both OCT and IVM imaging being performed consecutively. Despite a strong visual correlation between the modalities, quantitative analysis of matched vessel diameters revealed that OCT tends to overestimate the diameter of smaller ($< 30\mu\text{m}$) vessels in comparison to IVM. Furthermore, in both tumour and normal tissue within the window chamber, IVM consistently detected a lower vessel area than OCT, suggesting that many of the smaller vessels which were detected by OCT were not detected with IVM, particularly within tumours. Overall, OCT offered superior vessel contrast and increased depth penetration when compared to IVM. In addition, OCT was insensitive to any remaining layers of connective tissue (not removed during surgery) and was able to discern between flowing functional vessels and non-functional static vessels. Thus, once the mechanism of dilation of the smaller vessels is determined, OCT is capable of providing an accurate profile of the microcirculation.

OCIS codes: (170.3880) Medical and biological imaging; (110.4500) Optical coherence tomography; (110.0180) Microscopy; (170.2655) Functional monitoring and imaging.

5.1 Introduction

5.1.1 Background

In recent years, angiographic optical coherence tomography (OCT) has emerged as an effective modality for morphological imaging of the *in-vivo* microcirculation[1]. OCT is an optical modality, capable of capturing 3-dimensional tomographic datasets at a high spatial resolution over a depth range of 1-2mm. Measures of interframe speckle decorrelation between frames captured at the same spatial location are extracted and utilised to generate information pertaining to the depth and shape of local microvessels[2], [3]. Due to its unique combination of imaging speed, resolution and penetration depth, OCT has found direct clinical application in numerous fields. Notably within ophthalmology, where its non-invasive nature makes angiographic OCT an appealing alternative to the traditional gold standard fluorescein/indocyanine green angiography techniques[4] for the study of age-related macular degeneration[5]–[7], diabetic retinopathy[8], [9] and glaucoma[9]. OCT is also widely used in dermatology for the diagnosis and monitoring of non-melanoma skin cancer[10], [11], atopic-dermatitis[12] and wound-healing[13]. Numerous additional applications of OCT angiography have been developed within both neuroscience[14] and oncology[15].

Despite widespread application of the technique, there are few verification studies correlating the detected OCT vessel characteristics to other imaging modalities. Vakoc *et al* performed a direct comparison between a multiphoton microscopy (MPM) image and a corresponding optical frequency domain image (OFDI) by directly co-registering the images[16]. From this it was found that morphological measurements correlated well between the modalities for vessel diameters greater than $12\mu\text{m}$ ($r = 0.87$), however vessels diameters smaller than $12\mu\text{m}$ were overestimated by OFDI, resulting in poor correlation ($r = 0.36$)[16]. Another study by Inoue *et al* compared angiographic OCT images of ophthalmic type-1 neovascularisation with the gold-standard fluorescein angiography, highlighting that certain areas of neovascularisation were visible to OCT but not to fluorescein angiography[17]. However, the datasets were not co-registered to correlate morphological information.

Falavarjani *et al* used two-independent observers to manually measure the vessel diameters of 312 individual vessels within the human retina, directly comparing between registered OCT and colour-fundus images[18]. Overall vessel diameters were overestimated by OCT (mean difference = $17.6 \pm 1.5\mu\text{m}$, $p < 0.001$) with smaller vessels ($< 94.5\mu\text{m}$) being more affected by this dilatatory effect than larger vessels ($19.3 \pm 16.3\mu\text{m}$ compared to $15.6 \pm 14.4\mu\text{m}$ respectively, $p = 0.02$)[18]. In general, it appears clear the angiographic OCT measurements of morphological vessel metrics are not entirely accurate when compared to other optical modalities, thus detailed knowledge of such differences will allow necessary adjustments to be used when comparing OCT derived metrics.

5.1.2 Intravital Light Microscopy

Intravital microscopy (IVM) refers to a subset of microscopy which is usually performed through an attached window preparation. One such technique, termed the dorsal skin-fold window chamber (DSWC) model involves the surgical removal of a skin flap and underlying connective tissue/fat from the dorsum of a mouse such that optical clarity to the underlying circulation is achieved[19] (Fig. 5.1). The skin is then replaced with a transparent glass cover-slip, allowing conventional light microscopy to be performed longitudinally. The DSWC technique combined with IVM has proven to be an invaluable tool for the longitudinal study of tumour angiogenesis[20] and in the assessment of tumour growth characteristics[15], [21]. In addition, numerous angiographic OCT studies have utilised the DSWC model for vascular visualisation[16], [22]–[25] making it an excellent candidate for performing vessel metric validation studies.

Note: IVM refers to the microscopy of tissue imaged through a window (Usually glass). As such it can refer to a wide array of imaging modalities and techniques. For the purposes of this work IVM will refer to back-illuminated white light intra-vital microscopy performed through the DSWC model.

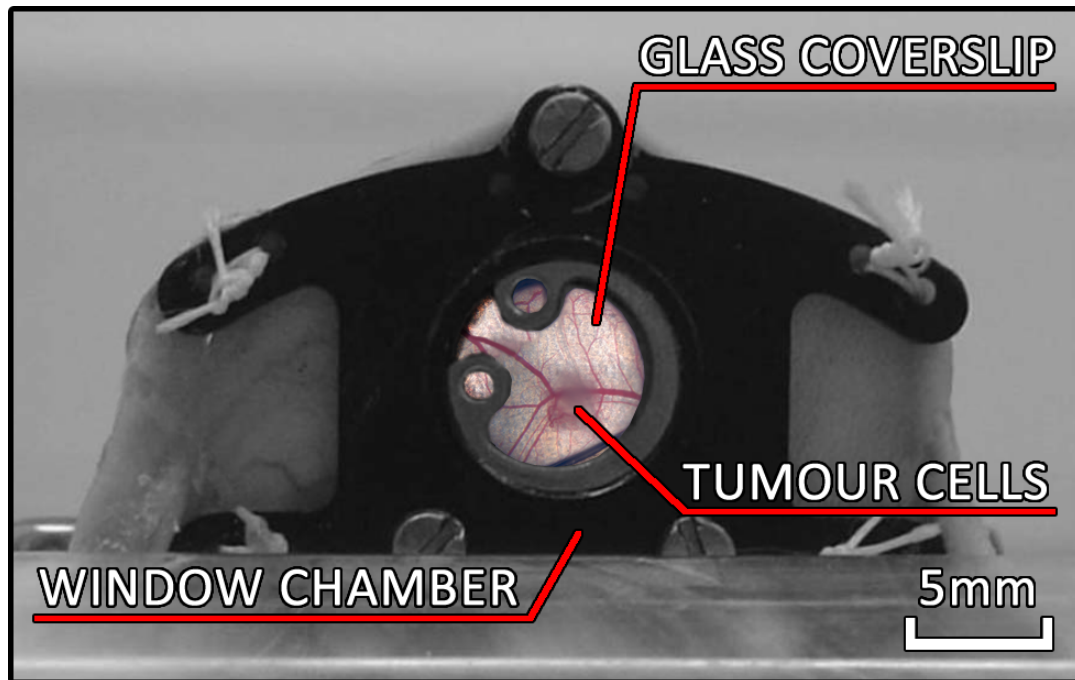


FIGURE 5.1: The DSWC model attached to the dorsum of a mouse. A circular region of skin is surgically removed from dorsal skin flap and a double-sided aluminium frame is attached to maintain mechanical stability. Fibrosarcoma tumour cells are placed on the centre of the exposed fascial surface and the chamber is then filled with saline and sealed using a glass coverslip, the coverslip is held in place using a metal O-ring.

5.1.3 Study aim

In this work, we aimed to simultaneously acquire both OCT and IVM images of DSWCs, allowing cross-correlation of vessel metrics to be performed between the modalities. Both normal baseline vasculature and the vasculature within fibrosarcoma tumours over-expressing differing isoforms of VEGF (120,188) were used for analysis. The study set out to assess the following hypotheses:

1. Vasculature that is *concurrently* visible through both OCT and IVM is *accurately* represented by OCT at all scales.
 2. All vasculature that is detected with IVM is also visible to OCT.
 3. There is a discernible difference in vessel morphology between tumours over-expressing differing VEGF isoforms (120,188).
-

While angiographic OCT does not necessarily require the use of a window chamber preparation to capture vascular morphology[26], light-microscopy is unable to penetrate through the upper layer of skin without the intra-vital window preparation. Thus in order to correlate vessel metrics, the DSWC is required.

5.2 Methods

All animal experiments were conducted according to the United Kingdom Animals (Scientific Procedures) Act 1986 (UK Home Office Project License PPL40/3649) and with local University of Sheffield ethical approval.

5.2.1 DSWC surgery

To enable direct comparison between simultaneously acquired IVM and OCT images of both regular and tumourous vasculature, DSWCs were surgically implanted into the rear dorsum of male severe combined immunodeficiency (SCID) mice (n=25), aged 12-16 weeks (25-30g). The technique is based on methodology described by Papenfuss *et al*[27] and detailed previously[28]. Briefly, prior to surgery, the mice were anaesthetized using a 1:1:2 mixture of Hypnorm (fentanyl citrate and flunarizine), Hypnovel (midazolam) and water, administered via intraperitoneal (IP) injection (5.3 μ l/g). Due to the relative optical transparency of mouse skin, the epidermal/-panniculus muscular layers were only removed from one side of the dorsal skin flap. An aluminium window chamber (total weight \approx 2g) was then implanted (Fig. 5.1).

A fibrosarcoma tumour fragment (cells pre-prepared as spheroids) consisting of cells expressing only the VEGF120 isoform (designated fs120) or the VEGF188 isoform (designated fs188) was placed on the exposed fascial surface. The entire chamber was then filled with saline and sealed using a transparent glass coverslip, facilitating optical access to the growing tumour while also providing mechanical stability and protection. To aid in recovery, buprenorphine (Vetergesic[®]) was administered as an analgesic ($3.3\mu\text{l/g}$) and antibiotic cream was applied around the edge of the window chamber. Following surgery, mice were housed singly in a warm room ($28\text{-}30^{\circ}\text{C}$) until imaging was required.

5.2.2 Imaging protocol

Imaging of the window chambers commenced 4 days post-surgery and was repeated every 1-2 days for up to 14 days depending on the observed tumour growth rate, with both IVM and OCT imaging being performed consecutively. Mice were restrained, unanaesthetised in a jig designed specifically for OCT/IVM imaging (Figs. 5.2 and 5.3).

IVM imaging

IVM imaging was performed first, with the jig being aligned to a back illuminated microscopy stage (Fig. 5.2). Transmitted-light IVM images were then acquired from the DSWC. Due to the limited FOV of these images at 10x magnification, three tiled images were acquired consecutively from the top, middle and bottom of the chamber and mosaicked together using a previously described stitching algorithm[29], providing a full view of the window chamber which could be compared to OCT.

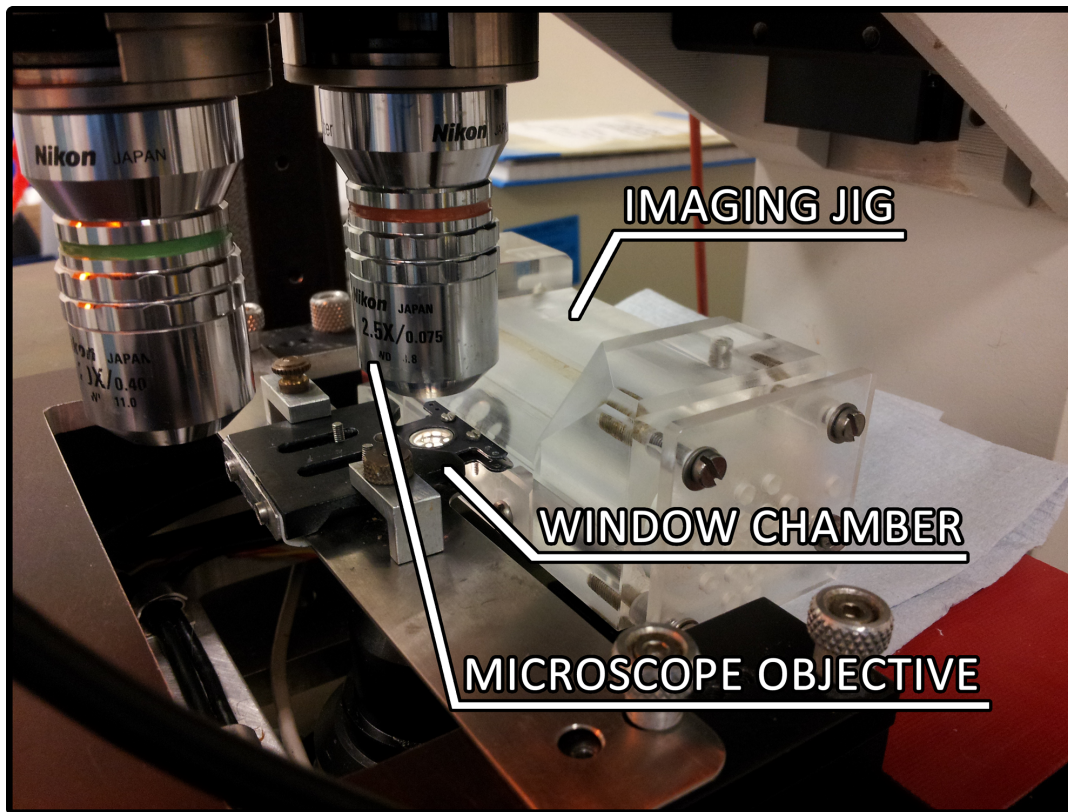


FIGURE 5.2: Imaging setup for transmitted light IVM of DSWCs, images were captured at 10x magnification and mosaicked together in software to form a full-field image of the DSWC.

OCT imaging

Following IVM imaging, the jig was fixed to a translational (x-y) microscope stage and the mobile OCT imaging probe was positioned using a clamp (Fig. 5.3). All OCT imaging for this study was performed using a commercial CE-marked multi-beam OCT system (Vivosight®, Michelson Diagnostics Ltd, Orpington, Kent, UK). This utilises a 20 kHz swept-source 1305nm Axsun laser ($\Delta\lambda = 147\text{nm}$), achieving a resolution of approximately $5\mu\text{m}$ axially and $7.5\mu\text{m}$ laterally (In tissue). For the purposes of this study, an $8\times 8\text{mm}$ area was scanned by stepping the beam in $10\mu\text{m}$ increments in the y-direction, 10-repeat scans were acquired at each spatial (y) location and used to calculate the angiographic speckle-variance signal using a previously described methodology[12], [30]. Each resulting 3D angiographic dataset was $8\times 8\times 2\text{mm}$ in size ($800\times 800\times 512$ pixels) and took approximately 6 minutes to acquire.

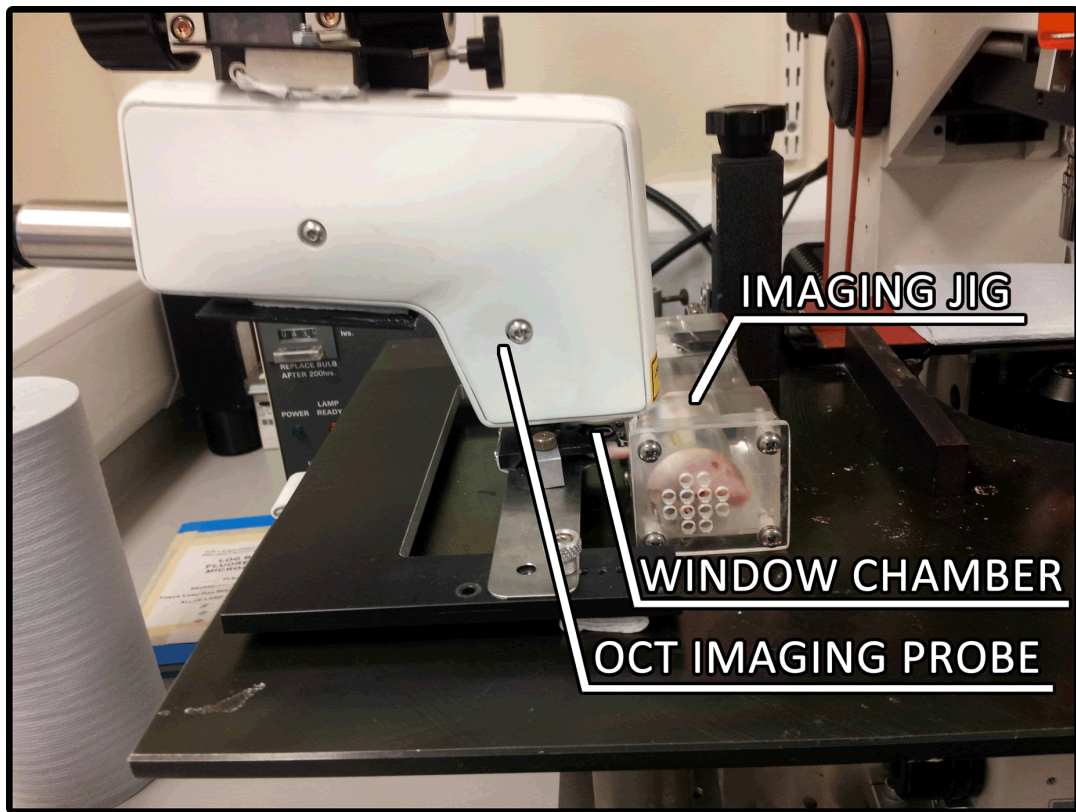


FIGURE 5.3: Imaging setup for OCT imaging of DSWCs

A MATLAB (R2017b - MathWorks) algorithm was developed in order to remove the influence of any curvature in the glass coverslip from the window chamber with respect to the OCT imaging beam and subsequent data generation. Automatic detection of the coverslip was deemed impractical due to reflective artefacts and dark regions where the overlaying metal frame blocked the OCT beam. To rectify this, manual selection of the coverslip depth was performed at 17-points across the window as shown in Fig. 5.4A, cubic interpolation was then performed between these points in order to detect the surface curvature of the coverslip, which was then flattened by axially shifting each A-scan.

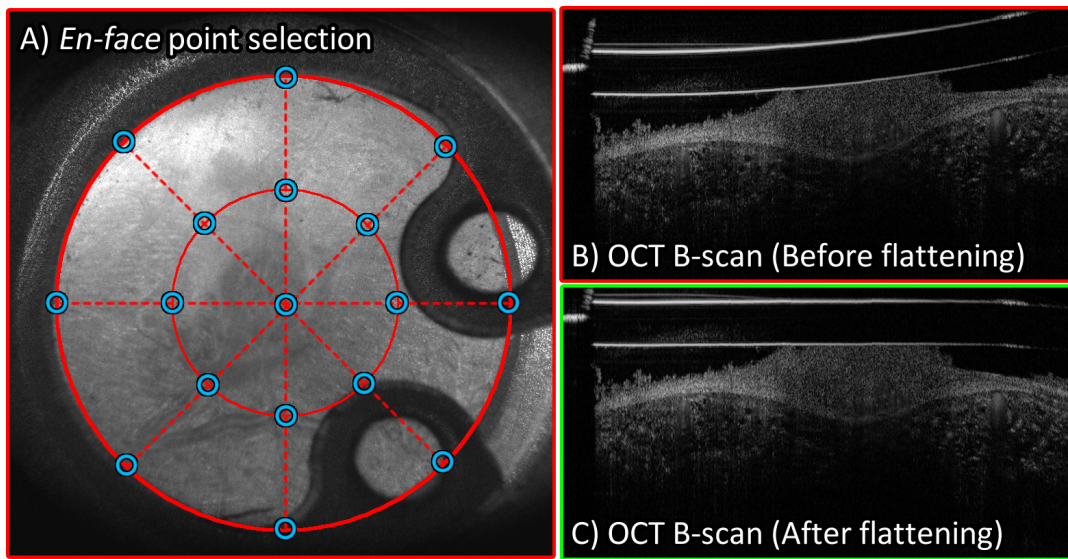


FIGURE 5.4: A) *En-face* point selection. Blue circles represent points where the coverslip depth is manually selected. 2D cubic interpolation is then used to find the surface curvature used for flattening. B) OCT B-scan before the flattening operation. C) OCT B-scan following the flattening operation.

Once the curvature of the glass coverslip had been removed, angiographic OCT images were produced by performing a mean-intensity projection over a depth range of $20 - 1250\mu\text{m}$ beneath the glass coverslip. Depth encoded images were also produced by capturing mean-intensity projections over the depths: $20 - 430\mu\text{m}$, $430 - 840\mu\text{m}$ and $840 - 1250\mu\text{m}$ and mapping these to the R,G and B channels of an RGB colour image. Due to the shadowing artefact that is inherent to angiographic OCT[31], shallow vessels have a presence in all colour channels (RGB), while a deeper vessel may only appear in the deeper colour channels (G or B).

5.2.3 Correlation of IVM and OCT datasets

Following the image acquisition steps detailed in Sec. 5.2.2 the resulting IVM and OCT datasets were misaligned and not suitable for direct comparison, thus image registration was performed in order to spatially align the images from each modality. Fig. 5.5 outlines this process. Firstly the IVM image (Fig. 5.5A) was processed using a contrast limited adaptive histogram equalization algorithm (CLAHE)[32],

which performed histogram equalization on small (127x127 pixel) blocks of the image, limiting the contrast of each block such that noise was not excessively amplified (Fig. 5.5B). For IVM, this step enhanced the contrast of the visible vessels against the underlying fascial surface. It was not necessary to perform CLAHE on the angiographic OCT images (Fig. 5.5C) due to their inherent flow sensitivity.

Registration was performed using an elastic vector-spline regularisation technique (bUnwarpJ - ImageJ[33]) which used manually defined landmarks on each image as a guideline before refining the estimate. A fine grid size was used for the deformation field, since translational, scaling and rotational offsets were expected together with smaller internal deformations between the modalities (Fig. 5.5D). The detected deformation field was then applied to the IVM image in order to align it with the OCT image (Fig. 5.5E). Fig. 5.5F shows a combined visualisation of the two modalities, where high signal intensity for OCT is shown in magenta, and high signal intensity for IVM is shown in green. Where both modalities show high signal intensity the colouration is white. Here the white colouration within the major visible vessels suggests that registration between the two modalities was successful.

The elastic image registration algorithm used here (bUnwarpJ[33]) minimises an energy function with weights (w) given by:

$$E = w_i E_{img} + w_\mu E_\mu + w_c E_{cons}$$

Here E_{img} referred to dissimilarity between the source and target images, E_μ referred to landmark constraints (Based on manually inputted landmarks across the images - i.e points that line up by eye) and E_{cons} was a consistency weight term that accounted for geometrical consistency between the deformation in both directions. Weights w_i and w_μ were set to 1 (Indicating equal weighting for the image/landmarks) and w_c was set to 10 empirically. The optimization is conducted as a Levenberg-Marquardt minimization which is further refined by a Broyden-Fletcher-Goldfarb-Shanno (BFGS) estimate of the local Hessian of the goal function[33], [34].

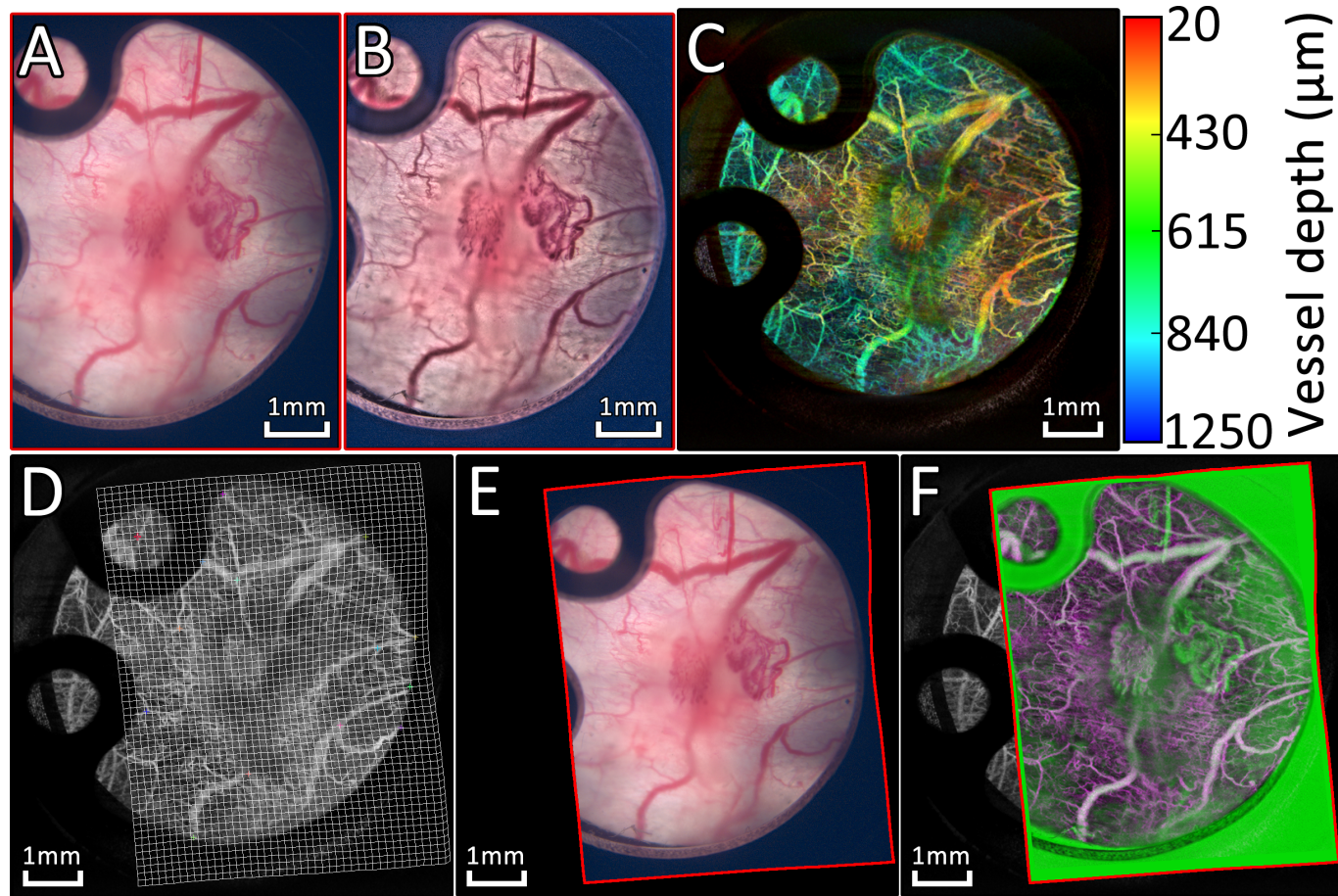


FIGURE 5.5: A) *En-face* IVM image of a DSWC 4-days post-surgery. B) The result of CLAHE being applied to the IVM image, improving vessel contrast against the pink fascial background. C) *En-face* depth resolved OCT image of the DSWC. D) The detected IVM deformation field (Red box) overlaid onto the OCT image, this deformation field was calculated using landmark-based vector-spline regularisation to register the two images together. E) The result of applying the deformation field to the IVM image. F) Overlay comparison of the two modalities following registration. High signal intensity with OCT appears magenta, high signal intensity with IVM appears green, high signal intensity with both appears white. Since the major visible vessels appear white on this combined comparison, it suggests that registration is successful and that corresponding vessels are now spatially aligned between modalities.

5.2.4 Skeletonisation of IVM and OCT datasets

To extract meaningful quantitative metrics from each image it was necessary to skeletonise the detected vasculature for both the OCT and IVM datasets. For this, the registered IVM image was converted into a grayscale format by eliminating hue and saturation information whilst retaining the luminance. The grayscale IVM image was then inverted such that vasculature had a high signal intensity against a dark background, similar to the angiographic OCT images. Following this, the same steps were applied to both the OCT and IVM images in order to first binarise the vessels and generate a vessel skeleton, then quantify the skeleton to extract metrics. Briefly, the images were median filtered using a 3x3 kernel and processed using a Hessian filtering algorithm which highlights the "vesselness" of an area through consideration of the eigen values of the local Hessian matrix[35]. This process was repeated over a range of expected vessel scales, from $10\mu m \rightarrow 500\mu m$, with the highest detection value across all scales being used for analysis. The resulting Hessian filtered images then contained values close to 1 for regions with high vascularity and 0 for regions devoid of vasculature, which was multiplied with the original images in order to suppress background noise. An adaptive thresholding algorithm was then applied in order to binarise each image[36], this algorithm takes into account localised variations in background illumination and thus was ideal for the skeletonisation of the IVM images, given that they often had shadows present or localised variations in light intensity.

Once binarised and skeletonised, the skeleton was broken into segments by removing bifurcation points from the network. Bifurcation points are the areas where a vessel splits into two or more vessels, so the removal of the bifurcation point where the split occurs essentially segments the network into smaller, non-connected vessel segments. Vessel diameters were calculated for each individual segment by doubling the average perpendicular distance from the skeleton to the edge of binarised vessel region. "Matching" vessel segments which were concurrently visible on both OCT and IVM were identified by considering skeleton sections with an overlap of at least 30-pixels in area, the diameter of both matched segments was then stored and

used in Fig. 5.10. Average vessel diameter (μm) was calculated by averaging the segment diameters across the entire DSWC. Vessel area (%) was calculated by dividing the area of the binarised image by the total area. Lastly, the fractal dimension of the skeleton was calculated using the box-counting method[37], which returns a value between 0 and 3, with lower values being indicative of a more regular network.

To improve bifurcation detection, the skeleton image was first thinned using a previously described algorithm[38]. Briefly, this removed both "corner pixels" as well as small spur pixels from the skeleton (See examples 1 and 2 below) which would result in the incorrect detection of bifurcations.

$$Ex_1 : \begin{bmatrix} 0 & 0 & 0 & 0 & 0 \\ 0 & 0 & 0 & 0 & 0 \\ 1 & 1 & 1 & 1 & 1 \\ 0 & 0 & 1 & 0 & 0 \\ 0 & 0 & 0 & 0 & 0 \end{bmatrix} \Rightarrow \begin{bmatrix} 0 & 0 & 0 & 0 & 0 \\ 0 & 0 & 0 & 0 & 0 \\ 1 & 1 & 1 & 1 & 1 \\ 0 & 0 & 0 & 0 & 0 \\ 0 & 0 & 0 & 0 & 0 \end{bmatrix} \quad Ex_2 : \begin{bmatrix} 0 & 0 & 0 & 0 & 0 \\ 1 & 1 & 1 & 0 & 0 \\ 0 & 0 & 1 & 0 & 0 \\ 0 & 0 & 1 & 1 & 1 \\ 0 & 0 & 0 & 0 & 0 \end{bmatrix} \Rightarrow \begin{bmatrix} 0 & 0 & 0 & 0 & 0 \\ 1 & 1 & 0 & 0 & 0 \\ 0 & 0 & 1 & 0 & 0 \\ 0 & 0 & 0 & 1 & 1 \\ 0 & 0 & 0 & 0 & 0 \end{bmatrix}$$

Skeleton bifurcation points were then detected and removed using the 'branchpoints' operation within MATLAB's *bwmorph.m* function combined with the *imdilate.m* function (Using a disk shaped structuring element with a radius of 1-pixel). For example, a binary image (A) consisting of a simple cross (+) would have detected branchpoints (B) which would be dilated to produce (C):

$$A(x,y) = \begin{bmatrix} 0 & 0 & 1 & 0 & 0 \\ 0 & 0 & 1 & 0 & 0 \\ 1 & 1 & 1 & 1 & 1 \\ 0 & 0 & 1 & 0 & 0 \\ 0 & 0 & 1 & 0 & 0 \end{bmatrix} \quad B(x,y) = \begin{bmatrix} 0 & 0 & 0 & 0 & 0 \\ 0 & 0 & 0 & 0 & 0 \\ 0 & 0 & 1 & 0 & 0 \\ 0 & 0 & 0 & 0 & 0 \\ 0 & 0 & 0 & 0 & 0 \end{bmatrix} \quad C(x,y) = \begin{bmatrix} 0 & 0 & 0 & 0 & 0 \\ 0 & 1 & 1 & 1 & 0 \\ 0 & 1 & 1 & 1 & 0 \\ 0 & 1 & 1 & 1 & 0 \\ 0 & 0 & 0 & 0 & 0 \end{bmatrix}$$

The segmented skeleton was then produced by multiplying the inverse of the dilated branchpoints ($1 - C$) with the original skeleton (A), leaving each individual vessel segment isolated from others:

$$A(x,y) * (1 - C(x,y)) = \begin{bmatrix} 0 & 0 & 1 & 0 & 0 \\ 0 & 0 & 0 & 0 & 0 \\ 1 & 0 & 0 & 0 & 1 \\ 0 & 0 & 0 & 0 & 0 \\ 0 & 0 & 1 & 0 & 0 \end{bmatrix}$$

More advanced methods of tracking the vascular tree have recently been proposed (e.g using machine learning algorithms[39]) which do not require prior skeletonisation or binarisation of the vessels, and thus are likely to be more accurate than the technique described here.

5.3 Results and discussion

5.3.1 Qualitative comparison between OCT and IVM

Fig. 5.6 shows the depth resolved OCT images alongside the registered IVM images in a selection of DSWCs containing baseline vasculature, prior to any tumour growth. Compared to the dense, disorganised and narrow circulation found in tumours, baseline vasculature offers a wide range of vessel scales and tends to be more sparse. Qualitatively estimated (and subjectively), the larger vessels within each chamber appear to have been accurately captured with angiographic OCT, as evidenced by a strong visual correlation between the OCT and IVM images. The contrast of smaller vessels was vastly improved with OCT, likely due to a low level of local haematocrit within these vessels causing the absorption based IVM to lack contrast against the pink fascial background. Fig. 5.6E shows a zoomed section at the location of the red star on Fig. 5.6A, with OCT; a thin superficial vessel is clearly visible in yellow, overlapping the larger green vessel which is deeper within the window. Comparatively, this vessel is almost completely invisible through transmitted light IVM. Furthermore the vessel appears slightly dilated with OCT, a concept which is discussed further in Sec. 5.3.2. Fig. 5.6F shows a zoomed section at the location of the blue star on Fig. 5.6C. Here a rich vascular network is visible with OCT but very few vessels can be observed through IVM. The mottled appearance of the IVM image suggests that direct-light visualization is being occluded by a layer of fatty/connective tissue which persisted following surgery, comparatively OCT appears minimally affected by this.

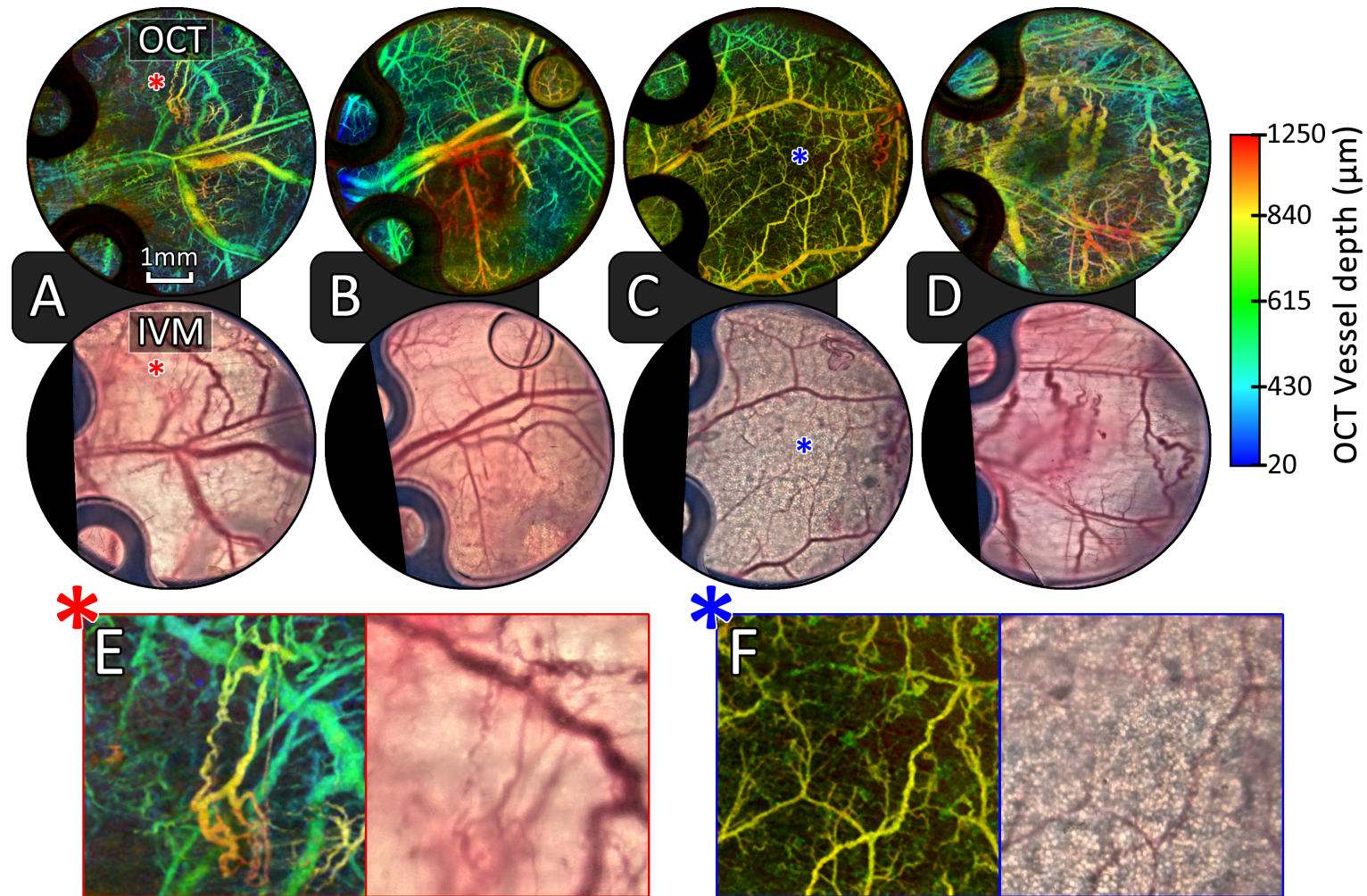


FIGURE 5.6: A-D) *En-face* OCT (Top) and IVM (Bottom) images of non-tumourous (baseline) vasculature within four different DSWCs. E) Zoomed FOV at the location of the red star on A. F) Zoomed FOV at the location of the blue star on C. OCT images are in 3D (Depth projected) format.

The presence of the fatty layer in Fig. 5.6C can be verified through observation of the OCT B-scans. Here a dark mottled layer which is about $100\mu\text{m}$ thick can be seen, the appearance of which matches previous histological/OCT comparisons of the fatty hypodermis layer within murine skin[26].

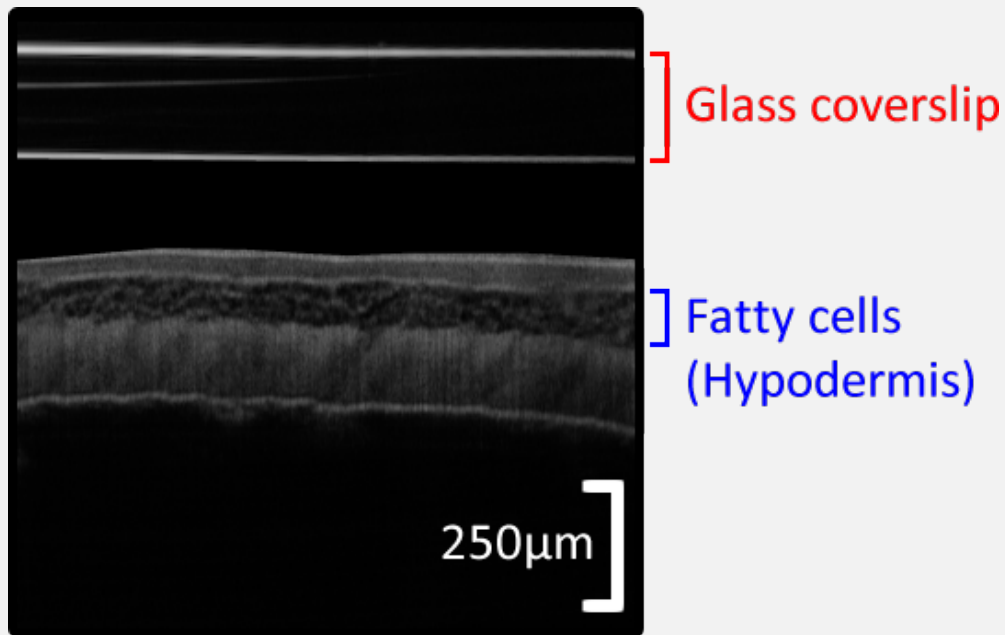


FIGURE 5.7: OCT B-scan of the tissue morphology within the window chamber from Fig. 5.6C, showing a layer of fatty cells.

Since the adipocyte cells that make up this layer are not highly scattering, they appear dark on OCT B-scans of the tissue and do not backscatter much of the incident OCT beam. As a result, angiographic OCT scans of regions with any remaining fatty or connective tissue maintain high vessel contrast while comparative IVM images of the region become rapidly degraded and potentially unusable for quantification purposes.

Two examples of OCT and IVM images captured within fully grown fibrosarcoma tumours are shown in Fig. 5.8. The tumour expressing only the VEGF-120 isoform (Fig. 5.8A/B/C - fs120) reached full size ($\approx 6\text{mm}$ diameter) 8-days post-implantation, while the tumour expressing only the VEGF-188 isoform (Fig. 5.8D/E/F - fs188) reached this size 11-days post-implantation. The current data is consistent with previous observations of these tumour types, where fs120 tumours exhibit increased proliferation and survival in comparison to fs188 tumours[40]. In addition, the unique morphologies of these tumour types previously observed with both IVM[41] and OCT[26], demonstrating that fs120 tumours tend to grow larger, more tortuous vessels than their fs188 counterparts, is again confirmed. Vessels in both the OCT and IVM images of the fs120 tumour (Fig. 5.8B/C) appear larger than those in the fs188 tumour (Fig. 5.8E/F).

Interestingly, angiographic OCT has detected a dense network of fluid that is only partially visible through transmitted light IVM, particularly at the core of each tumour. It is possible that many of the overlaying tubules which are visible on the zoomed OCT sections in Fig. 5.8B/E are actually carrying fluid that is not visible through absorption-based IVM such as vessels with a low local haematocrit or lymphatic vessels containing circulating tumour cells. For both tumour types, but most notably in the fs120 tumour, small sections of the vessel network are visible clearly with IVM, but the interlinking vessels become increasingly transparent. This effect may be a result of vasoconstriction causing high localised flow rates within the smaller vessels, the low concentrations of fast moving red blood cells then lack contrast on the IVM image, only appearing when the flow slows down and pools in the larger vessels. Another potential explanation is related to the depth of the vessels within the tissue, as the vast majority of vessels deeper than $430\mu\text{m}$ (visible as a green/blue colouration on the OCT images) are not visible on the IVM images. A visible example of this is the vertical blue vessel at $840\mu\text{m}$ depth indicated by the red star on Fig. 5.8E, which is absent from the corresponding IVM image seen on Fig. 5.8F.

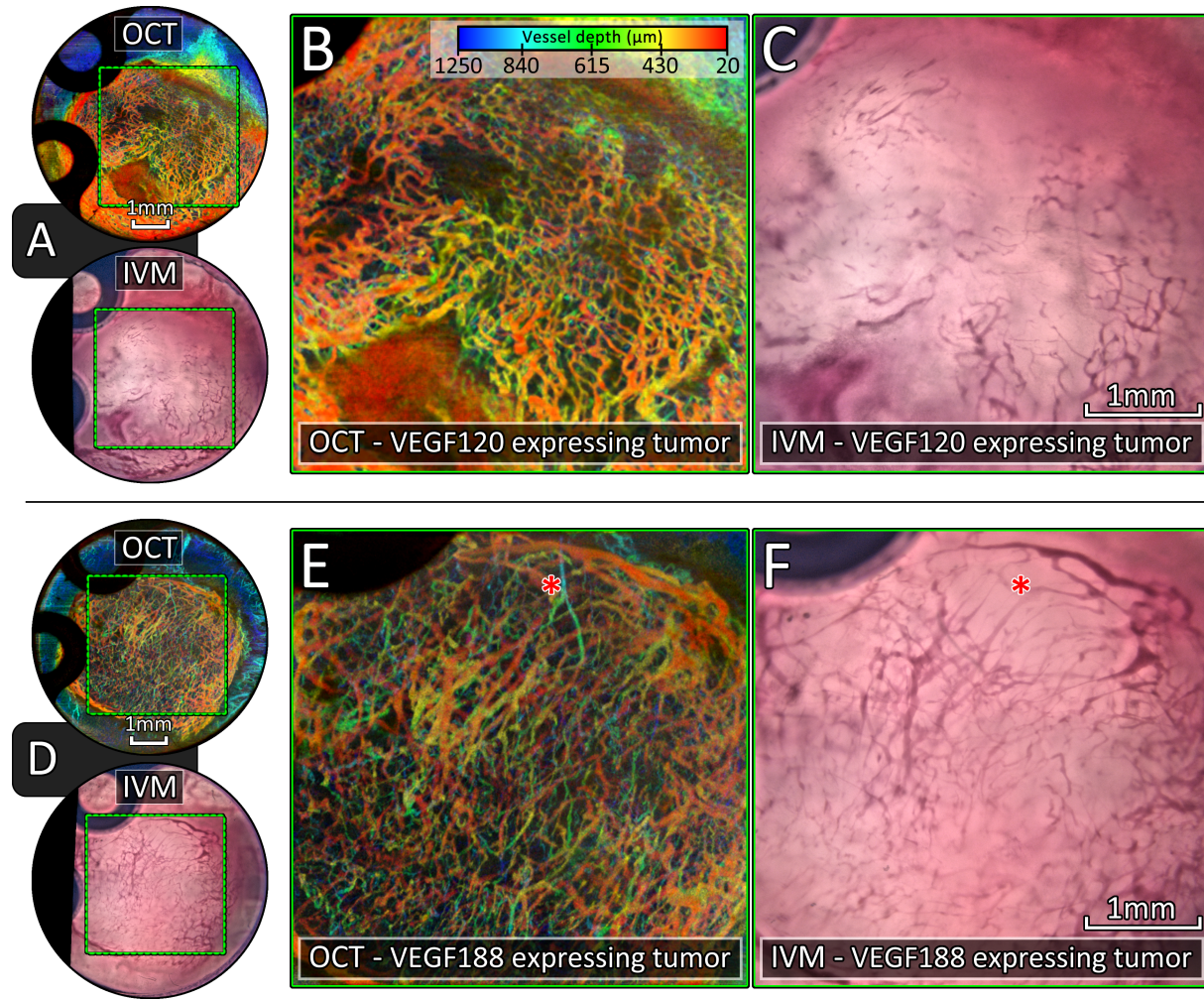


FIGURE 5.8: A) *En-face* OCT (Top) and IVM (Bottom) images of the vasculature within a fibrosarcoma tumour expressing the VEGF-120 isoform (fs120). B) Zoomed OCT image of the fs120 tumour (Green box on A). C) Zoomed IVM image of the fs120 tumour (Green box on A). D) *En-face* OCT (Top) and IVM (Bottom) images of the vasculature within a fibrosarcoma tumour expressing the VEGF-188 isoform (fs188). E) Zoomed OCT image of the fs188 tumour (Green box on D). F) Zoomed IVM image of the fs188 tumour (Green box on D). All OCT images are shown in 3D (Depth projected) format.

Fig. 5.9 shows the longitudinal progression of an fs188 tumour over a period of 8 days, the fibrosarcoma tumour fragment is clearly visible as a small dark spot close to the centre of the OCT images. The underlying vascular plexus, seen in orange on Fig. 5.9A is slowly pushed deeper into the window as the tumour grows in size, which is clearly visible due to the depth-resolved OCT images. The tumour microcirculation is first visible to both modalities 5-days post surgery (Fig. 5.9B) and steadily increases in both density and diameter over the following week. In general, across all days, visual co-registration between both modalities remains good, however the vascular sensitivity of OCT is greater, particularly in the centre of the tumour where IVM exhibits particularly poor vessel contrast. Fig. 5.9K shows a combined overlay of both modalities, with OCT mapped to a magenta colouration and IVM mapped to the green colouration. While most vessels appear white, indicating an equal level of signal from both OCT and IVM, many smaller vessels towards the centre of the tumour have a strong magenta colouration. This is evidence that OCT is exhibiting a comparably stronger signal within this region, even despite adaptive histogram equalization. The hazy green colouration around the exterior of the tumour is caused by darker shadows in the IVM images, some of which are caused by the metal O-ring (Fig. 5.1) on the rear of the window chamber, which can be seen casting a shadow through the chamber in the lower right corner of Fig. 5.9A-H. While these shadows could be removed through usage of a flow-sensitive IVM modality such as MPM or confocal fluorescence microscopy, they had minimal affect on the resulting vessel quantification described herein due to the aforementioned adaptive thresholding algorithm which was used to binarise the images for skeletonisation. This algorithm normalised the background intensity of small subsections of the image, and thus was able to account for shadowing caused by objects at the rear of the DSWC.

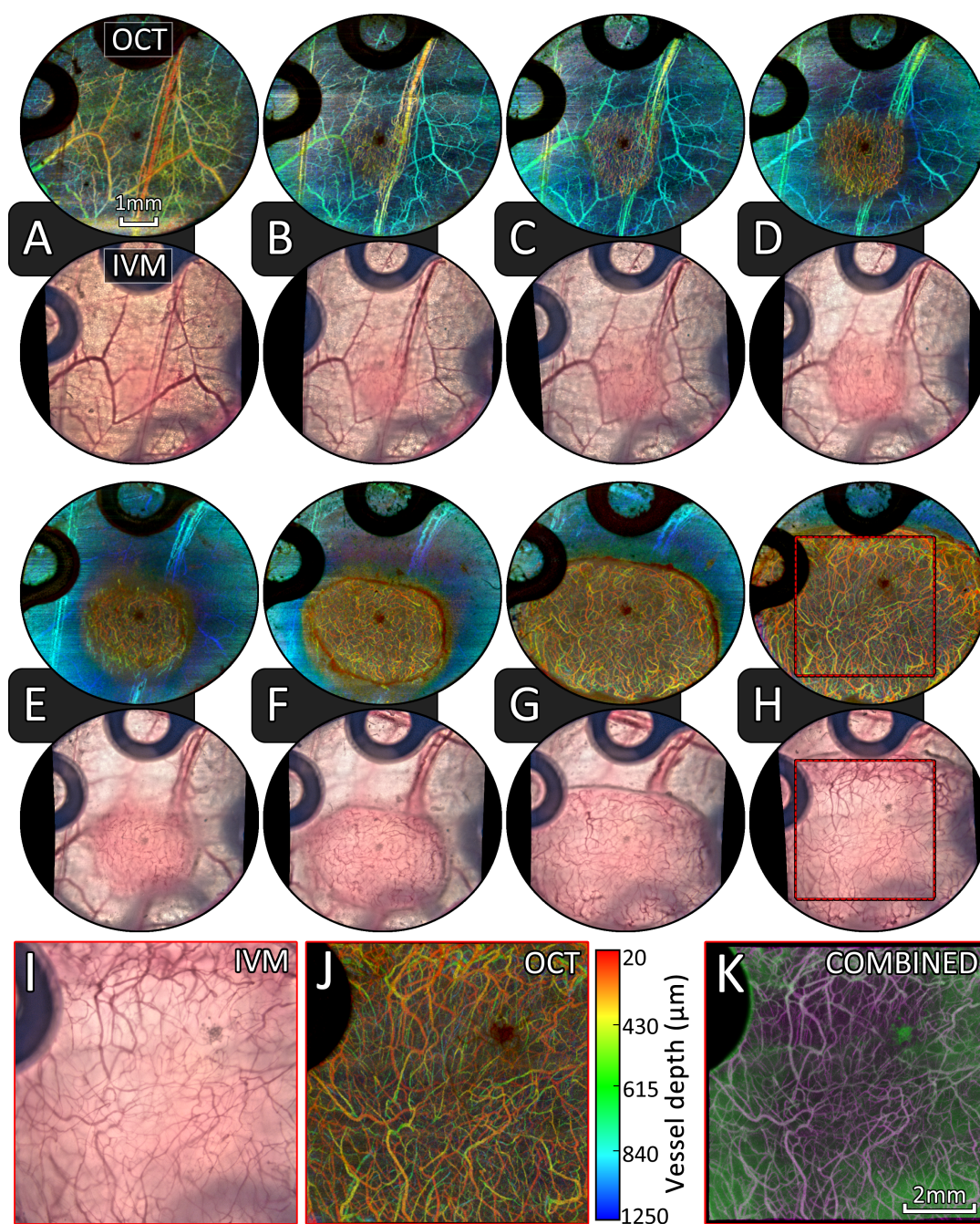


FIGURE 5.9: Longitudinal assessment of *en-face* OCT (Top) and IVM (Bottom) images of an fs188 tumour growing within a DSWC over a period of 8 days. All OCT images are shown in 3D (Depth projected) format. A-H) The window chamber as viewed by OCT and IVM 4/5/6/7/8/9/10/11 days post-implantation respectively. I-K) Zoomed FOV shown by the red dashed box on H. K) Overlay comparison of the two modalities following registration. High signal intensity with OCT appears magenta, high signal intensity with IVM appears green, high signal intensity with both appears white.

5.3.2 Quantitative comparison between OCT and IVM

Fig. 5.10 shows how the diameter of matched vessel segments varies between OCT and IVM. Vessel segments in this context are the individual vessel pieces that remain once bifurcation points (Points where one vessel splits into 2+ vessels) were removed from the complete vessel skeleton. Across all window chambers, a total of 676 vessel segments were automatically identified with sufficient overlap (30-pixels) between the modalities such that we were confident it was the same segment being measured with both modalities. The diameter of each segment was averaged along its length. The vast majority of detected vessels were small ($< 100\mu m$) due to their abundance, particularly within tumours. A 3rd order polynomial fit (Red line - Fig. 5.10) was mapped to the data in order to capture trends. Overall the correlation between measured diameters with OCT and IVM very closely matched the ideal $y = x$ line ($R^2 = 0.961$) however the data appears to deviate away from this line for vessels below $\approx 30\mu m$ in diameter as seen on the 3rd order polynomial fit ($R^2 = 0.968$).

Thus in agreement with the observations made previously[16], [18], it appears that smaller vessels are artificially dilated when observed with angiographic OCT. This effect may partially be explained as a result of spatial aliasing, given that the OCT datasets for this study were acquired with lateral spacing ($\Delta x, \Delta y$) of $10\mu m$, the Nyquist sampling criterion suggests that vessels below $20\mu m$ will be aliased and blur into neighbouring pixels, and likely become misrepresented by skeletonisation algorithms. This would explain why vessels $< \approx 30\mu m$ appear to be dilated here, while Vakoc *et al* observed a $\approx 12\mu m$ cut-off point between OCT and multiphoton microscopy (MPM) when sampling the OCT signal at $5\mu m$ intervals[16]. In this context, the cut-off point is the point at which the average measured size of vessels appeared to diverge between the modalities.

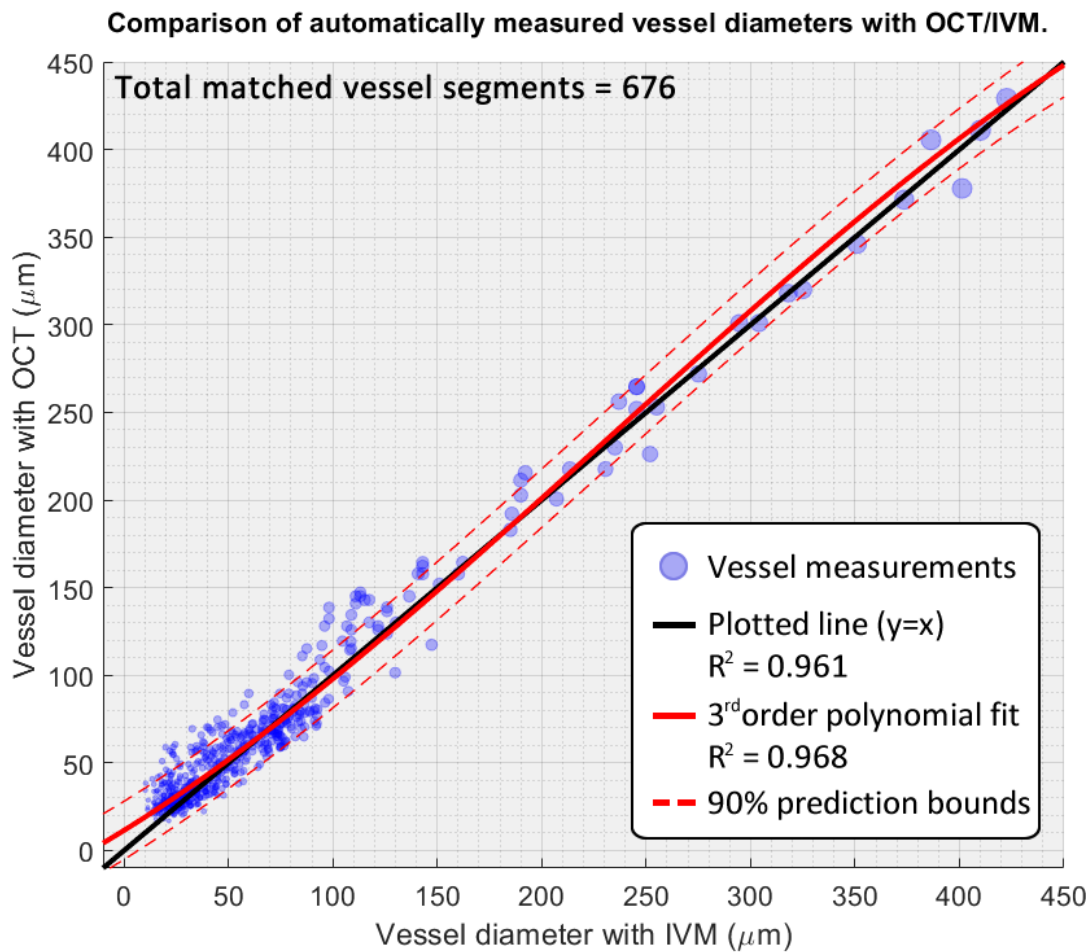


FIGURE 5.10: Scatter plot showing the difference in automatically measured vessel diameter between OCT and IVM. Each datapoint corresponds to an individual vessel segment which was concurrently visible to both modalities and detected with sufficient spatial overlap.

Fig. 5.11 shows a detailed analysis of the automatically measured vessel metrics for individual DSWCs, considering all of the vessels that were detected rather than matching vessel pairs. In total there were $n = 14$ baseline (non-tumourous) DSWC's analysed, only images captured shortly after implantation, before any tumour development had occurred were utilised for this cohort. A portion of these DSWCs went on to develop tumours, however this was deemed acceptable as the primary goal was a vascular morphology comparison between the modalities. A total of $n = 6$ DSWCs containing an fs120 tumour and $n = 8$ DSWCs containing an fs188 tumour were considered for analysis. Images showing the tumours at their largest

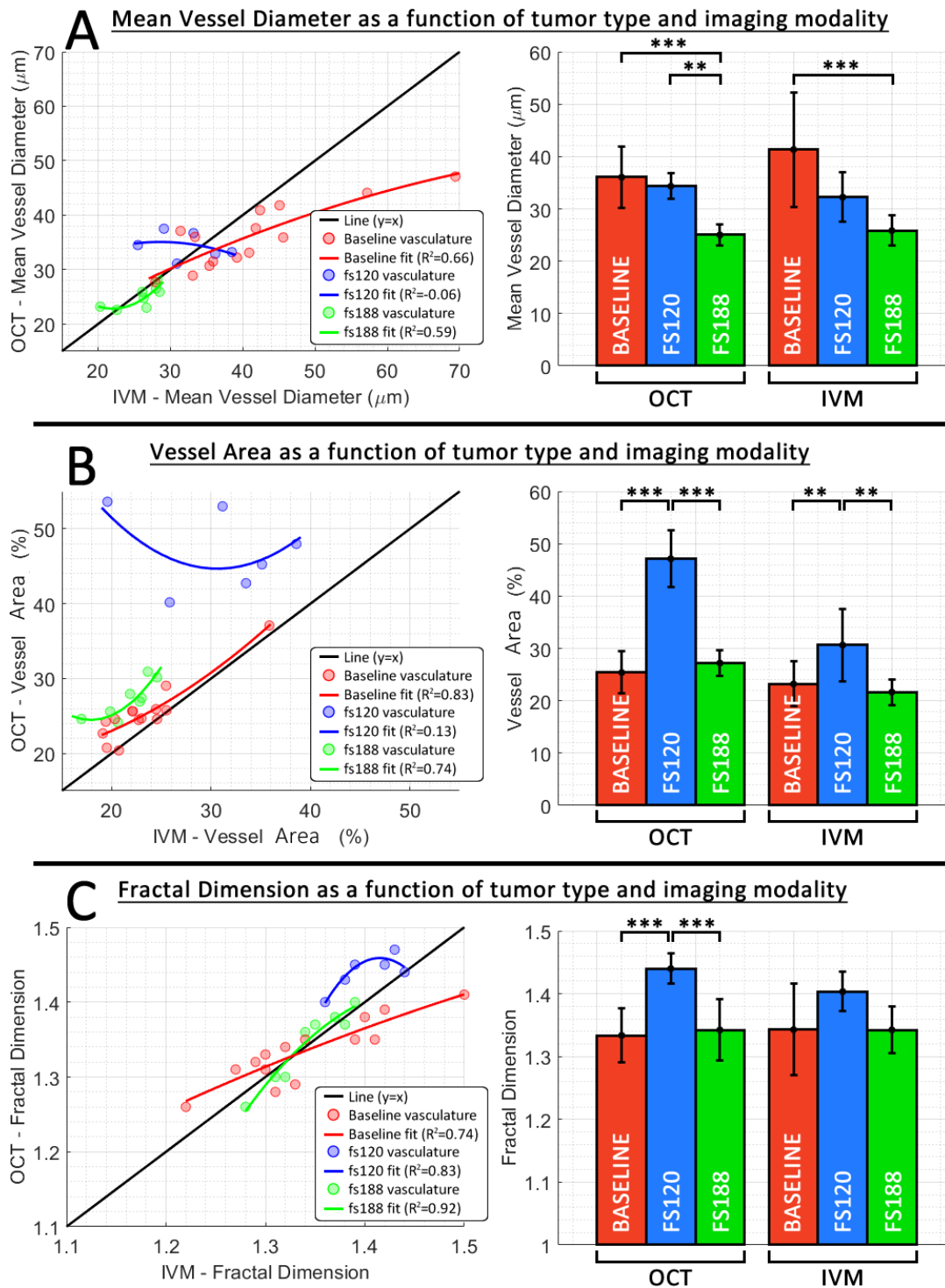


FIGURE 5.11: Graphs showing how the measured vessel metrics (A) Mean diameter, B) Vessel Area and C) Fractal dimension) varied as a function of both tumour type and imaging modality. Left side) Scatter plots where each datapoint refers to an entire DSWC. All fits were performed through optimisation of a 2nd order polynomial with R^2 values quoted. Right side) Bar charts showing the average values across all DSWCs. Bars: Mean metric value, Error bars: Standard deviation. Total number of DSWC's considered (n): Baseline=14, fs120=6, fs188=8. Stars indicate p-values as measured by a one-way ANOVA performed across each modality independently followed by Tukey's HSD (honest significant difference) test (* = $p < 0.05$, ** = $p < 0.01$, *** = $p < 0.001$).

($\approx 4 - 6\text{mm}$ diameter) were used for this purpose, however differing growth rates meant that the number of days, post-implantation was variable across the cohorts.

When considering vessel diameters (Fig. 5.11A), the majority of datapoints were situated below the $OCT = IVM$ line (Black line). This suggests that IVM is either detected more large vasculature than OCT (Inflating the mean) or is failing to detect smaller vasculature due a lack of contrast for many of the smaller vessels (as seen on Fig. 5.6E/F) which would also inflate the mean vessel diameter in comparison to OCT. To investigate this, all measurements were plotted in a histogram format (Fig. 5.12).

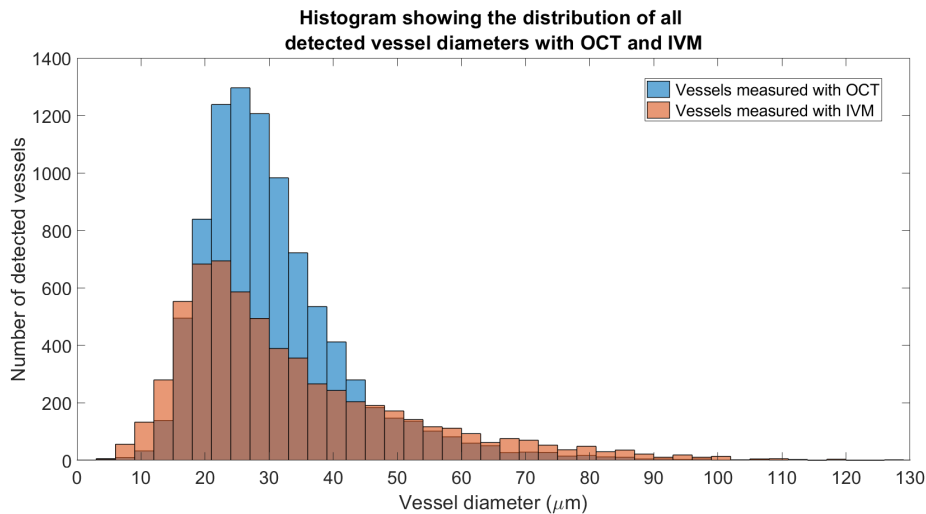


FIGURE 5.12: Histogram plot showing the number of vessels detected at each size across all DSWCs, including vessel segments which were only detected by one of the two modalities (OCT/IVM).

When observing the histogram in Fig. 5.12 it is clear that OCT is detecting a greater quantity of vessels in the $20 - 45\mu\text{m}$ range than IVM, which could explain why the mean vessel diameters are generally higher for IVM than OCT. For vessels sized below $20\mu\text{m}$, IVM detected more vessels than OCT, which is likely a result of these very small vessels appearing dilated through OCT as discussed above, and hence are being pushed into higher histogram bins. Given that these smaller vessels are far more abundant within tumours, this may explain why the tumour specific data (Green and blue lines on Fig. 5.11A) appear to be closer to the $OCT = IVM$

line than the baseline (non-tumourous) vasculature. The bar charts on the right of Fig. 5.11A reveal that for OCT, mean vessel diameter was significantly lower in the fs188 tumours compared to both the fs120 tumours ($p = 0.002$) and the non-tumourous baseline average ($p = 2.5e^{-5}$). However the difference between the fs188 and fs120 tumours did not reach significance when measured with IVM ($p = 0.34$). Overall, the visual observations made in Sec. 5.3.1 and Fig. 5.8 support the hypothesis that the fs188 tumours exhibit lower vessel diameters when compared to the fs120 variants.

The vessel area measurements shown in Fig. 5.11B support the above observations, with OCT consistently recording an increased vessel area compared to IVM, suggesting that certain vessels are not being detected by IVM but are being detected using OCT. The baseline (non-tumourous) data exhibits good correlation between modalities, with most datapoints being very close to the $OCT = IVM$ line. Thus, for datasets containing a range of vessel sizes from small to large we can expect similar measures of vessel area between OCT and IVM. Comparatively tumour vessels, particularly those in the fs120 DSWCs (Blue line) exhibit poor correlation between OCT and IVM. This is likely again due to the abundance of smaller vasculature within these tumours, if a portion of smaller vessels is unable to be detected with IVM, the visible vessel area will appear low in comparison with OCT. This is similar to the qualitative observations made in Sec. 5.3.1 and Fig. 5.8 whereby a large portion of fs120 vasculature remained undetectable with visible light IVM. The bar charts on the right show that for both OCT and IVM, a significantly higher vessel area was detected within the fs120 tumours when compared to both fs188 and non-tumourous baseline, in agreement with previous measurements[26].

Fractal dimension measurements were relatively consistent between the modalities, with most non-tumourous (baseline) and fs188 datapoints falling close to the $OCT = IVM$ line (Fig. 5.11C). A low value of fractal dimension in this context is indicative of a more regular, organized network of vasculature. Here, with OCT the fs120 tumours exhibited significantly higher fractal dimension than both the baseline and fs188 datasets, suggesting that these tumours display a disorganized and

irregular network of vessels, a phenotype that has been previously observed using both IVM[41] and subcutaneous OCT[26]. There was however, no significant difference detected between the fractal dimension of fs120 tumour vasculature and that of baseline circulation ($p = 0.10$) and fs188 tumour vasculature ($p = 0.15$), perhaps again due to the lack of connective linkages visible in the fs120 tumours with IVM, lowering the overall fractal dimensionality in comparison to OCT.

5.4 Conclusions

A direct comparison between angiographic OCT and transmitted-light IVM revealed several important nuances between the modalities. While OCT is capable of capturing and quantifying large vessels accurately, care must be taken when measuring the diameter of smaller ($< 30\mu\text{m}$) vessels due to a tendency of OCT to overestimate their inherent diameters. This effect was detected as a notable inflation of OCT vessel segment diameter between small vessels which were concurrently visible to both the OCT and IVM modalities.

Qualitative observation of the DSWCs showed that the vast majority of vessels which were visible to IVM, were also visible to OCT. We hypothesise that the few vessels which were not detected by OCT were unlikely to contain blood flow (non-functional), due to OCT being a flow sensitive modality. This may be a useful property of OCT for the study of tumour circulation, where it is often unclear whether vessels are functional or not. Comparatively, large portions of vasculature which was visible to OCT was either invisible or relatively low contrast when viewed through IVM, leading to a notable reduction in detected vessel area across most IVM DSWCs. This was particularly notable within the center of tumours, where a network of fluid flow was detectable with OCT but absent from IVM images. This lack of contrast with IVM is perhaps the reason why OCT consistently separated baseline, fs120 and fs188 tumour microcirculation with greater significance to that of IVM, for mean vessel diameter, area and the fractal dimension. Flow sensitive IVM methods, such as MPM or confocal fluorescence microscopy may rectify these limitations[15], however the requirement of a suitable fluorophore and the comparatively shallow depth penetration introduce limitations in the characterisation of tumour vessel networks.

In general, the high degree of visual correlation between IVM and OCT for all but the smallest vessels ($< 30\mu\text{m}$) provides confidence that accurate measures of the vascular network are being performed. Angiographic OCT offers a unique perspective of the microcirculation, enabling real time, non-invasive, depth-resolved angiographic imaging within tumours, providing superior vascular contrast to that

of transmitted-light IVM.

References

- [1] C. Lal and M. J. Leahy, "An Updated Review of Methods and Advancements in Microvascular Blood Flow Imaging", *Microcirculation*, vol. 23, no. 5, pp. 345–363, 2016, ISSN: 15498719. DOI: 10.1111/micc.12284 (cit. on p. 145).
- [2] J. Barton and S. Stromski, "Flow measurement without phase information in optical coherence tomography images.", *Optics express*, vol. 13, no. 14, pp. 5234–9, Jul. 2005, ISSN: 1094-4087 (cit. on p. 145).
- [3] D. M. Schwartz, J. Fingler, D. Y. Kim, R. J. Zawadzki, L. S. Morse, S. S. Park, S. E. Fraser, and J. S. Werner, "Phase-variance optical coherence tomography: A technique for noninvasive angiography", *Ophthalmology*, vol. 121, no. 1, pp. 180–187, 2014, ISSN: 01616420. DOI: 10.1016/j.optha.2013.09.002 (cit. on p. 145).
- [4] T. E. de Carlo, A. Romano, N. K. Waheed, and J. S. Duker, "A review of optical coherence tomography angiography (OCTA)", *International Journal of Retina and Vitreous*, vol. 1, no. 1, p. 5, 2015, ISSN: 2056-9920. DOI: 10.1186/s40942-015-0005-8 (cit. on p. 145).
- [5] Y. Jia, S. T. Bailey, D. J. Wilson, O. Tan, M. L. Klein, C. J. Flaxel, B. Potsaid, J. J. Liu, C. D. Lu, M. F. Kraus, J. G. Fujimoto, and D. Huang, "Quantitative Optical Coherence Tomography Angiography of Choroidal Neovascularization in Age-Related Macular Degeneration", *Ophthalmology*, vol. 121, no. 7, pp. 1435–1444, Jul. 2014, ISSN: 01616420. DOI: 10.1016/j.optha.2014.01.034 (cit. on p. 145).
- [6] T. E. de Carlo, M. A. Bonini Filho, A. T. Chin, M. Adhi, D. Ferrara, C. R. Baumal, A. J. Witkin, E. Reichel, J. S. Duker, and N. K. Waheed, "Spectral-Domain

- Optical Coherence Tomography Angiography of Choroidal Neovascularization", *Ophthalmology*, vol. 122, no. 6, pp. 1228–1238, Jun. 2015, ISSN: 01616420. DOI: 10.1016/j.opthta.2015.01.029 (cit. on p. 145).
- [7] E. Moulton, W. Choi, N. K. Waheed, M. Adhi, B. Lee, C. D. Lu, V. Jayaraman, B. Potsaid, P. J. Rosenfeld, J. S. Duker, and J. G. Fujimoto, "Ultrahigh-Speed Swept-Source OCT Angiography in Exudative AMD", *Ophthalmic Surgery, Lasers and Imaging Retina*, vol. 45, no. 6, pp. 496–505, Nov. 2014, ISSN: 2325-8160. DOI: 10.3928/23258160-20141118-03 (cit. on p. 145).
- [8] J. Lee and R. Rosen, "Optical Coherence Tomography Angiography in Diabetes", *Current Diabetes Reports*, vol. 16, no. 12, p. 123, Dec. 2016, ISSN: 1534-4827. DOI: 10.1007/s11892-016-0811-x (cit. on p. 145).
- [9] J. M. B. de Barros Garcia, D. L. C. Isaac, and M. Avila, "Diabetic retinopathy and OCT angiography: clinical findings and future perspectives", *International Journal of Retina and Vitreous*, vol. 3, no. 1, p. 14, Dec. 2017, ISSN: 2056-9920. DOI: 10.1186/s40942-017-0062-2 (cit. on p. 145).
- [10] M. Ulrich, L. Themstrup, N. De Carvalho, M. Manfredi, C. Grana, S. Ciardo, R. Kästle, J. Holmes, R. Whitehead, G. B. Jemec, G. Pellacani, and J. Welzel, "Dynamic Optical Coherence Tomography in Dermatology", *Dermatology*, vol. 232, no. 3, pp. 298–311, 2016, ISSN: 14219832. DOI: 10.1159/000444706 (cit. on p. 145).
- [11] O. Markowitz, M. Schwartz, S. Minhas, and D. M. Siegel, "Speckle-variance optical coherence tomography: a novel approach to skin cancer characterization using vascular patterns.", *Dermatology online journal*, vol. 22, no. 4, Apr. 2016, ISSN: 1087-2108 (cit. on p. 145).
- [12] R. A. Byers, R. Maiti, S. G. Danby, E. J. Pang, B. Mitchell, M. J. Carr, R. Lewis, M. J. Cork, and S. J. Matcher, "Characterizing the microcirculation of atopic dermatitis using angiographic optical coherence tomography", B. Choi, H. Zeng, and N. Kollias, Eds., International Society for Optics and Photonics, Feb. 2017, p. 100370V. DOI: 10.1117/12.2252407 (cit. on pp. 145, 150).

- [13] U. Baran, W. Choi, and R. Wang, "Towards the use of OCT angiography in clinical dermatology", *Progress in Biomedical Optics and Imaging - Proceedings of SPIE*, vol. 9689, no. February 2016, 2016, ISSN: 16057422. DOI: 10.1117/12.2214493 (cit. on p. 145).
- [14] U. Baran and R. K. Wang, "Review of optical coherence tomography based angiography in neuroscience", *Neurophotonics*, vol. 3, no. 1, p. 010902, 2016, ISSN: 2329-423X. DOI: 10.1117/1.NPh.3.1.010902 (cit. on p. 145).
- [15] S. J. Lunt, C. Gray, C. C. Reyes-Aldasoro, S. J. Matcher, and G. M. Tozer, "Application of intravital microscopy in studies of tumor microcirculation", *Journal of Biomedical Optics*, vol. 15, no. 1, p. 011113, 2010, ISSN: 10833668. DOI: 10.1117/1.3281674 (cit. on pp. 145–146, 171).
- [16] B. J. Vakoc, R. M. Lanning, J. A. Tyrrell, T. P. Padera, L. A. Bartlett, T. Stylianopoulos, L. L. Munn, G. J. Tearney, D. Fukumura, R. K. Jain, and B. E. Bouma, "Three-dimensional microscopy of the tumor microenvironment in vivo using optical frequency domain imaging", *Nature Medicine*, vol. 15, no. 10, pp. 1219–1223, 2009, ISSN: 1078-8956. DOI: 10.1038/nm.1971. arXiv: NIHMS150003 (cit. on pp. 145–146, 165).
- [17] M. Inoue, J. J. Jung, C. Balaratnasingam, K. K. Dansingani, E. Dhrami-Gavazi, M. Suzuki, T. E. de Carlo, A. Shahlaee, M. A. Klufas, A. El Maftouhi, J. S. Duker, A. C. Ho, M. Q.-E. Maftouhi, D. Sarraf, and K. B. Freund, "A Comparison Between Optical Coherence Tomography Angiography and Fluorescein Angiography for the Imaging of Type 1 Neovascularization", *Investigative Ophthalmology & Visual Science*, vol. 57, no. 9, OCT314, 2016, ISSN: 1552-5783. DOI: 10.1167/iovs.15-18900 (cit. on p. 145).
- [18] K. Ghasemi Falavarjani, M. Al-Sheikh, F. Darvizeh, A. A. Sadun, and S. R. Sadda, "Retinal vessel calibre measurements by optical coherence tomography angiography.", *The British journal of ophthalmology*, vol. 101, no. 7, pp. 989–992, Jul. 2017, ISSN: 1468-2079. DOI: 10.1136/bjophtho-2016-309678 (cit. on pp. 146, 165).

- [19] H. A. Lehr, M. Leunig, M. D. Menger, D. Nolte, and K. Messmer, "Dorsal skin-fold chamber technique for intravital microscopy in nude mice.", *The American journal of pathology*, vol. 143, no. 4, pp. 1055–62, Oct. 1993, ISSN: 0002-9440 (cit. on p. 146).
- [20] G. E. Koehl, A. Gaumann, and E. K. Geissler, "Intravital microscopy of tumor angiogenesis and regression in the dorsal skin fold chamber: mechanistic insights and preclinical testing of therapeutic strategies", *Clinical & Experimental Metastasis*, vol. 26, no. 4, pp. 329–344, Apr. 2009, ISSN: 0262-0898. DOI: 10.1007/s10585-008-9234-7 (cit. on p. 146).
- [21] G. M. Tozer, S. Akerman, N. A. Cross, P. R. Barber, M. A. Björndahl, O. Greco, S. Harris, S. A. Hill, D. J. Honess, C. R. Ireson, K. L. Pettyjohn, V. E. Prise, C. C. Reyes-Aldasoro, C. Ruhrberg, D. T. Shima, and C. Kanthou, "Blood vessel maturation and response to vascular-disrupting therapy in single vascular endothelial growth factor-A isoform-producing tumors.", *Cancer research*, vol. 68, no. 7, pp. 2301–11, Apr. 2008, ISSN: 1538-7445. DOI: 10.1158/0008-5472.CAN-07-2011 (cit. on p. 146).
- [22] A. Mariampillai, M. K. K. Leung, M. Jarvi, B. a. Standish, K. Lee, B. C. Wilson, A. Vitkin, and V. X. D. Yang, "Optimized speckle variance OCT imaging of microvasculature.", *Optics letters*, vol. 35, no. 8, pp. 1257–9, Apr. 2010, ISSN: 1539-4794 (cit. on p. 146).
- [23] S. Kim, T. Park, S.-J. Jang, A. S. Nam, B. J. Vakoc, and W.-Y. Oh, "Multi-functional angiographic OFDI using frequency-multiplexed dual-beam illumination", *Optics Express*, vol. 23, no. 7, p. 8939, 2015, ISSN: 1094-4087. DOI: 10.1364/OE.23.008939 (cit. on p. 146).
- [24] A. Maeda, M. K. K. Leung, L. Conroy, Y. Chen, J. Bu, P. E. Lindsay, S. Mintzberg, C. Virtanen, J. Tsao, N. A. Winegarden, Y. Wang, L. Morikawa, I. A. Vitkin, D. A. Jaffray, R. P. Hill, and R. S. DaCosta, "In vivo optical imaging of tumor and microvascular response to ionizing radiation.", *PloS one*, vol. 7, no. 8, e42133, Jan. 2012, ISSN: 1932-6203. DOI: 10.1371/journal.pone.0042133 (cit. on p. 146).

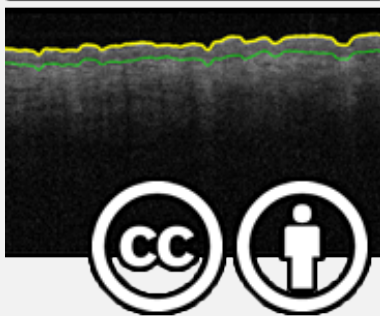
- [25] A. S. Nam, I. Chico-Calero, and B. J. Vakoc, "Complex differential variance algorithm for optical coherence tomography angiography", *Biomedical Optics Express*, vol. 5, no. 11, p. 3822, 2014, ISSN: 2156-7085. DOI: 10.1364/B0E.5.003822 (cit. on p. 146).
- [26] R. A. Byers, M. Fisher, N. J. Brown, G. M. Tozer, and S. J. Matcher, "Vascular patterning of subcutaneous mouse fibrosarcomas expressing individual VEGF isoforms can be differentiated using angiographic optical coherence tomography", *Biomedical optics express*, vol. 8, no. 10, pp. 459–467, 2017 (cit. on pp. 148, 160–161, 169–170).
- [27] H. D. Papenfuss, J. F. Gross, M. Intaglietta, and F. A. Treese, "A transparent access chamber for the rat dorsal skin fold", *Microvascular Research*, vol. 18, no. 3, pp. 311–318, Nov. 1979, ISSN: 0026-2862. DOI: 10.1016/0026-2862(79)90039-6 (cit. on p. 148).
- [28] G. M. Tozer, S. M. Ameer-Beg, J. Baker, P. R. Barber, S. A. Hill, R. J. Hodgkiss, R. Locke, V. E. Prise, I. Wilson, and B. Vojnovic, "Intravital imaging of tumour vascular networks using multi-photon fluorescence microscopy.", *Advanced drug delivery reviews*, vol. 57, no. 1, pp. 135–52, Jan. 2005, ISSN: 0169-409X. DOI: 10.1016/j.addr.2004.07.015 (cit. on p. 148).
- [29] S. Preibisch, S. Saalfeld, and P. Tomancak, "Globally optimal stitching of tiled 3D microscopic image acquisitions.", *Bioinformatics (Oxford, England)*, vol. 25, no. 11, pp. 1463–5, Jun. 2009, ISSN: 1367-4811. DOI: 10.1093/bioinformatics/btp184 (cit. on p. 149).
- [30] R. A. Byers, G. Tozer, N. J. Brown, and S. J. Matcher, "High-resolution label-free vascular imaging using a commercial, clinically approved dermatological OCT scanner", B. Choi, N. Kollias, H. Zeng, H. W. Kang, B. J. F. Wong, J. F. Ilgner, G. J. Tearney, K. W. Gregory, L. Marcu, M. C. Skala, P. J. Campagnola, A. Mandelis, and M. D. Morris, Eds., Feb. 2016, p. 96890M. DOI: 10.1117/12.2212222 (cit. on p. 150).

- [31] L. Conroy, R. S. DaCosta, and I. A. Vitkin, "Quantifying tissue microvasculature with speckle variance optical coherence tomography.", *Optics letters*, vol. 37, no. 15, pp. 3180–2, Aug. 2012, ISSN: 1539-4794 (cit. on p. 152).
- [32] K. Zuiderveld, "Contrast Limited Adaptive Histogram Equalization", in *Graphics Gems*, Elsevier, 1994, pp. 474–485. DOI: 10.1016/B978-0-12-336156-1.50061-6 (cit. on p. 152).
- [33] I. Arganda-Carreras, C. O. S. Sorzano, R. Marabini, J. M. Carazo, C. Ortiz-de-Solorzano, and J. Kybic, "Consistent and Elastic Registration of Histological Sections Using Vector-Spline Regularization", pp. 85–95, 2006, ISSN: 10959203. DOI: 10.1007/11889762_8 (cit. on p. 153).
- [34] C. Sorzano, P. Thevenaz, and M. Unser, "Elastic Registration of Biological Images Using Vector-Spline Regularization", *IEEE Transactions on Biomedical Engineering*, vol. 52, no. 4, pp. 652–663, Apr. 2005, ISSN: 0018-9294. DOI: 10.1109/TBME.2005.844030 (cit. on p. 153).
- [35] A. F. Frangi, W. J. Niessen, K. L. Vincken, and M. a. Viergever, "Multiscale vessel enhancement filtering", *Medial Image Computing and Computer-Assisted Invervention - MICCAI'98. Lecture Notes in Computer Science, vol 1496*, vol. 1496, pp. 130–137, 1998, ISSN: 13618415. DOI: 10.1016/j.media.2004.08.001 (cit. on p. 155).
- [36] D. Bradley and G. Roth, "Adaptive Thresholding using the Integral Image", *Journal of Graphics Tools*, vol. 12, no. 2, pp. 13–21, Jan. 2007, ISSN: 1086-7651. DOI: 10.1080/2151237X.2007.10129236 (cit. on p. 155).
- [37] K. Jurczyszyn, B. J. Osiecka, P. Ziółkowski, and P. Kowski, "The Use of Fractal Dimension Analysis in Estimation of Blood Vessels Shape in Transplantable Mammary Adenocarcinoma in Wistar Rats after Photodynamic Therapy Combined with Cysteine Protease Inhibitors", *Computational and Mathematical Methods in Medicine*, vol. 2012, pp. 1–6, 2012, ISSN: 1748-670X. DOI: 10.1155/2012/793291 (cit. on p. 156).

-
- [38] L. Lam, S.-W. Lee, and C. Suen, "Thinning methodologies-a comprehensive survey", *IEEE Transactions on Pattern Analysis and Machine Intelligence*, vol. 14, no. 9, pp. 869–885, 1992, ISSN: 01628828. DOI: 10.1109/34.161346 (cit. on p. 157).
- [39] S. Kalaie and A. Gooya, "Vascular tree tracking and bifurcation points detection in retinal images using a hierarchical probabilistic model", *Computer Methods and Programs in Biomedicine*, vol. 151, pp. 139–149, Nov. 2017, ISSN: 0169-2607. DOI: 10.1016/J.CMPB.2017.08.018 (cit. on p. 157).
- [40] C. Kanthou, G. U. Dachs, D. V. Lefley, A. J. Steele, C. Coralli-Foxon, S. Harris, O. Greco, S. A. Dos Santos, C. C. Reyes-Aldasoro, W. R. English, and G. M. Tozer, "Tumour Cells Expressing Single VEGF Isoforms Display Distinct Growth, Survival and Migration Characteristics", *PLoS ONE*, vol. 9, no. 8, C. L. Addison, Ed., e104015, Aug. 2014, ISSN: 1932-6203. DOI: 10.1371/journal.pone.0104015 (cit. on p. 161).
- [41] G. M. Tozer, S. Akerman, N. A. Cross, P. R. Barber, M. A. Björndahl, O. Greco, S. Harris, S. A. Hill, D. J. Honess, C. R. Ireson, K. L. Pettyjohn, V. E. Prise, C. C. Reyes-Aldasoro, C. Ruhrberg, D. T. Shima, and C. Kanthou, "Blood vessel maturation and response to vascular-disrupting therapy in single vascular endothelial growth factor-A isoform-producing tumors.", en, *Cancer research*, vol. 68, no. 7, pp. 2301–11, Apr. 2008, ISSN: 1538-7445. DOI: 10.1158/0008-5472.CAN-07-2011 (cit. on pp. 161, 170).

Chapter 6

Structural OCT measures of *in-vivo* skin deformation



This chapter contains excerpts, with permission, from the following published work:

***In-vivo* measurement of skin surface strain and sub-surface layer deformation induced by natural tissue stretching**

Raman Maiti, Lutz-Christian Gerhardt, Zing S. Lee, Robert A. Byers, Daniel Woods, José A. Sanz-Herrera, Steve E. Franklin, Roger Lewis, Stephen J. Matcher and Matthew J. Carré

Journal of the Mechanical Behaviour of Biomedical Materials

Vol. 62, pp. 556-569 (2016)

Under a Creative Commons license

<https://doi.org/10.1016/j.jmbbm.2016.05.035>

This chapter will focus on the OCT image processing tools which were developed for the purposes of this study and future applications.

Statement of contribution

Concerning the publication:

***In-vivo* measurement of skin surface strain and sub-surface layer deformation induced by natural tissue stretching.**

Contributor	Statement of contribution
Robert A. Byers Signed: _____	My primary contribution to this paper was in the development and validation of the OCT image processing algorithms, as such the paper has been entirely re-written to place a greater emphasis and provide more detail on this aspect of the work. <ul style="list-style-type: none"> • Development of the stratum corneum (SC) detection algorithm. • Integration and modification of the dermal-epidermal junction (DEJ) detection algorithm. • Development of a MATLAB GUI for data fitting, roughness calculation and data exportation. • Re-writing the manuscript for this thesis publication.
Raman Maiti Signed: _____	<ul style="list-style-type: none"> • Typing the original manuscript. • OCT/Digital Image Correlation (DIC) data collection (With L. Gerhardt). • Primary DIC data analysis, and analysis of post-processed OCT results.

Principle supervisor confirmation

I have sighted email or other correspondence from all co-authors confirming their certifying authorship.

Name: _____ Signature: _____
Date: _____

6.1 Introduction

The tribology of our skin is a fundamentally important aspect of everyday life. Frictional forces between our skin and object surfaces define our ability to manipulate and influence the space around us. Understanding the intricate mechanical and tribological properties of the skin which give rise to its unique properties is of great benefit to research areas such as skin physiology, the textile industry, friction dependant sporting activities, skin-care, cosmetic products and the treatment of friction induced injuries to the upper layers of skin[1]. Furthermore techniques which are capable of assessing skin function and frictional characteristics are of great benefit in the design of artificial skin[2], prosthetic implants[3] and wearable or implanted electronic devices[4].

Previously a wide range of techniques have been employed with the aim of assessing morphological or functional changes within the skin in response to applied mechanical force. These include: biaxial tensile testing[5], fluorescence laser scanning microscopy [6], shear experiments and real-time video recording[7], [8], atomic force microscopy based indentation[9], magnetic resonance imaging[10]. Both OCT[11]–[13] and digital image correlation (DIC)[7], [14], [15] have previously been used for the study of skin deformation properties, however few studies have considered the effect of skin strain on measurements of epidermal thickness.

This study aims to quantify the effects of induced skin strain as a result of forearm flexion on measured epidermal thickness and surface roughness at the elbow joint. As the upper layers of the skin (Epidermis, Dermis and Hypodermis) are firmly attached together, and in turn attached to the musculoskeletal system through network of fascia[7], it is plausible to expect that movement of the elbow joint will induce surface strains in the upper layer of the skin, modifying the localised skin morphology and surface topology. The study objectives were (1) to utilise structural OCT in order to measure changes in epidermal thickness and surface deformations (Roughness) then (2) correlate the results with DIC measurements of surface strains. To the best of our knowledge, this is the first study which combines these two methods in order to quantify surface strains and correlate with sub-surface deformation.

6.2 Materials and methods

6.2.1 Participant

The right volar forearm of a 38-year old Caucasian male was used for all DIC and OCT image collection. Hairs were shaved from the imaging site and the skin was cleaned with an alcohol wipe prior to imaging. This study was approved by the University of Sheffield ethics committee (Ref: 002074) and full informed consent was attained prior to any tests. All measurements were carried out at 20-22°C with a relative humidity of 40-50%.

6.2.2 Digital image correlation (DIC)

DIC is a full-field optical technique which tracks the displacement and deformation of a random pattern upon a material surface. Traditionally DIC has been used for the study of localised deformation within engineering materials[16] however it has found increasing application within biomechanical fields for observing displacements and strain within biological tissues[17].

For DIC, a random pattern is applied to the surface of the object, this should be sufficiently high in contrast such that differences between the reference pattern and a deformed variant can be tracked. A digital camera is used to capture images of the pattern prior to, and following deformation, with images being broken down into various blocks, or sub-images. A 2D displacement field is then calculated through cross-correlation of each of the pre-deformation sub-images with the post-deformation image, similar to the cross-correlation based image registration discussed in Sec. 2.1.3.

For this study, a black water-based ink was distributed randomly onto the skin by flicking the bristles of a toothbrush. Digital images were acquired in parallel from the left and right sides of the forearm using two Pike F505B cameras (Allied Vision

Technologies GmbH, Germany), both equipped with a 2452x2054 pixel monochromatic CCD sensor (Sony ICX625) and 50mm objective lens (XENOPLAN 2.8/50-0902, Schneider, Kreuznach). The usage of a double-camera DIC set-up enables accurate tracking of deformations across a curved 3D surface, reducing errors in the resulting displacement field[16]. This setup is shown in Fig. 6.1.

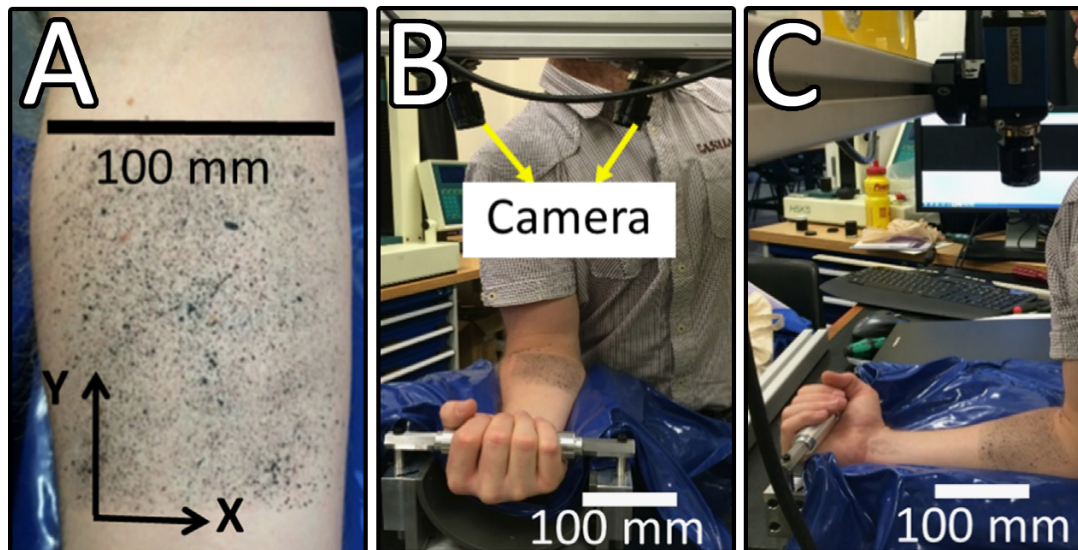


FIGURE 6.1: A) The random spray pattern on the volar forearm of the participant. B) The DIC setup showing the position of the two digital cameras and the vacuum pillow. C) Side view of the DIC setup. Image sourced, with permission from: R. Maiti *et al*, 2016.[18]

DIC technical details

- 30° stereo angle between the two CCD cameras.
- Cameras positioned $\approx 350\text{mm}$ from the surface of the volar forearm.
- Maximum field-of-view = $47 * 39\text{mm}^2$.
- Spatial pixel resolution = $20\mu\text{m}/\text{pixel}$.
- Sub-image size = $81 * 81$ pixels (Corresponding to 1.62mm^2).
- A step-size of 7-pixels was used between sub-images.
- Frames captured at a rate of $5\text{frames}/\text{sec}$.
- Back illuminated by a fluorescent white light source.
- System calibrated using VIC-3D DIC software (v7.2.1, Correlated Solutions, USA). Using a fixed grid pattern of known characteristics.

6.2.3 Optical coherence tomography

Volumetric structural OCT datasets were acquired from 10 sites on the volar forearm using a clinically approved Vivosight OCT system (Michelson Diagnostics, Kent). The scan location was selected as 50mm distal to the cubital fossa and encompassed an area of $25 * 40\text{mm}^2$ central to the arm. Each volume scan had a field-of-view of $6 * 6 * 2\text{mm}^3$ with 5mm spacing between each scan. This arrangement is illustrated in Fig. 6.2 below.

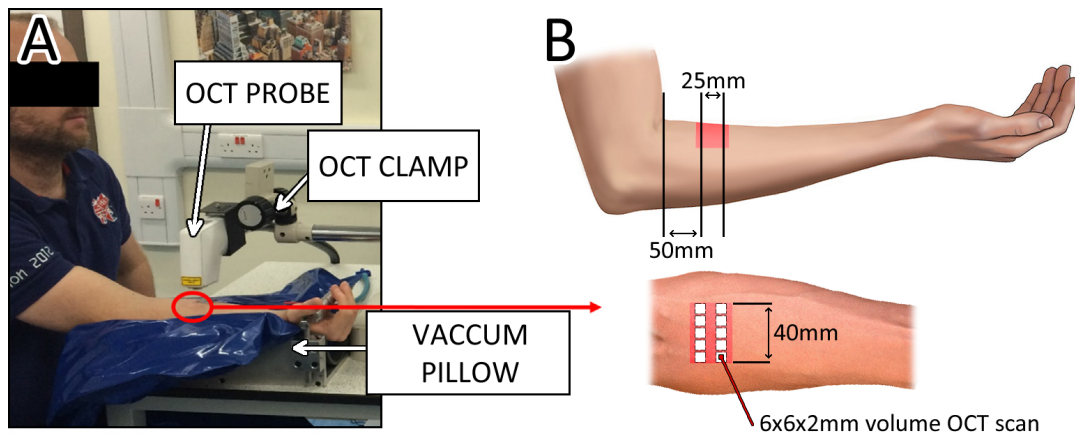


FIGURE 6.2: A) The OCT system setup B) The OCT scan locations on the volar forearm.

6.2.4 Experimental protocol

The right arm of the volunteer was positioned above a vacuum pillow as illustrated in Fig. 6.1 and Fig. 6.2. The vacuum pillow was then deflated such that the arm was fixed in place, this was to reduce the influence of motion artefacts during the imaging phase. DIC images were acquired at a rate of 5 frames/sec during the entire flexion/extension motion of the elbow joint. Comparatively OCT scanning was performed at two quasi-static arm positions, these being full extension of the joint, and 90° flexion.

6.2.5 Data analysis and processing

Strain analysis with DIC

Analysis of the DIC datasets was performed with VIC-3D DIC software (v7.2.1, CorrelatedSolutions, USA). This software utilises the two camera POVs to track the sub-images in a 3D space, it achieves this by cross-correlating the grey-value intensities of the reference image to that of the deformed image. Multiple sets of matching displacements can then be used to calculate a 3D deformation field.

From the resultant 3D deformation field, Lagrange strains resulting from skin deformation during the 90° -flexion \rightarrow 180° full extension were calculated. The skin

in this case being modelled as a fluid-filled soft composite material considered to have non-linear elastic properties[7]. For details regarding the full calculation of the Lagrange strain, please consult: Maiti *et al*, 2016.[18].

Epidermal thickness and skin roughness analysis with OCT

A MATLAB (R2014b - MathWorks) algorithm was developed in order to automatically extract both epidermal thickness and stratum corneum/dermal-epidermal junction (DEJ) roughness values from the OCT B-scans.

OCT processing algorithm details

This algorithm aimed to load a stack of 2D OCT B-scans and process each one in series, outputting quantitative values of epidermal thickness and stratum corneum/dermal-epidermal junction roughness.

Tagged Image File Format (.tiff) files were used as an input to the algorithm, if multiple files were present they would be processed in series. Each image had been filtered using a proprietary pre-processing algorithm (Michelson Diagnostics Ltd) which utilised prior knowledge of the beam foci lengths to blend the 4-channel structural OCT images outputted by the Vivosight. The algorithm itself is described in further detail in a publication by Holmes *et al*[19]. This suppressed speckle-noise while maintaining image resolution and contrast. The images were also mean filtered using a convolution kernel with higher weighting in the x-direction (Lateral) than the z-direction (Axial) in order to preserve resolution in the depth direction and avoid blurring of the skin layer interfaces. An example B-scan is shown in Fig. 6.3 below.

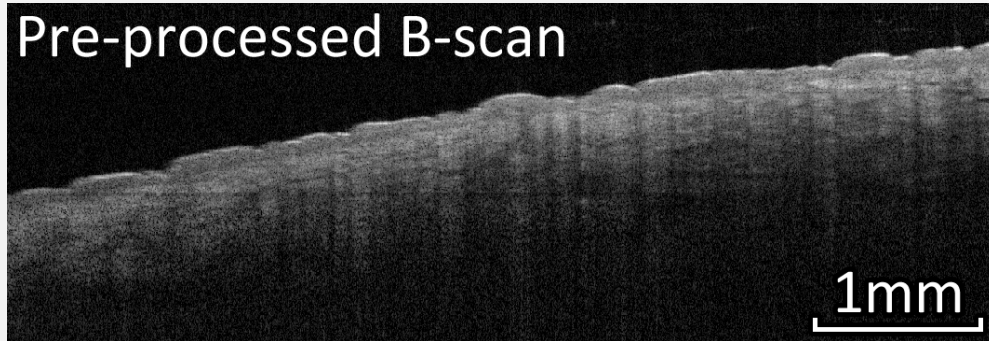


FIGURE 6.3: A pre-processed structural OCT B-scan of the volar forearm.

The first step involved automatic detection of the stratum corneum layer at the air-skin boundary. This was achieved using the same methodology as that used for skin surface flattening, outlined in Sec. 2.1.5. If automatic surface detection failed (e.g due to the presence of a hair or other scattering artefact), the user is presented with the option of manually selecting surface points such that shape-preserving piecewise cubic interpolation can be performed, generating a spline representative of the surface level.

The second step was designed to detect the subtle contrast change present at the DEJ, where a grainy texture derived from keratinocytes within the epidermis give way to the smooth and more scattering tissue of the papillary dermis[20]. At this location, a decreasing optical-intensity with depth within the epidermis gives way to an increasing optical-intensity with depth within the upper papillary dermis, which is detected as a local-minima within each A-scan[20]. Minima which are sufficiently connected are interpolated between to form the complete DEJ detection. DEJ detection can potentially be improved in the future through use of an ultra-high resolution OCT system, which offers increased contrast at the DEJ boundary[21].

Fig. 6.4 shows the resultant SC (Yellow line) and DEJ (Green line).

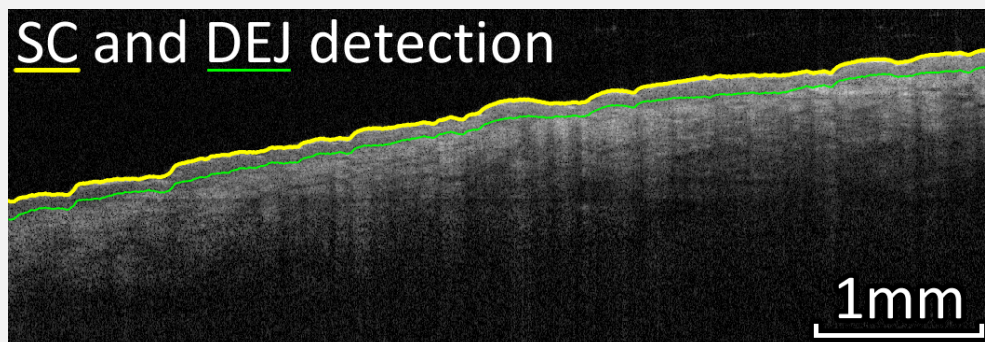
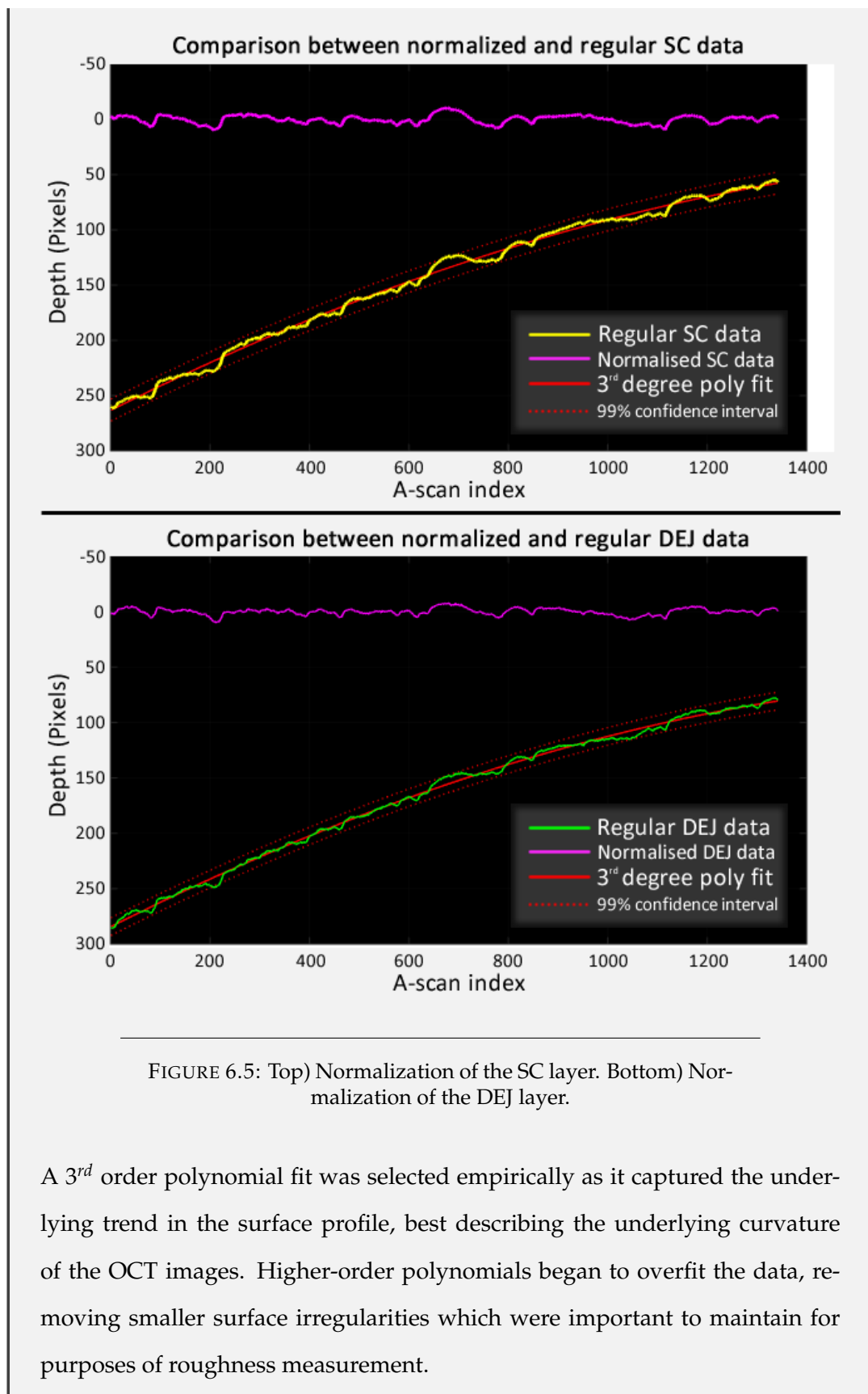


FIGURE 6.4: The same image as Fig. 6.3 processed to detect the SC (Yellow line) and DEJ (Green line).

While the DEJ's exact position has no direct validation, there is a widespread consensus within the literature that the boundary visible on structural OCT scans correlates with the position of the DEJ. Both through direct histological comparison[22] and the pathological alteration of this boundary in skin conditions which are known to alter the DEJ location[22]–[25].

There are three main factors which influence the detected skin surface level, firstly the roughness of the skin itself presents undulations in the tissue surface. Secondly the angle of the probe as it is held against the skin contributes to bulk shifts in the detected A-scans. Thirdly, natural curvature in the surface of the skin. For example on Fig. 6.4 it is clear that the left side of the image is lower than the right, which is caused by a combination of the second and third factors. In order to conduct reliable measures of layer roughness it was necessary to detect and remove any background curvature, such that the true surface roughness could be considered. This was achieved by fitting a 3rd order polynomial to both the detected SC and DEJ, and normalizing each layer around this. Fig. 6.5 shows this process.



Once the normalized surface profiles were determined (Pink lines on Fig. 6.5) surface roughness could be calculated. Image pixels were first converted into distance measurements at a ratio of $4.47\mu\text{m}$ per pixel. Skin surface roughness was then determined using the DIN ISO 1302[26] standard definition of arithmetic mean roughness (R_a) and 10-point roughness depth (R_z):

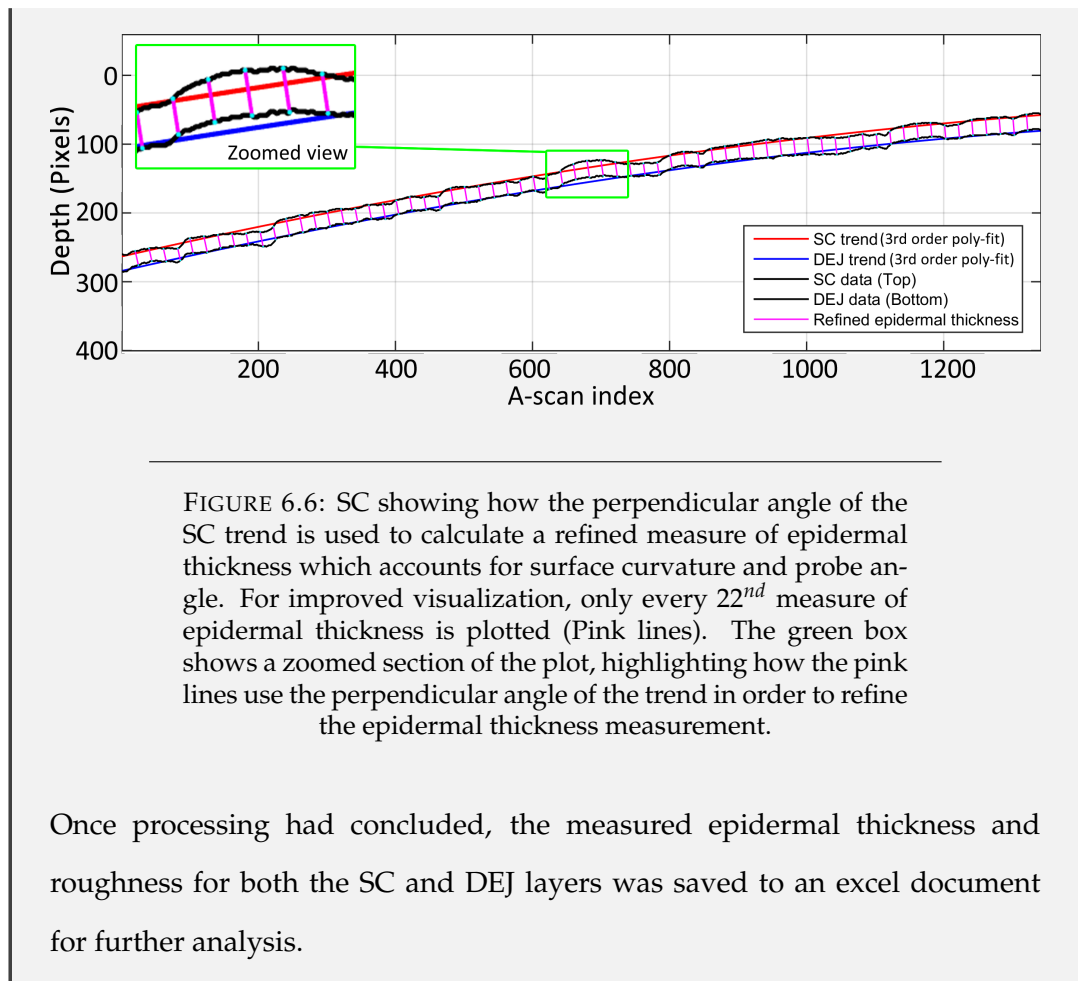
$$R_a = \frac{1}{n} \sum_{i=1}^n |y_i| \quad (6.1)$$

Here n represents the sampling length (Total image width) and y_i is the vertical distance from the mean line to the i^{th} data point.

$$R_z = \frac{1}{5} \sum_{i=1}^5 Rt_i \quad (6.2)$$

Here $Rt_i = \max_i(y_i) - \min_i(y_i)$, where Rt_i is the maximum profile height Rt for the i^{th} sampling length.

Epidermal thickness for each B-scan was calculated by averaging the measured thickness across the entire B-scan, with each pixel in the x-direction corresponding to $4.47\mu\text{m}$ in distance. Rather than simply measuring the thickness vertically in y, which fails to account for the general surface curvature, a refined measure of epidermal thickness was acquired at each x-location. For this, a line which was perpendicular in direction to the 3^{rd} order polynomial SC fit was calculated at each x-location, the intersection points of the regular SC and DEJ layers along this line were then detected and the Euclidean distance between the intersection points was then calculated as the epidermal thickness for that location. Fig. 6.6 illustrates how this refined measure of epidermal thickness is calculated.



6.2.6 Statistics

All statistical analysis was conducted within IBM SPSS Statistics 22 (IBM, Hampshire, UK)[27]. Paired student t-tests were applied to investigate for any significant differences between the recorded metrics as the elbow was displaced from 90°-flexion → 180° full extension. Probability levels with p values of less than 0.05 were described as statistically significant.

6.3 Results and discussion

6.3.1 Results of DIC analysis

Fig. 6.7 shows the Lagrange strain (E_{yy}) at the skin surface of both the 90°-flexion and 180° full extension quasi-static states as measured with DIC.

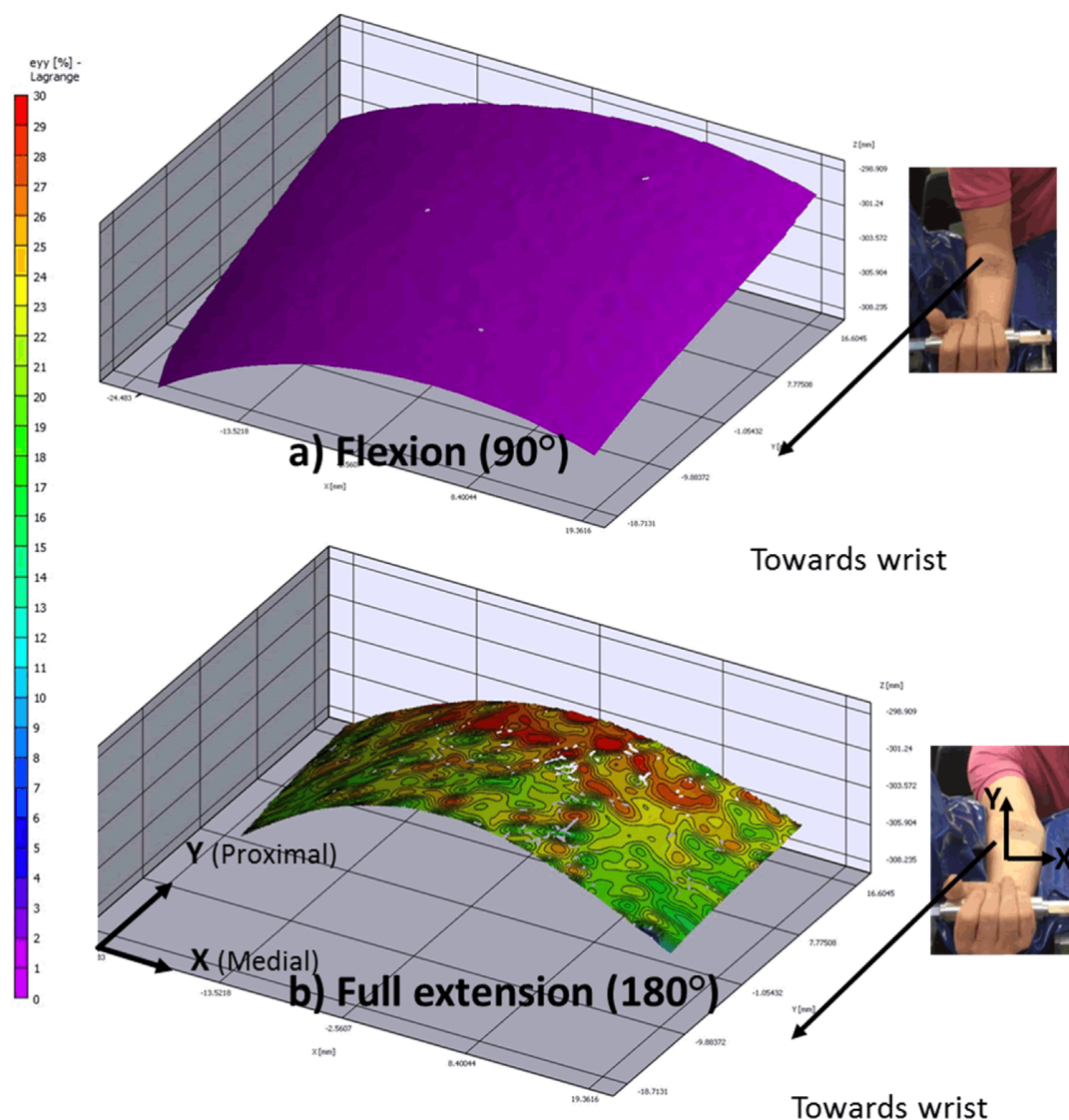


FIGURE 6.7: Contour plots of the skin surface strain field as measured by DIC. a) 90°-flexion b) 180° full extension. Image sourced, with permission from: R. Maiti *et al*, 2016.[18]

The highest Lagrange strains were detected close to the elbow joint as indicated by the red colouration on Fig. 6.7b, at this location strains upwards of 30% were

detected. At distal locations closer to the wrist, strains reduced ($E_{yy} < 20\%$). Across the entire region, the average detected Lagrange strain was approximately 23%.

The transition in Lagrange strain from 90°-flexion \rightarrow 180° full extension can be viewed as an animated GIF at the following location: <https://ars.els-cdn.com/content/image/1-s2.0-S1751616116301631-mmc1.gif>.

Table 6.1 lists the percentile changes in strain in both the compressive (x) direction and tensile (y) direction, as well as both the tensile and compressive principle strains (E_1 and E_2 respectively). The measured strains in the X and Y direction were $E_{xx} = -5.6 \pm 1.0\%$ and $E_{yy} = 23.3 \pm 2.2\%$ respectively, implying that the tensile component may dominate the overall skin deformation characteristics.

Strain	E_{xx} (%)	E_{yy} (%)	E_{xy} (%)	E_1 (%)	E_2 (%)	Area (cm^2)
Mean	-5.6	23.3	-7.6	26.1	-8.4	5.9
SD	1.0	2.2	1.7	2.3	1.2	1.1

TABLE 6.1: Average skin surface strains at 180° full extension. E_{xx} : Strain along medial forearm direction, E_{yy} : Strain along the proximal forearm direction, E_1 : Tensile principal strain, E_2 : Compressive principle strain.

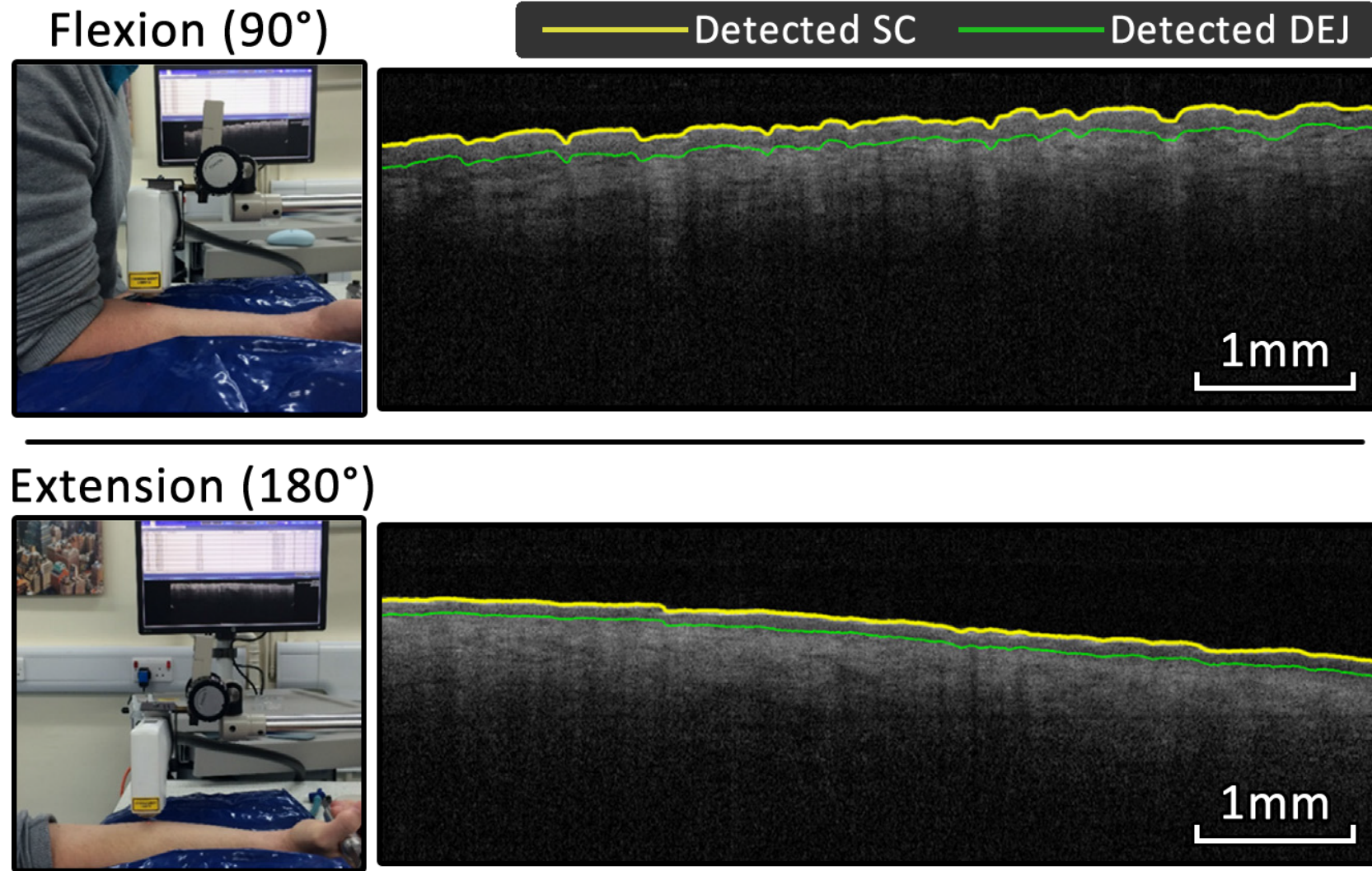


FIGURE 6.8: OCT B-scans of forearm skin in both the relaxed 90° -flexion quasi-static state (Top row) and the stretched 180° full extension state (Bottom row).

6.3.2 Results of OCT analysis

Fig. 6.8 shows an example of forearm skin viewed with OCT in both the flexion and full-extension states. Both the SC and DEJ became qualitatively smoothed during the full 180° extension. The average epidermal thickness across all ROIs (Fig. 6.2), as measured by the algorithm discussed in Sec. 6.2.5, reduced significantly ($p=0.001$) from $108 \pm 14\mu\text{m}$ at 90°-flexion to $90 \pm 12\mu\text{m}$ at 180° full extension, suggesting that under applied surface strain, a thinning of the epidermis is apparent and measurable.

Similarly, the measured skin roughness (R_a and R_z) at both the SC and the DEJ reduced from: $R_{a(SC)} = 14.2 \pm 2.6\mu\text{m}$ / $R_{a(DEJ)} = 15.3 \pm 3.1\mu\text{m}$ and $R_{z(SC)} = 75.7 \pm 16.7\mu\text{m}$ / $R_{z(DEJ)} = 81.4 \pm 18.6\mu\text{m}$ at 90°-flexion to $R_{a(SC)} = 8.4 \pm 2.2\mu\text{m}$ / $R_{a(DEJ)} = 8.4 \pm 3.5\mu\text{m}$ and $R_{z(SC)} = 38.4 \pm 11.0\mu\text{m}$ / $R_{z(DEJ)} = 40.4 \pm 15.3\mu\text{m}$ at 180° full extension. Supporting the qualitative observation of skin smoothing observed in Fig. 6.8.

This study aimed to link the surface strains induced due to forearm skin stretching with the underlying deformations within the SC and DEJ layers of the skin. Extension of the volar arm angle increased the principle tensile strain by 26.2% and was accompanied by an 16.7% reduction in epidermal thickness and a reduction in roughness at the SC of 40.8%(R_a)/49.3%(R_z) and similar reduction of 45.1%(R_a)/50.4%(R_z) at the DEJ boundary. To our knowledge, very little quantitative data exists which compares the effect of *in-vivo* skin stretching on the thickness of the epidermis and layer roughness, therefore further research is required in order to validate these findings such that consistent measures of skin layer thickness can be acquired across the body.

A full comparison between recorded literature values of epidermal thickness and surface roughness (R_a , R_z) values and those measured here can be found in the full text[18]. Briefly, the measured epidermal thickness range of $90 - 108\mu\text{m}$ closely matched the range in published literature ($60 - 128\mu\text{m}$). Values of R_a measured here ($8.4 - 15.3\mu\text{m}$) also closely matched the range in published literature ($7.2 - 26.8\mu\text{m}$ for Caucasian skin), and R_z ($38.4 - 81.4\mu\text{m}$) \rightarrow ($35.7 - 267.0\mu\text{m}$ in literature).

6.4 Limitations

Due to the DIC and OCT systems being in different locations, it was not possible to perform combined imaging during this study. Thus, in order to directly correlate between simultaneous measurements with each modality it will be necessary to decrease the time between measurements as much as possible. Despite this, care was taken to ensure that both OCT and DIC measurements were acquired at the same location, aided greatly by a consistent, well-defined anatomical landmark (birth mark) being present. Another area of interest is the transitional stages between the two well-defined arm positions considered here (90° -flexion and 180° full extension). In this case, the volume acquisition speed of the OCT system was insufficient in order to rapidly capture dynamic measurements of the skin, instead being reliant on quasi-static arm positions. Improvements in the OCT image registration process could however enable registration between measurements acquired with gradual angular changes in the arm, allowing us to track the evolution in epidermal thickness and skin-roughness as a function of the strain measured by DIC.

We were also unable to accurately quantify internal deformations during the scope of this study, thus any differences in deformation and strain behavior between the internal layers of the skin (Epidermis, Dermis) were ignored. Recently, DIC based algorithms have successfully been applied to track the speckle-patterns in OCT images during loading[28], providing an avenue by which surface strains (with camera based DIC) can be linked to sub-surface strains (with OCT based DIC).

6.5 Conclusions

This study has demonstrated the potential of a new OCT image analysis algorithm which is capable of extracting morphological skin parameters for direct comparison with skin strain data acquired with DIC. Changes in the angle of the volar forearm from 90°-flexion to 180° full extension resulted in increased (+26%) surface strains as measured by DIC, and caused a reduction in the epidermal thickness and layer roughness of the SC and DEJ. The combination of these modalities to simultaneously measure surface strain and layer deformation is a powerful method for the non-invasive study of structural skin changes and tissue response, particularly within areas such as damage assessment during skin loading, or the study of blister and decubitus ulcer formation.

References

- [1] M. Zhang and A. Mak, "In vivo friction properties of human skin.", *Prosthetics and orthotics international*, vol. 23, no. 2, pp. 135–141, 1999, ISSN: 0309-3646. DOI: 10.3109/03093649909071625 (cit. on p. 185).
- [2] M. Nachman and S. E. Franklin, "Artificial Skin Model simulating dry and moist in vivo human skin friction and deformation behaviour", *Tribology International*, vol. 97, pp. 431–439, 2016, ISSN: 0301679X. DOI: 10.1016/j.triboint.2016.01.043 (cit. on p. 185).
- [3] J. F. Ramírez, J. J. Pavón, and A. Toro, "Experimental assessment of friction coefficient between polypropylene and human skin using instrumented sclerometer", *Proceedings of the Institution of Mechanical Engineers, Part J: Journal of Engineering Tribology*, vol. 229, no. 3, pp. 259–265, Mar. 2015, ISSN: 1350-6501. DOI: 10.1177/1350650114526579 (cit. on p. 185).
- [4] Y. Li, J. Zhang, Y. Xing, and J. Song, "Thermomechanical Analysis of Epidermal Electronic Devices Integrated With Human Skin", *Journal of Applied Mechanics*, vol. 84, no. 11, p. 111 004, Sep. 2017, ISSN: 0021-8936. DOI: 10.1115/1.4037704 (cit. on p. 185).
- [5] H.-Y. S. HUANG, S. HUANG, C. P. FRAZIER, P. M. PRIM, and O. HARRYSSON, "DIRECTIONAL BIOMECHANICAL PROPERTIES OF PORCINE SKIN TISSUE", *Journal of Mechanics in Medicine and Biology*, vol. 14, no. 05, p. 1450 069, Oct. 2014, ISSN: 0219-5194. DOI: 10.1142/S0219519414500699 (cit. on p. 185).
- [6] J. Lademann, N. Otberg, H. Richter, L. Meyer, H. Audring, A. Teichmann, S. Thomas, A. Knüttel, and W. Sterry, "Application of optical non-invasive methods in skin physiology: a comparison of laser scanning microscopy and optical

- coherent tomography with histological analysis”, *Skin Research and Technology*, vol. 13, no. 2, pp. 119–132, May 2007, ISSN: 0909-752X. DOI: 10.1111/j.1600-0846.2007.00208.x (cit. on p. 185).
- [7] L.-C. Gerhardt, J. Schmidt, J. Sanz-Herrera, F. Baaijens, T. Ansari, G. Peters, and C. Oomens, “A novel method for visualising and quantifying through-plane skin layer deformations”, *Journal of the Mechanical Behavior of Biomedical Materials*, vol. 14, pp. 199–207, Oct. 2012, ISSN: 17516161. DOI: 10.1016/j.jmbbm.2012.05.014 (cit. on pp. 185, 190).
- [8] L. E., v. K. T.H.S., B. F.P.T., P. G.W.M., and O. C.W.J., “Large amplitude oscillatory shear properties of human skin”, *Journal of the Mechanical Behavior of Biomedical Materials*, vol. 28, pp. 462–470, Dec. 2013, ISSN: 1751-6161. DOI: 10.1016/J.JMBBM.2013.01.024 (cit. on p. 185).
- [9] A. P. Kao, J. T. Connelly, and A. H. Barber, “3D nanomechanical evaluations of dermal structures in skin”, *Journal of the Mechanical Behavior of Biomedical Materials*, vol. 57, pp. 14–23, Apr. 2016, ISSN: 1751-6161. DOI: 10.1016/J.JMBBM.2015.11.017 (cit. on p. 185).
- [10] G. G. Barbarino, M. Jabareen, and E. Mazza, “Experimental and numerical study on the mechanical behavior of the superficial layers of the face”, *Skin Research and Technology*, vol. 17, no. 4, pp. 434–444, Nov. 2011, ISSN: 0909752X. DOI: 10.1111/j.1600-0846.2011.00515.x (cit. on p. 185).
- [11] T. Gambichler, A. Pljakic, and L. Schmitz, “Recent advances in clinical application of optical coherence tomography of human skin”, *Clinical, Cosmetic and Investigational Dermatology*, vol. 8, p. 345, Jul. 2015, ISSN: 1178-7015. DOI: 10.2147/CCID.S69119 (cit. on p. 185).
- [12] G. Josse, J. George, and D. Black, “Automatic measurement of epidermal thickness from optical coherence tomography images using a new algorithm”, *Skin Research and Technology*, vol. 17, no. 3, pp. 314–319, Aug. 2011, ISSN: 0909752X. DOI: 10.1111/j.1600-0846.2011.00499.x (cit. on p. 185).

- [13] X. Liu, Z. Lu, R. Lewis, M. Carré, and S. Matcher, "Feasibility of using optical coherence tomography to study the influence of skin structure on finger friction", *Tribology International*, vol. 63, pp. 34–44, Jul. 2013, ISSN: 0301-679X. DOI: 10.1016/J.TRIBOINT.2012.08.020 (cit. on p. 185).
- [14] S. L. Evans and C. A. Holt, "Measuring the mechanical properties of human skin *in vivo* using digital image correlation and finite element modelling", *The Journal of Strain Analysis for Engineering Design*, vol. 44, no. 5, pp. 337–345, Jul. 2009, ISSN: 0309-3247. DOI: 10.1243/03093247JSA488 (cit. on p. 185).
- [15] M. Kwiatkowska, S. Franklin, C. Hendriks, and K. Kwiatkowski, "Friction and deformation behaviour of human skin", *Wear*, vol. 267, no. 5-8, pp. 1264–1273, Jun. 2009, ISSN: 00431648. DOI: 10.1016/j.wear.2008.12.030 (cit. on p. 185).
- [16] M. A. Sutton, "Digital Image Correlation for Shape and Deformation Measurements", in *Springer Handbook of Experimental Solid Mechanics*, Boston, MA: Springer US, 2008, pp. 565–600. DOI: 10.1007/978-0-387-30877-7_20 (cit. on pp. 186–187).
- [17] M. Palanca, G. Tozzi, and L. Cristofolini, "The use of digital image correlation in the biomechanical area: a review", *International Biomechanics*, vol. 3, no. 1, pp. 1–21, Jan. 2016, ISSN: 2333-5432. DOI: 10.1080/23335432.2015.1117395 (cit. on p. 186).
- [18] R. Maiti, L. C. Gerhardt, Z. S. Lee, R. A. Byers, D. Woods, J. A. Sanz-Herrera, S. E. Franklin, R. Lewis, S. J. Matcher, and M. J. Carré, "In vivo measurement of skin surface strain and sub-surface layer deformation induced by natural tissue stretching", *Journal of the Mechanical Behavior of Biomedical Materials*, vol. 62, pp. 556–569, 2016, ISSN: 18780180. DOI: 10.1016/j.jmbbm.2016.05.035 (cit. on pp. 187, 190, 196, 200).
- [19] J. Holmes and S. Hattersley, "Image blending and speckle noise reduction in multi-beam OCT", J. G. Fujimoto, J. A. Izatt, and V. V. Tuchin, Eds., Feb. 2009, 71681N. DOI: 10.1117/12.808575 (cit. on p. 190).

- [20] G. Abignano, S. Z. Aydin, C. Castillo-Gallego, V. Liakouli, D. Woods, A. Meekings, R. J. Wakefield, D. G. McGonagle, P. Emery, and F. Del Galdo, "Virtual skin biopsy by optical coherence tomography: the first quantitative imaging biomarker for scleroderma", *Annals of the Rheumatic Diseases*, vol. 72, no. 11, pp. 1845–1851, Nov. 2013, ISSN: 0003-4967. DOI: 10.1136/annrheumdis-2012-202682 (cit. on p. 191).
- [21] N. M. Israelsen, M. Maria, M. Mogensen, S. Bojesen, M. Jensen, M. Haedersdal, A. Podoleanu, and O. Bang, "The value of ultrahigh resolution OCT in dermatology - delineating the dermo-epidermal junction, capillaries in the dermal papillae and vellus hairs", *Biomedical Optics Express*, vol. 9, no. 5, p. 2240, May 2018, ISSN: 2156-7085. DOI: 10.1364/B0E.9.002240 (cit. on p. 191).
- [22] A. J. Coleman, T. J. Richardson, G. Orchard, A. Uddin, M. J. Choi, and K. E. Lacy, "Histological correlates of optical coherence tomography in non-melanoma skin cancer", *Skin Research and Technology*, vol. 19, no. 1, e10–e19, Feb. 2013, ISSN: 0909752X. DOI: 10.1111/j.1600-0846.2012.00626.x (cit. on p. 192).
- [23] E. Sattler, R. Kästle, and J. Welzel, "Optical coherence tomography in dermatology", *Journal of Biomedical Optics*, vol. 18, no. 6, p. 061 224, Jan. 2013, ISSN: 1083-3668. DOI: 10.1117/1.JBO.18.6.061224 (cit. on p. 192).
- [24] S. A. Alawi, S. Batz, J. Röwert-Huber, J. W. Fluhr, J. Lademann, and M. Ulrich, "Correlation of optical coherence tomography and histology in microcystic adnexal carcinoma: a case report", *Skin Research and Technology*, vol. 21, no. 1, pp. 15–17, Feb. 2015, ISSN: 0909752X. DOI: 10.1111/srt.12149 (cit. on p. 192).
- [25] J. Boadi, Z. Lu, S. Danby, M. Cork, and S. J. Matcher, "Optical coherence tomography demonstrates differential epidermal thinning of human forearm volar skin after 2 weeks application of a topical corticosteroid vs a non-steroidal anti-inflammatory alternative", vol. 8565, p. 85650C, 2013, ISSN: 16057422. DOI: 10.1117/12.2006104 (cit. on p. 192).
- [26] ISO, *ISO 1302 - Geometrical Product Specifications (GPS) — Indication of surface texture in technical product documentation*, 2002 (cit. on p. 194).

-
- [27] I. corp, *IBM SPSS Statistics for Windows, Version 22.0*, 2013 (cit. on p. 195).
- [28] C. Sun, B. Standish, B. Vuong, X.-Y. Wen, and V. Yang, "Digital image correlation-based optical coherence elastography", *Journal of Biomedical Optics*, vol. 18, no. 12, p. 121 515, Dec. 2013, ISSN: 1083-3668. DOI: 10.1117/1.JBO.18.12.121515 (cit. on p. 200).

Chapter 7

Further image processing

This chapter will contain details of smaller experiments and software developments which were conducted during the course of this PhD.

7.1 Scan setting optimisation

An initial experiment aimed to optimise and compare the morphological imaging capabilities of both speckle-variance OCT (svOCT) and correlation-mapping OCT (cmOCT) for angiographic images of vessels. For reference, both of these scanning and processing methodologies were introduced in Sec. 1.3.2. Volumes were repeatedly acquired from the dorsal palm of a volunteer using the Vivosight OCT system, volume acquisition parameters were chosen such that the acquisition time was close to 5 minutes. Between imaging sessions, the volunteer was able to unclip from the imaging probe and relax for 2 minutes, this helped to ensure that blood flow wasn't being increasingly occluded within the region. For each volume acquisition, individual variables were modified for each modality; for svOCT these variables were the gate-width (N) and y -spacing (Δy), for cmOCT the variables are the x -spacing (Δx), and y -spacing (Δy). Memory and digitiser limitations prevented large variations in x -sampling, despite this; over-sampling was enabled down to $1.118\mu m$ in x , approximately 6.7x finer than the lateral resolution of the Vivosight system ($7.5\mu m$). To enable comparison between variables, the total number of acquired pixels remained roughly the same for each volume acquisition ($N = 6$ being the exception due to

rounding), additionally all volumes were collected with a 6x6mm FOV with 512-pixels along each A-scan. For cmOCT, kernel sizes were fixed at $13.41 - by - 12\mu m$ for each repetition. The table below summarises the parameter choices.

Variables used when optimising svOCT and cmOCT						
Scan	Modality	X-spacing (Δx)	Y-spacing (Δy)	Gate-width (N)	Kernel size (X,Z)	Acquired pixels
A	svOCT	4.470 μm	15 μm	10	(1,1)	2,748,416,000
B		4.470 μm	12 μm	8	(1,1)	2,748,416,000
C		4.470 μm	9 μm	6	(1,1)	2,749,790,208
D		4.470 μm	6 μm	4	(1,1)	2,748,416,000
E		4.470 μm	3 μm	2	(1,1)	2,748,416,000
F	cmOCT	4.470 μm	3 μm	2	(3,4)	2,748,416,000
G		2.235 μm	6 μm	2	(6,2)	2,748,416,000
H		1.118 μm	12 μm	2	(12,1)	2,748,416,000

All acquired volumes were processed following the methodology discussed in Sec. 2.1, with the exception of the wavelet-FFT filtering such that the magnitude of BTM with each scanning strategy could be observed. Two distinct vascular plexuses were visible within the volumes, a superficial plexus consisting of fine branching vessels was visible approximately $180\mu m$ beneath the skin surface and a deeper plexus with wider vessels was visible at a depth of approximately $350\mu m$. Vascular signal is still present down to a depth of $600\mu m$, however the shadowing artefacts from more superficial vessels hide the detailed morphology. Fig. 7.1 shows a B-scan from the region that has undergone surface normalisation (Flattening), Figs. 7.2 and 7.3 shows mean intensity projections that were taken across specified depths of the skin for each of the acquired volumes.

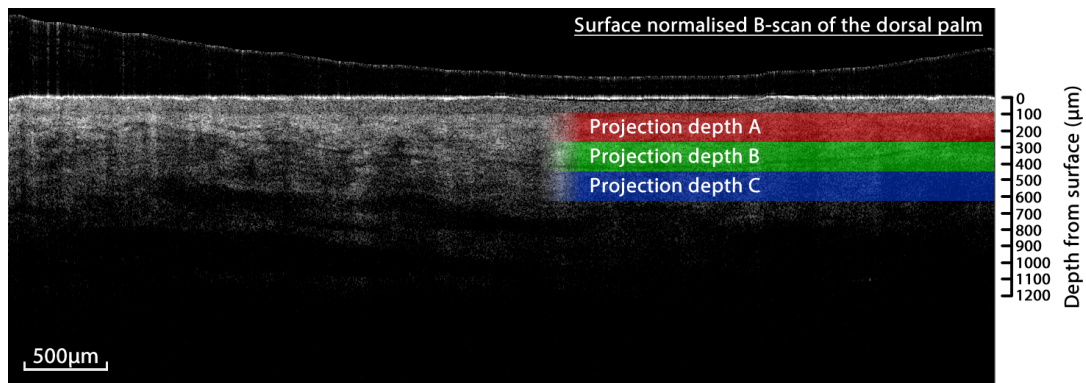


FIGURE 7.1: B-scan of the dorsal palm showing the projection depths used for Figs. 7.2 and 7.3. Epidermis is visible as a dark band that's approximately $100\mu m$ thick, vasculature is expected in the dermis just beneath this point.

Through observation of the results in Figs. 7.2 and 7.3, it is clear that the imaging protocol is able to reliably image the same area of skin in a repeatable, longitudinal fashion; despite there being 7 minutes (5 minutes imaging time + 2 minutes rest) between each acquisition start. Interestingly, with svOCT at gate-widths of 4-10 (Fig. 7.2A-D) there appears to be a loss of vascular signal in the lower quadrant of the data, visible across all projection depths. However at $N=2$ and for cmOCT (Fig. 7.3E-H), vasculature is clearly visible in this region. It is hypothesised that this may be due to localised pressure within the region, occluding the vasculature and either slowing or halting blood flow. The imaging head of the Vivosight probe is circular and presses gently against the skin thus it is likely that such bulk loss of signal is related to pressure rather than the imaging protocol.

For comparison of vascular morphology, Fig. 7.4 shows a zoomed FOV from each of the datasets. The field-of-view is shown by the green square on Fig. 7.3H.

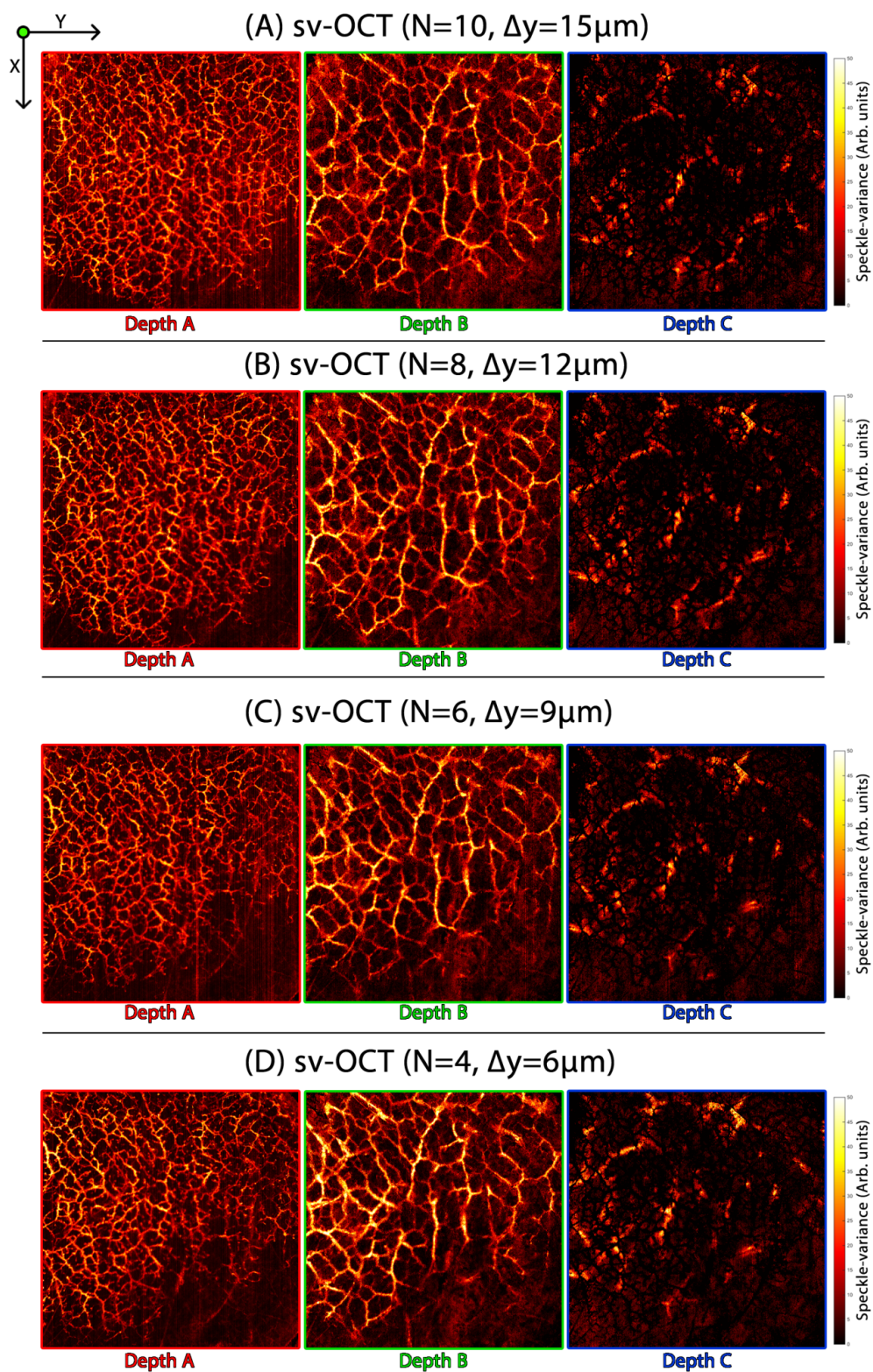


FIGURE 7.2: Mean intensity projections of collected data - projection depth is defined on Fig. 7.1. All images are 6-by-6mm. Images are subtractive across depth, that is ($\text{Depth B} = \text{Depth B} - \text{Depth A}$) and ($\text{Depth C} = \text{Depth C} - (\text{Depth A} + \text{B})$).

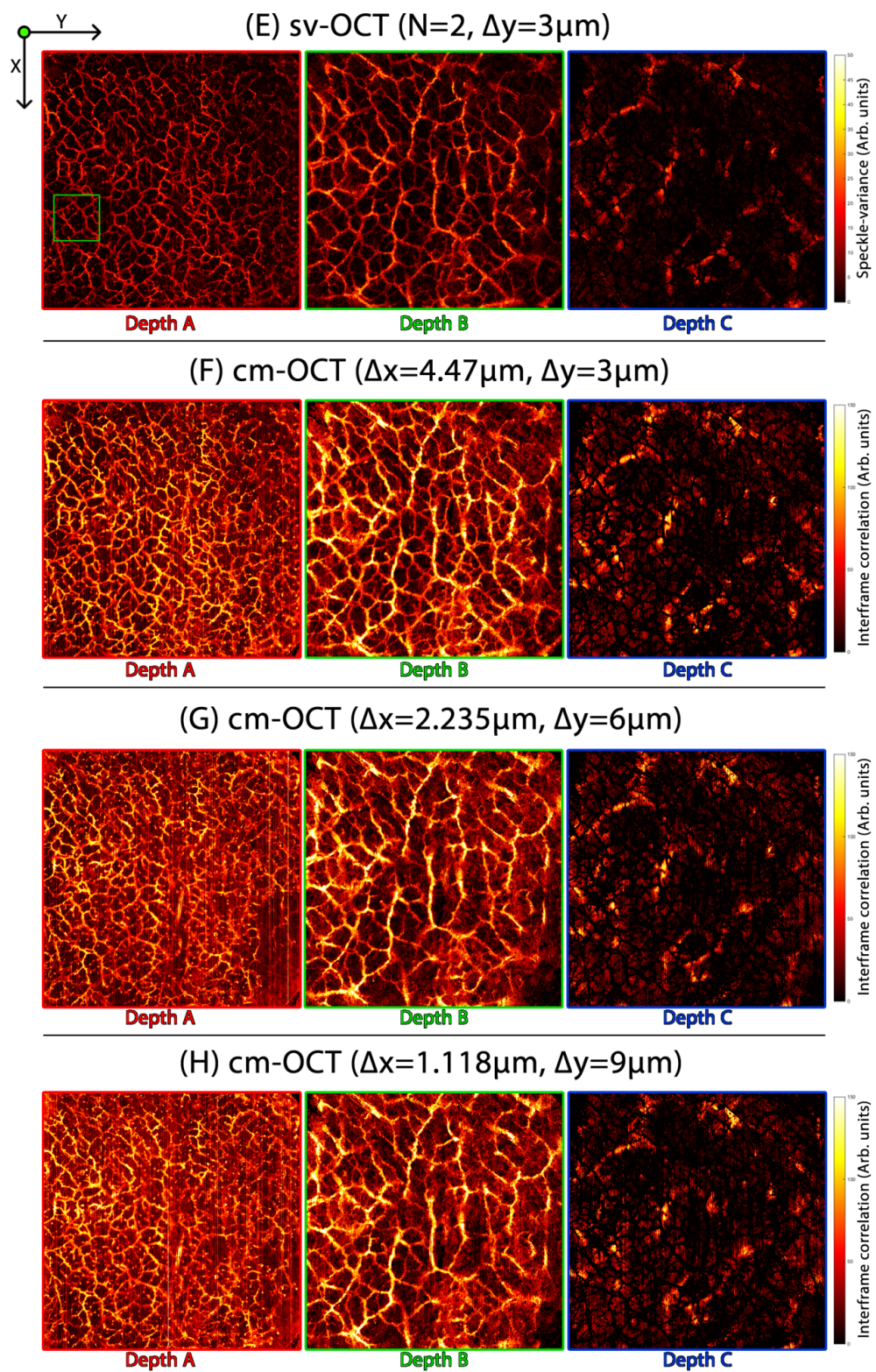


FIGURE 7.3: Continued from Fig. 7.2.

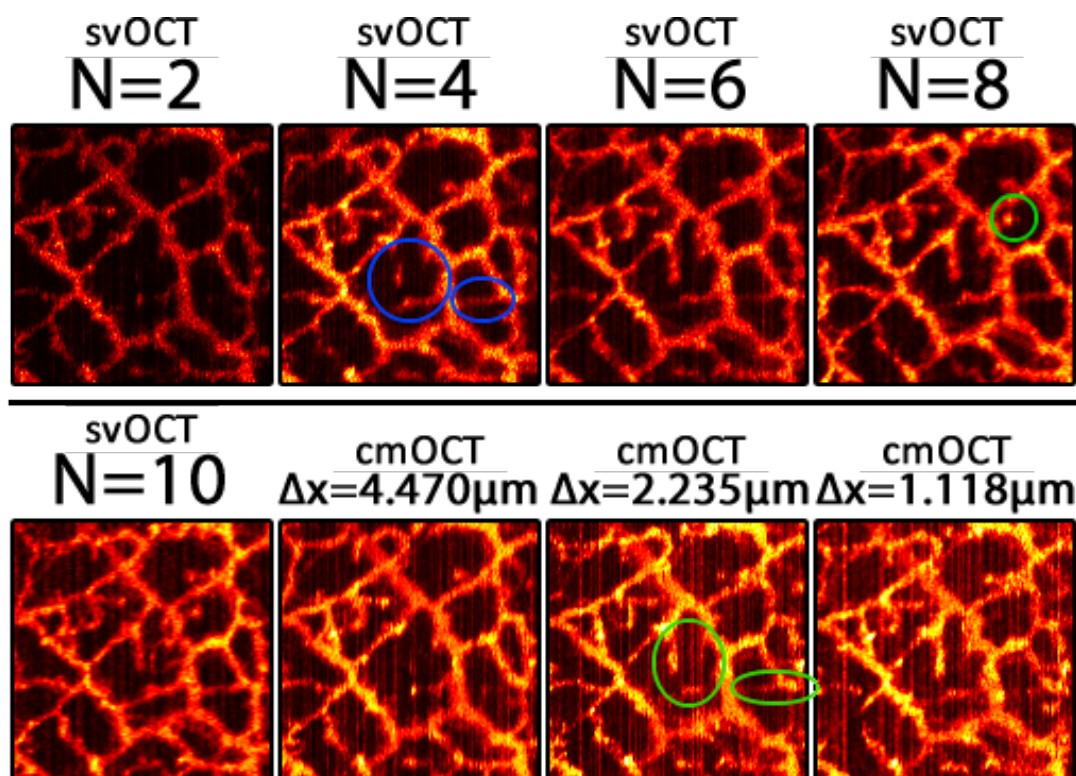


FIGURE 7.4: Zoomed sections of each of the imaging protocols (Captured from the green box FOV on Fig. 7.3E - Depth A panel)

For svOCT at $N=2$, contrast is notably poor with vessels appearing dim against the background, mean svOCT signal is 3.1246 for this volume. The mean svOCT signal rose slightly between $N=4$ (4.4427) and $N=10$ (5.5036), however there is little difference in visible vessel contrast; this suggests that the background may be contributing more to the mean signal at higher gate-widths ($N>4$). This increase in background svOCT signal may be due to longer dwell times at each spatial location, increasing the sensitivity to bulk tissue motion. Small vessels ($15 - 20\mu m$) such as those circled in blue on Fig. 7.4 are visible at gate-widths greater than 4, additional linkages (Circled in green) appear at $N>8$, suggesting that longer dwell times increase the sensitivity to very fine vasculature.

In the case of cmOCT visual vascular contrast remained relatively consistent regardless of the oversampling direction. Mean cmOCT signal increased from 22.14 at $\Delta x = 4.47\mu m$ to 22.43 at $\Delta x = 2.235\mu m$ and 24.05 at $\Delta x = 1.118\mu m$ however this increase could be attributed to increased BTM sensitivity as Δx is made smaller.

The reason for this increase in BTM sensitivity is due to a reduction in frame rate as the x-galvanometer is slowed down to facilitate oversampling in x; this results in a larger time-step between frames in which BTM can occur. Similarly to svOCT, the vessel linkages circled in green are only visible when longer dwell times are used.

It is clear that certain features are only visible when using a sufficiently high dwell time for each spatial location, this is likely due to the long decorrelation time that's typical of slow flowing blood. More specifically a dwell time equivalent to between 4-8 frames of acquisition (0.517-1.034s for the Vivosight) is shown to extract vascular contrast that was previously hidden. svOCT is advantageous in that the dwell time can be increased linearly as a function of N, such that the interframe time-step remains constant. In contrast, cmOCT in its traditional scanning pattern does not facilitate this, hence the only way to increase dwell time is to oversample in x. However as discussed above, this increases susceptibility to BTM artefacts which manifest themselves as vertical lines on the *en-face* images. The step-size Δy doesn't appear to influence the visualisation of the vasculature, providing it is maintained reasonably close to the lateral resolution limit of the machine. Given these results, the majority of scans within this thesis were captured using the svOCT protocol, using a gate-width of between 5-10 depending on the required scan speed. This helped to ensure that sufficient dwell-time was considered for the capturing of slower-flowing vessel linkages.

7.2 Quantitative capillary loop analysis

When compared to modalities such as orthogonal polarisation spectral imaging, one large advantage of OCT is that the data is 3-dimensional, with information being encoded as a function of depth. Visualising the data from an *en-face* perspective (x-y plane) enables one to evaluate the vascular morphology as a function of depth. As discussed in chapter 4, an interesting aspect of this is the potential to visualise the capillary loops themselves as they rise from the superficial vascular plexus through dermal papillae in order to provide the epidermis with nutrients. This is interesting from a clinical perspective as variations in quantitative metrics such as capillary

loop density ($CLD[\frac{Loops}{mm^2}]$) and median capillary loop area ($CLA[\mu m^2]$) have shown significant correlation to disease progression[1]. For example, avascular areas of skin as a result of local capillary loop loss are known to be indicative of early systemic sclerosis[1]. Furthermore, an increase in CLA owing to the presence of giant capillaries is one of the earliest known indicators of secondary Reynaud's phenomenon[2]. Thus the ability to accurately measure CLD and CLA is advantageous for the early detection and monitoring of certain diseases. Unfortunately, the small number of non-invasive imaging techniques that are capable of accurately quantifying CLD or CLA place strict limitations on locations that can be feasibly imaged *in-vivo*; owing to either a lack of depth penetration, or long image acquisition times. To date, video capillaroscopy (VC) is perhaps the most commonly used modality for microvasculature imaging, having being widely validated for clinical diagnostic purposes; particularly within the field of rheumatology[3]. This technique utilises a high magnification optical lens coupled with an illumination source to visualize subsurface vasculature in real time. Due to the highly scattering nature of visible light within the tissue, VC is limited to imaging areas such as the nail fold, where the capillary loops lie flat beneath a thin epithelium.

In order to evaluate the feasibility of OCT for measurements of CLD and CLA at regions unavailable to VC, OCT data sets were collected from 7 regions of the body and processed using the svOCT methodology. A MATLAB general user interface (GUI) was then designed to facilitate the extraction of quantitative metrics from the speckle-variance datasets. Firstly, the depth at which the capillaries first enter the field-of-view of the projection image was recorded and a 10-pixel deep mean-intensity projection image stored. This image was then thresholded into a binary state using Otsu's method[4], and morphological opening and closing operations were performed using a disk shaped structuring element of 2-pixel radius. These morphological operations reduced the influence of shapes that likely were noise derived but also resulted in the loss of very small ($< 10\mu m$ radius) capillary loops, likely increasing the recorded value of CLA. Lastly, connected components within

the 2D binary image were labeled and their centroid and area automatically calculated, anomalous detections could be manually removed from further consideration. From this, CLD was defined as the total number of valid detected centroids divided by the total area being imaged, a standard deviation of CLD was derived by considering the variance of CLD within 1mm^2 subsections. Median CLA was defined as the median area that each detected capillary loop occupies in the 2D *en-face* image. Eccentricity was calculated for each of the capillary loops using the `regionprops.m` function within MATLAB, with values close to zero indicating perfect circular projections and larger values indicating a more ellipsoid shape. Fig. 7.5 shows the results for the dorsal hand and ankle skin sites, while the detailed metrics of all skin sites are recorded in the table below.

Anatomical location	CLD (loops/ mm^2)	Median CLA (mm^2)	Mean eccentricity
Dorsal hand	36 ±4	0.0010±0.00052	0.62±0.28
Finger nail fold	39±12	0.0020±0.0024	0.74±0.24
Anterior elbow	24±8	0.0018±0.0020	0.65±0.27
Lower lip	15±3	0.0040±0.0025	0.80±0.24
Foot nail fold	21±6	0.0016±0.0017	0.67±0.26
Ankle	35±1	0.0029±0.0018	0.63±0.27
Dorsum of the foot	23±2	0.0020±0.0021	0.67±0.19

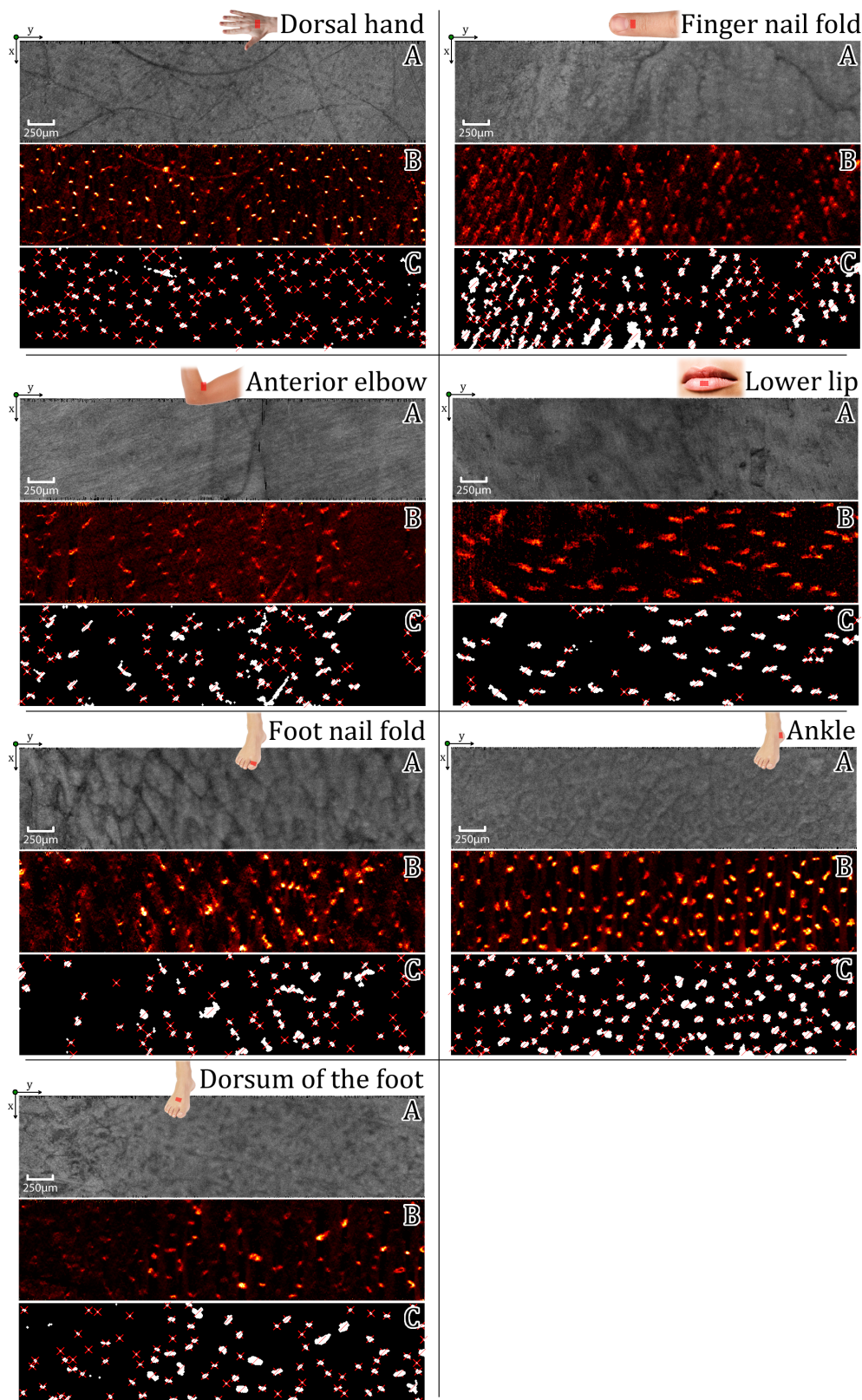


FIGURE 7.5: The results of data processing for each of the data sets. For each in turn: A) *En-face* MIP view of the structural (B-scan) data across 10-pixel depth. B) *En-face* MIP view of the speckle-variance data across a 10-pixel depth, selected as the point at which the capillary loops are first visible. C) Results of binarisation and centroid extraction, valid centroids are marked with red crosses.

Initially, it was clear that each anatomical region contained a unique capillary morphology. Furthermore, certain regions such as the finger nail fold and the anterior elbow were heterogeneous, with a changing capillary loop density at different regions of the tissue. Current literature suggests that the functional CLD within skin regions where capillary loops are arranged perpendicular to the skin surface is in the range of 14-30 per square mm[5], with the obtained data from the current study largely in agreement with this. Measurements of CLA exhibit high levels of variance, particularly in regions such as the finger nail fold or lower lip where the capillary loops are not rising perpendicular to the surface. This might suggest that a wide range of capillary sizes are present, however it is also possible that closely positioned loops are being anomalously detected as a single large loop due to the chosen threshold (The threshold was selected manually using the GUI shown in Fig. 8.3). Furthermore for regions such as the nail fold and lower lip where the capillaries rise at an angle to the surface, measurements of CLA are being inflated due the high eccentricity of the projections from an *en-face* perspective. For these regions, performing the imaging projection at an angle perpendicular to the loop direction would likely lead to more accurate measurements of CLA. Overall, care must be taken to correctly optimise both the binary threshold and angle of projection if accurate metrics are to be extracted. In future, more advanced methods of capillary loop detection could be performed using techniques such as multi-scale Hessian based spot enhancement, which has demonstrated the ability to effectively discern between overlapping "spots" in 2D gel electrophoresis images[6], which are close in appearance to *en-face* OCTA images of capillary loops.

7.3 Vascular response towards applied surface pressure

One fundamental limitation of the svOCT technique is the observed shadowing effect beneath detected vasculature, caused by the forward scattering of light. This shadowing limits visualisation of deep vascular plexuses as they may be overshadowed by more superficial vasculature. One proposed method of alleviating this effect is to narrow the superficial vasculature through applied pressure. Theoretically

the suspension or slowing of flow within the more superficial vasculature will lower the svOCT signal from that region, reducing the prevalence of shadowing and improving the visualisation of deeper vasculature.

In order to evaluate the effect of pressure on the local vasculature, 9 svOCT volumes ($\Delta x = \Delta y = 10\mu m$; $X = Y = 4mm$; $N = 3$) were collected from the dorsal hand, with each volume taking 56 seconds to acquire and process. Following each volume collection, the clamp which holds the Vivosight imaging probe was lowered vertically by a single click of its vertical stage such that an increasing, but unknown amount of pressure was applied to the imaging region. To help ensure that the pressure was applied uniformly across the skin, imaging was performed through a plastic disk which was in contact with the skin surface. Following data collection each volume was processed using the aforementioned svOCT methodology, and 3D depth resolved images corresponding to $313 - 625\mu m$ in depth with respect to the surface of the plastic disk were calculated.

Fig. 7.6 shows the effect of pressure application on the resulting vascular visualisation. It is clear that vascular signal is lost as pressure is increased, as evidenced by the almost complete lack of vascular signal in Fig. 7.6I/J. A loss of vascular signal in this context means that the flow rate of blood within the vessel has reduced, and is no longer sufficiently decorrelating the OCT signal over the dwell time of $N=3$ frames. Interestingly, vascular signal corresponding to superficial vessels and capillary loops (Red colouration) persists up to Fig. 7.6H and appears to be reducing at a similar rate to that of the deeper plexus (Green/blue colouration), indicating that the superficial vasculature is not necessarily occluded before the deeper vessels. Furthermore, as the deeper plexus is also being occluded by the applied pressure, it is unclear if any additional information regarding the deeper morphology has been attained. Notably the deeper, green/blue vessels that remain in Fig. 7.6H are presenting a thinner and more clearly defined diameter than the same vessels in Fig. 7.6B/C.

It is worth noting that skin surface furrows and corrugations are easily visible on Fig. 7.6I/J in the absence of vasculature. These are detected anomalously as a

result of a noise-dominated (High temporal variance) shadow being cast into the dermis beneath the signal-saturating surface furrows. While these shadows are normally removed through the binarisation and masking procedure, any vasculature that lies beneath the furrow would also be removed. One method of removing these artefacts without attenuating the local vasculature involves the use of an optical coupling gel on the skin surface in order to eliminate the shadowing beneath the surface features[7].

For future work, it may be beneficial to increase the dwell time at each spatial location (increase N). This would theoretically facilitate the visualization of slow flowing / stationary blood which has a longer decorrelation period than faster flowing blood[8]. In addition, quantitative pressure application; with a force transducer for example, may allow for measurements of internal vascular pressure by considering the point at which flow decreases below the detectable threshold for a given dwell time. It may also be useful to consider the relationship between surface deformation and the applied vertical pressure, similar to the analysis conducted in chapter 6 which looked at surface deformation in response to applied strain.

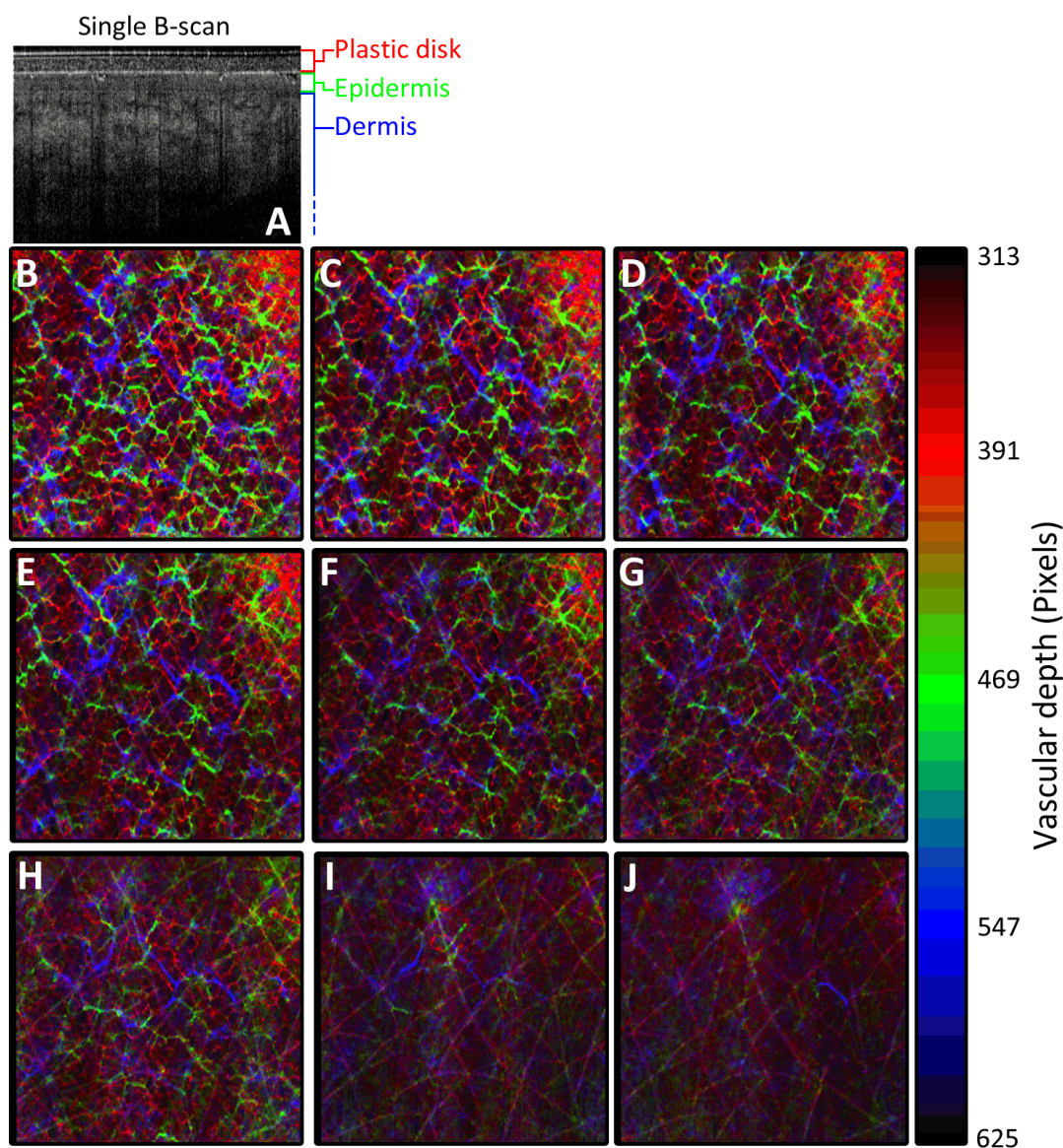


FIGURE 7.6: Effects of pressure application on the svOCT signal. A) $4 \times 2 \text{ mm}$ single B-scan showing the plastic disk and skin layers. B-J) $4 \times 4 \text{ mm}$ *en-face* depth resolved images calculated between the depths of $313 - 625 \mu\text{m}$, with pressure being incremented by a single click of the vertical stage between each volume acquisition.

7.4 Vascular response towards surface temperature

A second method of inducing superficial vasoconstriction involves the application of cold to the external surface of the skin. It has long been known that vasculature close

to the skin surface undergoes autonomic vasoconstriction in response to a fall in external temperature, due to the body's inherent homeostasis mechanisms. It is thought that this vascular response operates through a combination of central control (The temperature of blood to the brain), reflex control (Nervous stimulation within the skin) and local control (Direct regulation of the local muscles)[9], [10]. Knowledge regarding the magnitude of this effect was important for all *in-vivo* imaging, as vasoconstrictive effects could be largely responsible for large variation in vessel density if temperature is not carefully controlled. For a preliminary evaluation of this effect, the OCT imaging probe was positioned in the centre of a volunteer's dorsal palm, ice-packs were positioned immediately adjacent to the scanning site in order to gradually lower the temperature. Immediately following the ice-pack application, 9 svOCT volumes were collected using the same imaging parameters as the pressure test without use of the plastic disk. With each scan taking approximately 1 minute to acquire, the overall imaging corresponded to a total observation time of ≈ 9 minutes.

Fig. 7.7 shows the resulting *en-face*, depth resolved OCT images with 1 minute between each image. Interestingly a slight loss in svOCT signal from superficial (Red) vasculature is visible in the minute following the placement of the icepack (Fig. 7.7A) but this quickly recovers and is not visible on the 3-minute scan (Fig. 7.7C). Furthermore a second loss of vascular signal is apparent after 9 minutes (Fig. 7.7I), it is unclear if this second occurrence of vasoconstriction persists as imaging was stopped after 9 minutes. Though preliminary, these observations are in agreement with previously observed findings. The initial (0-1 minute) loss of signal could be attributed to a rapid transient vasoconstriction that is known to occur in response to a rapid drop in external temperature[9], [11]. A slower, sustained vasoconstriction has been reported to occur after 5-10 minutes in cases where the flow is unrestricted[9], this potentially explains the loss of signal after 9 minutes in the above tests.

One limitation of this brief study was that the thermal shock of the ice-pack was not quantified, that is the external temperature of the ice. Indeed the observed response is very likely to be a function of the induced temperature and application method and it may be useful to consider measurement using alternate methods of

inducing a temperature drop; such as partially submerging the hand in water at a fixed temperature. It is also important to understand how the ambient (room) temperatures affect angiographic scans, thus it may also be useful to quantify the vascular signal at a range of room temperatures.

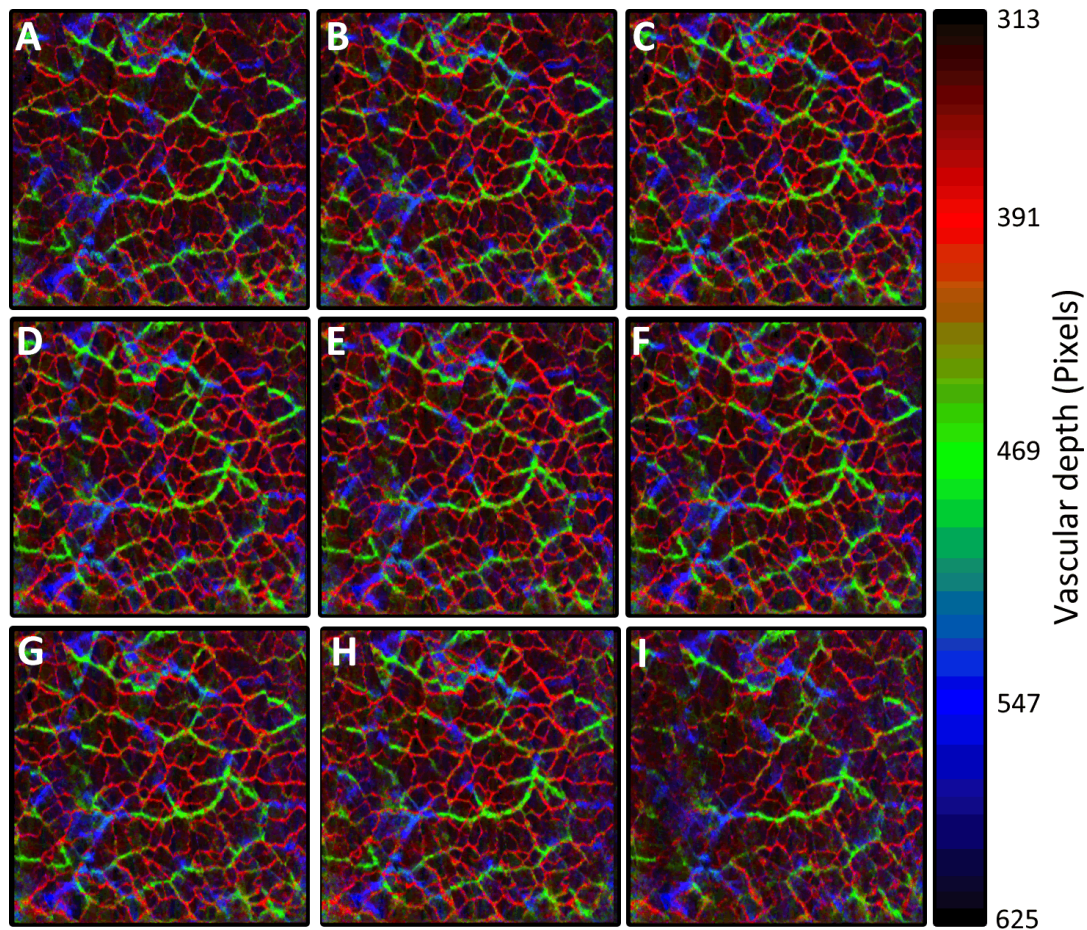


FIGURE 7.7: Effects of temperature on the svOCT signal. *En-face* svOCT images of the dorsal palm showing depth encoded vascular data in response to an ice pack application on the hand. A-I) Progression of the signal in 1 minute intervals following the icepack application.

7.5 Visualisation of wound healing processes

The ability to transiently visualise the stages of wound healing allows appropriate treatments and therapies to be designed such that adequate healing is achieved. Indeed structural OCT has already been demonstrated for the monitoring and assessment of wound healing stages[12], demonstrating comparable performance to that of histological analysis[13]. Furthermore, vascular remodeling plays an essential role in tissue repair during the wound healing process[14], consequently the morphology of local vasculature can be used as an indication of wound treatment efficacy[15]. Thus through utilisation of angiographic OCT techniques such as svOCT, information regarding angiogenesis during wound healing is obtained, with the structural information still available for consideration.

Fig. 7.8 shows the additional information that is gained by considering angiographic images of late-stage wound healing. Here, a $6 \times 6 \times 2 \text{mm}$ volume of skin was captured and processed using the svOCT methodology ($\Delta x = \Delta y = 10 \mu\text{m}$, $N = 7$). Despite being a small puncture wound, vascular sprouting and angiogenesis are visible at the receding edges of the scab. From an external perspective, localised erythema is visible around the wound (Fig. 7.8A) however the svOCT image provides a much more detailed view of the capillary morphology (Fig. 7.8C). Future work may aim to observe the progression of such wounds longitudinally over time.

Fig. 7.9 shows an earlier stage of the wound healing process, immediately after the removal of an ingrown hair follicle a $4 \times 4 \times 2 \text{mm}$ volume was captured using OCT and processed using the svOCT methodology ($\Delta x = \Delta y = 5 \mu\text{m}$, $N = 10$). The large bubble of exudate directly above the wound is transparent (non-scattering) by nature, and hence appears dark on both the structural B-scan and en-face svOCT image. Interestingly a pool of blood has accumulated in the dark region within the wound, and is highlighted as a bright area within the bubble on the svOCT image (Fig. 7.9B). Furthermore a loss of vascular signal in the area directly surrounding the wound supports the fact that these images are captured during the early inflammatory phase (1-10 minutes), where vasoconstriction occurs in order to prevent any

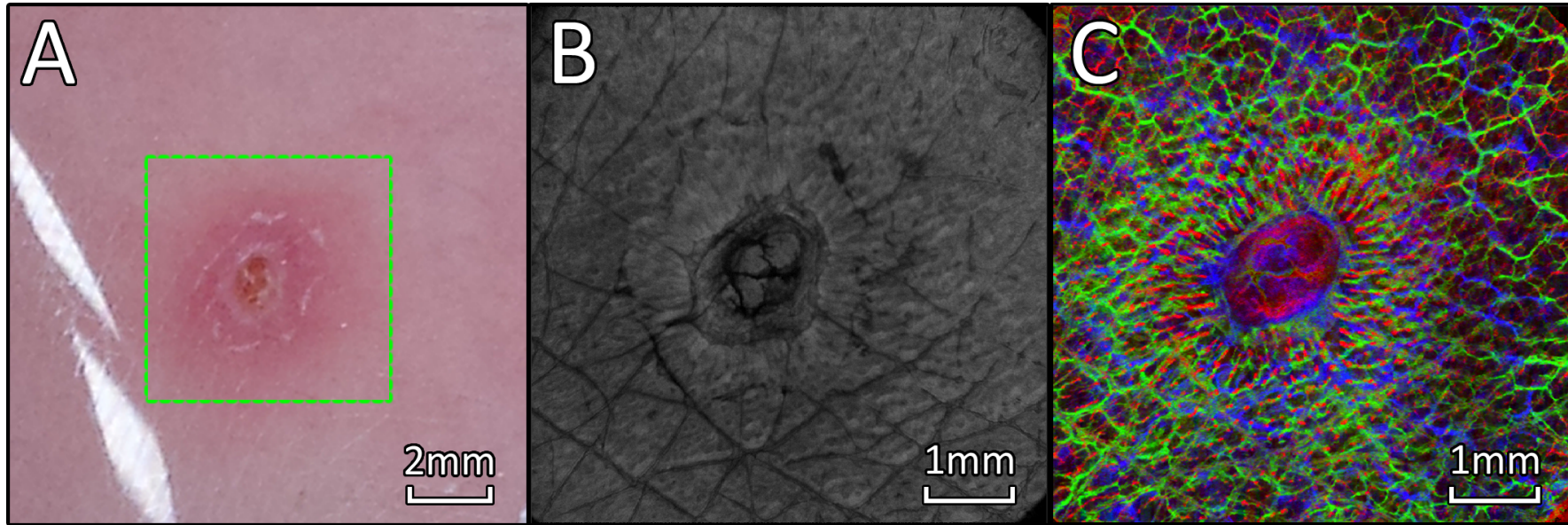


FIGURE 7.8: svOCT as a tool for visualising the wound healing progress. A) *En-face* photograph of a puncture wound approximately 4-5 days into the recovery period. Box signifies the location of B & C. B) *En-face* structural OCT projection of the skin over a depth of $200\mu\text{m}$ to $500\mu\text{m}$. C) *En-face* svOCT depth projection over a depth of $200\mu\text{m}$ to $500\mu\text{m}$. Red vessels are $200 - 300\mu\text{m}$ in depth, green vessels are $300 - 400\mu\text{m}$ in depth and blue vessels are $400 - 500\mu\text{m}$ in depth.

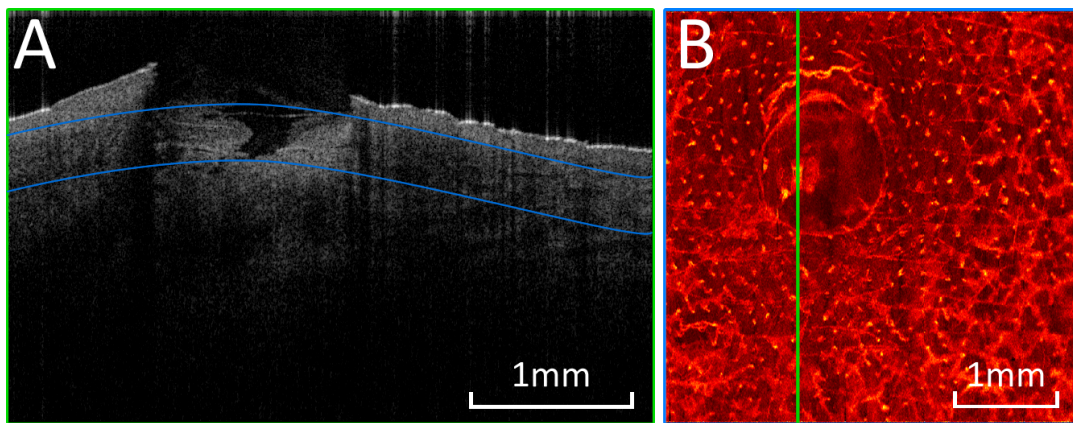


FIGURE 7.9: OCT visualisation following the removal of an ingrown hair follicle. A) B-scan of the region showing a large bubble of exudate directly above the wound. Blue lines signify the projection depth of B. B) *En-face* svOCT mean intensity projection of the 4x4mm region showing the local vasculature and capillary loops (Dots). Vertical green line signifies the position of the B-scan in A.

further blood loss. One drawback of this technique is the limited field-of-view, restricting visualization to relatively small lesions ($\approx 8 \times 8 \text{mm}$ maximum) however the following section discusses a method which can potentially be used to rectify this problem.

7.6 Enhanced field-of-view through vascular mosaicing

One limitation of the svOCT technique is the limited field-of-view (FOV) of the respective 3D datasets. This becomes increasingly problematic when frame-rate or dwell time restrictions are placed on the data, owing to either a particularly unstable area of skin or the need to detect slower flowing blood. While still maintaining a reasonable resolution, the simplest compromise is to reduce the image width (X) of the B-scans such that the frame-rate increases and the FOV decreases. This effect can be balanced by proportionally increasing the volume width (Y), however this results in wide rectangular shaped svOCT volumes which are often difficult to interpret.

A second method of offsetting the FOV loss due to frame-rate requirements involves mosaicking multiple svOCT datasets together such that their combined volume encompasses a greater area of skin. There must be some degree of overlap

between the volumes allowing for registration following processing. This OCT extension has previously been demonstrated for the retina[16] ($\approx 1.25\text{mm}$ overlap) and the volar forearm[17] (1.5mm overlap) with promising results.

In order to evaluate the efficacy of svOCT mosaicking using the Vivosight OCT system, 21 individual $4 \times 4 \times 2\text{mm}$ volume scans were collected from the dorsal hand using rapid acquisition settings ($\Delta x = \Delta y = 15\mu\text{m}$, $X = Y = 4\text{mm}$, $N = 2$). With these settings each volume took approximately 25 seconds to acquire, with the entire mosaic being captured in 512 seconds. Between scans, the imaging probe was manually aligned to a grid of dots which were stamped onto the skin (Fig. 7.10). The volumes were aligned based on their expected position (pink dot) with the resulting placement being refined using the MosaicJ plugin of FIJI[18].

Fig. 7.10 shows the resulting mosaic and accuracy achieved through simple manual repositioning of the imaging probe. Variations from the expected angle and position of the probe with respect to the skin are readily apparent, however the registration algorithms have corrected for these offsets. In addition, the averaging operation which was used to flatten overlapping sections has caused a visible blurring effect, likely due to variations in the localised noise. Despite these issues, the resulting wide field svOCT image provides clinically relevant information regarding the morphology of the microvasculature over a total area of $\approx 200\text{mm}^2$. This could be particularly beneficial when searching for abnormal vascular morphology of lesions which are not surface presenting.

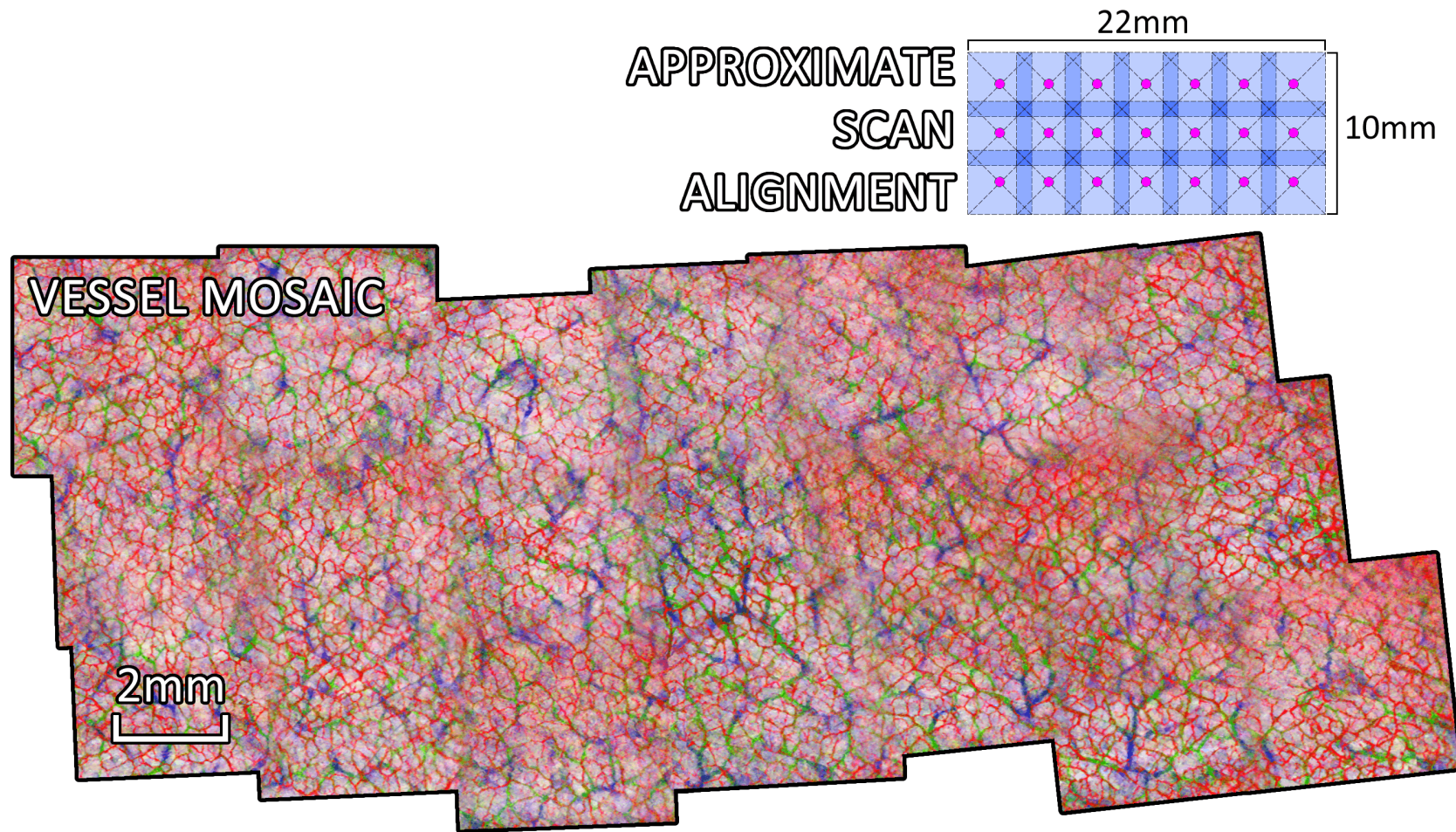


FIGURE 7.10: Top) Pattern of dots (pink) which were stamped onto the skin prior to mosaic image acquisition. Each dot has a spatial separation of 3mm from neighbour dots, corresponding to an imaging overlap of 1mm. Bottom) svOCT mosaic comprised of 21 individual $4 \times 4 \times 2 \text{mm}$ OCT volumes. Data is linearly depth encoded from red (160 – 360 μm) to green (360 – 560 μm) to blue (560 – 650 μm) to white (> 650 μm).

References

- [1] A. Scheja, A. Akesson, I. Niewierowicz, L. Wallin, and M. Wildt, "Computer based quantitative analysis of capillary abnormalities in systemic sclerosis and its relation to plasma concentration of von Willebrand factor", *Ann Rheum Dis*, pp. 52–56, 1996 (cit. on p. 216).
- [2] H. J. Anders, "Differentiation between primary and secondary Raynaud's phenomenon: a prospective study comparing nailfold capillaroscopy using an ophthalmoscope or stereomicroscope", *Annals of the Rheumatic Diseases*, vol. 60, no. 4, pp. 407–409, Apr. 2001, ISSN: 00034967. DOI: 10.1136/ard.60.4.407 (cit. on p. 216).
- [3] F. Gallucci, R. Russo, R. Buono, R. Acampora, E. Madrid, and G. Uomo, "Indications and results of videocapillaroscopy in clinical practice.", *Advances in medical sciences*, vol. 53, no. 2, pp. 149–57, Jan. 2008, ISSN: 1896-1126. DOI: 10.2478/v10039-008-0038-4 (cit. on p. 216).
- [4] N. Otsu, "A Threshold Selection Method from Gray-Level Histograms", *IEEE Transactions on Systems, Man, and Cybernetics*, vol. 9, no. 1, pp. 62–66, 1979, ISSN: 0018-9472. DOI: 10.1109/TSMC.1979.4310076 (cit. on p. 216).
- [5] J. Serup, G. Jemec, and G. Grove, *Handbook of Non-Invasive Methods and the Skin, Second Edition*. CRC Press, 2006, Pg. 682, ISBN: 1420003305 (cit. on p. 219).
- [6] S. Shamekhi, M. Hossein, M. Baygi, B. Azarian, and A. Gooya, "A novel multi-scale Hessian based spot enhancement filter for two dimensional gel electrophoresis images", *Computers in Biology and Medicine*, vol. 66, pp. 154–169, 2015. DOI: 10.1016/j.compbiomed.2015.07.010 (cit. on p. 219).

- [7] Y. M. Liew, R. A. McLaughlin, F. M. Wood, and D. D. Sampson, "Motion correction of in vivo three-dimensional optical coherence tomography of human skin using a fiducial marker.", *Biomedical optics express*, vol. 3, no. 8, pp. 1774–86, Aug. 2012, ISSN: 2156-7085. DOI: 10.1364/B0E.3.001774 (cit. on p. 221).
- [8] H. Ullah, A. Mariampillai, M. Ikram, and I. A. Vitkin, "Can temporal analysis of optical coherence tomography statistics report on dextrorotatory-glucose levels in blood?", *Laser Physics*, vol. 21, no. 11, pp. 1962–1971, Sep. 2011, ISSN: 1054-660X. DOI: 10.1134/S1054660X11190285 (cit. on p. 221).
- [9] S. Richards, *Temperature Regulation*. Springer, 2013, p. 212, ISBN: 1489927891 (cit. on p. 223).
- [10] *Peripheral Circulation in Man*, Symposium, John Wiley & Sons, 2009, p. 352, ISBN: 0470714875 (cit. on p. 223).
- [11] J. L. BUCHANAN, J. J. CRANLEY, and R. R. LINTON, "Observations on the direct effect of cold on blood vessels in the human extremity and its relation to peripheral vascular disease.", *Surgery*, vol. 31, no. 1, pp. 62–73, Jan. 1952, ISSN: 0039-6060. DOI: 10.5555/URI:PII:0039606052901955 (cit. on p. 223).
- [12] M. Kuck, H. Strese, S. A. Alawi, M. C. Meinke, J. W. Fluhr, G. J. Burbach, M. Krah, W. Sterry, and J. Lademann, "Evaluation of optical coherence tomography as a non-invasive diagnostic tool in cutaneous wound healing.", *Skin research and technology : official journal of International Society for Bioengineering and the Skin (ISBS) [and] International Society for Digital Imaging of Skin (ISDIS) [and] International Society for Skin Imaging (ISSI)*, vol. 20, no. 1, pp. 1–7, Feb. 2014, ISSN: 1600-0846. DOI: 10.1111/srt.12077 (cit. on p. 225).
- [13] N. S. Greaves, B. Benatar, S. Whiteside, T. Alonso-Rasgado, M. Baguneid, and A. Bayat, "Optical coherence tomography: a reliable alternative to invasive histological assessment of acute wound healing in human skin?", *The British journal of dermatology*, vol. 170, no. 4, pp. 840–50, Apr. 2014, ISSN: 1365-2133. DOI: 10.1111/bjd.12786 (cit. on p. 225).

-
- [14] I. Kumar, C. A. Staton, S. S. Cross, M. W. R. Reed, and N. J. Brown, "Angiogenesis, vascular endothelial growth factor and its receptors in human surgical wounds.", *The British journal of surgery*, vol. 96, no. 12, pp. 1484–91, Dec. 2009, ISSN: 1365-2168. DOI: 10.1002/bjs.6778 (cit. on p. 225).
- [15] L. A. DiPietro, "Angiogenesis and scar formation in healing wounds.", *Current opinion in rheumatology*, vol. 25, no. 1, pp. 87–91, Jan. 2013, ISSN: 1531-6963. DOI: 10.1097/B0R.0b013e32835b13b6 (cit. on p. 225).
- [16] H. C. Hendargo, R. Estrada, S. J. Chiu, C. Tomasi, S. Farsiu, and J. a. Izatt, "Automated non-rigid registration and mosaicing for robust imaging of distinct retinal capillary beds using speckle variance optical coherence tomography.", *Biomedical optics express*, vol. 4, no. 6, pp. 803–21, Jun. 2013, ISSN: 2156-7085. DOI: 10.1364/B0E.4.000803 (cit. on p. 228).
- [17] J. Enfield, E. Jonathan, and M. Leahy, "In vivo imaging of the microcirculation of the volar forearm using correlation mapping optical coherence tomography (cmOCT)", vol. 2, no. 5, pp. 1184–1193, 2011. DOI: 10.1002/jbio.201000103/abstract (cit. on p. 228).
- [18] P. Thévenaz and M. Unser, "User-friendly semiautomated assembly of accurate image mosaics in microscopy.", *Microscopy research and technique*, vol. 70, no. 2, pp. 135–46, Feb. 2007, ISSN: 1059-910X. DOI: 10.1002/jemt.20393 (cit. on p. 228).

Chapter 8

General discussion and conclusions

8.1 General discussion

The primary focus of this PhD research has been tied to the development and application of angiographic OCT (OCTA) using a commercial OCT system (Vivosight® - Sec. 2.1.1). The basic principles and current approaches towards OCTA in the literature were introduced in chapter 1, notably that there are three primary approaches towards extracting angiographic information from the interferometric OCT signal, those that utilise the intensity of the signal, those that utilise the phase of the signal and those that use a combination of both (Complex). The Vivosight system uses a swept-source 1305nm Axsun laser, which exhibits poor phase stability between sequentially acquired A-scans, making phase or complex based measures of angiographic signal unreliable. Thus it was decided that intensity based methods would be the most logical approach given the chosen OCT hardware. Of the considered intensity-based OCTA methods, speckle-variance OCT (svOCT) and correlation-mapping OCT (cmOCT) stood out as being both rapid to process and achievable to implement.

Thus, the first challenge was in the implementation of these acquisition algorithms to the existing Vivosight OCT hardware, which lacked the ability to acquire multiple sequential frames at the same spatial location in a step-wise manner; a requirement for both svOCT and cmOCT.

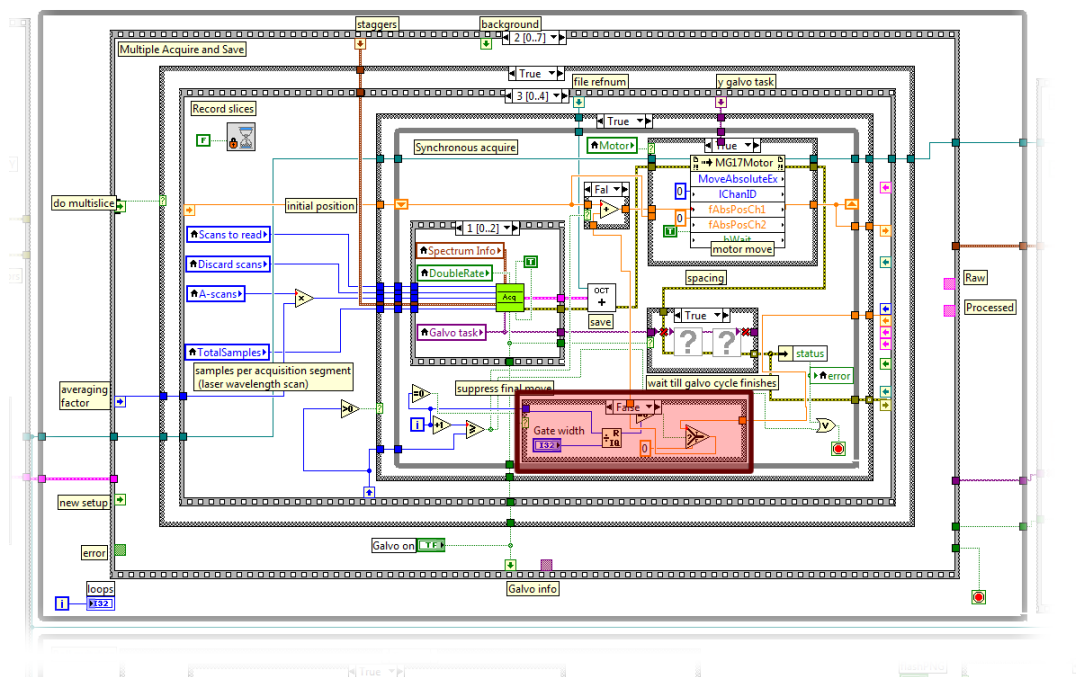


FIGURE 8.1: Red box) Region of LabView control code which was modified to facilitate a gate-width of frames acquired at the same spatial location. The y-galvanometer is only fed a stepping voltage when the frame-acquisition is a multiple of the gate-width.

Thankfully the manufacturer of the Vivosight system (Michelson Diagnostics Ltd, Orpington, Kent, UK) were able to provide a LabView framework and the associated *.dll* control files for the Vivosight hardware, which were modified such that repeat scanning of the same location could be performed (Fig. 8.1 shows an example of one such modification). Initially, the datasets acquired using these simple scanning strategies were highly susceptible to motion artefacts both as a result of patient and operator movement. Thus, developments in both the hardware and software of the scanning protocol were made, including: a fixable clamp for imaging (Sec. 2.1.1), in-plane and out-of-plane motion correction/compensation (Sec. 2.1.3), noise masking (Sec. 2.1.4), skin flattening (Sec. 2.1.5) and wavelet-fft filtering (Sec. 2.1.6).

Once the supporting algorithms were in place, angiographic OCT imaging was readily available on the Vivosight OCT system. It is worth noting that by this time, an alternative means of performing angiographic imaging had been developed by Michelson Diagnostics, however the two approaches had several key differences.

The acquisition time was notably shorter for OCTA performed using the Michelson Diagnostics algorithm, however the resulting image quality and vessel contrast were lower than that of the algorithm developed here. Thus the algorithm supplied with the Vivosight was ideal for rapid measures of vascularisation but did not facilitate studies of the vessel morphology. Fig. 8.2 shows a brief comparison between the two methods, as expected there is a notable trade-off between imaging time and image quality.

To further refine the processing methodology discussed here, a qualitative comparison between svOCT and cmOCT was performed with the goal of optimising the scan settings (Sec. 7.1). This study highlighted the importance of having a sufficiently long dwell time such that slower flowing blood can be detected, furthermore it highlighted how the dwell time of svOCT was flexible and could be increased simply by increasing the gate-width (N). As such svOCT was selected as the primary data acquisition/processing protocol for the remainder of the work. Investigations into the effects of temperature (Sec. 7.4) and applied surface pressure (Sec. 7.3) were also performed, highlighting the need for controlled, consistent experimental conditions to be maintained.

Chapter 3 covered the first major experiment conducted using the aforementioned OCTA methodology. Here, the initial goal was to investigate whether OCT has sufficient depth penetration in order to capture the microcirculation within subcutaneously implanted murine fibrosarcoma tumours. OCTA was able to capture the superficial vasculature within tumours solely expressing differing isoforms of VEGF (VEGF120 and VEGF188) and could even differentiate differences in vessel depth and morphology between the resulting networks. One notable limitation of this work was the use of gaseous anaesthesia, which was used during imaging in order to reduce the prevalence of motion artefacts. It was hypothesised that pronounced changes in day to day vessel density could be caused by the use of such anaesthetic, limiting the ability of OCTA to quantify subtle changes in the circulation over time. Furthermore to stabilise the region, physical contact had to be made between the OCT imaging probe and the surface of the tumour, applying an unknown

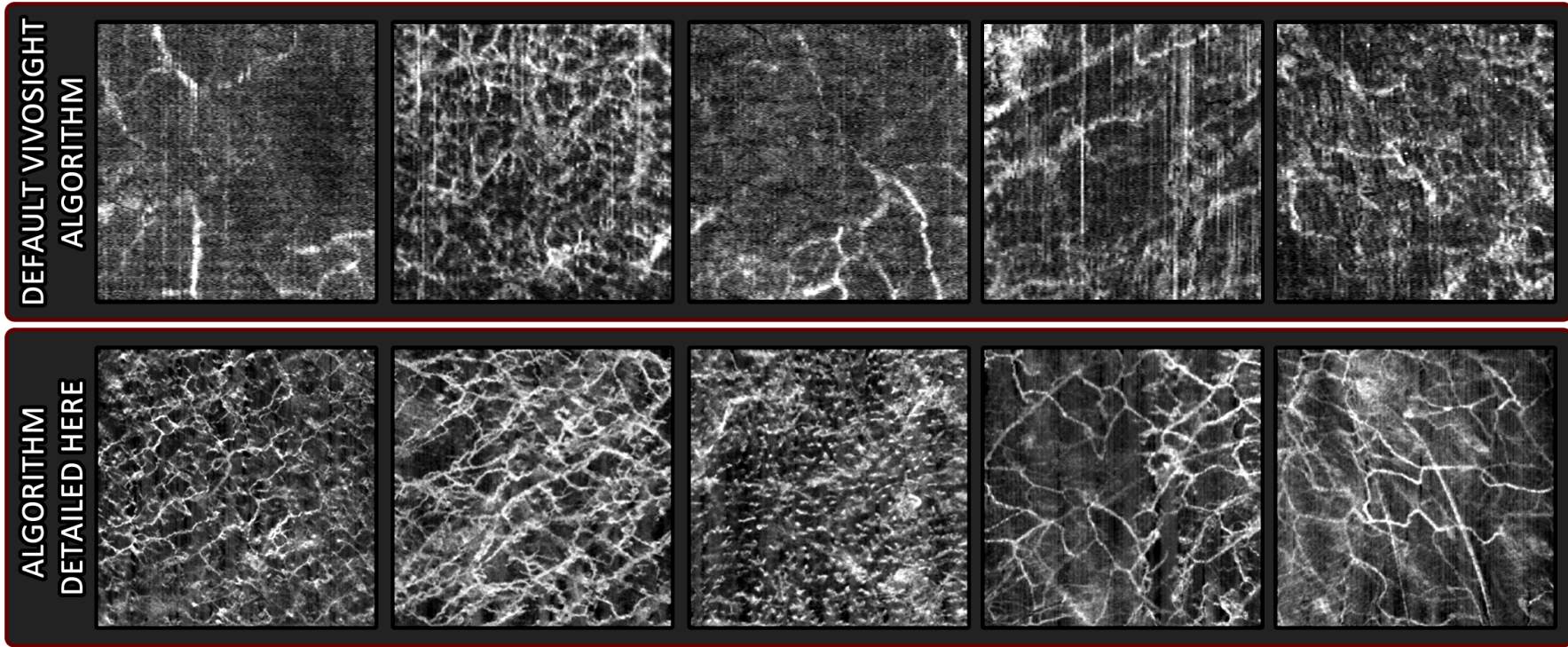


FIGURE 8.2: Top row) OCTA images of vasculature within either the cubital or popliteal fossa acquired using the default OCTA algorithm provided by Michelson Diagnostics (Marketed as "dynamic OCT"). Images were acquired and processed within ≈ 30 seconds. Bottom row) OCT images of vasculature within either the cubital or popliteal fossa acquired using the svOCT algorithm discussed here. Images were acquired within ≈ 100 seconds but required further offline processing (≈ 120 seconds to perform registration, correlation optimisation, speckle-variance, skin-flattening and Wavelet-FFT filtering). All images are 4x4mm and do not correspond to the same regions of skin.

amount of vertical pressure to the region. Such transient changes in vessel density were not present during the window-chamber study (Chapter 5), which did not utilise anaesthetic for imaging or apply vertical pressure to the vessels with the OCT probe, supporting the hypothesis that one of these factors may be the cause for day-to-day changes in visible vascularity. Despite these limitations, the ability of OCTA to transiently and non-invasively observe such tumours was demonstrated, notably the aggressive phenotype of the VEGF120 expressing tumours could be clearly seen. Providing the limitations are addressed; perhaps through application of a higher imaging-speed, future work could attempt to longitudinally observe the response of these tumours to anti-angiogenic therapy. One of the initial aims of this study was to see if OCTA could provide any additional insight into resistance mechanisms that arise within such tumours in response to therapy, however due to the complications with longitudinal imaging this was unfortunately out of the scope of this project.

While the experiments conducted in chapter 3 directly correlated OCT with histology sections for the purposes of measuring layer thickness and tumour infiltration, it was infeasible to align corresponding vessel segments between the modalities. Thus the accuracy of OCTA's vessel detection remained unclear. Chapter 5 set out to investigate this through direct correlation between intravital OCTA and intravital light microscopy (Termed IVM). Sequentially acquired *en-face* images of the circulation inside dorsal skin fold window chambers (DSWC's) with both OCTA and IVM allowed for subpixel image registration to be applied between the two modalities, aligning vessel segments to a high degree of accuracy. Quantitative skeletonisation was then performed on both images, allowing for large scale vessel comparison to be performed independent of manual measurement for the first time. Comparison of vessel segments which were visible to both OCTA and IVM mirrored results from the literature, with OCT tending to overestimate smaller vessel diameters. We hypothesised that the threshold of this effect is likely to be a function of both the lateral resolution (δx) and sampling density (Δx and Δy) of the OCT scans, and thus care must be taken when measuring small vessel diameters. Interestingly OCT exhibited

several key advantages over IVM during the course of this study. Firstly OCT detected higher vessel densities overall, particularly within tumours. Secondly, OCT remained insensitive to inactive vessels containing haemoglobin which were not actively flowing, contrast which is typically achieved using invasive fluorophores for flow-sensitive IVM. For these reasons, OCT offers a unique perspective of the tumour microenvironment and will likely remain a useful tool for window chamber studies in the future, in addition to being able to image subcutaneous tumours directly as discussed in chapter 3.

When translating the OCTA technique into human studies, one key difference in the vessel morphology quickly became apparent. At superficial depths within human skin, particularly regions with a thicker epidermis, a mottled texture of dots were visible in the *en-face* angiographic images. These dots were being caused by localised flow within the capillary loops, which were rising within dermal papillai, protrusions of the dermis up into the epidermis. Such loops were not visible in murine studies, likely due to the far thinner epidermis negating the need for any dermal papillai. An initial study into the capillary morphology at numerous sites was conducted (Sec. 7.2) with the aim of attempting to visualise capillary loops at sites typically inaccessible to video capillaroscopy (VC). For this a MATLAB GUI (Fig. 8.3) was developed in order to perform rapid segmentation and measurement of the loops. In general OCTA appeared to be effective at visualising the capillary loops at a wide range of locations across the body, however one limitation of the study was in areas where capillaries rise at an angle, common in regions such as the finger and toe nail fold tissue. The *en-face* segmentation of such loops would result in inflated density measurements, due to them not being segmented perpendicular to their axis. The rectification of which, perhaps through angled segmentation could be a focus of future work targeting the capillary loops.

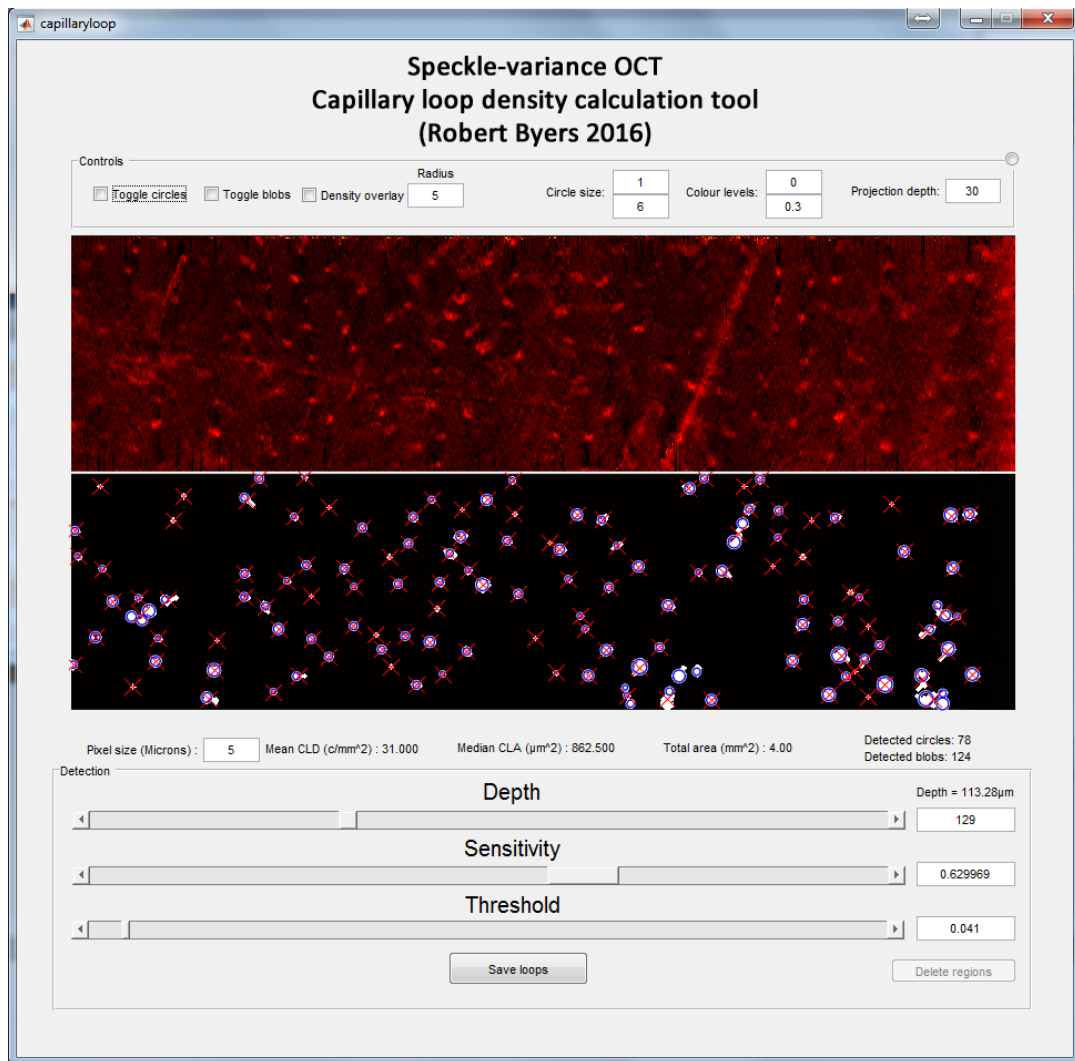


FIGURE 8.3: Image captured from the MATLAB GUI which was developed for purposes of capillary loop measurement. Given a svOCT dataset the user could then manually define the visual depth of the capillary loops, and specify a sensitivity parameter for *en-face* circle detection and a threshold for binarization. From this information, capillary loop density (CLD), depth and area (CLA) as well as the average eccentricity of the detected loops could be calculated.

The idea of observing the capillary loops was further expanded upon in chapter 4. More specifically, we aimed to see if there was any change in the capillary loops and underlying vascular plexus as a result of Atopic Dermatitis (AD), an inflammatory condition of the skin. A volunteer study was conducted in order to collect a large amount of scans with varying severity. In general, the capillary loops appeared to be slightly deeper in the skin for more severe cases of AD, however significance

was only gained when comparing healthy/clinically clear sites to those exhibiting more severe indicators of the condition. More interesting was an observed increase in the depth of the superficial vascular plexus, which appeared to be pushed deeper into the skin as the epidermis thickened. Furthermore, morphological changes in the shape of the vessels themselves may hold additional information regarding how the condition is progressing subclinically. Together these results may help shape our understanding of what happens within AD affected skin, particularly past the point of clinical remission. Future studies could look at the response of these metrics to various treatments, in order to track treatment efficacy over time.

Automated measurements of epidermal thickness were performed through segmentation of the epidermal and dermal layers of the skin. This was used during the AD study (Chapter 4) in order to correlate the thickening epidermis with a deepening superficial vascular plexus, here it was found that the epidermis and superficial vascular plexus respond in a similar manner towards localised inflammation. The technique also found application for looking at the deformation of the skin layers induced by natural skin stretching, which is discussed in chapter 6. This brief study demonstrated that the strains applied through extension of the forearm could reduce the measured epidermal thickness at the volar forearm by greater than 15%, highlighting the need for surface strains to be accounted for when performing sensitive measures of epidermal thickness variation.

8.2 Conclusion

Herein it has been demonstrated that high-resolution angiographic imaging is achievable using a commercial Vivosight OCT system, this could greatly facilitate multi-centre clinical studies. Motion artefacts arising from global decorrelation between frame acquisitions are effectively suppressed through both image registration techniques and the novel application of a combined wavelet/FFT algorithm. Vessel detection accuracy was validated for vessels greater than $30\mu\text{m}$ by directly registering OCTA with optical light microscopy, however smaller vessels appeared slightly dilated through OCTA. This implies that studies involving the quantification of smaller vessels with OCTA may overestimate metrics such as vessel density or area.

It has been demonstrated how oncological studies pertaining to murine fibrosarcoma tumours may benefit from OCTA. Notably, the ability to capture the superficial layer of subcutaneous tumour vasculature provides a uniquely high-resolution view of the tumour microcirculation over depth-ranges which are typically only accessible to lower-resolution imaging modalities. Limitations involving the applied surface pressure and use of gaseous anaesthetic may potentially be overcome in the future through use of faster OCT systems, allowing for the first time, non-invasive studies of resistance mechanisms towards anti-angiogenic agents to be studied at microscopic resolution inside subcutaneously grown tumours.

Direct clinical applications of the technique have been demonstrated, including the ability of OCTA to observe wound healing processes and track sub-clinical inflammation within AD affected skin. The latter observation builds upon previous studies using structural OCT to study the effects of corticosteroid treatment on the skin barrier. Moving forward, the combined usage of OCTA and structural OCT has a huge amount of potential for evaluating the efficacy of new treatments and drugs which have recently been developed in the battle against AD. Indeed, the preliminary results presented here have already attracted a great deal of commercial interest, with several key pharmaceutical companies expressing interest in pursuing the further development of OCTA based subclinical biomarkers of AD.

Appendix A

Appendix

A.1 Multi-beam Optical Coherence Tomography

As discussed in Sec. 2.1.1, all OCT images displayed in this thesis were captured using a multi-beam Vivusight OCT system[1]. Multi-beam OCT addresses the limits in depth over which a certain lateral resolution can be achieved at a certain wavelength with SS-OCT. This is achieved through the mosaicing of multiple beams, each with a focal region that is adjacent in depth to the neighboring beams. Fig. A.1 shows how beams of different focal region are generated, and Fig. A.2 shows this arrangement of beams within the tissue.

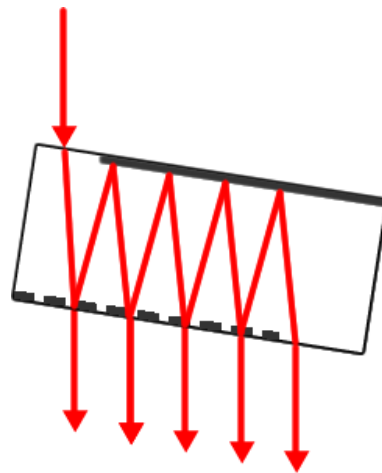


FIGURE A.1: Input laser light is split into multiple depth-offset sources through use of a rattle plate.

The result is four different OCT "channel" images which must then be combined together in order to achieve the benefit of multiple focal depths. One challenge is

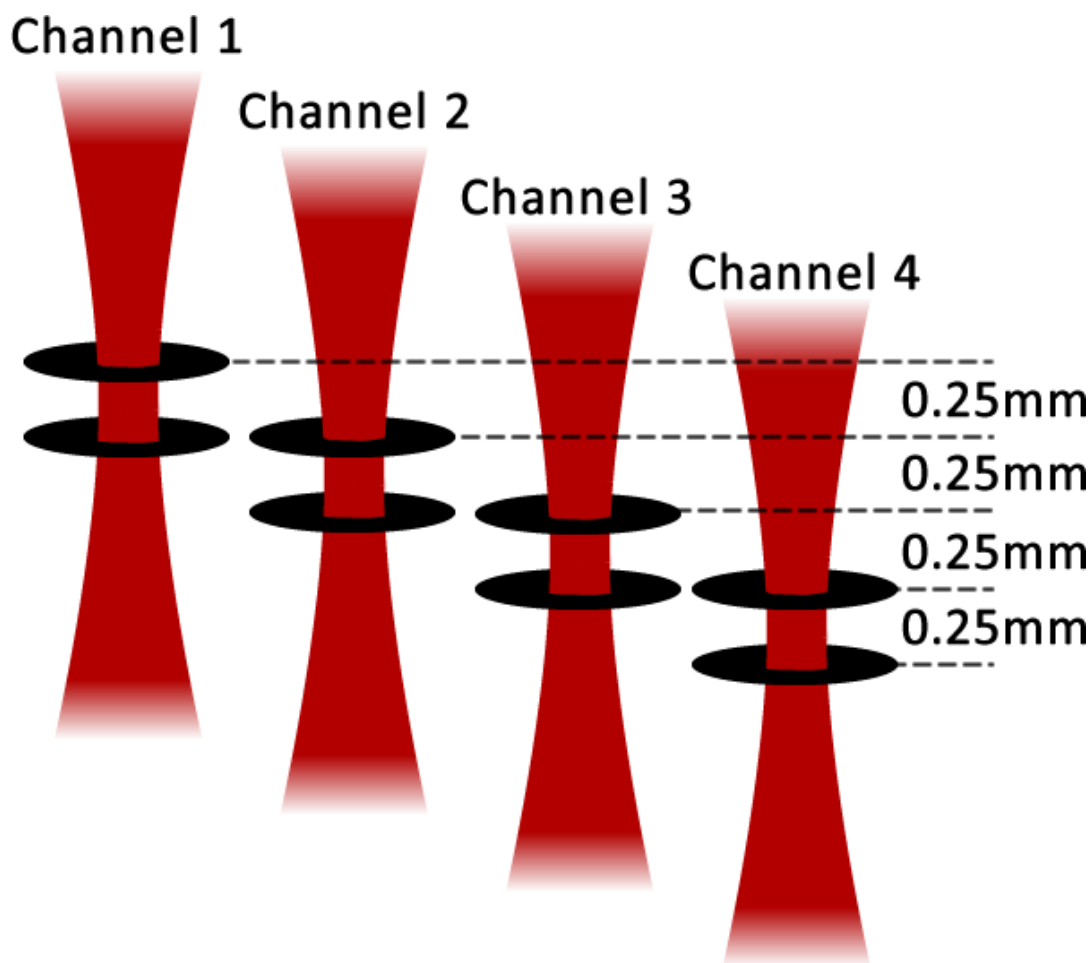


FIGURE A.2: The different depth-focused beams cover a range of 1mm in the tissue, maximising lateral resolution as a function of depth.

in this recombination step, as each beam follows a slightly different optical-path through the tissue, different beams will exhibit differing signal intensity for the same regions of tissue. Thus, a simple averaging operation between the channels will result in visible discontinuities at the channel borders, due to sharp changes in intensity. Furthermore, simply averaging the channels is counterproductive to the end goal of multi-beam OCT (consistent lateral resolution) as one would be effectively averaging out-of-focus beams with in-focus beams, limiting the advantage.

A proprietary blending algorithm was developed by Michelson Diagnostics Ltd[1] for the purposes of mosaicing the channels together with minimal loss of fine detail. An example of this algorithm recombining four channel images is shown in Fig. A.3.

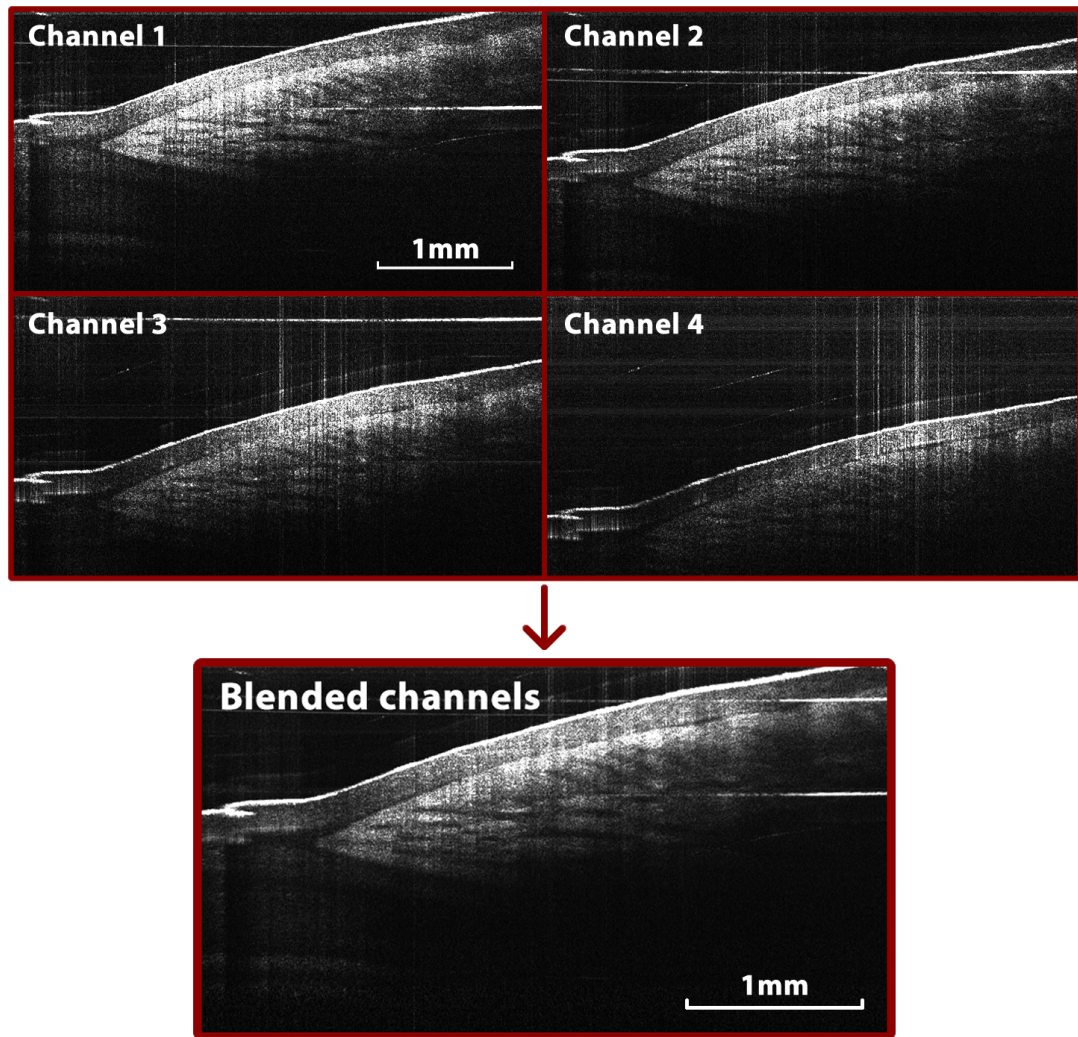


FIGURE A.3: Four channels of the Vivosight being blended together using a proprietary algorithm by Michelson Diagnostics Ltd

For this work, three of the four channels were discarded during image acquisition. With only a single channel being saved to disk and processed. The exception to this being the structural OCT images which were processed in chapter 6, which were not used for angiographic purposes and thus could be processed with the blending algorithm discussed above.

The following reasons explain why this decision was made:

- **Data acquisition time** - A high image acquisition speed is critically important for angiographic imaging, as shorter intervals between frames mean that bulk-tissue motion has less time to occur. The reduction from 4 channels to 1,

reduced the data throughput to disk by a factor of 4, meaning that subsequent scans could be performed faster as they were not waiting for data to save to disk.

- **Angiographic image quality** - It is unclear if the recombination of channel images affects the decorrelation measurement which is central to intensity based angiography.
- **Post-processing time** - The reduction of channels reduced the amount of offline processing time as there was no need to perform resampling/FFT on each channel or blend the channels together. Furthermore, the storage space of data on disk was reduced.

A.2 Sub-pixel accurate image registration

As discussed in Sec. 2.1.3, a simple method of correcting for in-plane bulk tissue motion is to register subsequent frames together such that any translational offset between them is minimised. While in the ideal case, full elastic (deformable) registration would be performed (potentially allowing for correction of internal deformations caused by palpation), the additional computational complexity and required computational time would be unfeasible to perform across large volumes of data. Instead a rapid method of aligning frames using a Fourier-transform based cross-correlation algorithm was adapted from Guizar *et al*[2] and modified to make use of the GPU architecture within MATLAB.

Processing time using the computer CPU (i7 3770K at 3.5 GHz) took on average 64ms per registered frame. Comparatively, performing the bulk of the processing on a GPU (Nvidia GTX 780) meant that processing time was 45ms per registered frame (Including the time taken to send/receive images from the GPU memory). This corresponds to a speedup of approximately 30% through usage of the GPU.

The algorithm used is detailed below:

FFT-based image registration (GPU enabled)

Algorithm written by Manuel Guizar Sicaïros & James R. Fienup. (2016)

Adopted for GPU usage by Robert A. Byers.

Citation for this algorithm:

"Efficient subpixel image registration algorithms," Opt. Lett. 33,156-158 (2008).

Manuel Guizar-Sicaïros, Samuel T. Thurman, and James R. Fienup,

Copyright (c) 2016, Manuel Guizar Sicaïros, James R. Fienup, University of Rochester

All rights reserved.

```
function [registered] = dftregistrationGPU(Image1,Image2,usfac)
```

Efficient subpixel image registration by crosscorrelation. This code gives the same precision as the FFT upsampled cross correlation in a small fraction of the computation time and with reduced memory requirements. It obtains an initial estimate of the crosscorrelation peak by an FFT and then refines the shift estimation by upsampling the DFT only in a small neighborhood of that estimate by means of a matrix-multiply DFT. With this procedure all the image points are used to compute the upsampled crosscorrelation.

This code is ideal for GPU development owing to the low memory requirements of the upsampled DFT and the potential to process numerous frames in parallel.

Inputs: Image1 - Reference image

Image2 - Image to be registered

usfac - Upsampling factor

Outputs: registered - Registered Image2 - the global phase difference is compensated for.

```
% Upload to GPU  
buf1ft = fft2(gpuArray(Image1));  
buf2ft = fft2(gpuArray(Image2));
```

```

if ~exist('usfac','var')
    usfac = 1;
end

[nr,nc]=size(buf2ft);
nr = gpuArray(nr); nc = gpuArray(nc);
Nr = ifftshift(-fix(nr/2):ceil(nr/2)-1);
Nc = ifftshift(-fix(nc/2):ceil(nc/2)-1);

if usfac == 0
    % Simple computation of error and phase difference without registration
    CCmax = sum(buf1ft(:).*conj(buf2ft(:)));
    row_shift = 0;
    col_shift = 0;
elseif usfac == 1
    % Single pixel registration
    CC = ifft2(buf1ft.*conj(buf2ft));
    CCabs = abs(CC);
    [row_shift, col_shift] = find(CCabs == max(CCabs(:)));
    CCmax = CC(row_shift,col_shift)*nr*nc;
    % Now change shifts so that they represent relative shifts and not indices
    row_shift = Nr(row_shift);
    col_shift = Nc(col_shift);
elseif usfac > 1
    % Start with usfac == 2
    CC = ifft2(FTpad(buf1ft.*conj(buf2ft),[2*nr,2*nc]));
    CCabs = abs(CC);
    [row_shift, col_shift] = find(CCabs == max(CCabs(:)),1,'first');
    CCmax = CC(row_shift,col_shift)*nr*nc;
    % Now change shifts so that they represent relative shifts and not indices
    Nr2 = ifftshift(-fix(nr):ceil(nr)-1);
    Nc2 = ifftshift(-fix(nc):ceil(nc)-1);
    row_shift = Nr2(row_shift)/2;
    col_shift = Nc2(col_shift)/2;
    % If upsampling > 2, then refine estimate with matrix multiply DFT
    if usfac > 2,
        %%% DFT computation %%%
        % Initial shift estimate in upsampled grid
        row_shift = round(row_shift*usfac)/usfac;
        col_shift = round(col_shift*usfac)/usfac;
        dftshift = fix(ceil(usfac*1.5)/2); %%% Center of output array at dftshift+1
        % Matrix multiply DFT around the current shift estimate
        CC = conj(dftups(buf2ft.*conj(buf1ft),ceil(usfac*1.5),ceil(usfac*1.5),usfac,...
            dftshift-row_shift*usfac,dftshift-col_shift*usfac));
        % Locate maximum and map back to original pixel grid
        CCabs = abs(CC);
        [rloc, cloc] = find(CCabs == max(CCabs(:)),1,'first');
        CCmax = CC(rloc,cloc);
        rloc = rloc - dftshift - 1;
        cloc = cloc - dftshift - 1;
        row_shift = row_shift + rloc/usfac;
        col_shift = col_shift + cloc/usfac;
    end
end

```

```

% If its only one row or column the shift along that dimension has no
% effect. Set to zero.
if nr == 1,
    row_shift = 0;
end
if nc == 1,
    col_shift = 0;
end

end

rg00 = sum(abs(buf1ft(:)).^2);
rf00 = sum(abs(buf2ft(:)).^2);
error = 1.0 - abs(CCmax).^2/(rg00*rf00);
error = sqrt(abs(error));
diffphase = angle(CCmax);

output=[error,diffphase,row_shift,col_shift];

% Compute registered version of buf2ft
if (usfac > 0),
    [Nc,Nr] = meshgrid(Nc,Nr);
    Greg = buf2ft.*exp(1i*2*pi*(-row_shift*Nr/nr-col_shift*Nc/nc));
    Greg = Greg*exp(1i*diffphase);
elseif (nargout > 1)&&(usfac == 0)
    Greg = buf2ft*exp(1i*diffphase);
end

registered = gather(abs(ifft2(Greg)));

return

```

Inline function: dftups

Upsampled DFT by matrix multiplication, can compute an upsampled DFT in just a small region.

```

function out=dftups(in,nor,noc,usfac,roff,coff)
[nr,nc]=size(in);
% Set defaults
if exist('roff','var')~=1, roff=0; end
if exist('coff','var')~=1, coff=0; end
if exist('usfac','var')~=1, usfac=1; end
if exist('noc','var')~=1, noc=nc; end
if exist('nor','var')~=1, nor=nr; end
% Compute kernels and obtain DFT by matrix products
kernc=exp((-1i*2*pi/(nc*usfac))*( ifftshift(0:nc-1).' - ...
    floor(nc/2) )*( (0:noc-1) - coff ));
kernr=exp((-1i*2*pi/(nr*usfac))*( (0:nor-1).' - roff )* ...
    ( ifftshift([0:nr-1]) - floor(nr/2) ));
out=kernr*in*kernc;
return

```

Inline function: FTpad

Pads or crops the Fourier transform to the desired output size. Taking care that the zero frequency is put in the correct place for the output for subsequent FT or IFT. Can be used for Fourier transform based interpolation, i.e. dirichlet kernel interpolation.

```
function [ imFTout ] = FTpad(imFT,outsized)
if ~ismatrix(imFT)
    error('Maximum number of array dimensions is 2')
end
Nout = outsized;
Nin = size(imFT);
imFT = fftshift(imFT);
center = floor(size(imFT)/2)+1;

imFTout = gpuArray.zeros(outsized);
centerout = floor(size(imFTout)/2)+1;

cenout_cen = centerout - center;
imFTout(max(cenout_cen(1)+1,1):min(cenout_cen(1)+Nin(1),Nout(1)), ...
    max(cenout_cen(2)+1,1):min(cenout_cen(2)+Nin(2),Nout(2))) ...
    = imFT(max(-cenout_cen(1)+1,1):min(-cenout_cen(1)+Nout(1),Nin(1)), ...
    max(-cenout_cen(2)+1,1):min(-cenout_cen(2)+Nout(2),Nin(2)));

imFTout = ifftshift(imFTout)*Nout(1)*Nout(2)/(Nin(1)*Nin(2));
return
```

FIGURE A.4: FFT-based image registration

A.3 Wavelet-FFT algorithm - Supporting information

Wavelet-FFT filtering[3] falls under a subset of destriping image processing algorithms which aim to suppress line or “stripe” artefacts within an image. Uniform horizontal stripes have high frequency components in the vertical direction, thus a basic implementation of a destriping algorithm may simply attenuate the frequencies along the vertical ($u_x = 0$) axis of the 2D FFT $F(u_x, u_y)$ of an image $f(x, y)$, while maintaining the offset coefficients at $u_y = 0$. Münch et al demonstrated that by first wavelet filtering the image, such that the detail, diagonal, vertical and horizontal components of an image are reversibly condensed into separate bands, FFT filtering can be performed only on the relevant artifact corrupted band, improving preservation of the underlying image information when compared to the purely FFT based method[3].

To perform a controlled comparison of the differences between simple FFT filtering and the combined Wavelet/FFT method used in this thesis, an angiographic

image (Fig. A.5A) captured without any visible motion artefacts had "artificial" motion artefacts added to it (Fig. A.5B).

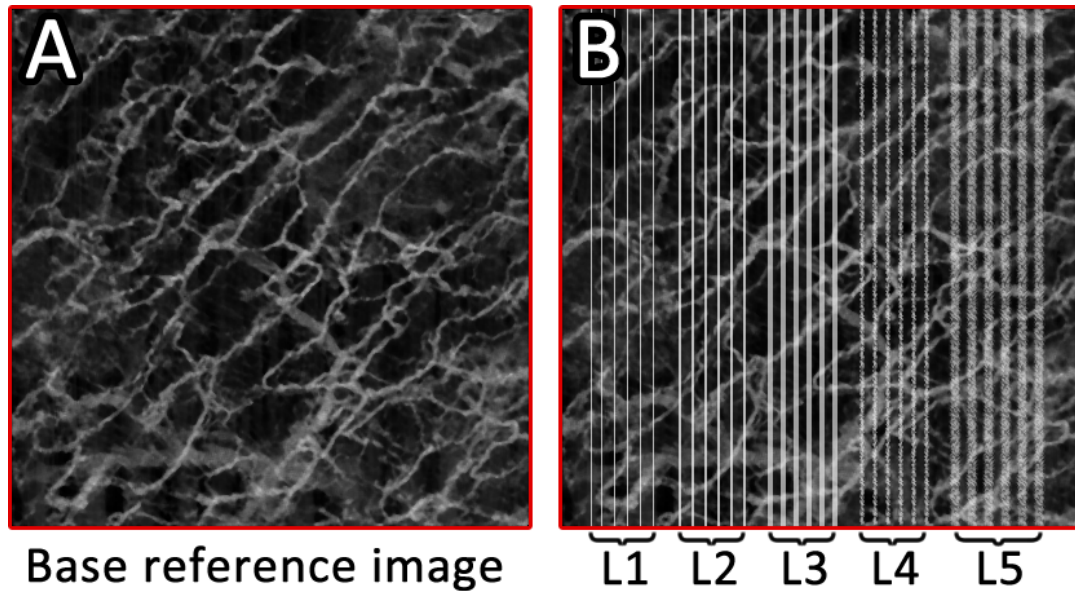
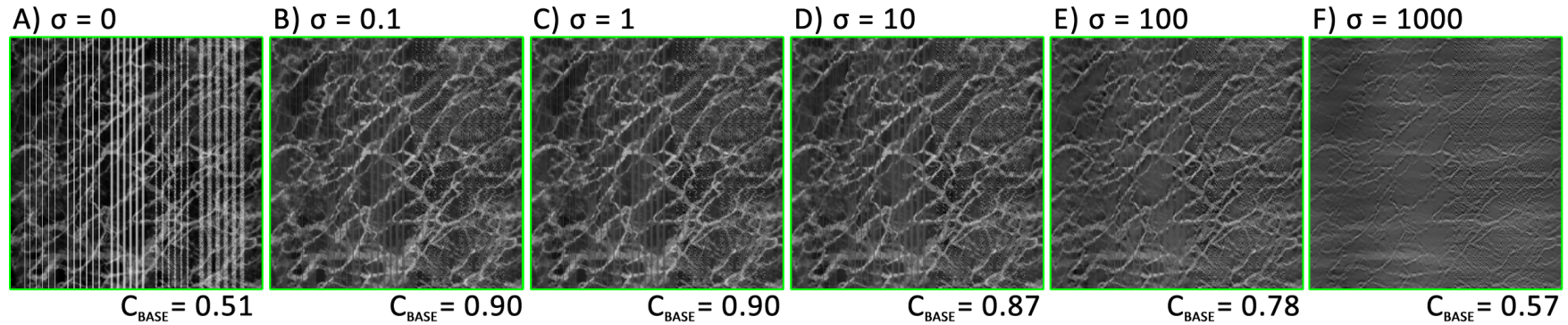


FIGURE A.5: A) A *en-face* angiographic image captured with minimal motion artefacts. B) Artificial motion artefacts which have been introduced to the image, from left to right becoming more challenging to remove: L1 = 1-pixel width, L2 = 2-pixel width, L3 = 4-pixel width, L4 = 4-pixel width "fuzzy lines", L5 = 6-pixel width "fuzzy lines".

From the left side of the image to the right, the added motion artefacts were made larger and more difficult to remove, allowing direct comparison between the ability of both processing methods for the removal of a range of image artefacts. Fig. A.6 shows the result of processing the artefact corrupted image with both algorithms. A value C_{BASE} has been calculated for each of the resulting images, this shows the 2D correlation coefficient between each image and the reference (non-corrupted) image (Fig. A.5A) as a metric of similarity. A value of C_{BASE} close to 1 would indicate that the artefacts have been entirely removed with no loss of structural information.

For the case of the FFT algorithm alone (Fig. A.6A-F), at $\sigma = 0.1$ there is a large jump in C_{BASE} from 0.51 to 0.90, suggesting that the majority of the artefacts had been removed successfully. Upon close inspection however, the larger artefacts are still visible (but are notably attenuated) up to a value of approximately $\sigma = 100$ before disappearing almost entirely at $\sigma = 1000$. One primary observation is the rapid reduction in C_{BASE} as σ is increased, this is caused by corruption of the underlying

FFT Filtering



Wavelet/FFT Filtering

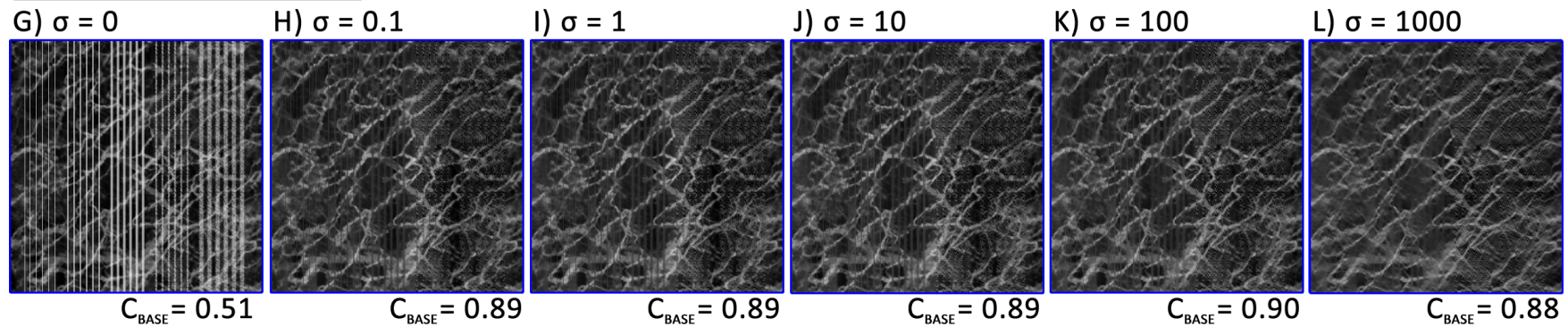


FIGURE A.6: Comparison between FFT filtering and combined Wavelet/FFT filtering for the removal of vertical line artefacts. A-E) Images processed using the FFT algorithm for a range of σ values: A) $\sigma = 0$, B) $\sigma = 0.1$, C) $\sigma = 1$, D) $\sigma = 10$, E) $\sigma = 100$, F) $\sigma = 1000$. G-L) Images processed using the combined wavelet-FFT algorithm (using a 5-level Daubechies filter) for a range of σ values: G) $\sigma = 0$, H) $\sigma = 0.1$, I) $\sigma = 1$, J) $\sigma = 10$, K) $\sigma = 100$, L) $\sigma = 1000$. The value C_{BASE} shown at the lower right corner of each image is the 2D correlation coefficient between that image and the original image (Fig. A.5A).

detail as the filter removes a wider range of artefacts. Notably, for complete removal of the wide and "fuzzy" artefacts (L3/L4/L5), the corruption of the underlying image results in a C_{BASE} that is only slightly higher (0.57) at $\sigma = 1000$ than the original corrupted image (0.51).

In comparison, the combined Wavelet-FFT algorithm (Fig. A.6G-L) offers similar performance for low values of σ . Interestingly, C_{BASE} for $0.1 \leq \sigma \leq 1$ is slightly lower than the pure FFT based method, suggesting that the combined approach may not be ideal for cases where motion artefacts are kept narrow. However, for removal of the wider artefacts at higher values of σ , the combined Wavelet/FFT method performed significantly better, maintaining high values of C_{BASE} even at $\sigma = 1000$. Fig. A.6L demonstrates almost complete removal of the more challenging artefacts (L3/L4/L5) with only a minimal degradation in the underlying image.

As the end goal of such algorithms is often to improve the reliability of subsequent quantification steps (i.e skeletonisation), the ability to remove bright interfering artefacts while minimally affecting the underlying image is a powerful tool. Overall, the simple FFT approach yielded good results for low values of σ but scaled poorly when tasked with the complete removal of more challenging artefacts. Indeed for cases with minimal motion-corruption, FFT filtering alone may actually be superior to the combined approach providing σ is kept low. Comparatively, the combined Wavelet/FFT approach is highly insensitive to parameter choice, making it an excellent candidate for general application across a wide range of images. The segmentation of the detail band through the wavelet operation means that even complete removal of vertical coefficients are unlikely to substantially degrade the image.

The source code used to generate these images can be found in Fig. ?? below:

Vertical FFT and combined Wavelet-FFT filtering

MATLAB implementation of the algorithms discussed in the following paper:

B. Münch et al., "Stripe and ring artifact removal with combined wavelet-Fourier filtering.," Opt. Express 17(10), 8567–8591 (2009).

Input: image - Input image to be filtered with both methods

sigma - Value of σ to be used.

```
function [imageFFT,imageWaveletFFT] = waveletFFT(image,sigma)
```

First, do the regular FFT filtering:

```
imageFFT = fftshift(fft2(image));
[y,x] = size(imageFFT);
```

Create a mask based on σ

```
mask = repmat((1-exp(-[-floor(y/2):-floor(y/2)+y-1].^2/sigma))',1,x);
% Maintain the central frequencies
mask(:,floor(size(mask,2)/2)-1:floor(size(mask,2)/2)+1) = 1;
```

Apply the mask to the FFT-image

```
imageFFT = imageFFT.*mask;
```

And revert back to the image domain

```
imageFFT = ifft2(ifftshift(imageFFT));
```

Next, do the combined Wavelet/FFT filtering:

Define the wavelet and order used

```
order = 5;
wavelet = 'db20';

detailBand = image;
```

Perform wavelet/FFT decomposition a total of $n = order$ times

```
for n = 1:order
    [detailBand,horizBand{n},vertiBand{n},diagBand{n}] = dwt2(detailBand,wavelet);
    vertiBandFFT = fftshift(fft(vertiBand{n}));
```

```
[y,x] = size(vertiBandFFT);
mask = repmat((1-exp(-[-floor(y/2):-floor(y/2)+y-1].^2/sigma))',1,x);
vertiBandFFT = vertiBandFFT.*mask;
vertiBand{n} = ifft(ifftshift(vertiBandFFT));
end
```

Rebuild the filtered wavelets by looping backwards a total of $n = order$ times

```
for n = order:-1:1
    detailBand = detailBand(1:size(horizBand{n},1),1:size(horizBand{n},2));
    detailBand = idwt2(detailBand,horizBand{n},vertiBand{n},diagBand{n},wavelet);
end

imageWaveletFFT = detailBand;
end
```

FIGURE A.7: MATLAB source code used to compare between FFT filtering and Wavelet-FFT filtering.

A.4 Fractal dimension analysis - Supporting information

Throughout this thesis, the Hausdorff fractal dimension was calculated using the box-counting method. This is detailed below and illustrated in Fig. A.8:

- 1) An binary image consisting of a vessel skeleton is used as an input to the algorithm.
- 2) The image is padded such that its dimensions are a power of 2 (To allow equal division into boxes).
- 3) Initial box size e is set to the size of the image in pixels.
- 4) The image is broken down into boxes of size e , the number of boxes containing any of the skeleton are counted and stored to $N(e)$.
- 5) If $e > 1$ pixel, then $e = \frac{e}{2}$ and the counting process is repeated from step 4.
- 6) The number of overlapping boxes $N(e)$ and box size e are plotted in log form ($\log(N)$ against $\log(1/e)$).
- 7) A 1^{st} degree polynomial is fitted to the data (Line-fit) using a Vandermonde matrix, the gradient of this line represents an estimate of the Hausdorff fractal dimension.

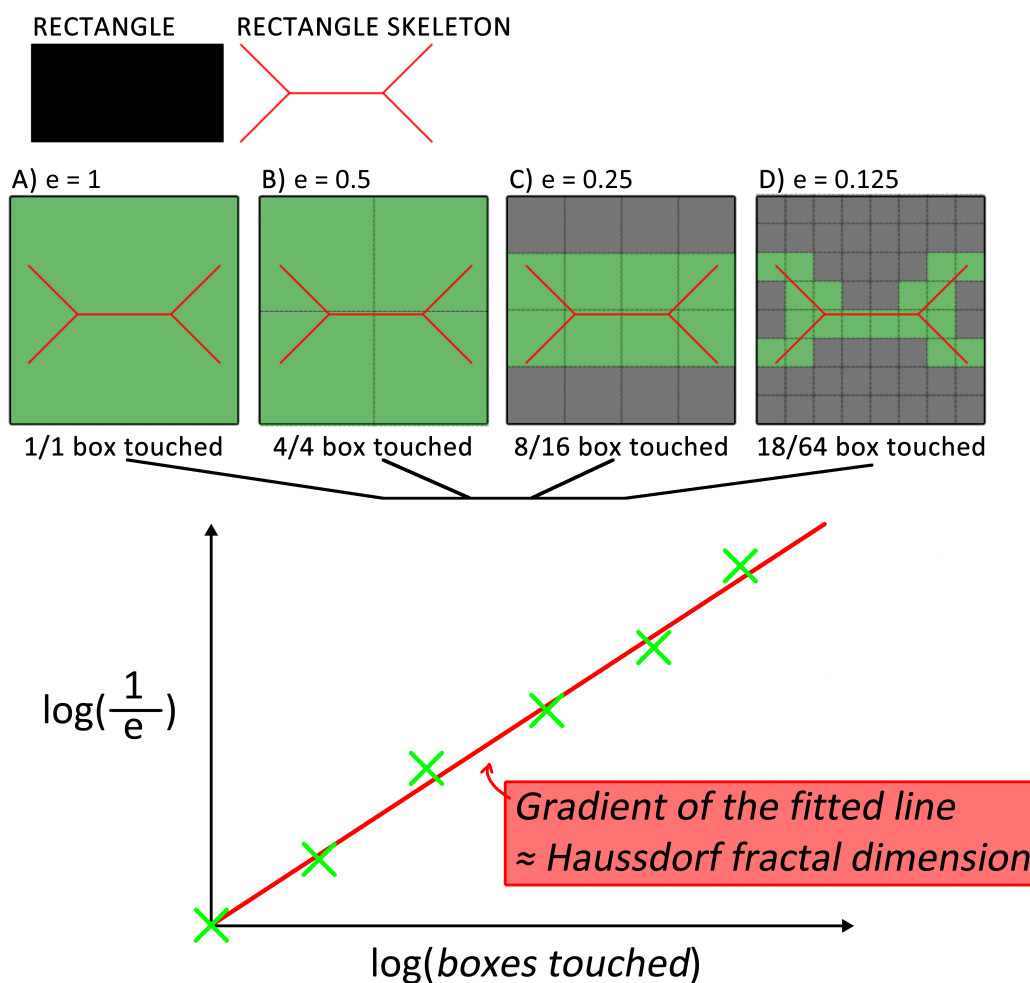


FIGURE A.8: The steps taken to calculate the fractal dimension of an object skeleton, demonstrated here using the skeleton of a simple rectangle. Boxes which the skeleton touch are counted across a range of different box sizes (A-D), these are then plotted as $\log\left(\frac{1}{e}\right)$ against $\log(\text{boxes touched})$ and a line is fitted to the data. The gradient of this resulting line represents an estimate of the Hausdorff fractal dimension.

A.5 ANOVA and Tukey's HSD test - Supporting information

One-way analysis of variance (ANOVA) statistical tests were used throughout the thesis to compare if several groups had a common mean. Most notably this was used in chapter 3 to compare the hypodermis thickness of murine skin, and in chapter 4 to compare between cohorts with differing severities of atopic dermatitis (AD). The tests were implemented using the Statistics and Machine Learning Toolbox within MATLAB ("anova1.m").

Observations (i) of a response variable are first assigned to groups corresponding to their measured independent variable (j) and recorded in a matrix (y_{ij}). In this thesis, the response variable was measured quantities, such as SPD/CLD or hypodermis thickness; while the independent variable was AD severity or tumour type. The one-way ANOVA tests the hypothesis that the mean values of each group ($\bar{y}_{.j}$) are the same, against the alternative hypothesis that at least one of the groups is different from the others. It is assumed that the model is of the form:

$$y_{ij} = \bar{y}_{.j} + \epsilon_{ij}$$

Here ϵ_{ij} is the random error component that is added to each mean, the assumed source of variance within each group.

The overall variation within the data is partitioned into two separate components:

- Firstly the overall sample mean $\bar{y}_{..}$ is subtracted from the sample mean of each group $\bar{y}_{.j}$ to establish the variation in the group means from the overall mean. $(\bar{y}_{.j} - \bar{y}_{..})$
- Secondly, the sample mean of each group $\bar{y}_{.j}$ is subtracted from each measurement (i) within the group to establish the variation within each group. $y_{ij} - \bar{y}_{.j}$

From these separate components, the total sum of squares (SST) is calculated by summing up the above two contributions:

$$\sum_i \sum_j (y_{ij} - \bar{y}_{..})^2 = \sum_j n_j (\bar{y}_{.j} - \bar{y}_{..})^2 + \sum_i \sum_j (y_{ij} - \bar{y}_{.j})^2$$

Here, n_j is the sample size for group j . If the inter-group variation is much larger than the intra-group variation, then it can be concluded that the group means are significantly different from each other. To gain more specific information about which

group means are different from other groups, it is necessary to perform further testing. While a series of student t-tests could be conducted in order to establish significance between the individual means, this is not recommended as each test that is conducted will compound the likelihood of errors as the tests themselves are not independent. To compensate for this, a multiple comparison procedure is used, in this case the Tukey's Honestly Significant Difference (HSD) Procedure was selected as it has proven to be conservative for one-way ANOVA with differing sample sizes (As is the case here)[4]. Tukey's HSD criterion rejects the null hypothesis H_0 between group means $\bar{y}_{.j1}$ and $\bar{y}_{.j2}$ if

$$\frac{|\bar{y}_{.j1} - \bar{y}_{.j2}|}{\sqrt{MSE(\frac{1}{n_{j1}} + \frac{1}{n_{j2}})}} > \frac{1}{\sqrt{2}} q_{\bar{y}, k, N-k}$$

Here MSE is the mean squared error, k is the number of groups, N is the total number of observations and q is the upper $100 * (1 - \bar{y})$ th percentile of the studentised range distribution.

A.6 Vivosight depth calibration

As OCT is a coherence gating technique, the image is effectively a plot of optical delay rather than a spatial depth. Indeed, as the propagation speed of light v varies as a function of the refractive index of the medium ($n = \frac{c}{v}$), exact measures of depth are highly dependent on the sample properties. It is, therefore extremely challenging to characterize precise depths within anisotropic tissues.

To calibrate the observed image depth with the Vivosight probe as a function of wavelength, images were acquired through a borosilicate glass (BSG) slide with known refractive index ($n = 1.514$) and thickness ($t = 1mm$). The pixel offset between the lower and upper glass faces was then measured (See Fig. A.9).

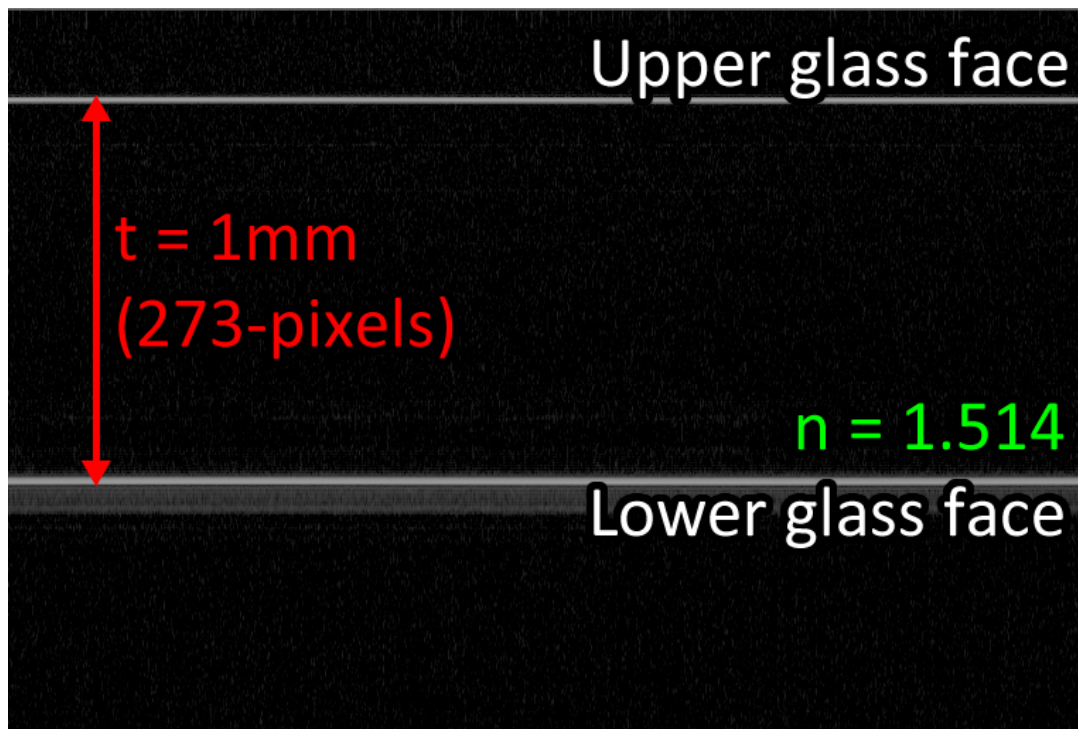


FIGURE A.9: Calibrating the depth measurements of the Vivosight with a glass slide of known refractive index ($n = 1.514$) and thickness ($t = 1mm$).

It is assumed that the refractive index in human dermal skin at 1305nm is approximately 1.4 based on prior observations[5], [6], thus the light would be expected to propagate $\frac{n_1}{n_2} = \frac{1.514}{1.4} = 1.08$ times faster in the case of skin compared to the glass slide. Since the light is effectively propagating through the coverslip twice, being backscattered from the lower glass face, the additional propagation time resulting from the increased refractive index is doubled. In this case, the light is traveling a distance $2t = 2000\mu m$ between the two faces of the coverslip, through glass this is detected as a distance of $273 * 2 = 546$ pixels (Or $3.7\mu m$ depth per pixel), for tissue this would be $\frac{273*2}{1.08} = 505$ pixels (Or $3.9\mu m$ depth per pixel). Depth measurements within this thesis have been calculated using this figure of $3.9\mu m$ per pixel from the surface of the skin.

A.7 Vivosight phase stability analysis

A phase-stability evaluation was conducted with the Vivosight OCT system in order to determine the feasibility of phase-based methods (See Sec. 1.3.3). For SD-OCT, a phase-sensitive image is generated by simply measuring the difference in phase between adjacent A-scans at a fixed depth. Under perfect conditions, one would expect a stationary reflector such as a mirror to have a constant phase with respect to time, however various factors can cause unwanted fluctuations in phase. Small mechanical vibrations of the sample, galvanometer jitter, wavelength sweep variability (in SSOCT), detection noise and trigger timing jitter describe some of the factors which can potentially make a system less "phase-stable".

To measure the phase-stability of the system, a mirror was placed close to the 0 OPD point and the lateral scanners disabled (fixed at 0/0). A total of 4560 A-scans were then collected with an interval of 0.05ms between scans. The phase at the surface of the mirror was then calculated (Fig. A.10).

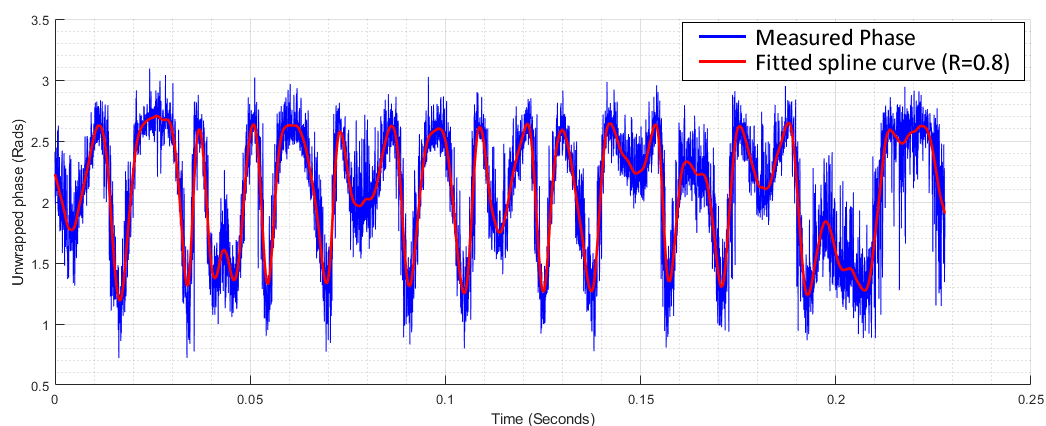


FIGURE A.10: Phase measured at the surface of a stationary mirror across 4560 A-scans with 0.05ms between each acquisition. The blue line represents the phase data, and the red line is a fitted smoothing spline curve which is later used to remove the large scale variations from the measurement (Likely to be mechanical vibrations).

Large fluctuations in phase were visible, likely caused by mechanical vibrations of the mirror due to the environment. To remove these, a smoothing spline was fit to the data before being subtracted from the raw phase data, effectively normalising the smaller phase fluctuations around 0 (Fig. A.11A)

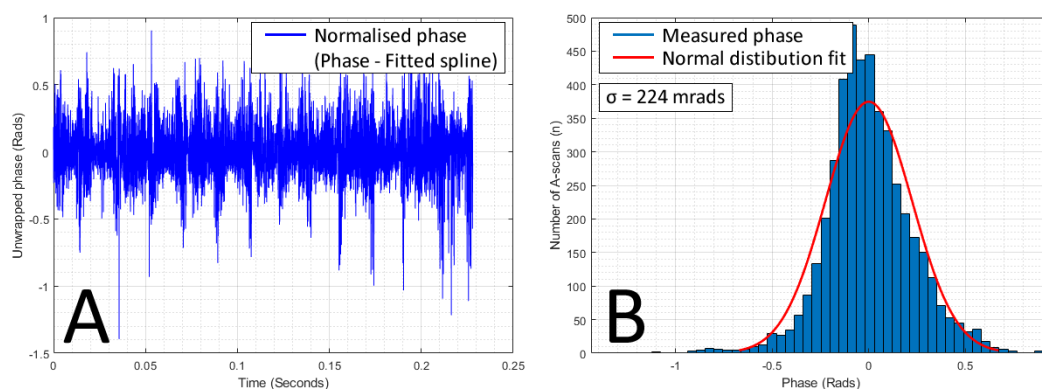


FIGURE A.11: A) Normalised phase - The result of subtracting the smoothing spline from the original data. The large fluctuations have been removed. B) Histogram plot of the resulting phase data. *Bars:* Counted phase distribution for 4560 A-scans. Bin size = 50 mrad. *Red line:* Gaussian (Normal distribution) fit to the data ($\mu = 0$ rads, $\sigma = 224$ mrad)

A histogram was generated by allocating the phase readings into bins of size 50 mrad, with a Gaussian (Normal distribution) being fitted to the data (Fig. A.11B). From this, the baseline phase stability was measured to have a standard deviation of $\sigma = 224$ mrad.

To evaluate this performance in the context of angiographic imaging, two scans were collected from a volunteers dorsal palm in order to compare between the intensity and phase based methods. The first volume scan was collected using a phase-based acquisition protocol, with each B-scan consisting of 4000 closely sampled A-scans ($\Delta x = 0.01\mu\text{m}$ spacing), an area of $4\times 4\text{mm}$ was scanned with $\Delta y = 10\mu\text{m}$ or 400 B-scans total. The second volume scan was collected using an intensity-based acquisition protocol similar to that described in Sec. 2.1.2, with each B-scan consisting of 400 A-scans ($\Delta x = 10\mu\text{m}$), 10-repeats ($N = 10$) over an area of $4\times 4\text{mm}$ ($\Delta y = 10\mu\text{m}$) or 4000 B-scans total. Both data sets were the same size on disk, and took approximately the same time to acquire.

The phase-based dataset was processed using a phase-variance algorithm, calculating the variance in the phase signal over 10-neighboring A-scans. The intensity-based dataset was processed using the speckle-variance algorithm, calculating variance in the intensity signal over the 10-repeat B-scans. For simplicities sake, no other

processing algorithms (e.g surface flattening, image registration, wavelet/fft filtering) were applied to the datasets. Fig.A.12 shows the results of this processing.

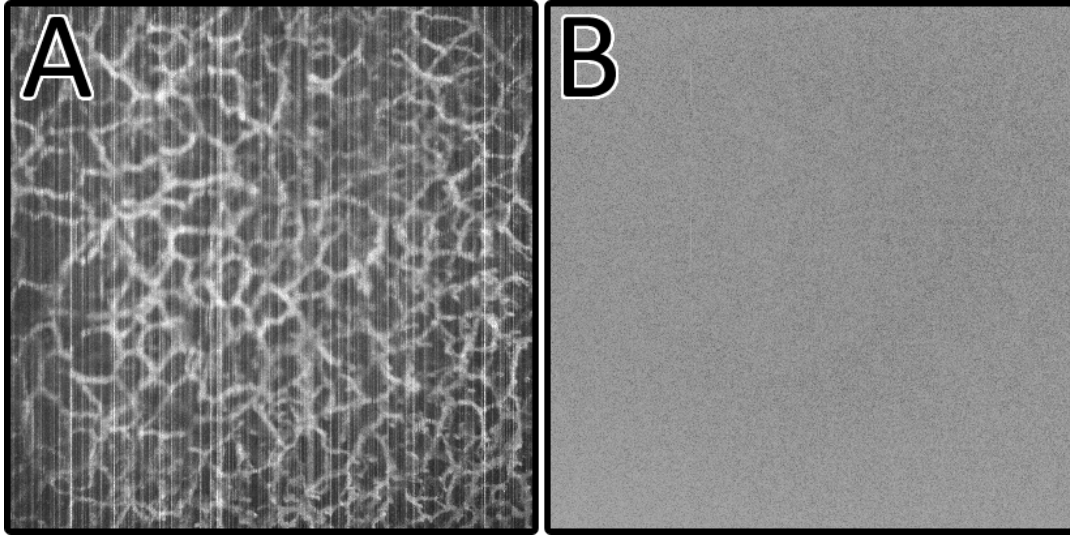


FIGURE A.12: A) *En-face* mean intensity projection of vessels acquired and processed using intensity-based methods. B) *En-face* mean intensity projection of vessels acquired and processed using phase-based methods. Both projections were calculated between depths of 50 and 200 pixels.

Unfortunately the phase-based method failed to exhibit any visible vessel signal, suggesting that the phase-stability of the system is not sufficient in order to discern variations in the phase caused by flow. Indeed, phase-variations may be reduced just by nature of the vessels, as Doppler based techniques are only sensitive to longitudinal flow velocity. As a result of the low contrast and additional sensitivity to motion, phase-based methods were not pursued further within this thesis, with intensity-based methods (svOCT and cmOCT) being used throughout.

Appendix References

- [1] J. Holmes, "Theory and applications of multi-beam OCT", Sep. 2008, p. 713-908. DOI: 10.1117/12.821006 (cit. on pp. 245–246).
- [2] M. Guizar-Sicairos, S. T. Thurman, and J. R. Fienup, "Efficient subpixel image registration algorithms", *Optics Letters*, vol. 33, no. 2, p. 156, 2008, ISSN: 0146-9592. DOI: 10.1364/OL.33.000156 (cit. on p. 248).
- [3] B. Münch, P. Trtik, F. Marone, and M. Stampanoni, "Stripe and ring artifact removal with combined wavelet-Fourier filtering", *EMPA Activities*, vol. 17, no. 2009-2010 EMPA ACTIVITIES, pp. 34–35, 2009, ISSN: 16601394. DOI: 10.1364/OE.17.008567 (cit. on p. 252).
- [4] Y. Hochberg and A. C. Tamhane, *Multiple comparison procedures*. Wiley, 1987, p. 450, ISBN: 9780470568330 (cit. on p. 260).
- [5] F. P. Bolin, L. E. Preuss, R. C. Taylor, and R. J. Ference, "Refractive index of some mammalian tissues using a fiber optic cladding method", *Applied Optics*, vol. 28, no. 12, p. 2297, Jun. 1989, ISSN: 0003-6935. DOI: 10.1364/AO.28.002297 (cit. on p. 261).
- [6] H. Ding, J. Q. Lu, W. A. Wooden, P. J. Kragel, and X.-H. Hu, "Refractive indices of human skin tissues at eight wavelengths and estimated dispersion relations between 300 and 1600 nm", *Physics in Medicine and Biology*, vol. 51, no. 6, pp. 1479–1489, Mar. 2006, ISSN: 0031-9155. DOI: 10.1088/0031-9155/51/6/008 (cit. on p. 261).